UNIVERSITY OF LIVERPOOL

Finite Element Modelling of Retinal Detachment

Thesis submitted in accordance with the requirements of the University of Liverpool for the degree of Doctor in Philosophy by

Ali Aboulatta

June 2021

I dedicate this thesis to my parents for their endless love, support and encouragement.

Abstract

Retinal detachment is a serious condition that most commonly occurs in the elderly; if left untreated, it can lead to complete or partial blindness [1]. Rhegmatogenous retinal detachment is the most common type of detachment of the retina. It occurs due to a tear in the retina that allows the passage of the vitreous to the space between the retina and the choroid [2]. In order to make sure that the retinal detachment does not progress to the macula, reducing or stopping the growth of the retinal detachment is vital in the period between diagnosis and surgery [3]. However, it is not known what loads on the eye contribute the most to retinal detachment progression. This study aims to identify the role of head movements and saccadic movements on retinal detachment progression. This has been done by creating a finite element model that includes all the eye components with assigned material properties. A mesh convergence study was carried out to identify the optimum mesh for the study. Primary results showed that saccadic eye movements apply less stress on the retina than head movement. Moreover, the results show that the size of vitreous detachment is proportional to the extent of retinal detachment.

A new experimental technique was developed to determine the vitreous properties. A custom-built computer-controlled test rig was designed to support, load and monitor eye globes' behaviour while being subjected to dynamic rotation cycles mimicking saccadic eye movement. A digital image correlation algorithm was developed to analyse the images obtained during the experiment to trace the movement of marked points on the vitreous surface with different radii from the posterior chamber's centre. The initial camera image was used to build a finite

element model of the test set up, which was used in an inverse analysis exercise to estimate the vitreous material properties. The inverse analysis exercise estimated the initial shear modulus, the long-term shear modulus and the viscoelastic decay constant of the porcine vitreous as 2.10±0.15 Pa, 0.50±0.04 Pa and 1.20 ±0.09 s^{-1}, respectively. Consideration of the viscoelasticity of vitreous was essential to represent its experimental behaviour. Testing the vitreous in close to its normal physiologic conditions produced estimations of the initial shear modulus and long-term shear modulus that were respectively smaller and larger than reported values [2, 4, 5].

The study produced useful results on the role of head and saccadic eye movements in the development of retinal detachment, indicating that head movements are more likely than saccadic movements to lead to retinal detachment progression. The study has also suggested that vitreous detachment size is directly proportional to the progression of retinal detachment. The study also has investigated experimentally the viscoelasticity of the vitreous humour in order to determine its initial and long-term shear moduli. The emphasis has been on testing and loading the vitreous in close to the natural physiological conditions, and hence removing some of the possible sources of errors introduced in earlier research.

Publications

The following journal articles were prepared in relation to this thesis:

Vroon, J., de Jong, J., Aboulatta, A., Eliasy, A., van der Helm, F., van Meurs, J., Wong, D. and Elsheikh, A., 2018. Numerical study of the effect of head and eye movement on progression of retinal detachment. *Biomechanics and Modeling in Mechanobiology*, 17(4), pp.975-983.

Aboulatta A, Abass A, Makarem A, Eliasy A, Zhou D, Chen D, Liu X, Elsheikh A. 2021. Experimental evaluation of the viscoelasticity of porcine vitreous. J. R. Soc. Interface 18: 20200849. https://doi.org/10.1098/rsif.2020.0849

Aboulatta A, Abass A, Makarem A, Eliasy A, Elsheikh A. Vitreous effect on the progression of retinal detachment due to saccadic and head movements (under Review by Journal of the Royal Society Interface)

Acknowledgements

Firstly, I would like to express my appreciation to Prof. Elsheikh for his guidance throughout the past 4 years. Without his valuable assistance, this work would have not been completed.

Similarly, I would like to express my sincere gratitude to my secondary supervisor, Dr. Abass, for his valuable assistance during the project.

Last but not least, I would like to thank all the members of the Ocular Biomechanical group at the University of Liverpool. Their generous advices and suggestions helped me a lot during my time here.

Table of Contents

List of Figures

List of Tables

List of Abbreviations

CCT	central corneal thickness
FE	finite element
FEA	finite element analysis
FEM	finite element modelling
GA	genetic algorithm
GAGs	glycosaminoglycans
IOP	intraocular pressure
IPM	inter-photoreceptor matrix
PCT	peripheral corneal thickness
PSD	power spectral density
PSO	particle swarm optimisation
PVD	posterior vitreous detachment
PVC	posterior vitreous cortex
RPE	retinal pigment epithelium
RMS	root mean square
RRD	rhegmatogenous retinal detachment

1. Introduction

1.1 Background

The eye is one of the essential components of the human body. It enables humans to observe objective information from the world. It allows people to perceive the world around us by characterising the colours and shapes of objects. The eyes are capable of adapting to changes in light conditions as well as to object position. By observing the depth and scale of the objects, they allow us to see in three dimensions.

The eyes' importance has attracted many scientists, over thousands of years, to understand and investigate its function. The first theorists of the eye are the Greek philosophers such as Plato and Empedocles [6, 7]. These ancient thinkers firstly believed that the sense of sight is similar to touch. A divine illuminating fire was thought to be contained in the eye. It was assumed that this illuminating fire was emitted out of the eye to detect the subject's environment. This theory is recognised as the emission or extra-mission concept [8].

The first to consider the eye's optics was Euclid of Alexandria; he believed in extra-mission concept and developed it to establish the law of reflection [9]. He managed to calculate the angle of reflection and incidence by considering that light came from within the eye. Later, it was proved that extra-mission is not the process of vision. However, Euclid's calculations were independent of light direction; therefore, they provided a strong basis for all the studies that followed [10].

Another theory was that of intro-mission; this was held around the time of Euclid of Alexandria. Aristotle believed that the object itself was projected into the eye by transmitting its shape. It was believed at this time that the organ of sight is a crystalline lens. This theory was also assumed by Galen, a Greek surgeon [11].

During the Islamic era, in the 8th to 12th century, the concept of intro-mission developed into a theory that the rays of light pass through the pupil into the eye. This process transmits the object's information, rather than a part of the object itself [12]. In 984 AD, Ibn Sahl was the first to describe the mathematics used to explain the path of light related to the refractive index and incidence angle [13]. Ibn Al-Haytham, another Islamic scientist, conducted many experiments to develop binocular vision theories. He explained the interaction of light and the cornea and the eye's anatomy in the Book of Optics [14].

In the early 17th century, a German scientist, Johannes Kepler, was the first to find out that the images are projected on the retina, and are reversed and inverted by the eye lens. Kepler is considered the father of modern refractive correction such as contact lenses, glasses and refractive surgeries [15].

Between 1642 and 1726, Sir Issac Newton investigated the eye by inserting a needle behind the ocular globe. After Newton, scientists concentrated on sensory aspects to examine vision science. These aspects included the image captured on the retina and the perception of colour.

Despite research and development of many treatments for different visual conditions for thousands of years, there are still huge numbers of patients suffering from visual diseases such as glaucoma, retinal detachment and myopia. For instance, retinal detachment occurs with rates of around 20 in 100,000 per year [16]. Retinal breaks exist in about 6% of eyes in both autopsy and clinical studies [17]. In the Netherlands, 18.2 in 100,000 are diagnosed with retinal detachment [18]. Moreover, in the 1980s, 12 in 100,000 were diagnosed in the United States [19]. Degenerative retinal cases such as age-related macular degeneration and retinitis pigmentosa affect nearly two million people in the United States [20]. On the other hand, a

condition such as myopia affects 84% of the East-Asian urban populations [21-23]. In the western world, glaucoma affects 105 million globally; 5.2 million of those are considered blind [24].

1.1.1 Ocular biomechanics and simulation

Until the mid-1960s, biomechanics did not properly appear as a separate field of study; only in recent decades that it has been used in vision science [25]. There has been a significant improvement in the representation of the human eye using biomechanics. Many numerical and mathematical models of the human eyes have been simulated to describe the response of the ocular globe to internal and external forces, and the mechanical response of the eye to injuries, diseases and surgeries [26-30].

Researchers have investigated the human eye over the last decades using finite element modelling (FEM). The majority of these researches used finite element methods to study the damage caused in the eye due to impacts. Rossi et al. [5], Uchio et al. [31], Karimi et al. [32], Liu et al. [2] and Stitzel et al [33] investigated the impact of an external source or explosion on the eye. They mainly focused on scleral or corneal tearing; only Liu et al. [2] studied the effect of an impact on retinal detachment.

Moreover, Hans et al. [34] studied retinal detachment due to the baby shake syndrome. Liu and Hans [2, 34] investigated the pressure exerted on the retina due to the vitreous. The vitreous was modelled as a viscoelastic or elastic solid. Only Liu et al. considered retinal adhesion. One of the main drawbacks of the above studies is lack of validation. Only Stitzel et al. [33] managed to validate their models against experimental data, and Liu et al. [2] validated their model against Stitzel's. However, the rest of the studies mentioned above failed to validate their models [34-36].

Scott [37] and Ooi et al. [38] used a finite element model to study the damage that occurred to the eye due to external heat transfer. Others used the finite element

method to study the mechanics of the cornea [39-41]. Few created a finite element model to mimic a specific situation such as a surgical incision [42] or a method for estimating the material properties [43]. Finite element modelling was also used to study the mechanics of the orbit [44].

It is believed that mechanics plays a significant role in the mechanism leading to retinal detachment. Nevertheless, mechanical understanding of the retinal detachment process is still limited. Few studies have been carried out focusing on retinal detachment, and most of these studies focus on the external source impact that led to retinal detachment [5, 31]. Other studies investigate the vitreous body motion and how it leads to retinal detachment [45-47]; none of the mentioned research studied the interaction between the gel and the liquid phase of the vitreous. They all assumed either a completely liquid or gel-like vitreous. This interaction is possibly one of the causes of retinal detachments.

1.1.2 Retinal detachment

Retinal detachment is the separation of the sensory retina from the pigment epithelium. The development of retinal detachment occurs via numerous pathways, including vitreoretinal disorders, such as myopia, that affect the eye's overall shape and size. Moreover, metabolic disease, like diabetic retinopathy, and trauma can lead to retinal detachment [48]. The detachment of the retina could be classified as non-rhegmatogenous or rhegmatogenous.

i Non-rhegmatogenous retinal detachment

Non-rhegmatogenous retinal detachment could take place in two cases. It can occur due to shear traction, without tearing the retina. It can also occur due to the accumulation of subretinal fluid in the subretinal region (the space between the sensory retina and the pigment epithelium). This happens because of damage of the retinal pigment epithelium (RPE), as a result of hypertension rather than a retinal break.

ii Rhegmatogenous retinal detachment

Rhegmatogenous retinal detachment (RRD) is the most common type of retinal detachment, it results from a break in the sensory retina. This break is mostly produced by the vitreous traction on the retinal surface. The vitreous physically pulls a tiny part of the sensory retina away from the pigment epithelium; this is known as retinal tear [49-51]. Retinal detachment can be initiated at the tear flaps by traction at the surface of the adjacent retina. Due to the retinal tear, fluid from the vitreous cavity may also flow into the subretinal space, as it can be seen Figure 1.1. Therefore, vitreous traction and fluid flow into the subretinal space can lead to a retinal tear, leading to RRD.

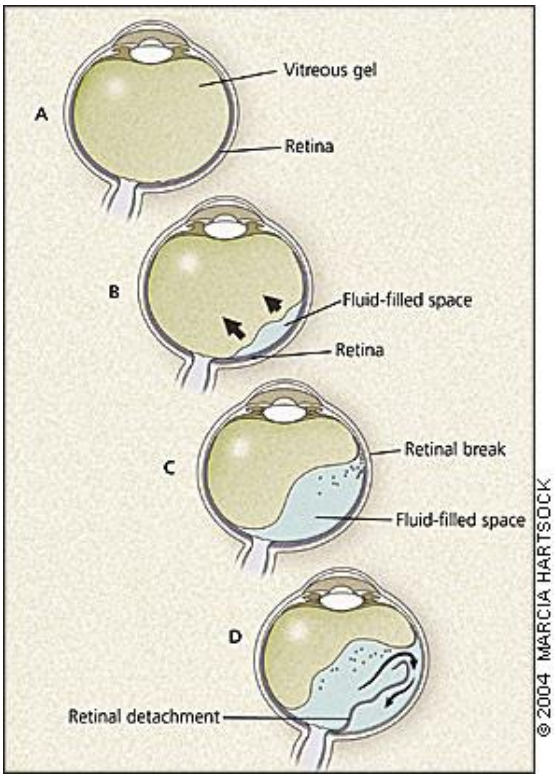

Figure 1.1: Development of retinal detachment. (A) 100% gel vitreous fills the vitreous cavity. (B) Vitreous starts to shrink due to ageing. (C) The vitreous traction leads to retinal break. (D) The liquified vitreous flows into the subretinal space [52]

Retinal break takes place when there is a discontinuity of the neurosensory retina. When the break is due to focal loss of the tissue, it is referred to as a retinal hole.

Vitreous traction can cause horseshoe (flap) tear, which is the most common tear. The horseshoe tears result from the vitreous traction pulling a horseshoe-shaped thin curvilinear flap into the vitreous cavity. This flap contracts to become smaller than the break and this happens due to losing its blood supply. The other type of tear is the linear retinal tear.

The subretinal fluid movement in the space between the retina and the choroid will pull the retina away from the choroid. Researchers have investigated the RRD problem clinically to understand its mechanism. Fatt et al. [53] reported that RRD takes place due to a pre-existing hole in the retina. Quintyn et al. [54] described the mechanism of the subretinal fluid in the pigment epithelium. Few mathematically modelled the retinal detachment by considering surface tension effect and neglecting shear stress [55].

1.2 Scope of research

To further improve the numerical simulation of ocular biomechanics, efforts are needed to help identify conditions that specifically promote extension of retinal detachment. Medical conditions such as glaucoma and myopia have been investigated using numerical analysis [28, 56]. Moreover, retinal detachment due to impacts has been studied by many researchers [2, 57]. However, none of these researchers studied the interaction between the gel and the liquid phase of the vitreous. They all assumed either a completely liquid or gel-like vitreous.

Moreover, this interaction was never considered as one of the possibilities leading to RRD. The effect of the vitreous size or shape on retinal detachment has not been studied, even though vitreous detachment is the main cause leading to RRD. A numerical model is needed to provide some new insight into this gap in knowledge.

Components such as the cornea and the sclera have been much researched over an extended period [58-60]. This has considerably helped our understanding of the mechanical properties related to the eye microstructure. On the other hand, the

vitreous, which accounts for 80% of the eye volume and has a considerable role in eye mechanics, was investigated by many research groups, however, subjecting the eye to non-physiologic conditions led to a wide variation in these parameters. Moreover, some of the parameters determined cannot be employed in Finite Element Analysis (FEA) software. Therefore, a method to measure vitreous properties while keeping and testing the tissue in close to its natural physiologic conditions is needed.

Therefore, this study's scope mainly includes the evaluation of the viscoelasticity of the vitreous gel and the effect of the vitreous shape and volume on retinal detachment.

1.3 Aim and objectives

The research aims to improve the understanding of effect of head and saccades movements on the progression of retinal detachment and to quantify effect of the interaction between the vitreous and its neighbouring structures. To achieve this aim, the following objectives needed to be fulfilled:

- To develop methods to construct characteristic, specimen-specific, geometries of the ocular globe
- To develop an algorithm that is capable of meshing the irregular components of the ocular globe
- To develop a user-friendly tool to generate and mesh the eye models automatically
- To determine the viscoelastic parameters of the vitreous using inverse analysis
- To validate the numerical model against ultrasound scans

1.4 Outline of the thesis

In this thesis, a novel numerical model of the ocular globe that includes the outer layer, retina, choroid, vitreous and liquified vitreous is presented. The model was designed to simulate the interaction between the vitreous and its neighbouring structures. The effect of vitreous volume and vitreous detachment size on the progression of retinal detachment were investigated. A novel approach to determine the viscoelasticity of the vitreous was proposed. A summary of the remaining chapters in this thesis is given below:

- Chapter 2 reviews the latest research into the geometry of the eye and numerical modelling of the ocular globe. The material parameters used in the simulations are introduced, as well as the parameters describing the dynamic loading of the eye. The theories of constitutive modelling and inverse analysis are also introduced.
- Chapter 3 describes the methods used to build the numerical model. A novel meshing algorithm is introduced. Bespoke software to generate numerical models of the ocular globe is presented. The effect of the vitreous volume and detachment size on the progression of retinal detachment is investigated. An overall discussion and a conclusion of the present study are provided.
- Chapter 4 describes the methods and procedures related to the estimation of the viscoelasticity of the vitreous. The experimental techniques and the design of the test rig are presented. The results and the validation in the optimisation algorithm used in the inverse analysis are shown. An overall discussion and a conclusion of the present study are provided.
- Chapter 5 provides an overall discussion of the thesis and its key conclusions; it also includes several recommendations for future work.

1.5 Novel contributions of the thesis

The elements of novelty in this thesis include:

- A novel algorithm to mesh the irregular geometry of the eye globe has been proposed
- A full eye model that includes all eye components, including the aqueous, lens, liquified vitreous and vitreous, is proposed for the first time
- Bespoke software to automatically generate and mesh the ocular globe was built
- A novel technique to measure the vitreous properties while keeping and testing the tissue in close to its natural physiologic conditions was developed

2. Literature Review

2.1 Introduction

The literature review starts with a description of the ocular globe anatomy and material properties. The geometry and dimensions of the ocular globe are covered. Moreover, explanation of conditions, such as posterior vitreous detachment (PVD) and retinal detachment, is also included. Mechanical properties of the ocular globe and their abnormality, which could lead to ocular diseases, are introduced. Additionally, constitutive modelling methods and mathematical principles that consider the eye tissue's microstructure are presented. The movements of the eye are shown, and their effects are covered. Finally, the particle swarm optimisation algorithm is introduced, and its implementation in the field of ocular biomechanics is covered.

2.2 Ocular globe anatomy

The eye consists of three layers or coats; the fibrous tunic layer, the vascular tunic and the inner layer. The fibrous tunic layer or the outer layer is made up of the cornea and the sclera. The vascular tunic or the middle layer is composed of the ciliary body, choroid, iris and pigmented epithelium. As shown in Figure 2.1, the lens' posterior cavity is filled by the vitreous humour or the vitreous body. In addition to the three layers, there are three fluid chambers; these chambers are the posterior chamber which is between the lens and the iris, the anterior chamber which is between the iris and the cornea, and finally the vitreous chamber, between the retina and the lens [61]. A thick fluid, vitreous humour, is enclosed in the vitreous chamber. This fluid provides the eye with its shape, and it is the path the light passes through before

reaching the optic nerve, this is how signals, such as images and information are transmitted to the brain, making vision possible [62].

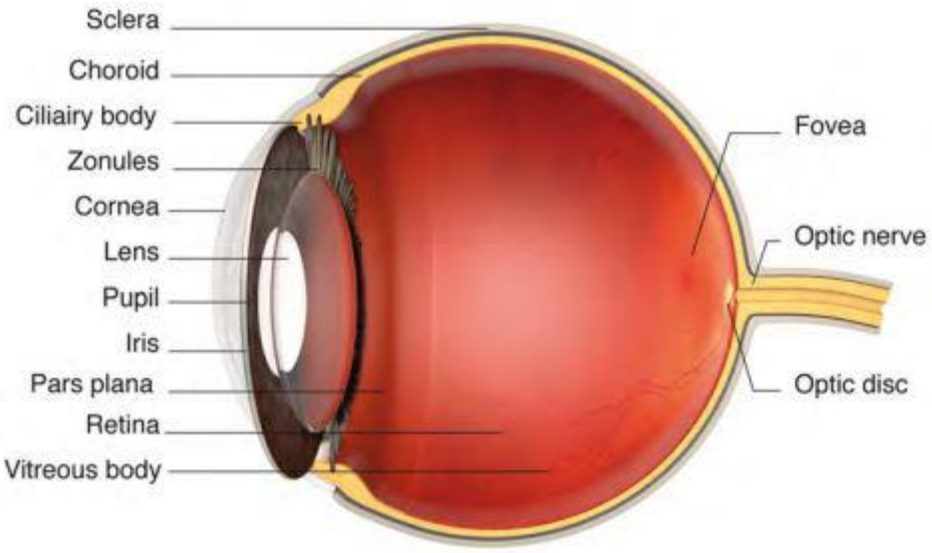

Figure 2.1: Anatomy of the ocular globe [63]

2.2.1 Cornea

The cornea is the clear front surface of the eye. It is located in front of the pupil and the iris, and it permits light to enter the eye. The cornea is a crucial element of the fibrous tunic layer. It offers the ocular contents with a rigid protective envelope. Two-thirds of the eye's optical power are accounted for in the anterior corneal surface. The cornea's contribution to the formation of the ocular image can be affected by the deviation in shape caused by injury, disease and surgery [40]. The cornea is one-sixth the sclera's size with an approximated central radius of 7.87 mm and diameters in the superior-inferior and the nasal-temporal directions of 11.75 and 10.6 mm, respectively [64]. The anterior curvature of the cornea flattens towards the limbal junction with an asphericity of 0.82. The limbal junction or limbus is the intersection of the sclera and the cornea. The limbus is a transitional zone with widths of 2 and 1.5 mm in the superior-inferior and nasal-temporal, respectively.

In adult eyes, the peripheral corneal thickness (PCT), near the limbus, is 670 µm [65] increasing to a central corneal thickness (CCT) of 550 µm [66-68]. A study by Galgauskas et al. [69] found that from age 20-29 to age 80-89, CCT thinned from 563±44 to 540±35 mm. Therefore, a central spherical radius of 6.40 mm with asphericity of 0.62 can describe the change in thickness of the posterior cornea's topography [64].

2.2.2 Sclera

The sclera borders with the cornea and covers the rest of the eyeball. It acts as a tough barrier that prevents intraocular structures from sustaining injuries. The sclera serves as an attachment for the extraocular muscles; moreover, it controls the eye's shape during significant events that promote globe deformation, such as accommodation, eye movements and intraocular pressure (IOP) fluctuations. The sclera ensures the stability of vision and that the globe does not break-up [70]. Therefore, the sclera has good strength and a degree of elasticity. These properties have to be maintained while remodelling to allow the eye's growth to be proportional to its refractive power and to replace damaged extracellular matrix components. This is vital to ensure that the globe remains free from major refractive error throughout life [71]. The sclera is the largest section of the ocular globe. It is spherical with a radius of 11.5 mm for an adult eye [72]. In early ages, the scleral thickness is relatively homogeneous. However, it thins in the equatorial and thickens in the posterior region from around 4-5 years old. For adults, thickness ranges from approximately 1000 µm in the posterior region, thinning to 400–500 µm at the equator and then thickening to 500–600 µm at the limbus [73, 74].

2.2.3 Lens

The lens is located behind the iris, and its main job is to focus light onto the retina. The lens is separated anteriorly by the epithelium capsule and by the posterior capsule. Therefore, any damage to the capsule could lead to cataracts (cloudy area

in the lens that leads to a decrease in vision) [75]. The cortex is a softer material surrounding the nucleus, the innermost part of the lens. Zonules are tiny wires that suspend the capsular-like bag enclosing the lens. The lens contains 65% water; this percentage decreases with ageing [76]. The lens modifies its shape to adjust for distance or close vision, this process is called accommodation [77]. To increase its ability to focus on near objects, the lens thickens. However, due to ageing, the lens gets more flexible and gradually loses its accommodation ability. This leads to presbyopia [78].

2.2.4 Aqueous

The anterior segment of the ocular globe is filled with aqueous humour. The aqueous humour is a thin, watery fluid that occupies the space between the iris and the cornea. The ciliary body, the component of the eye that lies behind the iris, continually secretes the aqueous humour. This transparent fluid gives the ocular globe its shape and form, and nourishes the lens and the cornea. It regulates the IOP and provides a transparent medium for its optical function [79]. The essential factor in the formation of the aqueous humour is the transportation of certain solutes. The rate of active solute transport by the ciliary epithelium is the main factor affecting the aqueous secreted amount [80]. The exchange of solute between the cornea and the aqueous is vital for normal corneal metabolism.

2.2.5 Vitreous humour

Underneath the lens, a cavity is filled with a gel-like substance called the vitreous humour. The vitreous has several functions, including mediating the growth of the eye [81], supporting ocular tissues [82, 83] and maintaining a clear path of light rays to the retina [81]. The vitreous provides metabolic requirements to the ocular globe [84]. Moreover, the vitreous protects the eye during any mechanical damages [83].

The vitreous is a delicate, transparent, gel-like structure composed of uniformly distributed collagen fibrils inside a protein, salt and hyaluronic acid solution; Figure

2.2 [85]. Apart from a few cells, the vitreous body is considered largely acellular [63]; by weight, the vitreous is 99% water, 0.1% macro-molecules and 0.9% salts [85]. The macro-molecules are glycosaminoglycans (GAGs) structural proteins, including the collagen and non-collagen fibrils [86]. These fibrils run parallel to each other and are attached, forming a branching meshwork (Figure 2.2). The GAGs are molecules that act like a sponge; water sticks to these molecules, which then helps to maintain the pressure-volume relationship. There are different types of GAGs; however, the most significant three are hyaluronic acid, chondroitin sulphate and heparin sulphate [87, 88].

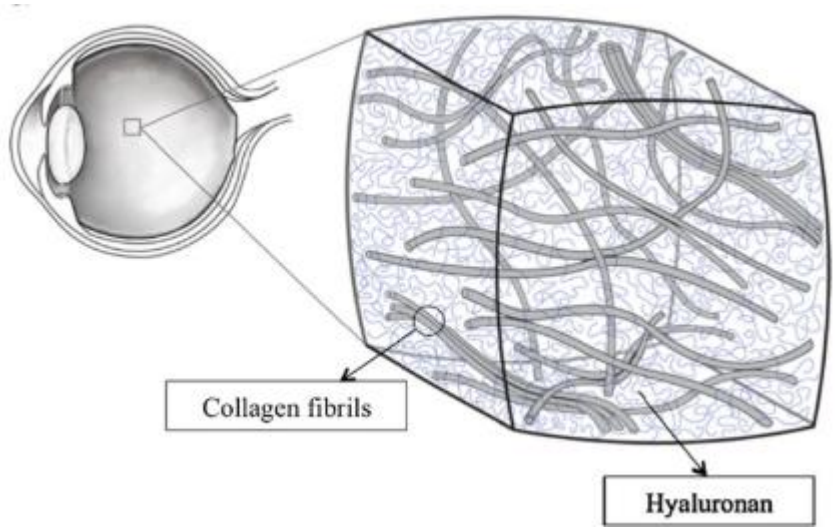

Figure 2.2: A schematic of the macromolecular structure of the vitreous [89]

There are several different types of collagen fibrils; the vitreous body includes type II, V, IX and XI fibrils [90]. If the vitreous is in a gel-like state, type II collagen fibrils connect forming a network. On the other hand, if the vitreous is liquefied, the fibrils are aggregated with one another [91]. The combination of hyaluronic acid and collagen fibrils dictates the vitreous mechanical integrity [92-95]. Therefore, the properties of the vitreous change with the distribution of those components.

The vitreous looks like a sphere with a segment removed anteriorly to provide a depression for the lens. It fills around 80% of the whole eye volume, and it consists of three partitions: the vitreous base, vitreous core, and the vitreous cortex [96]. The

latter is located against the retina and includes the vitreous outer layer, at which the collagen fibres are packed together more densely than the core; therefore, the vitreous body is thicker than at the core. On the anterior side, behind the lens lies the anterior hyaloid membrane, which is the anterior boundary of the vitreous. The vitreous base is located at the equator, where the vitreous is tightly attached to the eyeball. Forming the boundary between the retina and the vitreous body is the posterior hyaloid membrane. Most of the collagen fibrils are originated in the vitreous base. Due to the high concentration of protein fibrils in the vitreous base, the collagen fibrils fan out and fill the vitreous cavity (Figure 2.3) [84].

iii Vitreous detachment

The vitreous humour is attached to the retina throughout the entire cavity. The strength of this adhesion is different from one location to another. The major retinal vessels, the disk margin and the areas closest to the periphery are the typical areas of stronger adhesion [84, 97]. The separation of the vitreous humour usually starts from the posterior pole and advances towards the periphery; this happens due to ageing. The separation is not necessarily uniform; it can occur in one area but be absent in an adjacent area [98].

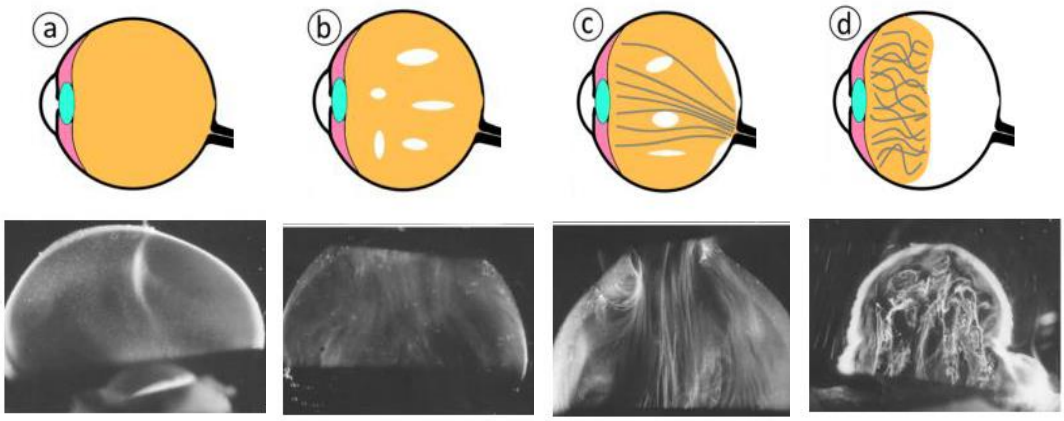

Figure 2.3: Schematic of the ageing process. Images on the bottom represent real scans of the vitreous body. Images are provided for patients who are (a)33 weeks old, (b) 6 years old, (c) 59 years old and (d) 88 years old [84, 99]

As age advances, vitreous liquefaction begins [100, 101]; the explanation behind this is the aggregation of collagen fibrils leading to a collapse of the network inside the vitreous [102]. A young person's vitreous consists of 100% gel, with no free fluid; with ageing, 20% of the total vitreous volume liquefies. More than half of the vitreous body is liquefied by the age of 90 years old [97]. Sebag [84] carried out experiments to study the changes in vitreous structure that occur with ageing. It was found that the vitreous of a 33-week-old human showed a remarkably homogenous appearance (Figure 2.3*a)*. A 6-year-old human vitreous exhibited the onset of irregularities, but no detachment nor distinct fibres (Figure 2.3*b)*. Figure 2.3*c* shows the vitreous body of a 59-year-old human, where the presence of different fibres and classification of the vitreous body can be seen. Finally, Figure 2.3*d* shows the vitreous body of an 88-year-old human; thick clear fibres can be observed as well as reduction in the vitreous size and the separation of the vitreous body.

However, vitreous liquefaction with age is not fully understood due to the lack of reliable measurements of the vitreous mechanical properties in its natural state. Moreover, vitreous liquefaction can cause PVD [103, 104] and retinal detachment, which can cause blindness [105, 106]. For some cases of retinal detachment, vitreous replacement is needed. The vitreous is replaced with a substitute, during vitrectomy, that resembles the vitreous mechanical properties to maintain the IOP inside the eye globe [107-109].

Furthermore, vitreous liquefaction can lead to other problems, such as vitreoretinal diseases that requires pharmacological treatment where drugs are injected in the eye. To decrease the side effects to the tissues of intravitreally injected drugs and increase the therapeutic advantages, the concentration and the distributions of drugs need to be predicted before injection [110]. In the liquefied region, the efficacy of drug delivery through the vitreous reduces because of the reduction of gradients in the drug concentration, which has lower mechanical properties [111]. Thus, accurate measurements of the mechanical properties of the vitreous can help to understand drug transport in vitreous with liquefied areas.

Deficiencies in the vitreous molecular structure and viscoelastic properties have been reported to increase the risk of developing glaucoma, RRD, retinal tear, retinal oedema, vitreous haemorrhage, and choroidal detachment [81, 112, 113]. Moreover, the adhesion of the vitreous to the surrounding ocular structures may make the removal of the vitreous challenging during vitrectomy where the vitreous is to be replaced with a substance such as silicone oil [89, 114].

iv Studies to measure the vitreous mechanical properties

There have been several attempts to describe the composition, structure, and material properties of the vitreous. Significant studies have focused on developing approaches to measure the vitreous humour's mechanical properties (Table 2-1).

Table 2-1: Measurement of viscoelastic properties of the vitreous humour.

Authors	Approach	Parameter
Zimberlin et al. [4]	Cavitation rheology	Elastic modulus Bovine: 120 - 660 Pa
Nickerson et al. [115]	Rheometer using cleated tools	Dynamic shear modulus Porcine: 2.2 – 17 Pa Bovine: 7 – 32 Pa
Bettelheim et al. [92]	Dynamic compression	Dynamic storage modulus Bovine: 3 – 4 Pa
Zimmerman et al. [93]	Relaxation of scattering	Elastic shear modulus Human: 0.05 Pa
Sharif-Kashani et al. [89]	Shear rheometry	Dynamic storage modulus Porcine: 1.08 Pa

Pokki et al. [112]	Magnetic microprobes	Elastic modulus and viscosity Porcine: 13.4 Pa, 96.4 Pa.s
Yoon et al. [91]	Acoustic radiation	Elastic modulus and viscosity Porcine: 8.3 – 34 Pa, 0.035 – 0.052 Pa.s
Lee et al. [116]	Magnetic micro-rheometry	Elastic shear modulus Porcine: 1 Pa Bovine: 3 Pa
Liu et al. [2]	Inverse analysis	Short- and long-term modulus Porcine: 10 Pa and 0.3 Pa
Rossi et al. [5]	Multi-objective optimization	Short- and long-term modulus Porcine: 10 Pa and 2 Pa

The studies used several techniques, such as cavitation rheology [4]. For example, Zimberlin et al. [4] adopted a cavitation rheology technique in which a syringe needle was inserted into the posterior chamber to induce elastic instability via slow pressurization. The pressure at which the instability occurred was then related to the mechanical properties of the vitreous. Moreover, Zimberlin compared measuring the vitreous mechanical properties in vivo and ex vivo. It was reported that monotonic reduction in the mechanical properties of the vitreous after removal from the eye is due to the collapse of the internal network [4, 115].

A study by Nickerson et al. [115] quantitively measured bulk vitreous mechanical properties using 25 mm diameter cleated tools . Others measured qualitatively the phenomena related to physiological changes in the eye [92, 93, 117]. For example, Bettelheim et al. [92] measured the vitreous dynamic viscoelastic properties by subjecting the vitreous to compression. On the other hand, Zimmerman et al. [93] measured human vitreous viscoelasticity in vivo by recording the relaxation of a

scattering pattern. Aguayo et al. [117] studied the vitreous liquefaction using nuclear magnetic resonance (NMR) spectroscopy and imaging.

Pokki et al. [112] measured the vitreous body's viscoelasticity using intraocular magnetic microprobes. The probe was inserted into the vitreous and a camera was used to track the probe's location while wirelessly exerting a magnetic force applied by a magnetic field. A different approach was introduced by Yoon et al. [91] to measure the viscoelastic properties of the porcine vitreous. Yoon and colleagues used a microbubble-based acoustic radiation force to measure the spatial variations of Young's modulus and the shear viscosity of the vitreous humour.

Using a stressed-control shear rheometer, Sharif-Kashani et al. [89] studied the dynamic deformation of porcine vitreous. In another study by Lee et al. [116], the vitreous mechanical properties were obtained from a rheology test using a magnetic micro-rheometer to study small volumes of vitreous samples after extraction from the eye. Liu et al. [2] performed an inverse analysis of Lee's experimental data to obtain the vitreous mechanical properties used in FEA.

Delori et al. [118] conducted experiments to record and measure the deformation of the globe under the high-speed impact . Rossi et al. [5] determined the vitreous material parameters using multi-objective optimization performed on the test data of eye impact experiments carried out by Delori et al. [118].

2.2.6 Choroid

Between the retina and the sclera lies the choroid, consisting of blood vessels that feed parts of the retina. It receives its blood supply from the central retina artery that emerges from the back of the eye [119]. The choroid provides almost 90% of all eye layers' blood supply. It feeds the eye with the needed nourishment to conduct basic cellular functions and removes waste products from the eye. Choroid stiffness is around 374.5 ± 119.3 x 10^3 Pa at a strain of 0.471 ± 0.19 [120]. The thickness of the choroid is approximately 0.21 ± 0.03 mm [120].

2.2.7 Retina

The retina is the light-sensitive layer that lines the inside of the eye. It includes around 126 million sensory cells, which absorb the light entering the eye. These cells are divided into cones and rods; the latter cells are sensitive to light and dark changes, while the cones can detect colour differences. The macula is the central point of the retina where most of the cones are located, and enables vision during daylight. In contrast, the periphery of the central point enables vision in the dark due to the presence of more rods than cones [63]. The retina is divided into a few main regions: the equatorial retina, which lies around the equator, and the peripheral retina, which is anterior to the equator. The boundary, which is the border between the retina and the pars plana, part of the ciliary body, is called the ora serrata.

The retina consists of two layers of neuronal connection and four layers of cells. In addition, the Muller cell is a structural cell that extends through all the retinal layers. The retinal layers are, from inner to the outer retina [121]:

- ***Inner limiting membrane*** – acts as the boundary between the retina and the vitreous. It is laid down by the Muller cells with connections to the hyaloid membrane of the vitreous
- ***Nerve fibre layer*** – the inner surface ganglion cells' fibres pass tangentially towards the optic nerve
- ***Ganglion cell layer*** – is formed of the ganglion cells' axons and cell bodies [122]
- ***Inner plexiform layer*** – includes the synapses between horizontal, bipolar, and amacrine cells
- ***Inner nuclear layer*** – contains the cell bodies of the Muller cells, horizontal cells, bipolar cells, and amacrine cells
- ***Outer plexiform layer*** – also comprises horizontal and bipolar cells, as well as the receptor synapses

- ***Outer limiting layer*** – comprises the junctional complexes from the photoreceptors and Muller cells
- ***Photoreceptor layer*** – transduces light into neuronal signals
- ***Retinal pigment epithelium*** – the last layer before the choroid, it protects the function of the receptors by providing a blood-retinal barrier

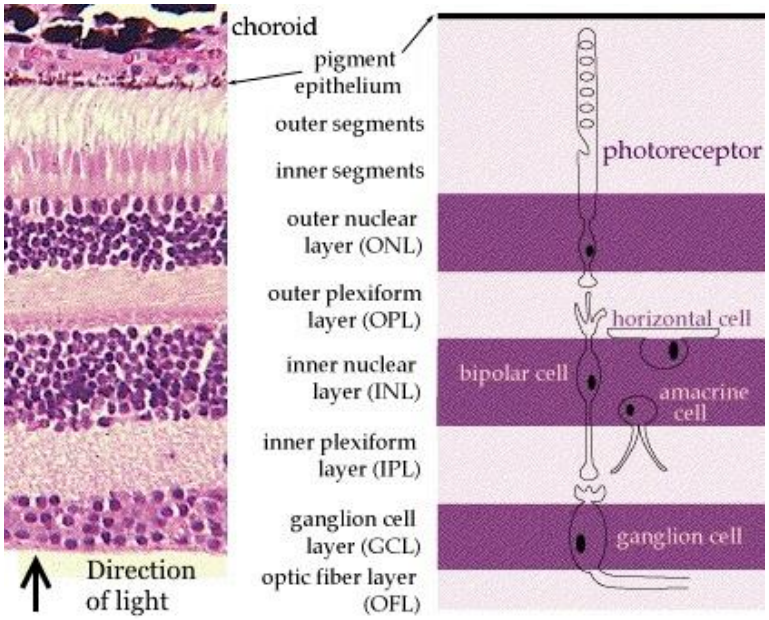

Figure 2.4: Anatomy of the retina, including a cross-section of all retinal layers [99]

i Retinal detachment

Rhegmatogenous retinal detachment

RRD is the most common retinal detachment type. When the vitreous body is wholly attached to the retina, retinal detachment is not likely to happen (Figure 2.5*a)*. Due to ageing, substantial biochemical, structural, and rheological changes occur to the vitreous body [84]. Large liquid vitreous pockets start to form (Figure 2.5*b*) due to the hyaluronic acid-collagen changes; this process is called synchisys. As a result, shrinkage of the vitreous body occurs due to the condensation and the shortening of the collagen fibres (Figure 2.5*c)*.

Moreover, due to the adhesion's physiological weakening between the retina's inner layer and the vitreous cortex, which occurs mainly in the posterior eye segment, the posterior vitreous cortex (PVC) separates due to the liquefied vitreous leaking into the retro-cortical space. This process is called PVD, during which, the PVC acts as an interface between the liquefied and the gel-like vitreous. Due to the coexistence of vitreous-gel and liquified vitreous in the vitreous cavity, and due to the movements of the head and the ocular globe the vitreous is forced to accelerate and decelerate rapidly. These movements play a role in the separation between the vitreous body and the retina. The creation of retinal tear is dependent on the magnitudes of the forces taking place in the vitreous cavity. The vitreous dynamic traction pulls on one side, and the inter-photoreceptor matrix glue, pigment epithelium pump and the tensile strength of the retina itself resist on the other side [97]. If the traction caused by the vitreous movement is too significant, a retinal tear is created (Figure 2.5*d)*.

This retinal tear situation has three possible consequences:

- Due to the retina's initial tear and under the influence of the same tractional forces, the retina tears again. The retina section attached to the vitreous body (Figure 2.5*e)* becomes loose from the retina, while the rest of the retina stays attached. This could cause the patient to experience a floating shadow in their field of vision.
- The opposing forces keep the retina attached, as seen in Figure 2.5*d*. However, the patient continues to experience flashes due to the tractional forces.
- The retina completely detaches (Figure 2.5*f*) due to the dynamic traction overcoming the attachment forces. The retinal detachment spread depends on the strength of the traction and shear stresses on the retina and the attachment forces' strength.

RRD takes place when the liquified vitreous leaks through to the sub-retinal space, between the pigment epithelium and the photoreceptor layer, via the retinal tear [97]. Retinal tears occur in about 15% of patients with PVD. RRD is most likely to happen in the superior-temporal quadrant [123] and most likely around the equator [124].

The fluid collected underneath the retina is called the sub-retinal fluid (Figure 2.5*f)*. RRD takes place in about 12 out of 100,00 people (0.01% annual risk); it is a primary reason for blindness in western countries [125].

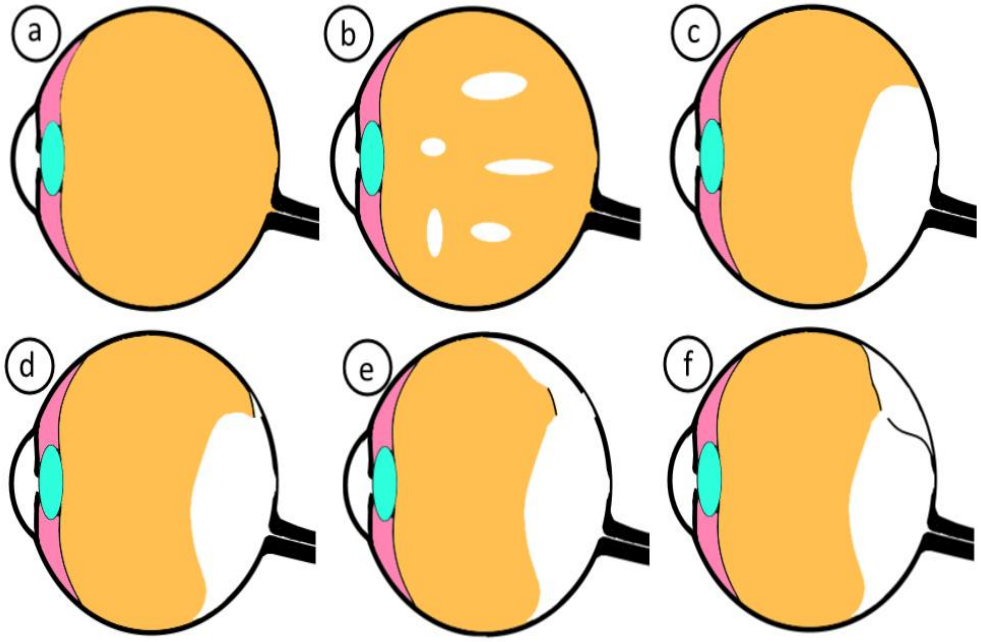

Figure 2.5: Process leading to a retinal detachment. Schematic shows (a) a healthy vitreous, (b) a partially liquified vitreous, (c) a partially detached vitreous, (d) a recently created retinal tear, (e) a torn part of the retina, (f) a fully formed retinal detachment [99]

Further leakage of the sub-retinal fluid may lead to the macula's detachment; this can lead to substantial consequences, given that patients are most likely to lose their sight if the detachment progresses to the macula. This situation leads to permanent visual loss as the fovea (located at the macula's centre) loses its retinal blood supply and becomes entirely dependent on the choroid blood vessels [126].

Tears vary from one patient to another; the most common one is the flap tear (or horseshoe tear). Horseshoe tears are more common in middle age and appear more often near the equator of the eye [125]. Tears also vary in sizes and numbers between patients; the vast tear spans more than three clock hour positions.

ii Retinal adhesion

Retinal attachment is vital for its functioning. Two main factors ensure the attachment of the retina. Firstly, the inter-photoreceptor matrix (IPM) glue. Secondly, the retinal pigment epithelium (RPE) pumps out the virtual sub-retinal cavity fluid towards the choroid [97].

The retinal IPM occupies the space between the retinal pigmented epithelium and the neural retina [127]. The IPM glue plays a significant role in retinal adhesion; indeed, it is known from previous studies that introducing any enzymes that degrade the proteoglycans in the IPM glue leads to a substantial loss of retinal adhesion [128, 129].

The RPE pumps out fluid towards the choroid from behind the retina. The significance of this pump is apparent by the fact that the retina detaches post mortem [130]. Moreover, in eyes diagnosed with myopia, reduced pumping by the RPE contributes to the development of a central retinal detachment [97]. Drugs that can interfere with this active transport reduce the adhesiveness of the retina [131]. The pumping rate of the whole RPE is $3.5\ \frac{mL}{day}$, around 50% of the vitreous volume per day [54].

Retinal adhesion forces

There have been several attempts to measure the retinal adhesion forces. Most of these attempts' measurements were given in units of force per unit length, as shown in Table 2-2.

Kita et al. [132] carried out in vivo tests on rabbit eyes and proved that the adhesion force is equal to $1.8\ \pm 0.2\ \times 10^2\ \frac{dyn}{cm}$. In another study by Kita and Marmor [133],

the adhesion force was found to be $1.4 \pm 0.03 \times 10^2 \frac{dyn}{cm}$ in monkeys, $1.8 \pm 0.18 \times 10^2 \frac{dyn}{cm}$ in cats, and $1.0 \pm 0.07 \times 10^2 \frac{dyn}{cm}$ in rabbits.

Marmor et al. [134] conducted peeling experiments in vitro on rabbit eyes by injecting a small amount of fluid underneath the retina with a micropipette. They showed that the peeling force was in the range of $25\ mg$ for a 5-millimetre strip peeled at the rate of $24\ mm/min$, within the first 20 minutes after removing the eye from the extraocular muscles.

DeGuillebon et al. [135] also carried out peeling measurements in vitro on rabbits' retinas. They showed that the peeling force was $50\ to\ 100\ mg$ for a 6.5 millimetres strip peeled at the rate of $2 - 42\ mm/min$.

Liu et al. [2] used the results of Kita and their own experiments to calculate the retinal adhesion in units of pressure. This was done by injecting a balanced salt solution using a micropipette into the sub-retinal space. The sub-retinal pressure was measured with another micropipette connected to a pressure transducer inserted in the sub-retinal space. Retinal adhesion was estimated to be $340 \pm 78\ Pa$.

Table 2-2: Experimental values of retinal adhesion

Study	Species	Number of specimens	Adhesion
Kita et al. [132]	Rabbit	87	$180 \pm 20\ dyn/cm$
Kita and Marmor [133]	Monkey	6	$140 \pm 3\ dyn/cm$
	Cat	4	$180 \pm 18\ dyn/cm$
	Rabbit	25	$100 \pm 7\ dyn/cm$
Marmor et al. [134]	Rabbit	8	$30 - 50\ dyn/cm$
DeGuillebon et al. [135]	Rabbit	72	$76 - 154\ dyn/cm$
Liu et al. [2]	Rabbit	10	$340 \pm 78\ Pa$

iii Retinal detachment treatment

Numerous treatments are available for retinal detachment. The treatment options include sclera buckling surgery, pneumatic retinopexy, or vitrectomy. The right treatment is identified for each patient individually.

Sclera buckling surgery is generally conducted in patients with less complicated retinal detachment [136-140]. It is performed by sewing an encircling band under the ocular muscles, around the sclera's circumference. An indention in the eyewall is created by placing a grooved buckle at the tear level under the band. This indentation causes the retinal tear to be pressed against and closed by the choroid and the sclera. To reduce the subretinal fluid volume, a transscleral puncture can be performed. Retinal adhesion can be achieved by applying cryocoagulation (the use of extreme cold in surgery to destroy a diseased tissue) around the tear. In order to achieve stronger adhesion, a bubble of expandable gas is injected into the eye. This technique is derived from the scleral resection that was introduced by Muller in 1903 [63].

In pneumatic retinopexy, in cases of highly localised retinal detachment without any abnormalities, a gas bubble is injected into the eye, and cryocoagulation is conducted at the retinal tear location [86, 141-148].

Vitrectomy is conducted in the more complicated cases e.g., giant retinal tears [145, 147], severe preoperative proliferative vitreoretinopathy [149], and vitreous haemorrhage. Vitrectomy is performed by removing the vitreous through three small openings in the pars plana. The openings are made 3-5 mm from the corneal limbus [150]. One of the openings is for the infusion of fluid to maintain pressure inside the eye. The second is to include a fibre optic light source to illuminate the eye [151]. The third opening is to allow the surgeon to work bimanually. The retina is re-attached after the procedures using cryocoagulation. Oil or a gas bubble can also be injected in order to maintain the pressure on the retina. Silicone oil is used to guarantee continuous support of the retina.

iv Material properties of the retina

The retinal material properties are known to be anisotropic and inhomogeneous [120]. The properties are dependent on the existence of blood vessels and arteries [152]. Table 2-3 shows the values for retinal stiffness. Chen et al. measured transition strain, which is defined as the strain where the highest elastic modulus occurs. Vroon et al.[153] implemented this non-linearity into a finite element model by curve fitting the Ogden material model [154] over the measurements. In addition, Chen and Weiland measured the retina's elastic modulus in the presence of veins and arteries [152].

Another study by Qian et al. [155] determined the retina's mechanical properties in vivo through an inverse analysis to minimise the error between experimental and numerical results. The experiment was carried out by causing acute high IOP and then scanning the retina images under different IOP. Finally, using inverse analysis, the parameters of a constitutive model of the retina and choroid were determined.

Table 2-3: Literature values of retinal stiffness

Study	Species	Number of specimens	Parameters
Chen et al. [120]	Human	10	Transition strain 0.035 ± 0.003 Lowest modulus $0.2 \pm 0.2 \times 10^3\ Pa$ Highest modulus $12.5 \pm 10.1 \times 10^3\ Pa$
Chen et al. [120]	Porcine	10	Transition strain 0.034 ± 0.004 Lowest modulus $0.3 \pm 0.3 \times 10^3\ Pa$ Highest modulus $19.5 \pm 12.2 \times 10^3\ Pa$
Chen et al. [152]	Human	5	Transition strain (vein) 0.018 ± 0.002 Transition strain (artery) 0.016 ± 0.001 Transition strain (no vessels) 0.016 ± 0.001 Modulus (vein) $50.90 \pm 42.39 \times 10^3\ Pa$ Modulus (artery) $38.48 \pm 16.64 \times 10^3\ Pa$

			Modulus (no vessels) $11.12 \pm 6.10 \times 10^3\ Pa$
Vroon et al. [153]	Human	-	Ogden $n = 1$ $\propto_1 = 0.00239$ $\mu_1 = 0.005$
Qian et al. [155]	Cat	1	Ogden $n = 2$ $\propto_1 = 0.00227$ $\mu_1 = 0.0811$ $\propto_2 = 0.00421$ $\mu_2 = 0.0.0652$

μ: shear modulus; α: strain hardening exponent

v Retinal thickness

The thickness of the retina is not homogeneous throughout the eye. At the foveal floor, the retina is thinnest (0.1,0.15-0.2 mm); at the foveal rim, the retina is the thickest (0.23,0.32 mm). On the other hand, beyond the fovea and until the equator, the retina rapidly thins. Finally, the retina is thinnest of all at the ora serrata (0.08 mm) [156].

2.3 Material behaviour of the ocular tissue

Ocular numerical models have been used in various biomechanical applications, disease management and medical device development [39, 56, 58, 157-159]. Low cost and faster evaluation are the main advantages of computer-based simulations over laboratory experiments. Nevertheless, the efficiency of numerical simulations relies on many factors such as geometry, boundary conditions, loading and material properties; the latter is usually the vital feature characterising the behaviour of the material in numerical simulations [58, 157, 160, 161].

There has been significant growth in interest in characterising the biological tissues based on nonlinear continuum mechanics theory. Biological tissues are

heterogeneous composite materials made of different media, including connective, epithelial, neuronal and muscular [162]. Constitutive theories aim to develop mathematical models in order to reproduce the real behaviour of biological tissues. This section will introduce the relevant constitutive models developed in the past, to provide context to the presented study.

2.3.1 Hyperelastic behaviour

Hyperelastic material is a type of constitutive model for ideally elastic material for which the relation between stress and strain is driven by a strain energy density function. There are many models of hyperelastic material which are available in many finite element (FE) packages and are easy to apply.

The Ogden model is one of these models, and it is useful in the study of the material behaviour of ocular tissues [39]. The numerical model used to describe material behaviour for the ocular globe components such as the cornea, sclera and retina during loading was a hyperelastic Ogden model, used in many early studies on soft tissues [163-165].

The Ogden model is presented in the equation below in terms of strain energy per unit volume, W:

$$W = \sum_{i=1}^{N} \frac{2\mu_i}{{\alpha_i}^2}\left(\overline{\lambda_x}^{\alpha_i} + \overline{\lambda_y}^{\alpha_i} + \overline{\lambda_z}^{\alpha_i} - 3\right) + \sum_{i=1}^{N} \frac{1}{D}(J-1)^{2i} \qquad 2.1$$

In Equation 2.1, W is the strain energy per unit volume; N is the function order (taken as 1); μ and α are the shear modulus and the strain hardening exponent, respectively, $\overline{\lambda_k}$ the deviatoric principal stretches = $J^{-1/3} \times \lambda_k$ (k=1, 2, 3), λ_1, λ_2, λ_3 the principal stretches, J = λ_1 λ_2 λ_3. D is a compressibility parameter $= \frac{3(1-2\nu)}{\mu(1+\nu)}$ calculated assuming the tissue was nearly incompressible [166],[167] with a Poisson's ratio, ν, of 0.48 [163, 168].

In order to describe the nonlinear stress-strain curve, isotropic models such as Ogden are implemented. However, the heterogeneity and anisotropy induced by ocular microstructure cannot be addressed. Whitford [60] calibrated the Ogden material parameters based on an inflation test of a full ocular globe and determined nine groups of material properties for the cornea, limbus and sclera combined. These nine sections were used to create the profiles of the experimental deformation of human eyes.

2.3.2 Viscoelasticity

Viscoelasticity is an essential mechanical property of the ocular tissue. This is the property of materials that exhibit both elastic (spring-like) and viscous (dashpot-like) characteristics when undergoing deformation. The relationship between stress and strain for viscoelastic materials depends on time. Viscoelastic materials include three vital behaviours: hysteresis, creep and stress relaxation [59]. The mechanical behaviour of a viscoelastic material depends on both temperature and time.

To date, viscoelastic properties has been described for different species such as porcine [89, 115, 116, 169-171], ovine [170, 172], bovine [92, 115, 116, 170, 171, 173, 174], rabbit [175] and human vitreous bodies [170, 176, 177].

The three basic models that are used to model viscoelasticity are the Kelvin-Voigt model, Burgers model, and the Maxwell model. Each of these models differs in the arrangement of the dashpots and springs.

i Kelvin-Voigt model

The kelvin-Voigt model consists of a parallel connection of a spring and dashpot, as shown in Figure 2.6.

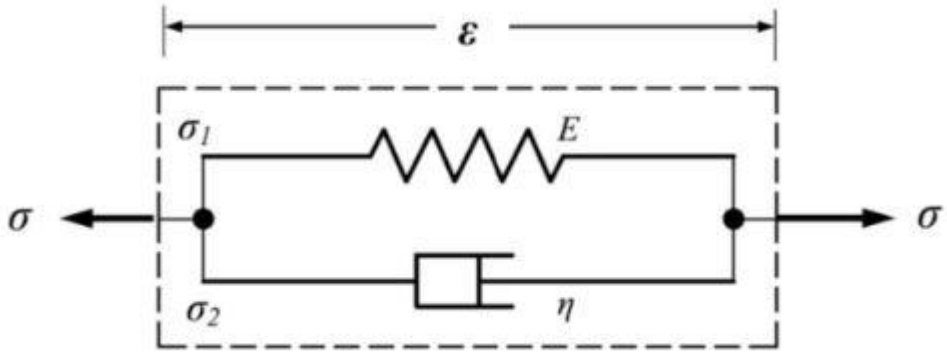

Figure 2.6: Rheological representation of the Kelvin-Voigt model [178]

The strain experienced by the dashpot is similar to the that experienced by the spring [178]. The total stress of this arrangement can be obtained by adding up the stresses in the dashpot and spring:

$$\sigma = \sigma_1 + \sigma_2 \qquad 2.2$$

The stress-strain relation of the Kelvin-Voigt system is:

$$\sigma = E\varepsilon + \eta\,\dot{\varepsilon} \qquad 2.3$$

In the generalized Kelvin model, there are multiple springs and dashpots connected in series, as shown in Figure 2.7

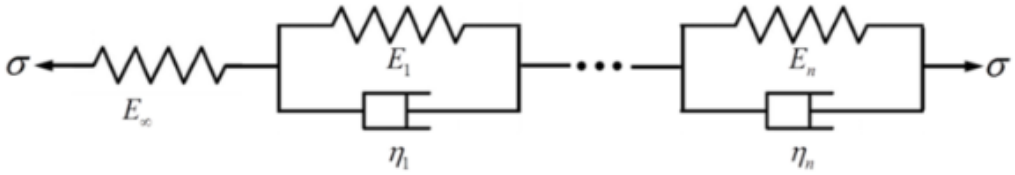

Figure 2.7: Schematic of a generalised Kelvin-Voigt model consisting of n Kelvin elements connected in series [178]

Based on equation 2.3, the strain and stress in each kelvin element are related by the below equation:

$$\sigma_i = E_i\varepsilon_i + \eta_i \frac{\partial \varepsilon_i}{\partial t} \quad 2.4$$

Due to arrangement of the elements in series, the total strain is the sum of the internal strains of all elements, while the stress at each element is the same. Therefore, the total stress and strain are described by:

$$\sigma = \sigma_\infty + \sigma_i \quad 2.5$$

$$\varepsilon = \varepsilon_\infty + \sum_{i=1}^{n} \varepsilon_i \quad 2.6$$

ii Burgers Model

The burgers model consists of two springs and two dashpot and can be represented using kelvin representation, as shown in Figure 2.8.

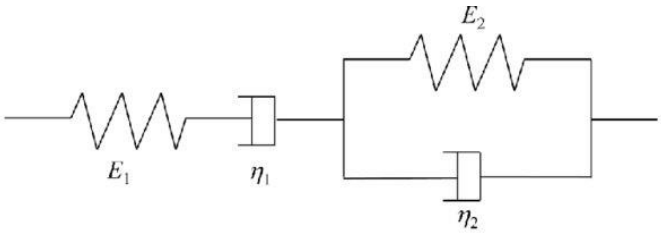

Figure 2.8: Schematic representation of Burgers model [179]

Given that the kelvin material has a viscosity η_1 and elasticity E_1, the dashpot has a viscosity η_2 and the spring has an elasticity E_2, the burgers model has the constitutive equation [180]:

$$\sigma + \left(\frac{\eta_1}{E_1} + \frac{\eta_2}{E_1} + \frac{\eta_2}{E_2}\right)\dot{\sigma} + \frac{\eta_1\eta_2}{E_1E_2}\ddot{\sigma} = \eta_2\dot{\varepsilon} + \frac{\eta_1\eta_2}{E_1}\ddot{\varepsilon} \quad 2.7$$

Where σ is the stress and ε is the strain.

iii Maxwell model

The Maxwell model is a two-element model that consists of a linear viscous dashpot element and a linear spring connected in series, as can be seen in Figure 2.9 [181].

Figure 2.9: the Maxwell model [182]

The constitutive equation for a material which responds as a linear spring of stiffness E is:

$$\sigma = E\,\epsilon_2 \qquad 2.8$$

where σ is the stress and ϵ_2 is the strain of the linear spring.

This material's response to a creep-recovery test is to undertake an instantaneous elastic strain with loading and to keep that strain as the load is applied. In addition, the material launches an instantaneous de-straining immediately after the removal of the load.

The next element responds like a piston filled with a viscous fluid called a viscous dashpot. In order to achieve strain, the piston is dragged through the fluid. The constitutive equation for a material that responds as a dashpot is:

$$\sigma = \eta\,\dot{\epsilon_1} \qquad 2.9$$

where η is the viscosity of the material and $\dot{\epsilon_1}$ is the strain-rate ($\frac{\delta\varepsilon}{\delta t}$).

In order to achieve equilibrium, stress in both elements must be the same. As both elements are connected in series, the total strain is equal to the summation of the two elements' strain.

$$\epsilon = \epsilon_1 + \epsilon_2 \quad 2.10$$

In order to combine equations 2.8, 2.9 and 2.10, Laplace transformation is applied. Laplace transformation is mainly used to reduce differential equations, such as $\dot{\epsilon_1}$, to algebraic [183]. The resulting expressions for equations 2.8 and 2.9 after applying Laplace are:

$$\widehat{\sigma_s} = E\,\widehat{\epsilon_{2s}} \quad 2.11$$

$$\widehat{\sigma_s} = \eta\, s\,\widehat{\epsilon_{1s}} \quad 2.12$$

where s is a complex number frequency parameter.

By combining equations 2.10, 2.11 and 2.12:

$$\hat{\epsilon} = \frac{\widehat{\sigma_s}}{E} + \frac{\widehat{\sigma_s}}{\eta\, s} \quad 2.13$$

Furthermore, by rearranging the above equation, the following frequency domain expression is obtained:

$$E\,\eta\, s\,\hat{\epsilon} = \widehat{\sigma_s}\, s\,\eta + E\,\widehat{\sigma_s} \quad 2.14$$

The model's response to various stress or strain conditions can be obtained after applying inverse Laplace transformation to equation 2.13.

$$\dot{\epsilon} = \frac{\dot{\sigma}}{E} + \frac{\sigma}{\eta} \quad 2.15$$

In the stress relaxation test, the history of the strain is assumed as a step function:

$$\epsilon_{(t)} = \epsilon_o\, \mu_{(t)} \quad 2.16$$

$$\mu_{(t)} = \begin{cases} 0, & t < 0 \\ 1, & t \geq 0 \end{cases}$$

where ϵ_o is the strain at time zero and $\mu_{(t)}$ is the step function.

Using the strain step function below along with equation 2.16, the Laplace transformation of equations 2.9 and 2.10 gives:

$$\hat{\epsilon}\, s = \frac{\hat{\sigma_s}\, s}{E} + \frac{\hat{\sigma_s}}{\eta\, s} \qquad 2.17$$

$$\hat{\epsilon} = \frac{\epsilon_o}{s} \qquad 2.18$$

since Laplace transformation of $\mu_{(t)}$ is $\frac{1}{s}$.

Combining equations 2.17 and 2.18, the strain response equation below is obtained:

$$\epsilon_o = \frac{\hat{\sigma_s}\, s}{E} + \frac{\hat{\sigma_s}}{\eta\, s} \qquad 2.19$$

The above equation could be rearranged to get the following stress response:

$$\hat{\sigma_s} = \epsilon_o E \left(\frac{1}{s + \frac{E}{\eta}} \right) \qquad 2.20$$

It is known that $\frac{\eta}{E}$ is equal to the relaxation time, τ [183]. using Laplace transformation, since $L^{-1}(\frac{1}{s+ a}) = e^{-at}$, the stress-extension relationship for a single mode Maxwell model can be expressed as:

$$\sigma_{(t)} = \epsilon_o E . e^{\frac{-t}{\tau}} = \sigma_o e^{\frac{-t}{\tau}} \qquad 2.21$$

With the known stress, σ_o, at $t = 0$, the unknown parameter, t, is identified using the method of least squares.

For multiple relaxation times, the stress-extension relation is described by the generalised Maxwell mode. For instance, in the generalised Maxwell model, there are multiple springs and dashpots connected in parallel, as shown in Figure 2.10. As all elements are connected in parallel, strain is constant, and the total stress is the

summation of all the element's stresses. An extra isolated spring is added to represent arrheodictic behaviour [184].

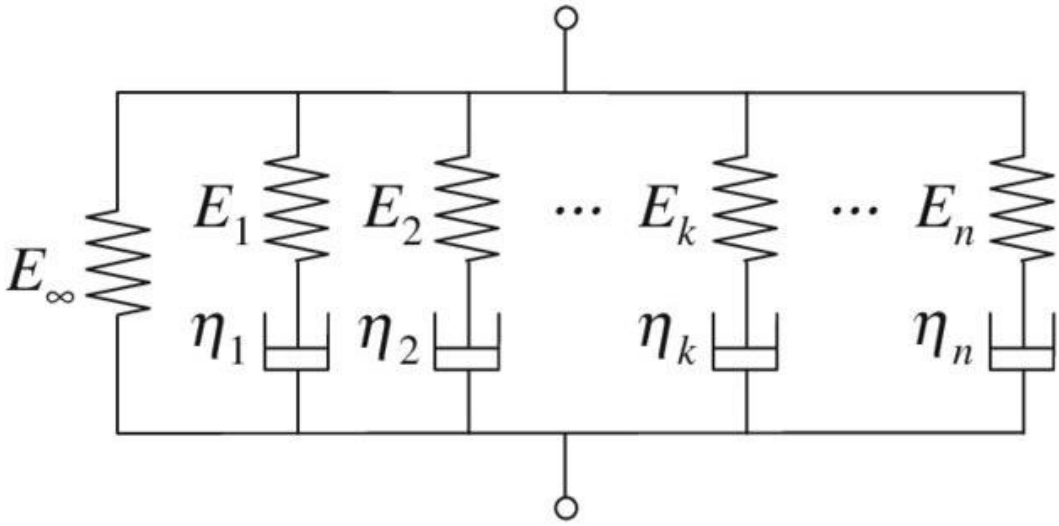

Figure 2.10: Schematic of a generalised Maxwell model consisting of n Maxwell elements connected in parallel [185]

$$\sigma_{(t)} = E_\infty \epsilon_o + \sum_{i=1}^{N} \epsilon_o \, E_i \, e^{\frac{-t}{\tau_i}} \qquad 2.22$$

Or, in another form:

$$\sigma_{(t)} = \epsilon_o \left(E_\infty + \sum_{i=1}^{N} E_i \, e^{\frac{-t}{\tau_i}} \right) \qquad 2.23$$

The relaxation modulus $E_{(t)}$, which is essentially the Prony series representation, is defined as:

$$E_{(t)} = \left(E_\infty + \sum_{i=1}^{N} E_i \, e^{\frac{-t}{\tau_i}} \right) \qquad 2.24$$

Here E_∞ is the infinite modulus, and at $t = 0$, the instantaneous modulus is defined as:

$$E_o = E_\infty + \sum_{i=1}^{N} E_i \qquad 2.25$$

A pair of E_i and τ_i is referred to as a Prony pair [184].

ABAQUS representation

In many modern finite elements systems (Abaqus, ANSYS), viscoelasticity is implemented through the use of Prony series, which is a representation of the Maxwell model. Therefore, in the presented study Maxwell model was used to model the viscoelasticity of the vitreous.

In this section, the Prony series parameters used ABAQUS to represent the Maxwell model are derived. ABAQUS assumes that the viscoelastic material is defined by a Prony series expansion of the dimensionless relaxation modulus.

The ratio between E_i and E_o is referred to as m_i. By substituting E_i in equation 2.24 with $m_i E_o$, the following expression is obtained:

$$E_{(t)} = \left(E_\infty + \sum_{i=1}^{N} m_i \, E_o \, e^{\frac{-t}{\tau_i}} \right) \qquad 2.26$$

If the above equation is expressed in terms of shear and bulk modulus, the following equations are obtained:

$$G_{(t)} = \left(G_\infty + \sum_{i=1}^{N} g_i \, G_o \, e^{\frac{-t}{\tau_i}} \right) \qquad 2.27$$

$$K_{(t)} = \left(K_\infty + \sum_{i=1}^{N} k_i \, K_o \, e^{\frac{-t}{\tau_i}} \right) \qquad 2.28$$

where G is the shear modulus, K is the bulk modulus, g_i is the ratio between the shear modulus, G_i and the instantaneous shear modulus, G_o, and k_i is the ratio between the bulk modulus, K_i , and the instantaneous bulk modulus, K_o. The instantaneous shear and bulk moduli are determined from the values of the user-defined instantaneous elastic moduli E_o and υ_o, where:

$$G_o = \frac{E_o}{2(1+\upsilon_o)} \qquad 2.29$$

$$K_o = \frac{E_o}{3(1-2\upsilon_o)} \quad 2.30$$

In order to obtain the long-term shear and bulk moduli, when $t = \infty$, the equations below are used.

$$G_\infty = G_o\left(1 - \sum_{i=1}^{N} g_i\right) \quad 2.31$$

$$K_\infty = K_o\left(1 - \sum_{i=1}^{N} k_i\right) \quad 2.32$$

Finally, the set of Prony series parameters used to define viscoelasticity on ABAQUS are k_i, g_i and τ.

2.3.3 Modelling fluid-structure interaction

In ABAQUS, there are several ways to model the fluid-structure interaction, eg using fluid-filled cavities, surface-based cavities, equation of state and coupled fluid-structure interaction [186]. In the present study, the surface-based cavity option was used to model the liquified vitreous. Comparisons between fluid-filled cavities and surface-based cavities have been carried out in previous research [187]. The results of their analysis showed that both methods were exactly the same when using ABAQUS/Explicit.

Surface-based cavity allows coupling between the structure and the fluid enclosed inside. To model the fluid-structure interaction using this method, the following points need to be fulfilled. Firstly, the presence of a finite element model of the structure. The surface covering the cavity boundary needs to be defined, for coupling between the pressure produced by the fluid and the deformation of the structure. Finally, the fluid behaviour needs to be defined.

2.4 Eye movements

2.4.1 Head movement

While there is considerable literature regarding the impact of accelerations on the head, there are almost no data on the effects of day-to-day head movement. Head movements differ between situations and patients; however, the studies mentioned below provide guideline for typical day to day accelerations of the human head.

When the head moves, the eye experiences both components of rectilinear and angular acceleration. Bussone [188] carried out 700 experiments to determine the angular and linear acceleration of the head's movement during daily activities. The resultant maxima were 931.3 rad/s^2 for angular acceleration, 93.6 m/s^2 for linear acceleration, and 9.03 rad/s for angular velocity. Bussone reported that no day to day task would produce angular acceleration more than 1000 rad/s^2.

Kavanagh et al. [189] reported the head's acceleration is half the gravity when walking. This was confirmed by Woodman and Griffin [190], who also reported angular acceleration in pitch direction to be 40 rad/s^2.

Falling into a chair or hopping off a step results in acceleration of 10.1 and 8.1 g, respectively, as reported by Allen et al. [191]. The main drawback of this study is that the lateral acceleration was ignored. A helmet was used to conduct the measurements that might have affected the results by causing higher acceleration than usual.

For the current study, the distance moved is defined to be 2 millimetres and using the same time span as that of saccadic movements. The accelerations caused by this movement is smaller than those created by jogging but more extensive than those produced by walking [189]. These accelerations are similar to those caused by sitting down in a chair or due to a cough motion [192].

2.4.2 Saccadic movement

In natural vision, the eyes shift from one location to another several times per second. This is called saccadic eye movements. A saccade's primary function is to change the point of fixation in order to direct the fovea, the most sensitive region of the retina, to a specific element of the object of perception. The eye remains in a state of fixation for about 95% of the total time due to the saccadic movements' short duration and high velocity. Lamansky [193] studied saccades for the first time in 1869 and these have since been studied in detail and quantified [194].

In normal conditions, the saccade's amplitude does not usually exceed 20°. Very often, rotations of the eyes exceeding 15° may be a combination of two or three saccades, or accompanied by a related rotation of the head. Around 99% of eye movements are less than 15° saccades in amplitude [195].

Under normal conditions, the eye's saccadic movement duration is only a function of the angle around which the eye rotates when changing the points of fixation. The following equation may be used to show the relationship between the angle around which the eye rotates and the duration [194]:

$$T = 0.021 \ \propto_o^{2/5} \qquad 2.33$$

where T is the duration of the saccades in seconds, and $\propto_o$ is the angle in degrees around which the eye rotates.

For saccades less than 15°, the change in the angle of the eye rotations during the saccade's time can be described using the following equation:

$$\propto (t) \ = \frac{\propto_o}{2}\left((1 - \cos\left(\frac{\pi}{T}t\right)\right) \qquad 2.34$$

Therefore, angular velocity (ω) of the saccades was determined using the relationship [196]:

$$\omega = \frac{\propto_o \pi}{2T} \sin(\frac{\pi}{T} t) \qquad 2.35$$

where *t* is the time at which $\propto$ and ω are calculated. This formula can only be applied to saccades less than 20°.

The linear velocity, v, of the corneal centre during saccades can be obtained by assuming that the eye's diameter is 2.4 cm, and by using equation 2.30.

$$v = 0.021\ \omega \qquad 2.36$$

Velocity increases smoothly based on the angular velocity equation until it reaches the peak and then falls gradually to zero. Moreover, the time for the decrease and the increase of the velocity during saccades is almost equal [194].

2.5 Retinal detachment modelling

Researchers have investigated the human eye over the last decades using finite element modelling (FEM). The majority of these researches used finite element methods to study the damage caused in the eye due to impacts. For instance, Rossi et al. [5], Uchio et al. [31], Karimi et al. [32], Liu et al. [2] and Stitzel et al. [33] investigated the impact of an external source or explosion on the eye.

Rossi et al. [5] tested the hypothesis that blunt trauma may cause peripheral retinal and macular tears. Rossi's study focused on the observation of macular hole after inadvertent BB shot in a previously vitrectomized eye. Their computer model (see Figure 2.11) was generated from generic eye geometry and included components of the eye such as aqueous, cornea, sclera, vitreous, retina and lens.

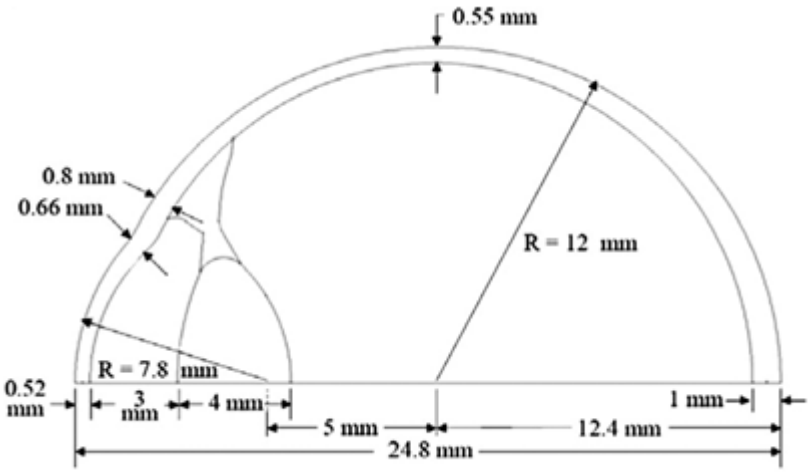

Figure 2.11: The structure and the dimension of the eye model used in Rossi's study [5]

Karimi et al. [32] determined the stresses and deformations of the human eye components, including the cornea, sclera, aqueous, retina, vitreous and lens, attributed to PBW induced by trinitrotoluene (TNT) explosion using a finite element model. The model created by Karimi et al. (see Figure 2.12) didn't take into consideration the liquefaction of the vitreous or the choroid.

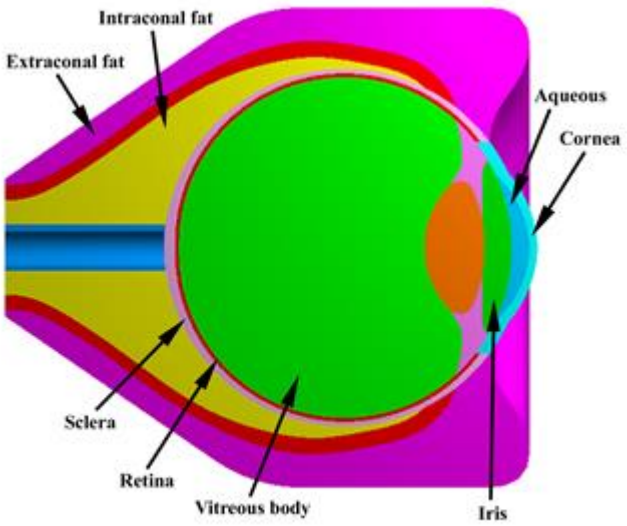

Figure 2.12: The FEM of the human eye used in Karimi's study [32]

On the other hand, Hans et al. [34] studied retinal detachment due to the baby shake syndrome. Hans et al. included almost all the ocular globe components in their model, however, vitreous liquefaction was not modelled. Moreover, the retinal thickness was assumed to be uniform, neglecting the variation studied by Chen et al. [152]. Liu et al. [2] developed a finite element model to study the mechanism of traumatic retinal detachment in blunt impact (See Figure 2.13). The model included most of the eye components such as the cornea, sclera, lens, retina, vitreous and aqueous. However, components such as the choroid and liquified vitreous were not included.

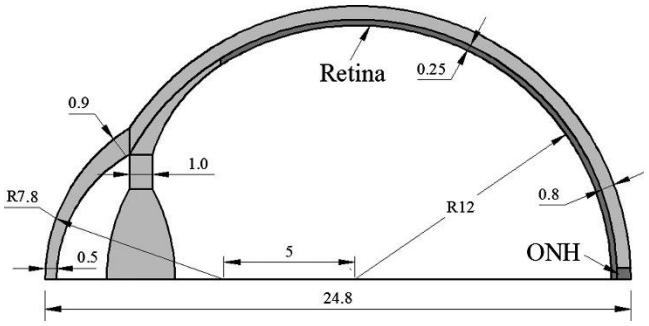

Figure 2.13: The structure and the dimension of the eye model used in Liu's study [2]

Liu and Hans [2, 34] investigated the pressure exerted on the retina due to the vitreous. The vitreous was modelled as a viscoelastic or elastic solid. Only Liu et al. considered retinal adhesion. One of the main drawbacks of the above studies is lack of validation. Only Stitzel et al. [33] managed to validate their models against experimental data, and Liu et al. [2] validated their model against Stitzel's. However, the rest of the studies mentioned above failed to validate their models [34-36].

Vroon et al. [153] investigated the role of the saccadic eye movements and head movements on the progression of retinal detachment. The model used in Vroon's study (Figure 2.14) was based on geometric and material properties found in the literature. The results showed that head movements are able to cause loads that can lead to retinal detachment. Vroon's study was the first to use numerical analysis to study the progression of retinal detachment. The main drawback of this study is the simplicity adopted in the material properties used in eye model. Moreover, Vroon et

al. assumed that the retinal and the choroid as one component. Thus, when modelling retinal detachment, the retina and the choroid were separated from the sclera, rather than from the choroid.

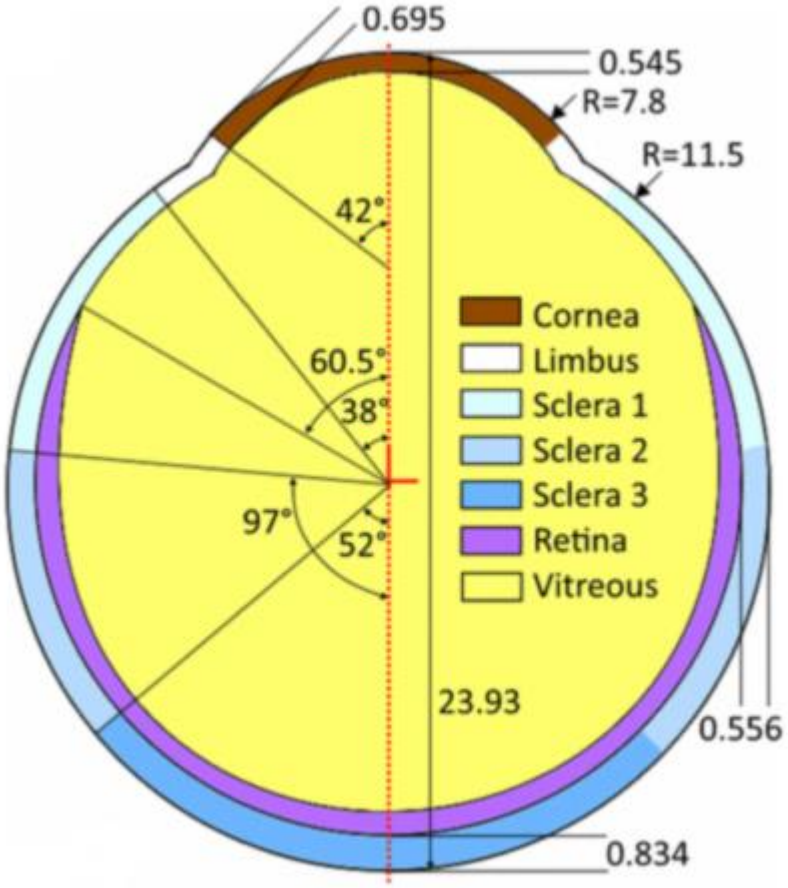

Figure 2.14: The structure and the dimension of the eye model used in Vroon's study [153]

Repetto et al. [1] studied how the traction exerted by the detached vitreous on the retina can arise from saccadic eye movements. Numerical simulations were conducted of a 2D model of the vitreous chamber within a rigid spherical sclera subjected to 10^{o} rotations around the vertical axis. The vitreous chamber was split into two regions: one occupied by the liquified vitreous, and the other occupied by the vitreous gel. The results provided a justification for the hypothesis that saccades

could lead to high tractions on the retina, in the presence of PVD, which may lead to retinal tear.

Angunawela et al. [197] evaluated the fluid dynamics and fluid shear stress on the retina due to saccadic eye movements and sudden head movements after vitrectomy. The eyeball in Angunawela's model was modelled as a sphere which was filled with water and air. This study showed that head and saccades movements after vitrectomy generate shear traction that is below the published retinal adhesion strength. However, sudden head movements generate tractions similar to the retinal adhesion force.

Di Michele et al. [198] studied the vitreoretinal tractions during PVD using a mechanical model. The evolution of the PVD was described by developing a continuum model of a shrinking soft body that represents the vitreous-gel. Di Michele et al. correlated the shape of the detached vitreous with the intensity of vitreoretinal tractions. One of Di Michele's limitations is modelling the vitreous chamber as a rigid sphere, neglecting the deformability of the vitreous chamber.

Bayat et al. [199] conducted numerical simulations to investigate how the oscillatory motions influence flow dynamics of partial vitreous liquefaction. Bayat et al. subjected harmonic motions to a developed 3D spherical model of the vitreous. Their numerical model was validated by comparing the obtained results with analytical solution and a good agreement was observed. The maximum stress produced in Bayat's model was located on the equatorial plane at the cavity wall near the interface layer.

Scott [37] and Ooi et al. [38] used a finite element model to study the damage that occurred to the eye due to external heat transfer. Others used the finite element method to study the mechanics of the cornea [39-41]. Few created a finite element model to mimic a specific situation such as a surgical incision [42] or a method for estimating the material properties [43]. Finite element modelling was also used to study the mechanics of the orbit [44].

2.6 Inverse analysis

There are many situations in which data is acquired from some phenomenon which cannot be seen. The task of utilising gathered data to recreate a mathematical model for example is called inverse analysis. Inverse analyses are performed to determine the set of input parameters to achieve desired outputs. An inverse analysis is effective for determining unknown parameters and for predicting future deformation based on the parameters.

Many tissues exhibit highly nonlinear behaviour, and experimental techniques sometimes don't give the stress-strain relations [60, 200-202]. Therefore, it is essential to use inverse analysis to optimise material parameters in order to determine the actual stiffness of soft tissues. To find the proper parameters that characterise material behaviour, inverse analysis is carried out by combining the optimisation algorithms with finite element software [60, 203, 204].

2.6.1 Particle swarm optimisation

The particle swarm optimisation (PSO) method was first introduced by Eberhart and Kennedy [205]. PSO is based on socio-psychological principles that are inspired by swarm intelligence, which is built on social behaviour understanding [205]. Recently, without involving FE, PSO method has been used in many engineering applications [206-209]. However, Mthembu et al. [210] combined PSO with FEM to achieve the most fitting numerically-predicted deformation behaviour using data attained for an experiment of a simple beam. Later studies showed the reliability of PSO and its efficiency when combined with FE methods, especially in structural mechanics applications [211-213].

Over the last decade, the PSO method was updated, and many of its drawbacks have been decreased. In the governing equations below, PSO utilises the particles position (X_{id}) to present the variables that need to be optimised. Then, by updating X_{id}, PSO

converges to a solution. In the PSO algorithm, each particle's position is described by vectors in the search space; see equation 2.37 [214]:

$$V_{id} = wV_{id} + c_1 r_1 (p_{id} - x_{id}) + c_2 r_2 (p_{gd} - x_{gd}) \quad 2.37$$

$$x_{id} = x_{id} + V_{id} \quad 2.38$$

where V_{id} is the velocity of each particle represented by i and has the same dimension, d, as the number of variables being optimised. w is changeable based on the iteration history, and is the inertial weight used to control the movement velocity of the particle. Normally $w = 1.1$, however, this value would be doubled or halved when the same value is achieved from less than two or more than five consecutive iterations. This occurs when achieving a local minimum or skipping the global optimum. c_1 and c_2 are constants equal to 1.49, and refer to cognitive and social factors. These two constants control the effects of the particle itself and a swarm on the velocity. r_1 and r_2 are random numbers drawn from a uniform distribution. p_{id} is the best achieved position of the particle up to the current iteration. p_{gd} is the global best position in the swarm. Once better positions are achieved, both best positions are updated by the calculation of the error.

By avoiding using the same global term, neighbourhood search strategies will ensure the particles' diversity if a premature convergence to local optimum takes place. Wang et al. [215] verified this method by implementing it in the algorithm. For equation 2.32, x_{id} is the particles' current positions that will then be used for the next evaluation. Based on the new velocity and the old position of the particle, the new position is calculated. Furthermore, the new velocity comprises three terms. The first term is the old velocity, the second term is the local information of the particle (fitness) and, finally, the third term is the neighbouring information, which can be dealt with as the individual and social behaviour in a swarm [215].

In contrast to the classic version of the PSO, the advanced algorithm has improved immensely in the areas where it used to achieve the premature convergence or local optima [205, 216-219]. Compared to other algorithms, the PSO has advantages in the rate of convergence, accuracy and reliability. This is due to the changeable inertial weight and neighbourhood search strategy. To avoid local optimum, other strategies could be implemented within the algorithm. These strategies could be the introduction of constriction factors or constraint functions [220, 221].

PSO has been compared with other optimisation algorithms such as Genetic Algorithm (GA), and it showed its advantages. Hassan et al. [222] have compared GA and PSO in an early study by applying them on optimisation problems. GA showed the same effectiveness on finding the best solution as PSO. However, PSO found the best solution with significantly better computational efficiency. Another study by Schutte et al. [223] investigated GA and PSO's performance on the determination of an ankle joint kinematic model to re-generate computer movement data. The results showed that PSO was less affected by variable scaling. This means higher stability, especially on optimisation problems with different scales.

In ocular biomechanics research, PSO is rarely used, even though research mainly concentrates on the sclera's mechanical parameters and the cornea. In the only study to apply PSO to ocular biomechanics, Magalhaes et al. [224] implemented PSO to adjust the cornea's material properties and showed the potential of PSO in biomechanics by evaluating and comparing the results with HEEDS (commercial software). The study demonstrated the superior performance of PSO as compared to HEEDS.

2.7 Summary

RRD is one of the sight-threatening conditions that could lead to blindness if left untreated [105, 106]. PVD is one of the leading causes of retinal detachment. Condensation of the collagen fibrils in the vitreous body occurs as a result of ageing; this leads to the appearance of liquid pockets within the vitreous [225]. When they

merge, these liquid pockets, especially at the posterior pole of the ocular globe, cause the vitreous to detach from the retina. During eye movements (saccades or head), the detached vitreous applies traction on the retina [50], especially at the vitreous base region (the region above the equator of the eye, where adhesion between the retina and the vitreous is strongest). When the traction applied due to the vitreous movement exceeds the adhesion between the retina and the vitreous, a retinal tear or break can occur.

In some cases, the retinal tear allows the liquified vitreous to enter the subretinal space and detaches the retina [97]. The patient's visual ability is generally better if retinal detachment has not progressed to the macula; however, it is as yet unknown what kinds of load contribute the most to the progression of retinal detachment.

The material properties of the human eye are relatively well known and reported in the literature. However, most of these materials are assumed to be linear and isotropic. For instance, the characteristics of the vitreous, which is one of the main factors involved in retinal detachment, has been investigated by many researchers. Numerous different techniques have been used to study its composition and parameters [226]. As some methods subjected the tissue to non-physiologic conditions led to a wide variation in the parameters reported in the literature.

When the head moves, the eye has both components of rectilinear and angular acceleration [188]. The eyes, in natural vision, shift from a location to a new location several times per second. These are called saccadic eye movements [193]. Saccadic and head eye movements have been modelled in several studies, however, the effect of eye movement in the initiation and retinal detachment progression has not been thoroughly investigated. Furthermore, a natural dynamic effect, such as eye movement, has never been used to investigate the ocular tissues' material properties.

FEA has been successfully used in several studies to determine the ocular tissues' material properties. In many modern FEAs (ABAQUS, ANSYS), viscoelasticity is implemented through the use of the Prony series, which is a representation of the

Maxwell model. Only two researchers used the Maxwell material model to simulate the vitreous in FEA [2, 5]. Both used different approaches to measure the properties of the vitreous, and the variation between the parameters used by these two researchers is significant.

Inverse analysis is one of the potential methods used to calibrate material parameters. PSO is one such algorithm that can be used in optimisation. The advantages of PSO in the engineering fields demonstrate this algorithm's potential for ocular biomechanics [210].

3. Vitreous Effect on the Progression of Retinal Detachment

3.1 Introduction

The vitreous chamber, enclosed anteriorly by the lens and posteriorly by the retina, is the eye's largest chamber. The chamber is filled with the vitreous – a gel-like material with viscoelastic properties [46, 85, 96]. With ageing, substantial biomechanical, rheological and structural changes take place in the vitreous [225], including condensation and shortening of the vitreous collagen fibres, leading to shrinkage of the vitreous body and the development of large liquid pockets. Moreover, the liquefied vitreous may enter the retro-crotical space due to the weakening of adhesion between the vitreous and the inner layer of the retina, which can result in the separation of the posterior vitreous cortex (PVC); this process is called PVD [1].

Retinal detachment occurs when the neurosensory retina (NSR) separates from the retinal pigment epithelium (RPE), and fluid gathers within this potential space. The most common type of retinal detachment is RRD, which occurs when the liquefied vitreous enters the subretinal space through a retinal break produced by traction forces. PVD often leads to RRD by generating the traction forces necessary to produce the retinal tear. Therefore, patients diagnosed with PVD are also at risk of developing RRD [227].

One of the main causes of retinal detachment progression is eye rotation, which creates traction forces on the retina [1]. In order to reduce these traction forces, RRD patients are usually advised to rest in bed before surgery [228]. This advice is generally combined with head positioning on the detachment side to use gravity to

stop detachment progression. However, this technique is assumed to have limited value as the difference in density between the retina and the vitreous is small [229].

Despite the significant role of retinal and vitreous biomechanics on retinal detachment, few studies have considered this topic, most of which focused on the impact of external sources [2, 5, 32-34, 36]. Other studies investigated the vitreous body motion and the process through which it led to retinal detachment [230, 231]. Only Vroon et al. [153] investigated the effect of head and eye movements on retinal detachment progression. None of the mentioned researches, except for Vroon et al., studied the interaction between the gel and the liquid phase of the vitreous; they all assumed either a completely liquid or gel-like vitreous. Only Repetto et al. [1] considered the two phases of the vitreous and the effect of saccadic eye movement, however using a 2D numerical model. This interaction is possibly one of the causes of retinal detachment. This study aims to address this gap due to the interaction between the vitreous gel and liquid through a numerical study investigating the effects of both head and eye movements in retinal detachment development.

3.2 Methodology

The methodology focused on building and testing a FEM of the ocular globe. The technique discussed in this chapter is expected to provide the plan undertaken to build a numerical model of the ocular globe to understand the traction forces applied on the retina and the initiation of retinal detachment. Therefore, this chapter starts with the process to build the eye model (Section 3.2.1) and the meshing algorithm built specifically for this study (Section 3.2.2). Then, the graphical user interface (GUI) was constructed to create, modify and mesh the ocular globe without understanding or operating the underlining code (Section 3.2.3). The parametric studies to investigate the eye model's tendency on parameters such the vitreous detachment size and the volume of the vitreous body are discussed in Section 3.3. Lastly, in Section 3.4, the algorithm developed to calculate the traction stress causing the retina to detach is described.

3.2.1 Ocular globe geometry

i Outer layer

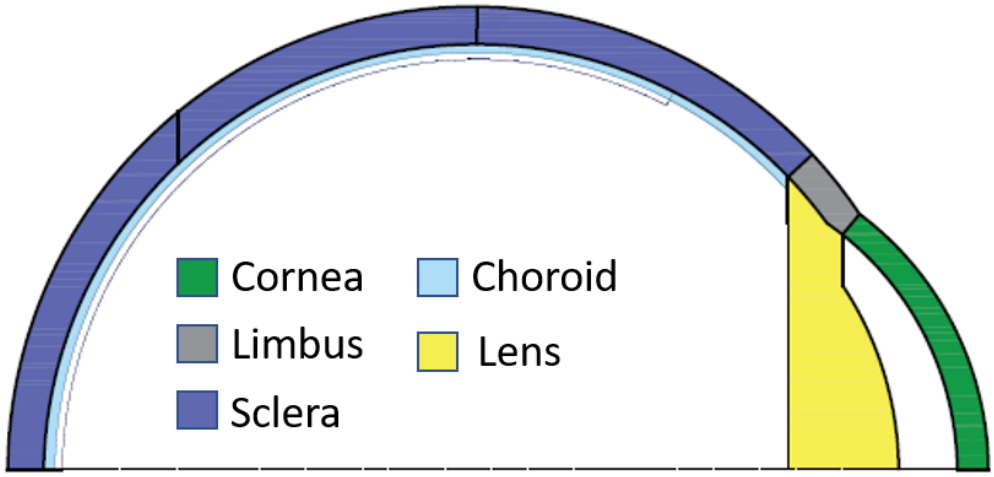

Figure 3.1: The structure of the eye in cross-section

This section describes the method used to create the ocular globe's geometry in the form of a FEM and the technique used to quantify errors.

When modelling the human ocular globe, several different variables are considered. The model had to include the cornea, sclera, limbus, aqueous, lens, vitreous, retina, choroid and liquified vitreous (Figure 3.1). Using custom-built software, shown in Figure 3.2, created by the University of Liverpool Ocular Biomechanics group, an idealised geometry of the ocular globe that includes the cornea, limbus and sclera was generated.

As seen in Figure 3.2, to produce the idealised model using the bespoke software, some factors need to be controlled. These factors include:

- Central cornea thickness (CCT)
- Peripheral cornea thickness (PCT)
- Central corneal radius
- Corneal shape factor (p)
- Corneal diameter

- Scleral radius
- Scleral thickness

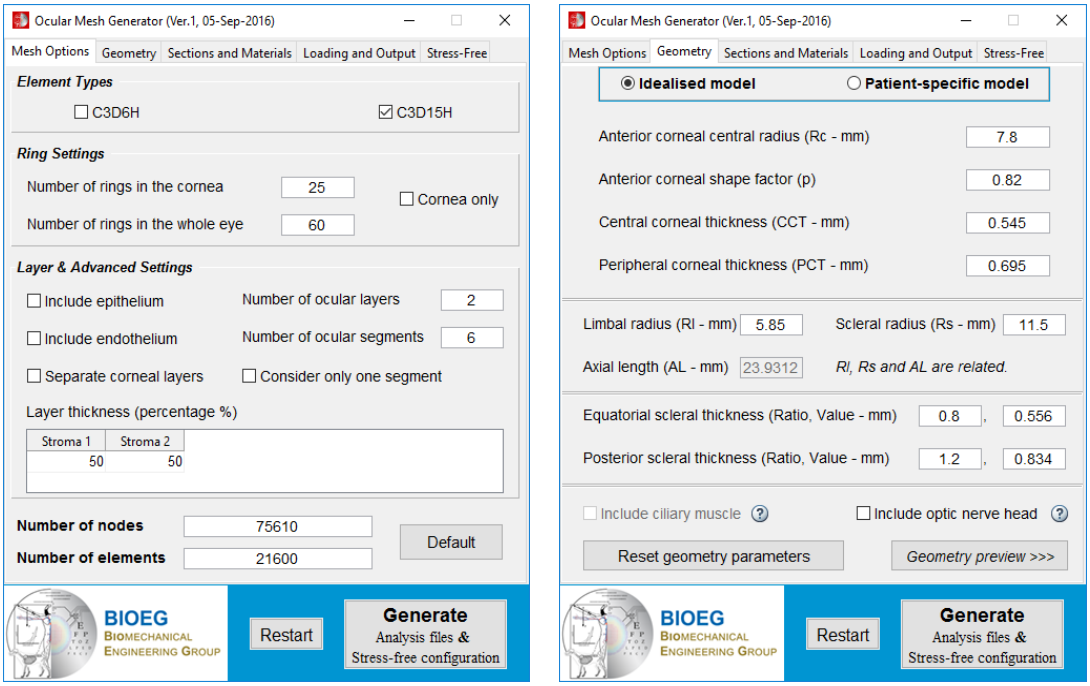

Figure 3.2: Graphical user interface (GUI) designed by the Biomechanical Engineering Group, University of Liverpool, to create models of the human eye globe

Along with controlling the geometry of the model, the software is able to control the mesh arrangement and refinement using the below variables:

- Number of corneal and scleral rings
- Number of element layers

One corneal section and three scleral sections are used because a single material definition is commonly assigned to the cornea. In contrast, material properties for the sclera are provided with three regions (anterior, equatorial and posterior regions). Certain numbers of rings in both the sclera and the cornea are used to create the limbus. The number of these rings is calculated based on the selected numbers of the corneal and scleral rings.

The element type used to create the geometry is C3D6H which has a triangular prism shape. The model is rotationally symmetric around the anterior-posterior axis and

assumed the cornea had an ellipsoidal shape defined by an anterior central radius (ACR = 7.8 mm), a central corneal thickness (CCT = 0.545 mm), a peripheral corneal thickness (PCT = 0.695 mm) and a shape factor (p = 0.82) – these values were reported earlier as being mean measurements of healthy eyes [39, 153, 232]. The sclera part of the models was built with a spherical external surface with radius (RS = 11.5 mm) [232], and a thickness that varied linearly from the PCT at the limbus to the equatorial scleral thickness (EST = 0.8 PCT) at the equator and the posterior scleral thickness (PST = 1.2 PCT) at the posterior pole as reported in an earlier study [40]. The radius of the limbus was taken as 5.85 mm based on earlier reports [233, 234]. These dimensions led to the axial length of the eye model being 23.9 mm; Figure 3.1.

The software generates geometry as a system of finite elements. These elements are defined by nodal cartesian coordinates and written to an input file (*.inp). This file can then be used directly by the finite element solver. The geometry is imported to the solver as an orphan mesh, which means that the mesh has no parent geometric information.

An example of the idealised model generated by the GUI is shown in Figure 3.3.

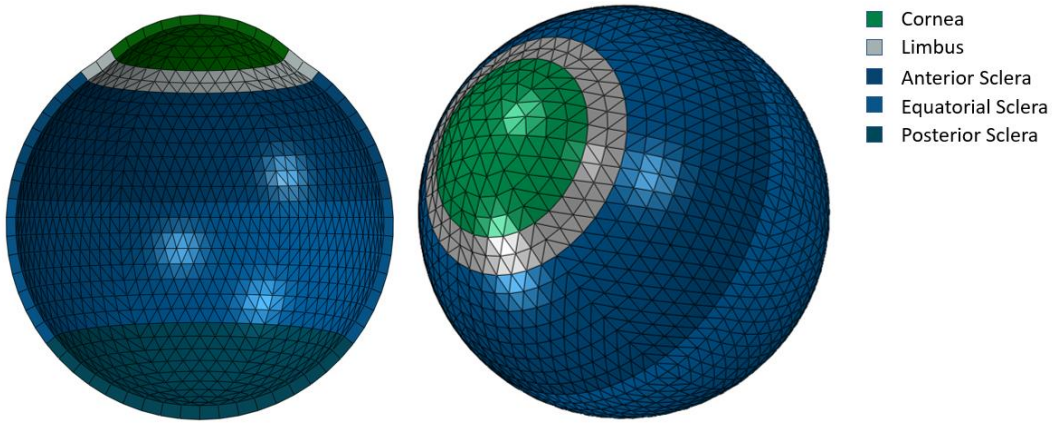

Figure 3.3: Example of finite element model of the ocular globe

ii Choroid and retina

After producing the ocular globe outer layer using the mesh generator explained above, the study aimed to create the geometries and structures of the remaining eye components, such as the retina, choroid, lens, vitreous and aqueous, that are not provided by the mesh generator.

Firstly, the choroid is the eye's vascular layer, containing connective tissues and lying between the retina and the sclera. The choroid was built as a layer attached to the sclera. The thickness of the choroid used to create the model is discussed in section 2.2.6.

The nodes produced by the mesh generator were imported into MATLAB, and the inner nodes of the sclera, starting from the ora serrata to the posterior pole of the eye, were used to form the outer layer of the choroid. These nodes were then converted into a spherical coordinates system, as shown in Figure 3.4. These new spherical nodes were duplicated and, by changing their radii, a new layer of nodes was formed. The new radius was a function of the thickness of the choroid. This new layer includes the choroid's inner layer, and it has two common factors with the outer layer, which are the two angles from the z-axis and the x-axis, as shown in Figure 3.4.

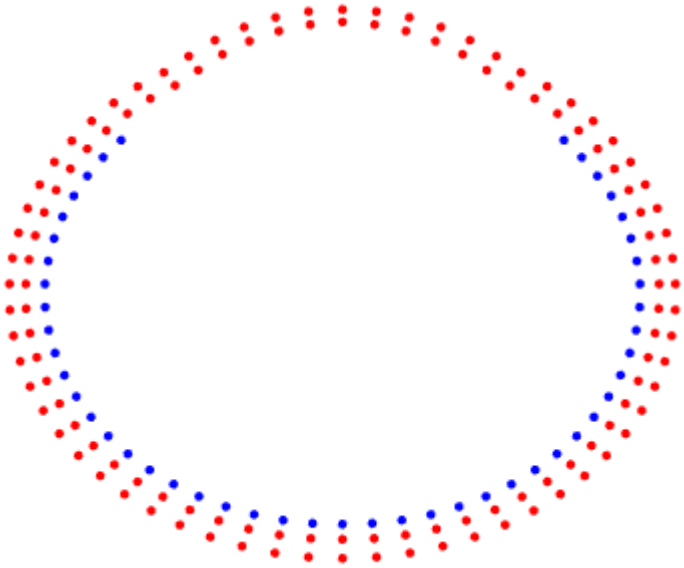

Figure 3.4: Cross-section of the ocular globe showing the eye (red) and choroid (blue) nodes

The retina is a thin layer of tissue that lines the back, inner surface of the ocular globe. The retina's purpose is to receive light that has been focused by the lens and convert it into neural signals. In the model, the retina was built as a thin layer attached to the choroid. The thickness of the retina varies from one region to another (see Section 2.2.7).

Like the sclera, the inner nodes of the choroid were duplicated twice to form the retina's inner and outer boundary. The retina's outer layer has the same coordinates of the choroid; however, the retina's inner nodes were obtained after converting the nodes of the new duplicated choroid nodes into the spherical coordinate system and multiplying their radii by a function of the retinal thickness. The reason the retina and the choroid do not share the same nodes between them is to allow separation in order to model retinal detachment. Figure 3.5 shows the new retinal layer that lines the back of the ocular globe.

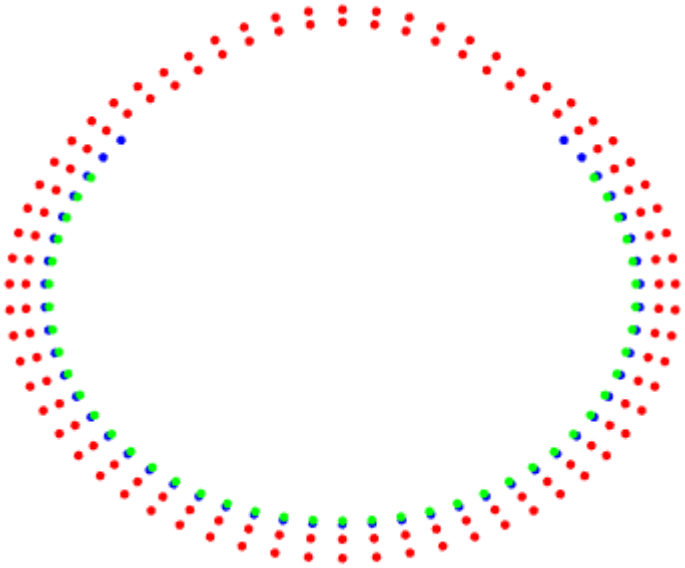

Figure 3.5: Cross-section of the ocular globe showing the initial nodes creating the choroid (blue) and the retina (green)

iii Lens

The lens is a transparent structure that, together with the cornea, allows light refraction to be focused on the retina. It can focus on objects at various distances, by changing its shape in order to change the focal length of the eye.

The geometry of the lens was created to allow modifying it by changing the height and the curvature of 5 points, as shown in Figure 3.6. This was done to be able to model the accommodation process in the future if needed. The surface formed by these five points acts as the lower surface of the lens. Similarly, the top boundary of the lens was managed through the use of the same parameters. As the ocular globe's idealised model is symmetrical, these points were then duplicated around the z-axis to form a 360^{o} shape.

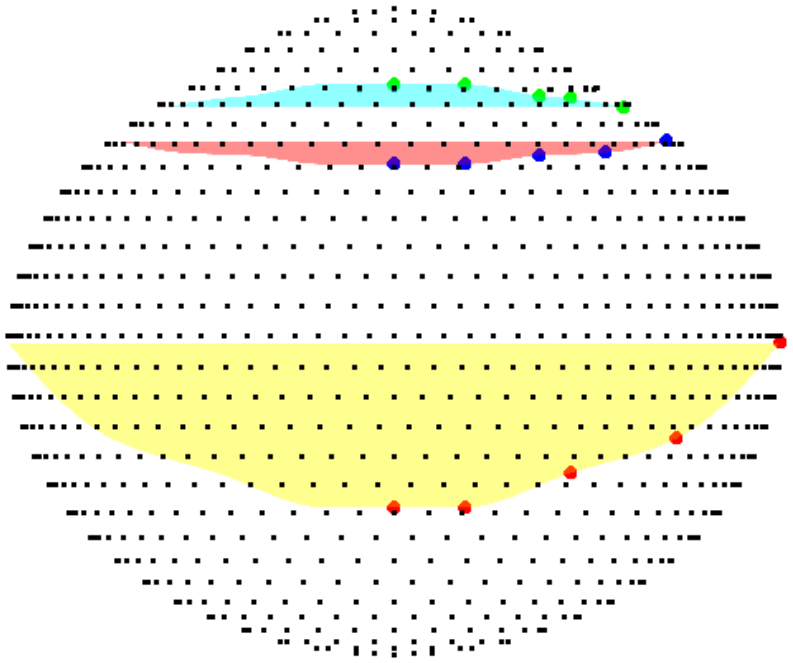

Figure 3.6: 3D rendering of the ocular globe showing the surfaces and points controlling the shape of the vitreous (yellow) and the lens (red-cyan)

iv Vitreous

The vitreous body is the clear gel that fills the space between the lens and the retina. The vitreous liquefies due to ageing (see Section 2.2.5). In order to model the separation between the gel and the liquid phases of the vitreous, both the liquified and the gel vitreous were treated as two different parts.

Firstly, the gel-vitreous was created using the same concept used for the lens; five adjustable points were created to form the lower surface of the vitreous. In order to allow the modelling of different vitreous detachment cases, the height and the radius of the five points are changeable. The surface created by these five nodes acts as a separator between the vitreous-gel and the liquified-vitreous. In other words, the surface (in yellow) shown in the figure above acts as an upper surface for the liquified vitreous and lower surface for the vitreous gel. On the other hand, the lens lower surface (in red) acts as the top surface of the vitreous body. The vitreous side

boundary was created by duplicating the choroid and the retina coordinates lying in the region between the lens lower boundary and the vitreous lower boundary.

As with the lens, all the nodes forming the upper and lower surfaces were duplicated around the z-axis with reasonable angular spacing between them to create a 360^{o} shape of the vitreous, as seen from Figure 3.6.

Finally, the liquified vitreous was created using the lower surface of the vitreous as the upper boundary, and the nodes of the retina below this surface as the lower boundary (see Figure 3.6).

v Aqueous

The aqueous is a watery fluid located between the lens and the cornea. The corneal inner surface is used to form the upper boundary of the aqueous, and the upper surface of the lens acts as the lower boundary, as can be seen in Figure 3.6.

3.2.2 Meshing algorithm

Finite element analysis (FEA) software are used to build predictive computational models of real-world scenarios. The accuracy of the FEA model is directly dependant on the FE mesh that is used. The FE mesh is used to subdivide the computer-aided design (CAD) model into smaller domains called elements, over which the set of equations is solved. The smaller these elements are, the finer the mesh and the more realistic the solution.

Due to the ocular globe having a complicated geometry and, as using the solver's automatic mesh gives an inaccurate result, the creation of a meshing algorithm that can mesh all eye geometries was essential. This meshing algorithm was developed specifically for this study. The main aim of the presented technique is to allow an easy way to control the mesh density of all eye components and mesh any complicated geometry to simulate retinal detachment.

An in-house meshing algorithm was built to mesh the irregular structures of the eye components with regular mesh. This meshing technique was used to implement consistent elements to ensure consistent results. The section below explains the process undertaken to build the meshing algorithm.

The mesh is based on Nooshin and Tomatsuri's configuration of diamatic domes [39, 235]. All parts were treated separately, and the inner and outer surfaces, explained in the previous section, act as the boundaries enclosing each component of the ocular globe. First of all, all cartesian coordinates of the outer and inner boundaries of the surfaces mentioned previously in section 3.2.1 were converted to spherical coordinates. After interpolating both surfaces to achieve a common factor, which was their angle measured from the positive axis, and by duplicating and changing the radii of the nodes forming the two surfaces, new nodes between the two surfaces were generated to form a new layer in between them. The number of layers is defined at the beginning to generate the number of duplicated nodes of the outer surface nodes. Then the distance between each node in the inner and outer surface is measured. This distance is divided by the number of layers defined to calculate the distance between each layer. Figure 3.7 shows the new layers formed between the inner and the outer surface of the liquified vitreous.

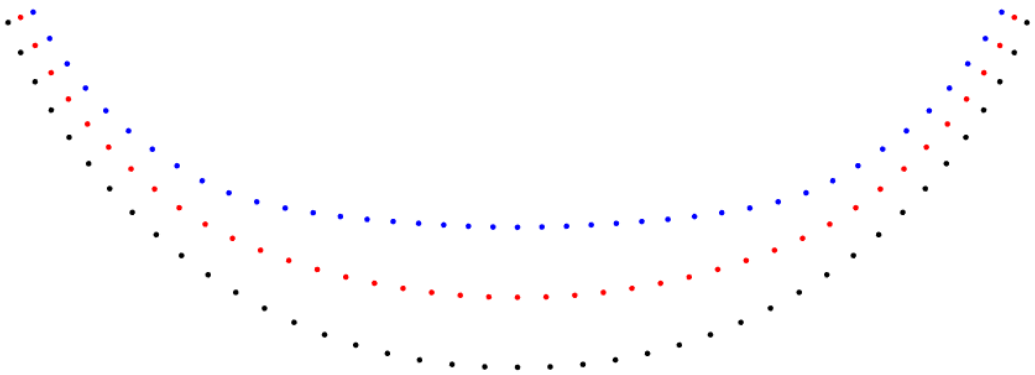

Figure 3.7: Cross-section of the liquified vitreous showing the new layer (red) formed between the upper (blue) and lower (black) boundaries

Due to the vitreous-gel large geometry, the upper and lower surfaces and the sides were combined to form one surface that acts as the outer surface for the vitreous gel. The inner surface of the vitreous gel was created in the centre of the geometry in the shape of a sphere with the same number of nodes as the outer surface, as shown in Figure 3.8. The radius of the sphere could be modified based on the desired mesh. Using the same principles mentioned above, layers were created between the vitreous gel's inner and outer surface. Finally, all the generated nodes are assigned a node number to be used for the element arrangement explained in the next section.

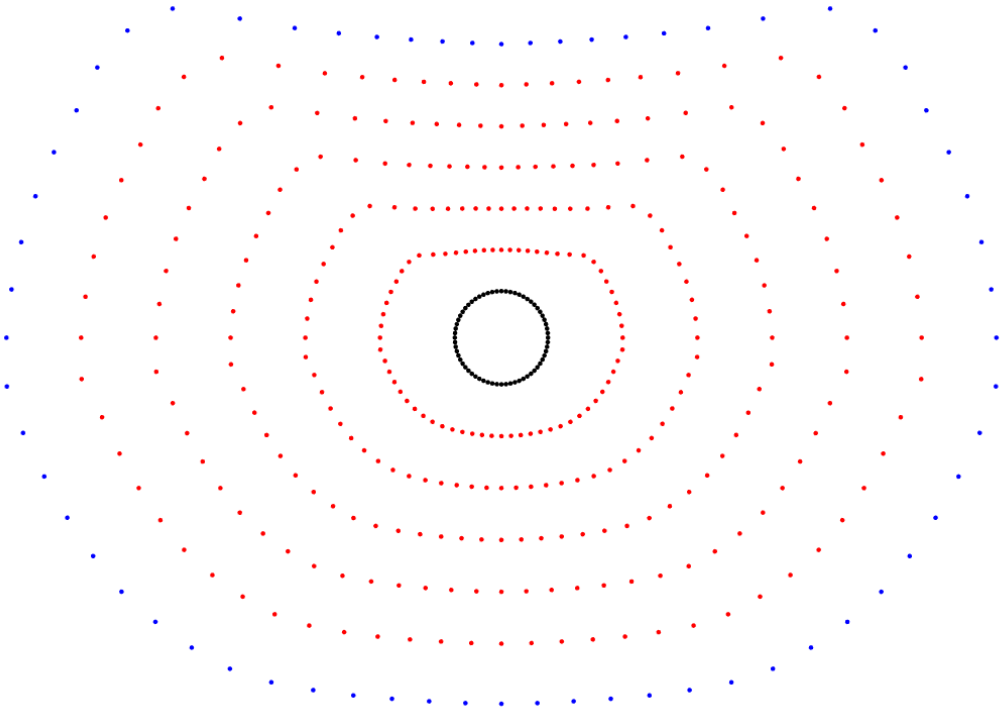

Figure 3.8: Cross-section of the vitreous body showing the new layers (red) formed between the inner (black) and outer (blue) surfaces

Once all the required nodes were created, the next step was to develop the elements forming the mesh. The algorithm could generate 6- or 8-noded elements which can be defined in the solver. The arrangement used by the algorithm for both the 6- and 8-noded element is already defined by ABAQUS.

A 6-noded element, for example, consists of 6 nodes arranged as shown in the picture below. The solver reads the element based on a specific arrangement. The only exception was the innermost layer of the vitreous elements formed of tetrahedral elements (C3D4), taking three nodes of the middle sphere and a node at the centre of the mesh to form the element.

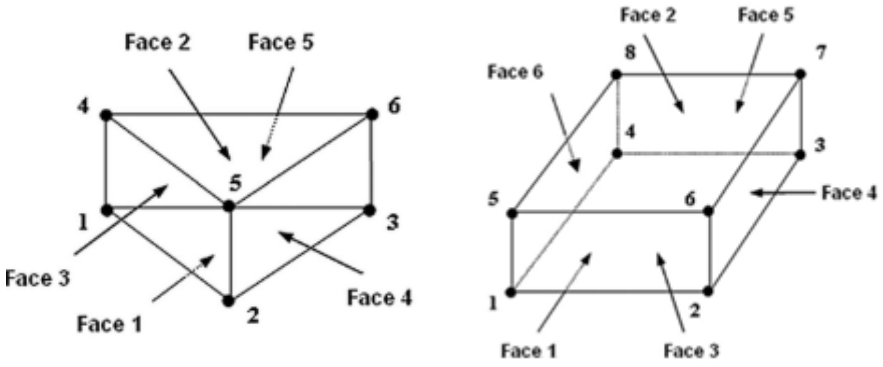

Figure 3.9: 6-noded and 8-noded arrangements as described in ABAQUS documentation [186]

In order to create the elements, three sets of elements were defined at the start: the blue, gold and grey, as can be seen from Figure 3.10. Each set of elements was created separately, then the three sets were combined. This was done to have a sequence of the node numbers that can be easily coded in MATLAB.

The number of elements in the middle is pre-defined in the algorithm. As indicated in grey in Figure 3.10, for example, the number of elements or the base is pre-defined to be six elements. In addition to the base, the number of rings desired is also pre-defined. In order to calculate the number of elements in each ring, the equation below is used.

$$Element\ per\ Ring = (0: Number\ of\ Rings) * base$$

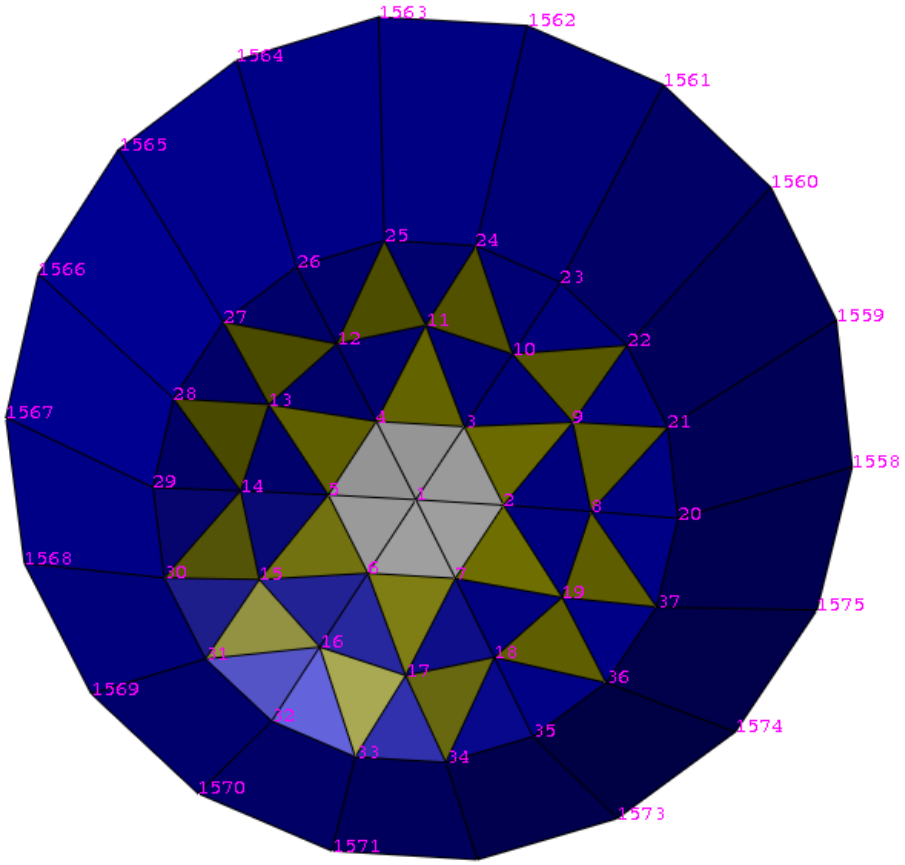

Figure 3.10: 6-noded elements arrangements as defined in the meshing algorithm

Then the first node in each ring was identified using the cumulative sum of the number of elements per ring:

$$First\ node = [1\ \ cumsum(Element\ per\ Ring) + 2]$$

Starting with the blue set, the first element had to connect nodes 2, 8 and 9 from the top face, as shown in Figure 3.10. The second element connects 3, 9 and 10, and for the third element 3, 10, and 11, etc.

The algorithm identifies each of the three nodes in each element separately, then combines them to form the element, as can be seen in the table 3-1.

For node 1, an array of 0 and 1 was created. This array (C1) has the same size as the number of elements per ring. The cumulative sum of this array was calculated to be used in the equation below. This equation determines node 1 in all elements.

$$Node\ 1 = First\ node + cumsum(C1)$$

Finally, the last node was replaced with the first node in the ring to form the array in Table 3-1 for node 1.

Table 3-1: Nodes forming the elements in the first ring

Node 1	Node 2	Node 3
2	8	9
3	9	10
3	10	11
4	11	12
4	12	13
5	13	14
5	14	15
6	15	16
6	16	17
7	17	18
7	18	19
2	19	8

As shown in Table 3-1, the array for node 2 starts with the first number in the second ring and increases gradually by 1. It can be noted that node 3 array is equal to the node 2 array plus 1. The only exception is the last node which was replaced by the first node in the ring. The three arrays were then combined, forming the top 3 nodes of the first ring elements. The bottom three nodes were determined by adding the number of nodes per layer to the top 3 nodes.

The gold and grey elements were then formed using similar equations, as mentioned before. Finally, this process was repeated for each layer to create the mesh shown in Figure 3.11.

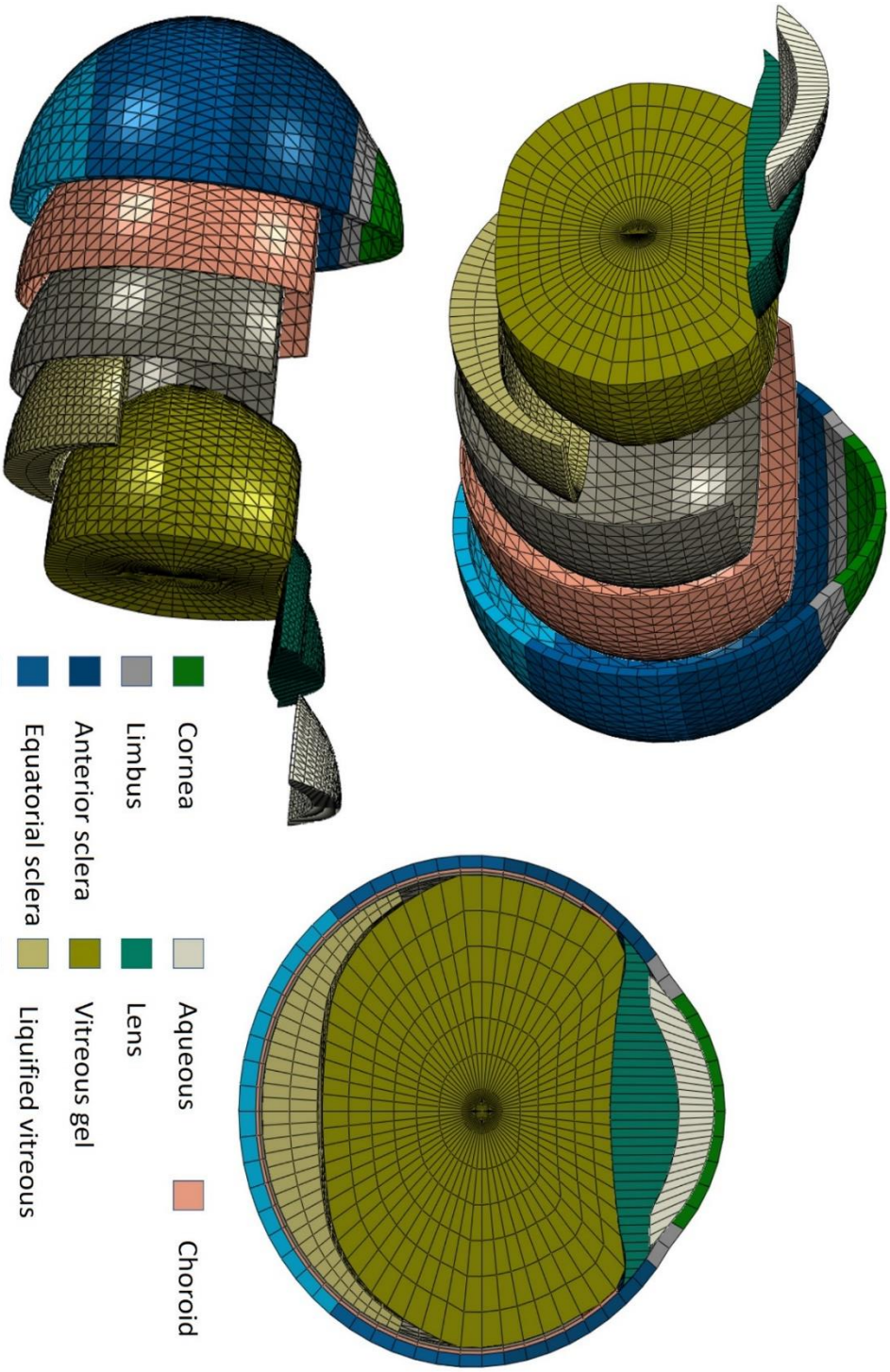

Figure 3.11: A 3D rendering of the numerical model showing the mesh layout

A similar method was developed to generate 8-noded elements, as can be seen in Figure 3.12.

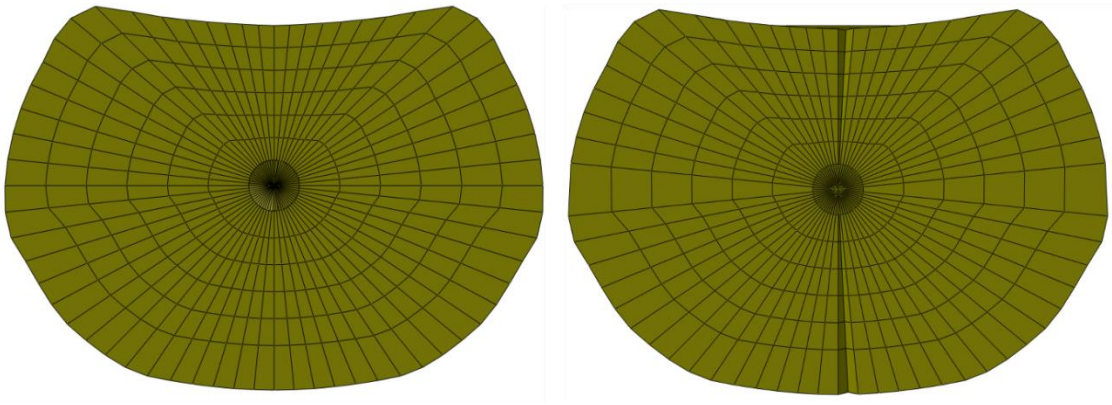

Figure 3.12: Cross-section of the vitreous body generated with 6-noded (left) and 8-noded (right) elements

To allow the meshing of asymmetrical objects, a feature that enables a change of the mesh's centre to any point was added. This was done by shifting the centre of the mesh while keeping the outside boundary's geometry, as it shown in Figure 3.13.

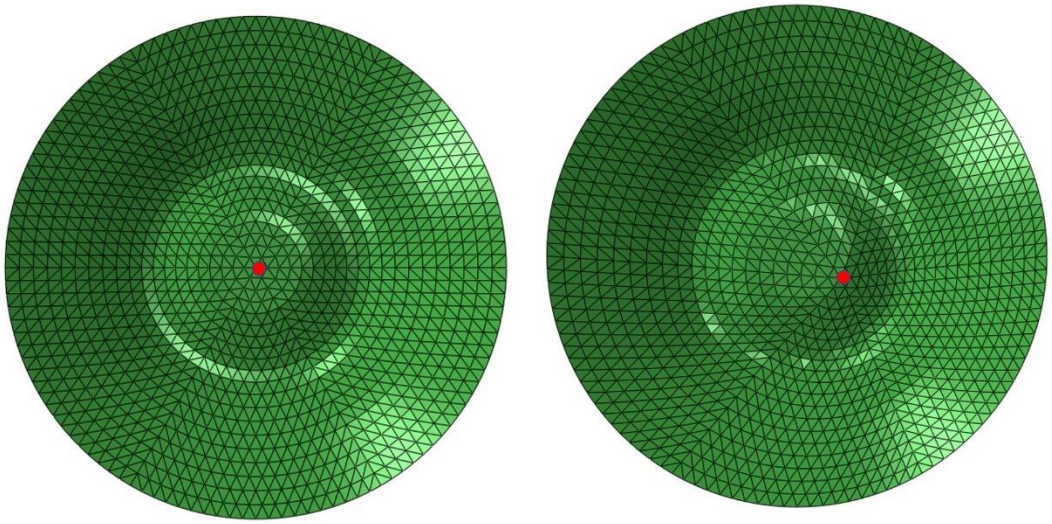

Figure 3.13: A 3D rendering of the liquified vitreous showing change in the centre of the mesh. The red point shows the centre of the mesh

Another important feature was added to the meshing algorithm, to allow for an increase in the number of nodes in specific areas in the mesh. Instead of having elements with the same size everywhere in mesh, this feature increases the mesh

size in some regions and decreases it in others. The reason this feature was added was to be able to only refine the mesh in particular areas of interest without the need to change the number of elements or nodes. This feature was created by generating a logarithmically spaced vector when duplicating the nodes around the z-axis, instead of the equally spaced distance between them. The spacing between the nodes is either increased or decreased based on the application.

Figure 3.14 shows the mesh of the liquified vitreous using equally spaced elements and logarithmically spaced elements.

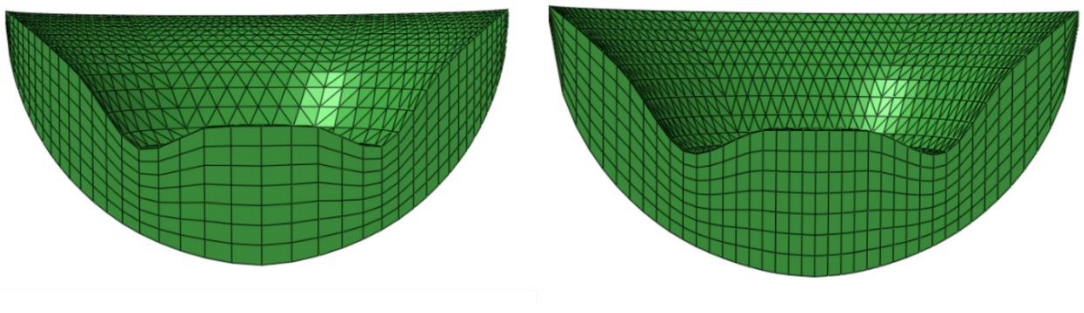

Figure 3.14: Cross-section of the liquified vitreous showing the change in element size

3.2.3 Retinal detachment generator

Bespoke software was developed from scratch specifically for this study, using MATLAB, for the task of generating characteristic models. A GUI was built to let the program's use without the need to operate or understand the underlining code.

With this software, the geometry of the eye is imported from the mesh generator software discussed previously. The Retina Detachment Generator (RDG) software allows the user to control the shape of the lens, vitreous gel, liquified vitreous and retina. The software provides the user with the interface shown in Figure 3.15. The user could load an idealised model of the ocular globe or a patient-specific model. Also, the user has the option to add the retina and the choroid.

The software was made to be as user friendly as possible, by using different tabs to control the shape of the lens, vitreous and retina in order to reduce the size of the

interface as much as possible. Moreover, buttons are provided to modify the height and radius of each parameter controlling the shape of the vitreous or the lens. In addition to the buttons, the user can still input the values manually if needed.

An instant visual display of how the model looks is also provided, as shown in Figure 3.16. Once the user chooses the vitreous and the lens shape, the software will automatically calculate the volume of the vitreous. An option for the 100% vitreous model without liquified vitreous is also provided.

Another feature provided by the software is the ability to generate an existing retinal detachment. Through the retina tab, the user can define the size and location of the retinal detachment, as shown in Figure 3.15. Currently, the software only allows the user to choose two locations. The user can specify the detachment's size by identifying the angle between both ends of the detachment vertically and around the z-axis.

The orientation option located at the bottom allows the user to display the ocular globe from every angle before generating the final model.

Along with controlling the model geometry and the exclusion/inclusion of the eye model, the software was built to control the arrangement and mesh refinement of the following variables:

- Number of rings
- Number of layers
- Centre of the mesh
- Types of elements (6- or 8-noded elements)
- Element size

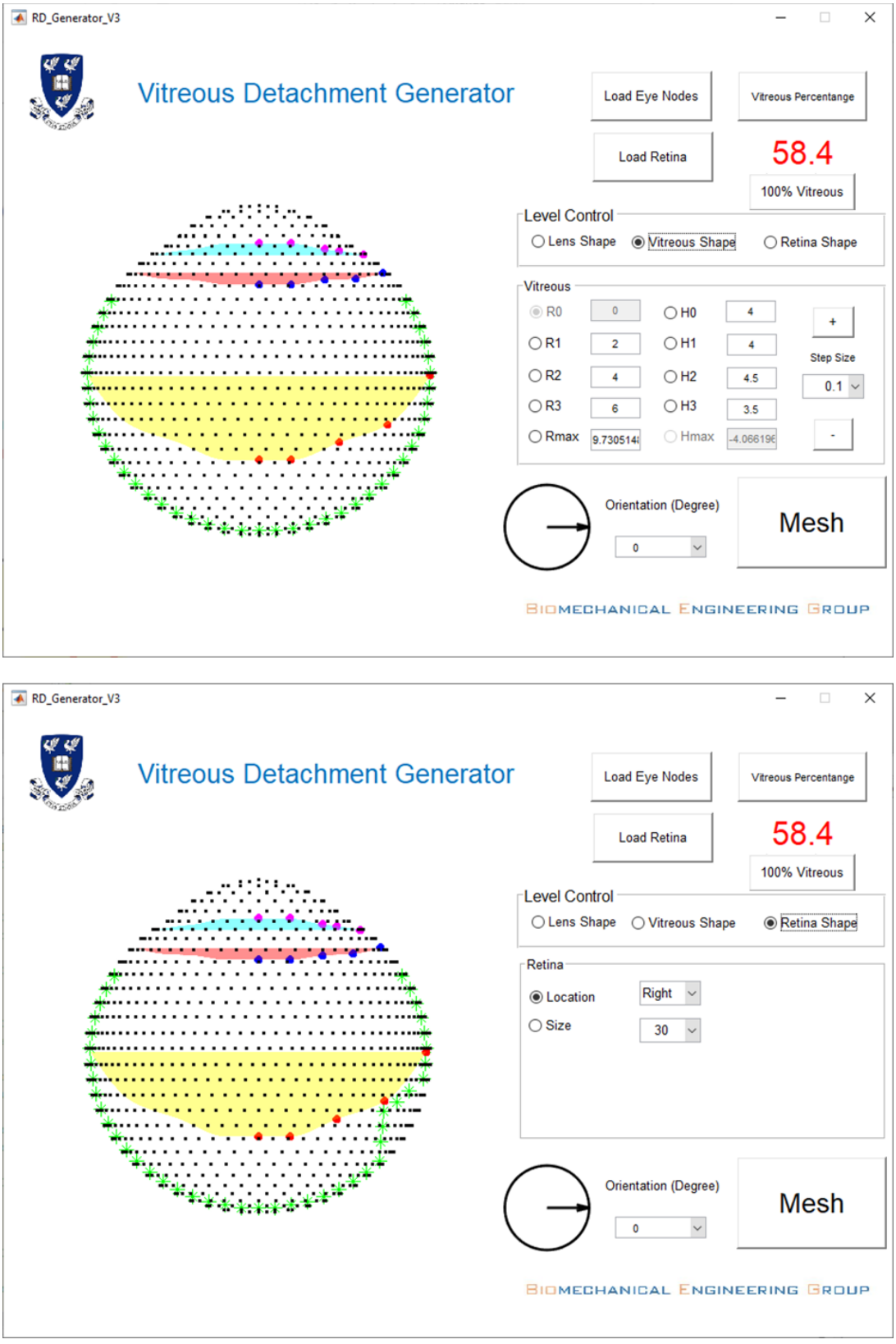

Figure 3.15: GUI designed to produce geometrically characteristic models of the human eye globe. This view of the GUI illustrates how to control vitreous, lens and retina shape

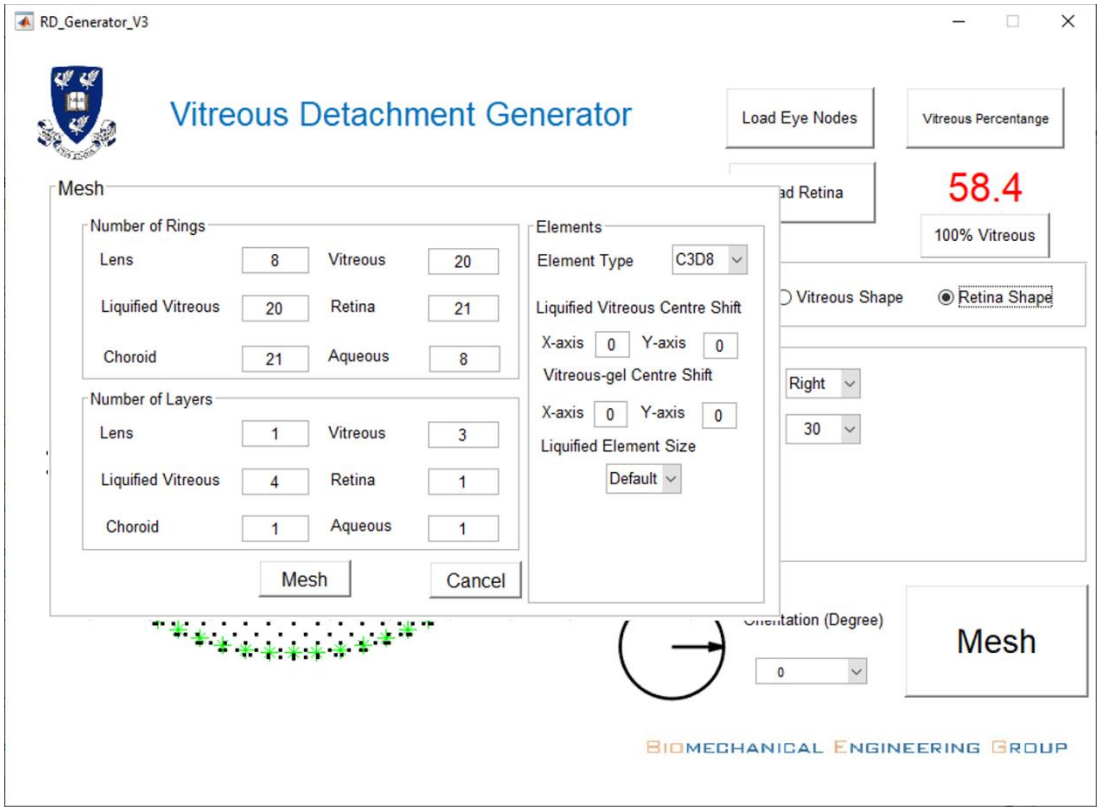

Figure 3.16: GUI designed to produce geometrically characteristic models of the human eye globe. This view of the GUI illustrates how to control the mesh of the model

The centre of the mesh is only applicable for the vitreous-gel and the liquified vitreous. The element size modification is only applicable to the liquified vitreous, as it can be seen in Figure 3.16.

Finally, once the user is satisfied with the geometry and the mesh, the software generates an input file (*.inp) to be read by ABAQUS. This method directly provides the mesh geometry to the solver as an orphan mesh. In addition to the geometry and mesh refinement, the input file includes element sets defining all parts of the ocular globe. An example of the input file produced by the software can be seen in Appendix 1.

This software helped produce models for the parametric studies and the mesh convergence study mentioned in the next section. It was also helpful for future novice users of the software. It secures the source code against corruption, and provides the convenience of speed.

3.2.4 Meshing algorithm validation

In order to validate the meshing algorithm, the ocular globe was created and meshed twice; first with the Bio Engineering Group mesh generator (See section 3.2.1), secondly with the meshing algorithm developed in this study. The ocular globe generated by the Bio Engineering Group has already been validated in earlier studies [39, 40, 58, 60, 153]. The two models were generated to have the same number of layers and rings. Using the same boundary conditions, the displacement of certain nodes was monitored when IOP was applied on the internal surface of the eye.

3.2.5 Mesh convergence study

The FEM divides the model into discrete points, each point adds degrees of freedom to the system, hence the more degrees of freedom in the model the better it will capture the structural behaviour. Mesh refinement is not always necessary in the entire model, it could be done in some areas only if needed. A higher level of accuracy can be achieved by increasing the number of elements and having a very fine mesh. However, increasing the number of cells can lead to more prolonged time consumption and the need for more computational resources. In order to concurrently satisfy both efficiency and accuracy of the analysis results, a mesh convergence study is required.

The liquefied vitreous mesh and the rest of the eye mesh were built independently, and the mesh convergence study was carried out on the eye model to identify the best mesh. The mesh convergence of the sclera, cornea, retina, choroid, aqueous and vitreous had been conducted separately (Figure 3.17); the liquefied vitreous was then added to the chosen mesh, and another mesh convergence study was carried out. The mesh was modified several times by creating a mesh using the fewest/reasonable number of elements to allow a new mesh to be recreated with denser element distribution. A model of the eye, rotating 15 degrees to the right and then 0.25 sec staying still, was simulated and the displacements, velocities and stresses of several nodes and elements in the vitreous were identified in each mesh.

The data were then analysed and the results were compared against each other. The flowchart (Figure 3.18) shows the nine models simulated to carry out the mesh convergence study. It shows the number of elements in each eye component, such as the retina, outer eye, vitreous, choroid and lens.

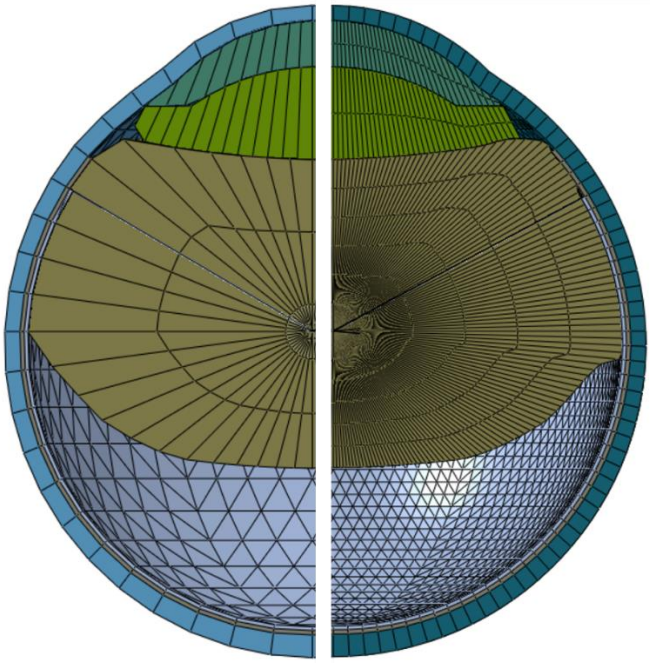

Figure 3.17: Geometry of the ocular globe showing difference between coarse (left) and fine (right) mesh

3.2.6 Material properties

The material properties of the eye model components assumed in the study are shown in 3-2. The most accurate and most recent material data have been used in this model. It was made sure that all the material parameters used in this study were validated in earlier studies. Based on the literature and available material properties, the cornea, sclera, limbus and retina were modelled as hyperelastic materials [161], represented by Ogden's constitutive model (See section 2.3.1). The lens, choroid and aqueous were assumed to be linear elastic, represented by the Young's modulus values listed in Table 3-2 [2, 236, 237]. On the other hand, the vitreous was modelled as a viscoelastic material [226].

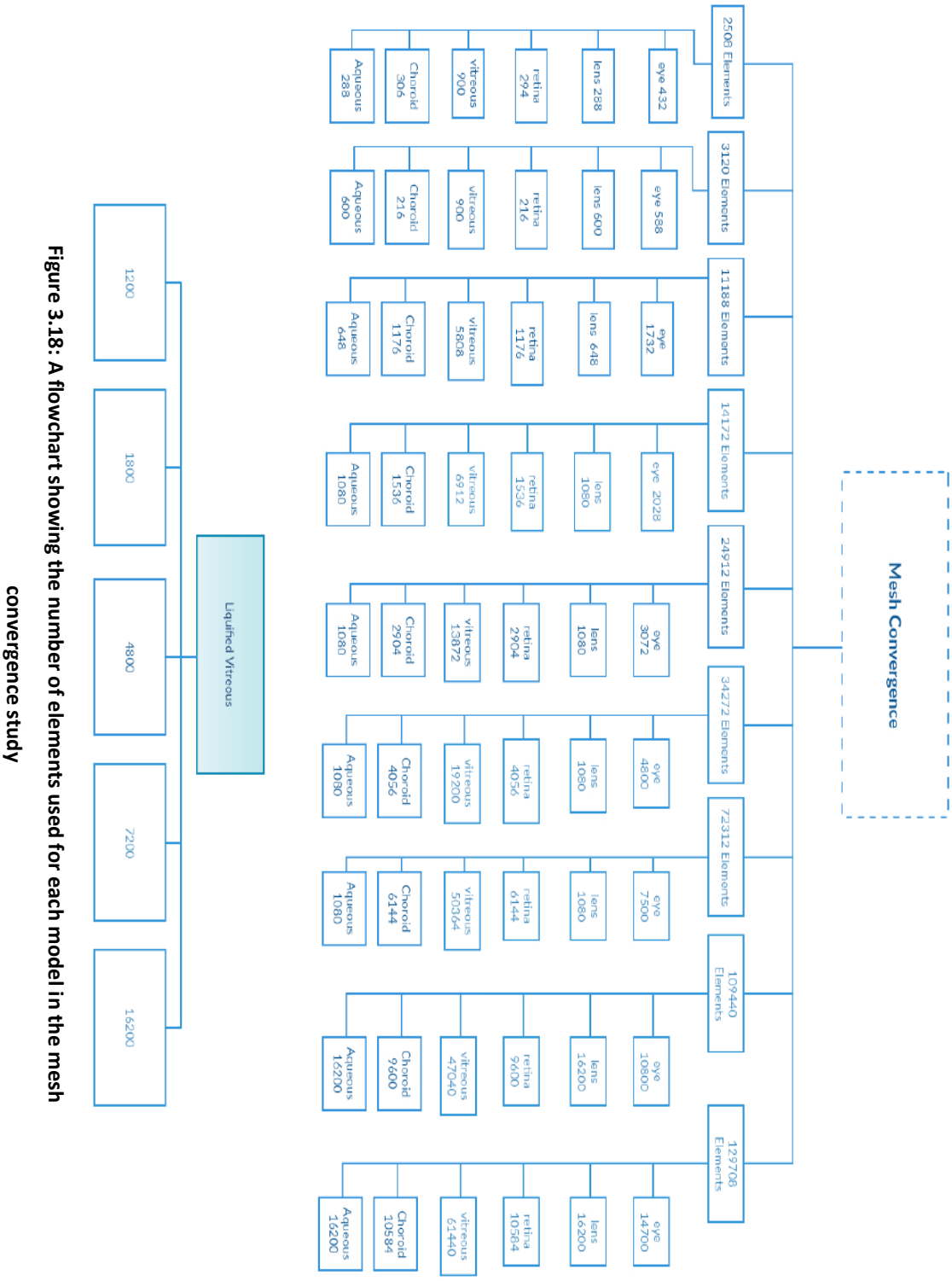

Figure 3.18: A flowchart showing the number of elements used for each model in the mesh convergence study

Table 3-2: Material and physical properties of the different regions of the numerical models

Region	Density (kg/m^3)	Material behaviour	Constitutive models and stiffness parameters
Cornea [161]	1061	Hyperelastic	Ogden: $n = 1$ $\mu = 0.0541\ MPa$ $\alpha = 110.4$
Anterior Sclera [161]	1076	Hyperelastic	Ogden: $n = 1$ $\mu = 0.2709105\ MPa$ $\alpha = 150$
Equatorial Sclera [161]	1076	Hyperelastic	Ogden: $n = 1$ $\mu = 0.133279\ MPa$ $\alpha = 150$
Posterior Sclera [161]	1076	Hyperelastic	Ogden: $n = 1$ $\mu = 0.133279\ MPa$ $\alpha = 150$
Limbus [161]	1076	Hyperelastic	Ogden: $n = 1$ $\mu = 0.2709105\ MPa$ $\alpha = 150$
Retina [120]	1033	Hyperelastic	Ogden: $n = 1$ $\mu = 0.012021\ MPa$ $\alpha = 145$
Lens [2]	1078	Elastic	$E = 6.88\ MPa$
Choroid [236]	1000	Elastic	$E = 0.159\ MPa$
Aqueous [237]	1000	Elastic	$E = 0.037\ MPa$
Vitreous [226]	1000	Viscoelastic	$G_o = 2.1 * 10^{-6}\ MPa$ $G_\infty = 0.5 * 10^{-6}\ Pa$ $\beta = 1.2\ s^{-1}$

μ: shear modulus; α: strain hardening exponent; E: elastic modulus; G_o initial shear modulus; G_∞ infinite shear modulus; β: viscoelastic decay constant

3.3 Parametric studies

The following two parametric studies were carried out to study the dependency of the model on certain parameters such as the volume of the vitreous and the size of the vitreous detachment. Moreover, another two parametric studies were carried out to investigate the effect of the parameters mentioned above on retinal detachment progression during head and eye movements. All the parametric studies were carried out twice using two methods to model the liquified vitreous.

3.3.1 Parametric study 1

Using the vitreous detachment software, multiple models were created. The common factor between these models is the attachment point of the vitreous to the retina. For this presented study, a vitreous detachment was assumed in all the models. However, the retina was firmly attached to the choroid, assuming no retinal detachment would occur. The size of the vitreous was varied in each model, creating eight models with different vitreous volume. This study investigates the effect of the vitreous volume on the retinal traction during head and saccadic eye movements.

i Models creation

The most crucial factor in this parametric study was maintaining the same shape of the vitreous while changing the volume. One variable had to be changed at a time; if the vitreous body's curvature varied from one model to another, this could cause inconsistencies in the results. Therefore, a way to change the vitreous volume while keeping the vitreous shape was developed to ensure consistency.

Firstly, the shape desired for the vitreous was created, as shown in Figure 3.19. This shape was created to have precisely 50% vitreous body (indicated in red). The new shape acts as an upper surface, and the posterior pole of the eye acts as the lower surface. It is important to note that the lower surface represents the 100% vitreous body (Blue). The two surfaces were then divided into a set of equal points and, to

increase accuracy, the number of points was maximised as much as possible. Furthermore, all the nodes in the two surfaces were converted into spherical coordinates; this was actioned to have common factors between the opposite nodes, such as the azimuth and the elevation angles.

In addition, the distance between each opposite two points was calculated by subtracting each node's radius, in the 50% layer, from the radius of its opposite node in the 100% layer. Each distance was then divided by the number of layers desired, N, in order to calculate the distance between the layers at each point. The new distance was then subtracted from the radius of points at the 100% vitreous layer, forming a new set of nodes between the two layers.

The new set of nodes was then used as a new lower surface, and the above process repeated but with $N_{new} = N_{old} - 1$. This process iterates until $N_{new} = 0$ and all the layers nodes are created, as can be seen in Figure 3.19. Finally, the new nodes were converted back into a cartesian coordinate system and imported into the custom-built MATLAB code mentioned in Section 3.2.3 to mesh the new vitreous.

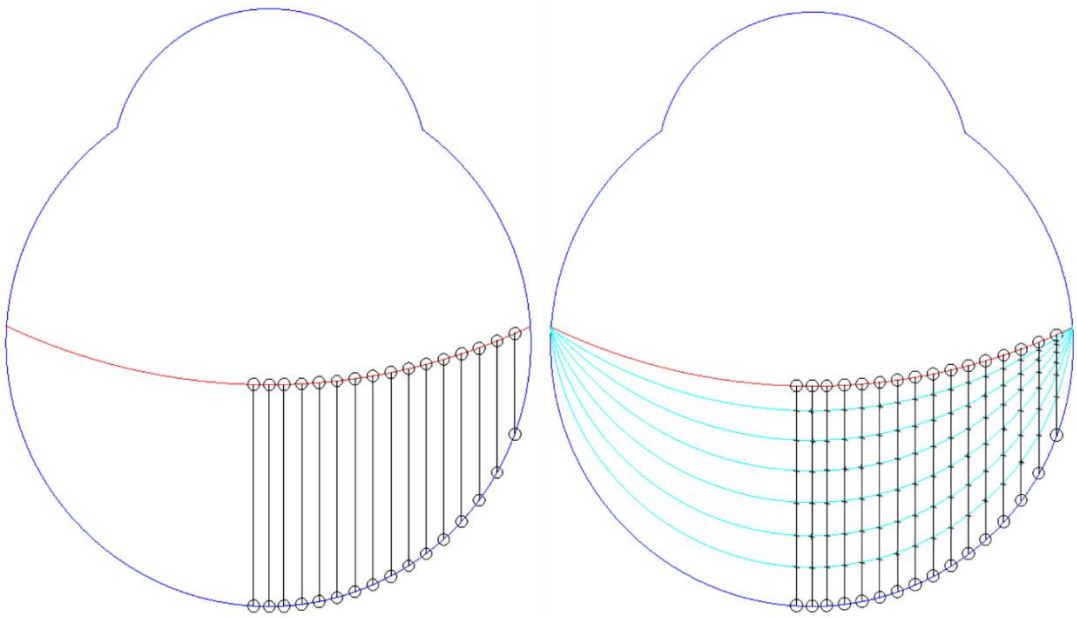

Figure 3.19: Schematic drawing of ocular globe showing the process to create the models used in parametric study

After meshing the vitreous, the nodes forming the upper and lower layers were exported and used in a different custom-built code to create and mesh the liquified vitreous. The vitreous and the liquified vitreous were then combined with the other eye components forming the models shown in Figure 3.20. For the presented study, eight models were created, representing the vitreous volume of 72.5% to 90%. The common factor between these models is the detachment point of the vitreous from the retina, which reflected one of the common clinical cases after consultation with veteran vitreoretinal surgeons and selected at a location below the equator [198]. This location allowed simulation of the range of vitreous volumes.

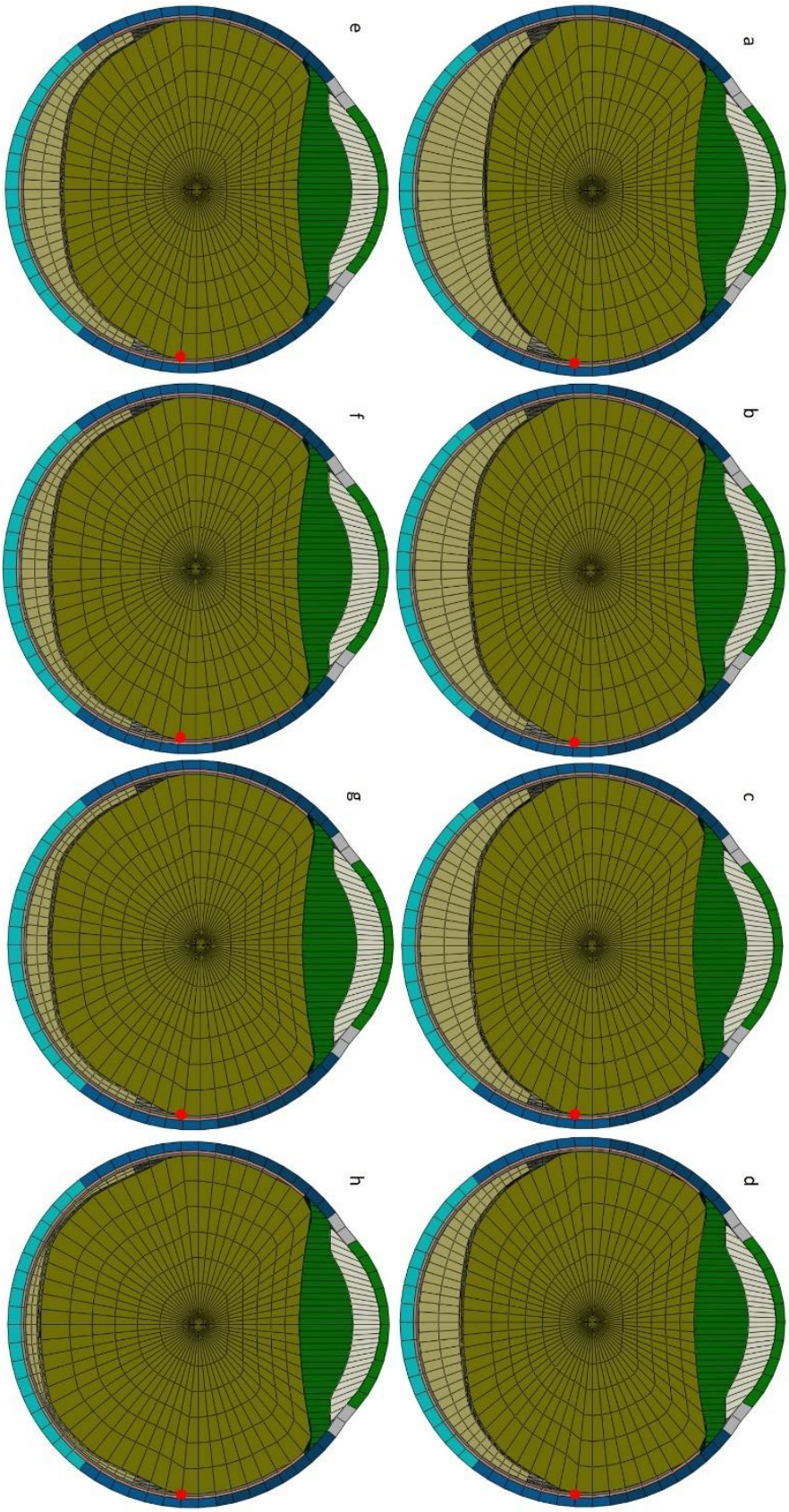

Figure 3.20: The numerical models with vitreous volumes of (a) 72.5%, (b) 75%, (c) 77.5%, (d) 80%, (e) 82.5%, (f) 85%, (g) 87.5% and (h) 90%. The red point indicates the points of interest at which the traction was measured

ii Load cases

Two load cases were used to investigate the difference between saccadic and head eye movements. It's known that most saccades do not exceed 15 degrees [196]. Therefore, the load case defined to represent the eye movement was 10 degrees. This saccadic eye movement is a fast and large saccade, larger than 95% of all saccades [196]. In order to import this load to ABAQUS, the two equations below were used to define the rotation over time. This load case consisted of the defined saccade movement as well as the second movement of stationary simulation. The second movement was chosen to be 0.5 seconds, giving the vitreous time to rest.

$$T = 0.021 \ \propto_o^{2/5} \tag{3.1}$$

$$\propto (t) \ = \frac{\propto_o}{2}\left(1 - \cos\left(\frac{\pi}{T}t\right)\right) \tag{3.2}$$

where T is the time for one saccade, $\propto$ is the saccade angle in degrees and t is the time.

Using an equation similar to equation 3.2, the head movement was defined as a linear transition (see equation 3.3). The transition size was defined to be 2 millimetres, as shown in Figure 3.21, and the period was kept the same as the saccade. The reason this movement was chosen is due its acceleration being close to the one produced by the defined saccades. The acceleration chosen for the head movement simulation is comparable to sitting down on a chair or a cough motion [192]. This motion is smaller than those created by jogging but more extensive than those created by walking [189].

$$s(t) \ = \frac{s_o}{2}\left(1 - \cos\left(\frac{\pi}{T}t\right)\right) \tag{3.3}$$

where s is the translation over time in millimetres.

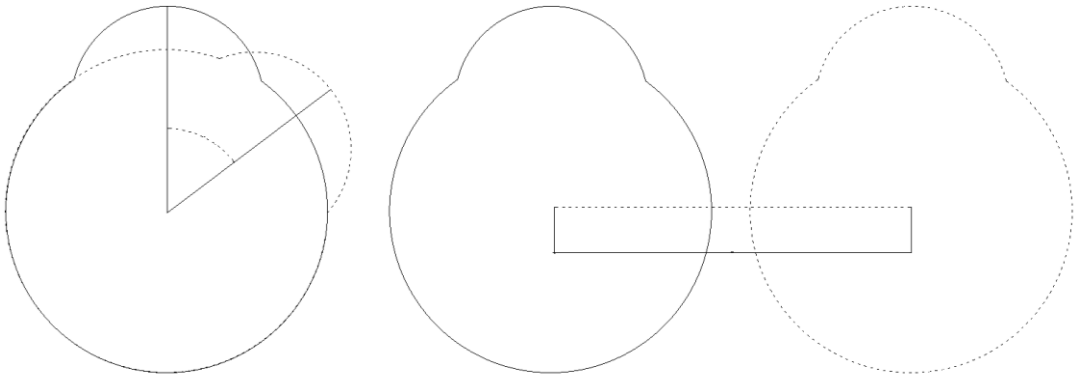

Figure 3.21: A schematic drawing of the ocular globe showing the difference between the saccadic (left) and head (right) eye movements

iii Boundary conditions

ABAQUS/Explicit was used for this study, as it can simulate transient dynamic events and it can effectively handle severe nonlinear behaviour such as contact. The movements were calculated using the previously mentioned equations. For the 10-degree rotation, the time period was found to be 0.0527 seconds. The rotation angle was converted to radians and defined in ABAQUS as a displacement/rotation boundary condition. As ABAQUS requires the amplitude to be defined for this particular boundary condition, the rotation angle value over time was calculated using MATLAB, and tableized and imported to the solver. The outside nodes of the cornea, sclera and limbus were coupled to a reference node at the centre of the eye and the movement was applied to this reference node, as shown in Figure 3.22. A general contact between all eye components was defined to avoid any penetration between the parts. In order for the model to be stable a frictionless contact couldn't be set therefore the coefficient of friction for this contact was assumed to be a small value of 0.04. Any value smaller than this led to instability in the simulations.

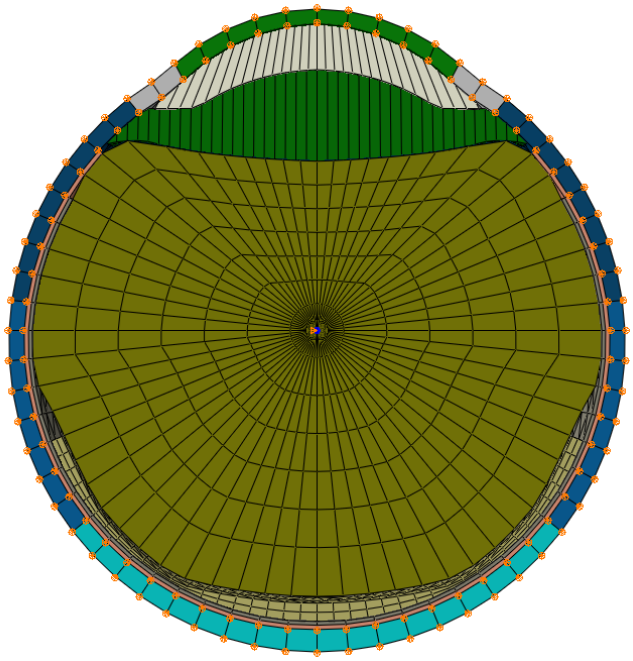

Figure 3.22: A cross-section of the numerical model showing the boundary conditions applied to the outer layer to simulate the eye movement

iv Liquified vitreous

The fluid between the retina and the vitreous was modelled using two methods. Firstly, the parametric study was carried out using continuum elements to model the liquified vitreous, as shown in Figure 3.23. The shear modulus of the vitreous was reduced to represent vitreous liquefication. A shear modulus that is half the modulus used for the vitreous was used to define the liquified vitreous material parameters. Liu et al. [2] used continuum elements with half the vitreous material parameters to model vitreous liquefaction. Liu and colleagues' study demonstrated a strong correlation when performing a Pearson correlation test. Correlation analysis indicated that their eye model could predict dynamic response when subjected to blunt impact.

In the second method, the continuum elements representing the liquified vitreous were removed. The space between the retina and the vitreous was modelled using ABAQUS' FLUID CAVITY option (Section 2.3.3). The fluid cavity was considered by an

enclosing surface and a bulk modulus to describe the compressibility. In order to simulate near incompressibility, the bulk modulus was set at 1 *kPa*. The free fluid mass was added evenly to the elements surrounding a cavity using the non-structural mass option provided by ABAQUS. Vroon and Jong [145] used the fluid cavity to model the liquified vitreous, and demonstrated a strong behaviour between numerical and clinical data of the ocular globe.

3.3.2 Parametric study 2

Contrary to the first parametric study, the common factor between all models created for this study is the vitreous volume. In order to investigate the effect of vitreous detachment size on retinal traction during head and eye movements. The volume of the vitreous was kept the same at 82.5% of vitreous chamber while changing the vitreous-retina attachment point. This volume enabled simulation of the PVD progression for cases where vitreous volume remained unchanged. Similar to the first parametric study, the retina was firmly attached to the choroid.

i Model creation

Like the first parametric study, the most important factor was to maintain the vitreous shape in all models. Changing the vitreous attachment point while keeping the volume the same was challenging. However, this was done by maintaining the angle between the vitreous and the retina in all models. It was found that changing the angle between the retina and the vitreous, Figure 3.23, led to inconsistencies in the results. Therefore, after producing all the models using the Vitreous Detachment software, the models were imported to MATLAB. Using a custom-built code, the lower surfaces of the vitreous for all models were modified to achieve the same angle between the retina and the vitreous. This was done by identifying the nodes in the vitreous lower surface and the retina, and by calculating the angle in between. This angle was then modified to be the same in all models. Following this, the vitreous

volume was re-calculated. The coordinates of these nodes were modified to keep the volume constant in all models.

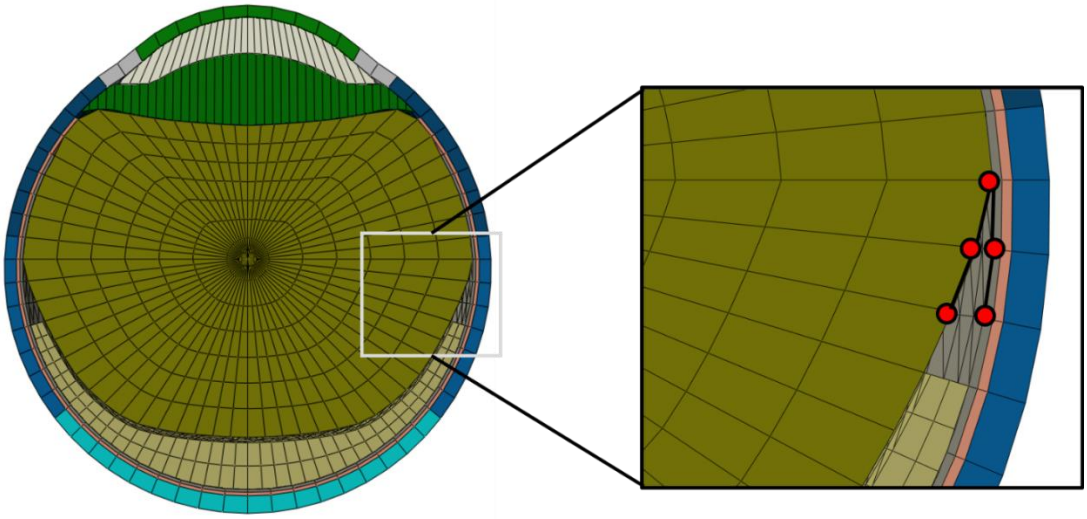

Figure 3.23: A cross-section of the ocular globe showing the method used to fix inconsistencies in the results

Six models were created for this study, with various vitreous-retina attachment points. The first point was chosen to be the node at 10 degrees above the equator, as shown in Figure 3.24. The last model was chosen to be at approximately 15 degrees below the equator, with the remaining models at 5-degree intervals.

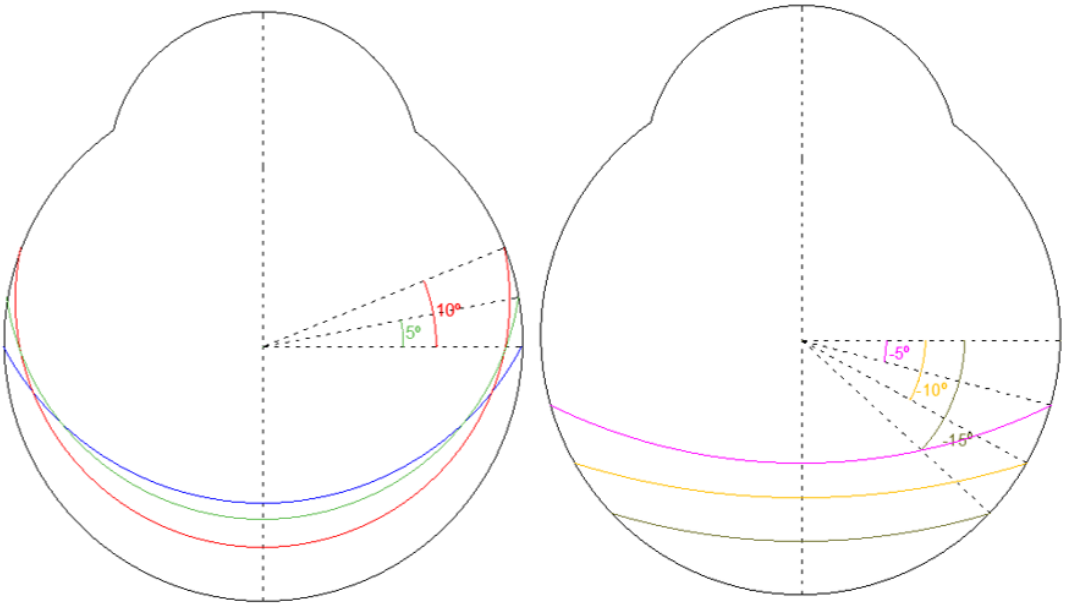

Figure 3.24: A schematic drawing of the ocular globe showing the process to create the models used in the second parametric study

After fixing all the vitreous surface shapes, the new lower surface of the vitreous was taken into MATLAB to create the liquified vitreous. The vitreous and the liquified vitreous were then combined with all the eye components forming the models in Figure 3.25.

Similar to the first parametric study, the eye model simulations were carried out twice to investigate the effect of head and eye movements on retinal tractions. Moreover, the liquified vitreous was modelled using the two methods mentioned in Section 3.3.1.

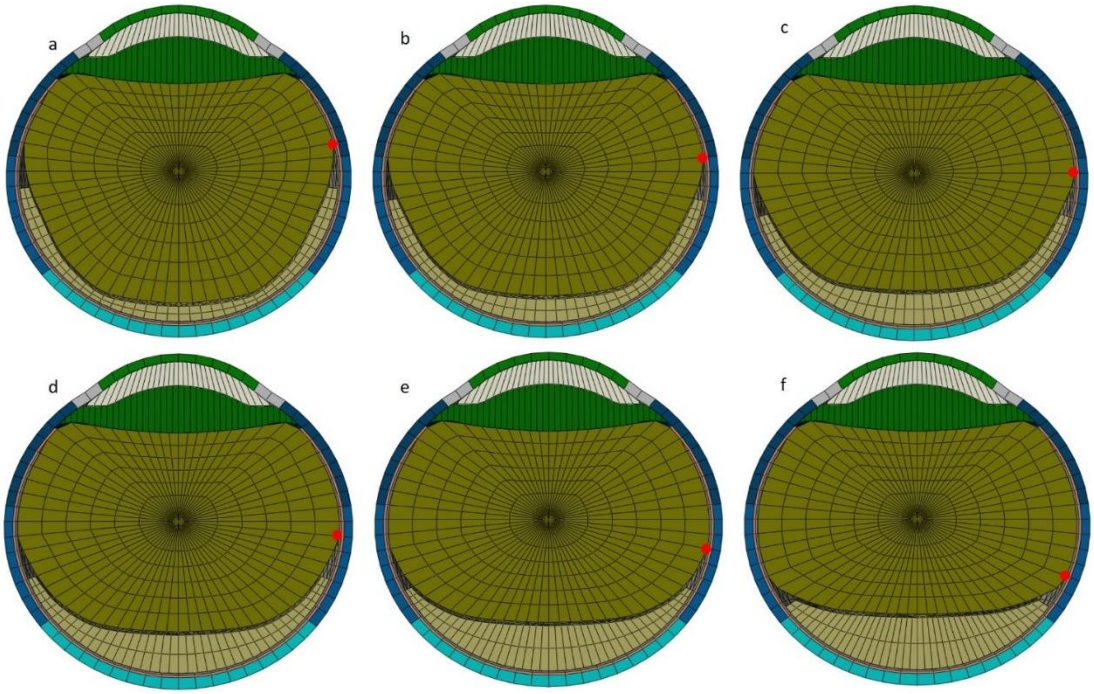

Figure 3.25: The numerical models with vitreous detachment starts at (a) 10° above the equator, (b) 5° above the equator, (c) the equator, (d) 5° below the equator, (e) 10° below the equator and (f) 15° below the equator. The red point indicates the points of interest at which the traction was measured

3.3.3 Parametric study 3

This study was carried out to investigate the progression of retinal detachment caused by the vitreous volume. Similar to parametric study 1, eight models were created. These models have one common factor: the size of the vitreous detachment. The only varying factor is the volume of the vitreous.

i Model creation

The same models used for parametric study 1 were used for this study; the only difference was the introduction of a new layer between the retina and the choroid. This layer was used to simulate and track retinal debonding from the choroid.

In order to not change the geometry of the ocular globe, the choroid layer created previously was split into two layers; the choroid, which has almost 50% of the

choroidal thickness, and the debonding layer, which is a very thin layer as can be seen in Figure 3.26.

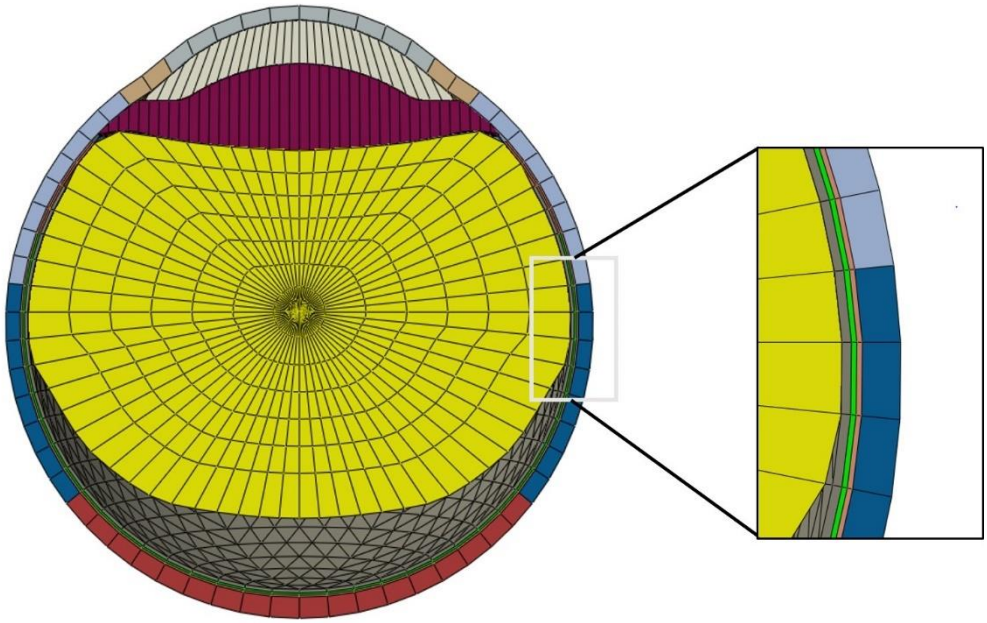

Figure 3.26: Cross-section of the ocular globe showing the new layer (green) introduced between the retina (grey) and the choroid (orange)

The intermediate layer was modelled to have the same number of elements as the choroid and the retina. The new layer shares the same nodes with the retina and the choroid, as shown in Figure 3.27.

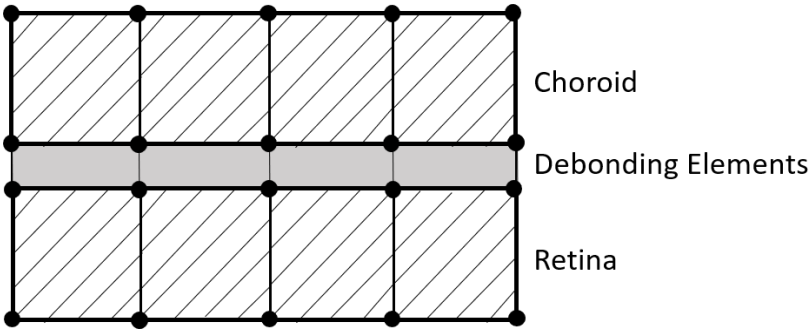

Figure 3.27: Cohesive elements sharing nodes with the retina and choroid elements

The 'cohesive elements' option in ABAQUS was used to model this new layer. Cohesive elements are used to bond two different components. Often the cohesive elements completely degrade in tension and shear as a result of the deformation. By

default, these elements hold their resistance to compression even if their resistance to other deformation modes is entirely degraded.

ii Damage criteria

A damage criterion was defined to delete the cohesive elements once they are entirely damaged. Therefore, contact between the choroid and the retina is modelled throughout the analysis.

The elements were modelled using a 6-noded three-dimensional cohesive element (COH3D6). The material properties of the cohesive elements were defined using the "damage for traction-separation laws" option in ABAQUS. This option allows the definition of maximum normal and shear stress that the elements can stand before they fail. The extent of retinal detachment was measured in the 3D models by allowing the thin cohesion layer between the choroid and retina to disappear at locations where the maximum traction exceeded a certain threshold. A threshold of 3 Pa was selected, based on the value of the average traction obtained from the first two studies. However, that was the only known parameter in the process. Therefore, in order to determine the other parameters leading to element deletion, a multi-objective optimisation was performed on a sample model of the eye.

The optimisation was carried out while varying the following parameters:

t_n	Nominal stress for normal-only mode;
$t_{s,1}$	Nominal stress for first direction (shear);
$t_{s,2}$	Nominal stress for second direction (shear);
δ	Displacement at failure; and
E	Elastic modulus

Optimisation was carried out to determine the above values that cause the elements to disappear at specific stress levels. ABAQUS provides a STATUS field output; this offers each element's status as active (1) or inactive/disappeared (0). These data were extracted for each model, and the stress at each point of the inactive element

was calculated. This stress was then compared to the pre-defined stress, and the root mean square (RMS) error was calculated.

iii Load cases

In contrast with the first two parametric studies, this study didn't have the second step where the eye stays still after the saccades. The effect of multiple saccades was investigated by rotating the eye multiple times with no rest in between. The saccade was repeated three times in a row for each test. The study was carried out three times in order to evaluate the effect of different saccade angles. The eye was subjected to tests with maximum rotations of 5^o, 10^o, and 15^o.

Moreover, the effect of head movement on the progression of retinal detachment was also studied and compared to the saccadic eye movements. Here, the eye was subjected to a transition, where the transition size was defined to be 2 millimetres, and the period was kept the same as the 10^o saccade. Similar to the saccadic eye movement, the effect of head movement on the progression of retinal detachment was investigated by moving the eye multiple times with no rest between each step.

Similar to the other parametric studies, the eye model simulations were carried out twice using the two methods to model the liquified vitreous, as mentioned in Section 3.3.1.

3.3.4 Parametric study 4

This study was carried out to investigate the progression of retinal detachment caused by the vitreous detachment size. Similar to parametric study 2, 6 models were created; these models have one common factor: the size of the vitreous volume and only varying factor is the size of the vitreous detachment.

The models used for parametric study 2 were imported to MATLAB and the layer discussed in Section 3.3.3 was added. The same boundary conditions were applied; the simulations were carried out three times to investigate retinal detachment

progression due to the three eye rotation speeds, as compared to the effect of head movement. Finally, the study was repeated using the FLUID CAVITY option to simulate the liquified vitreous.

3.4 Traction calculation

3.4.1 Stress rotation

ABAQUS documentation was considered to accurately calculate the traction applied on the retina (which causes retinal detachment). ABAQUS provides several types of stresses such as von mises, contact stress, Tresca, and principal stresses. ABAQUS provides stresses acting on *XYZ* planes (Figure 3.28); however, due to the eye's rotation during saccadic eye movements, the stress perpendicular to the sclera is the stress causing the traction. ABAQUS's contact stress (CSTRESS) is the stress perpendicular to the surface, causing the traction. This option in ABAQUS is only available if contact is defined between the surfaces. However, in the parametric studies mentioned before, the MPC option was used to tie the retina to the choroid and vitreous. The MPC doesn't allow the contact stress to be calculated by ABAQUS. Therefore, a custom code was created to analyse the stress applied on the retina, and automatically calculate the stress perpendicular to the sclera, where traction pulling the retina and choroid apart is defined as positive.

The stress tensor is a contravariant second-order tensor, which means it transforms under the coordinate system's change. The component σ_{xx}, for example, in the initial coordinate system is transformed into $\sigma_{xx}{}''$ in the new system according to the tensor rule shown below.

$$\sigma''_{xx} = A\sigma A^T$$

$$\begin{bmatrix} \sigma_{xx}{}'' & \tau_{xy}{}'' & \tau_{xz}{}'' \\ \tau_{yx}{}'' & \sigma_{yy}{}'' & \tau_{yz}{}'' \\ \tau_{zx}{}'' & \tau_{zy}{}'' & \sigma_{zz}{}'' \end{bmatrix} = \begin{bmatrix} a_{xx} & a_{xy} & a_{xz} \\ a_{yx} & a_{yy} & a_{yz} \\ a_{zx} & a_{xy} & a_{zz} \end{bmatrix} \begin{bmatrix} \sigma_{xx} & \tau_{xy} & \tau_{xz} \\ \tau_{yx} & \sigma_{yy} & \tau_{yz} \\ \tau_{zx} & \tau_{zy} & \sigma_{zz} \end{bmatrix} \begin{bmatrix} a_{xx} & a_{yx} & a_{zx} \\ a_{xy} & a_{yy} & a_{zy} \\ a_{xz} & a_{yz} & a_{zz} \end{bmatrix}$$

where a is a rotation matrix with components in *XYZ* planes.

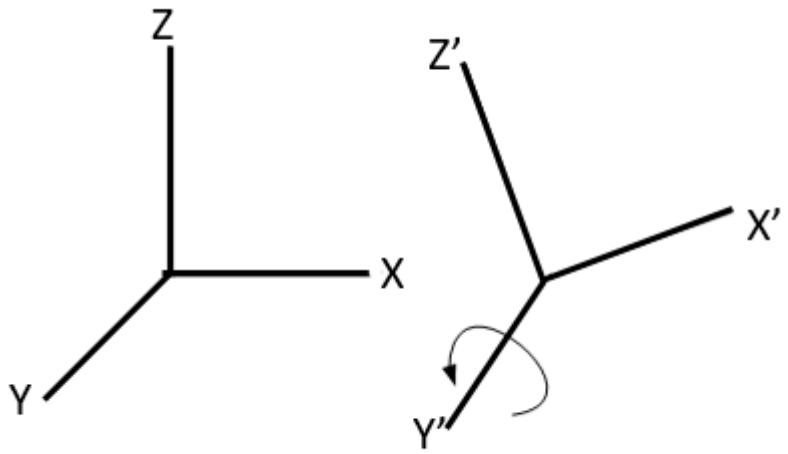

Figure 3.28: Schematic of XYZ axes before and after applying rotation

At t=0, the stress-causing traction is assumed to be the stress towards the eye's centre perpendicular to the sclera. However, once the eye starts to rotate, the stress in x or z directions are not normal on the surface. As such, a bespoke code was designed to extract the stresses tensor matrix, $\begin{matrix}\sigma_{xx} & \tau_{xy} & \tau_{xz}\\ \tau_{yx} & \sigma_{yy} & \tau_{yz}\\ \tau_{zx} & \tau_{zy} & \sigma_{zz}\end{matrix}$, for all the retinal nodes from ABAQUS. This matrix represents the normal stresses on the diagonal and shear stresses off-diagonal. These stresses are based on ABAQUS' default coordinate system. However, as mentioned before, the ocular globe rotates while the default coordinate system does not. In addition to the stress tensor matrix, the change in displacement in x, y and z planes of all the retinal nodes was extracted. The difference in displacement was then added up to the initial coordinates to get the exact coordinate at each time step.

The bespoke code calculates the acute angle, μ, between the line extended from the node of interest and the centreline, as can be seen from Figure 3.29. Using μ, the angle, ɣ, between the z-axis and the line extended from the node of interest is then calculated.

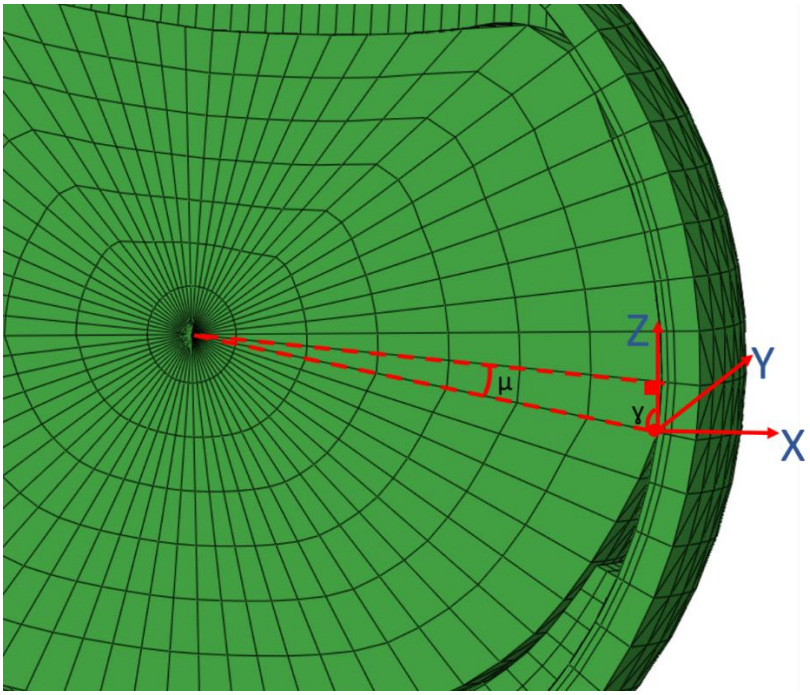

Figure 3.29: Cross-section of ocular globe showing XYZ axes and the angles calculated to rotate the stress directions

Using the angle ɣ and stress in the x and z directions, the stresses were rotated anticlockwise around the y-axis to calculate the stress perpendicular to the surface, as shown in Figure 3.29, using the transformation matrix below. The bespoke code automatically transforms the stress at each time step based on the new coordinate system.

$$\begin{bmatrix} \sigma_{xx}'' & \tau_{xy}'' & \tau_{xz}'' \\ \tau_{yx}'' & \sigma_{yy}'' & \tau_{yz}'' \\ \tau_{zx}'' & \tau_{zy}'' & \sigma_{zz}'' \end{bmatrix} = \begin{bmatrix} cos\gamma & 0 & sin\gamma \\ 0 & 1 & 0 \\ -sin\gamma & 0 & cos\gamma \end{bmatrix} \begin{bmatrix} \sigma_{xx} & \tau_{xy} & \tau_{xz} \\ \tau_{yx} & \sigma_{yy} & \tau_{yz} \\ \tau_{zx} & \tau_{zy} & \sigma_{zz} \end{bmatrix} \begin{bmatrix} cos\gamma & 0 & -sin\gamma \\ 0 & 1 & 0 \\ sin\gamma & 0 & cos\gamma \end{bmatrix}$$

In order to validate this algorithm, a comparison with the contact stress option provided by ABAQUS was carried out. Two finite element models of the eye were created, one using MPC and the other using contact between the retina and the choroid. The contact stress was extracted from ABAQUS as well as the stresses tensor matrix. These stresses matrices were analysed and transformed using the method explained above. The results were then compared against the contact stress.

3.5 Results

3.5.1 Mesh convergence

i Meshing algorithm validation

For the purpose of validating the meshing algorithm developed in this study, two models of the ocular globe were generated using the new meshing algorithm and using the Ocular bio mechanics mesh generator, respectively. Figure 3.30 shows the displacement map of the ocular globe when IOP was applied on the inner surface of the eye. The displacement of the apex node was monitored and the RMS error between the two models was calculated and found to be 1.3%.

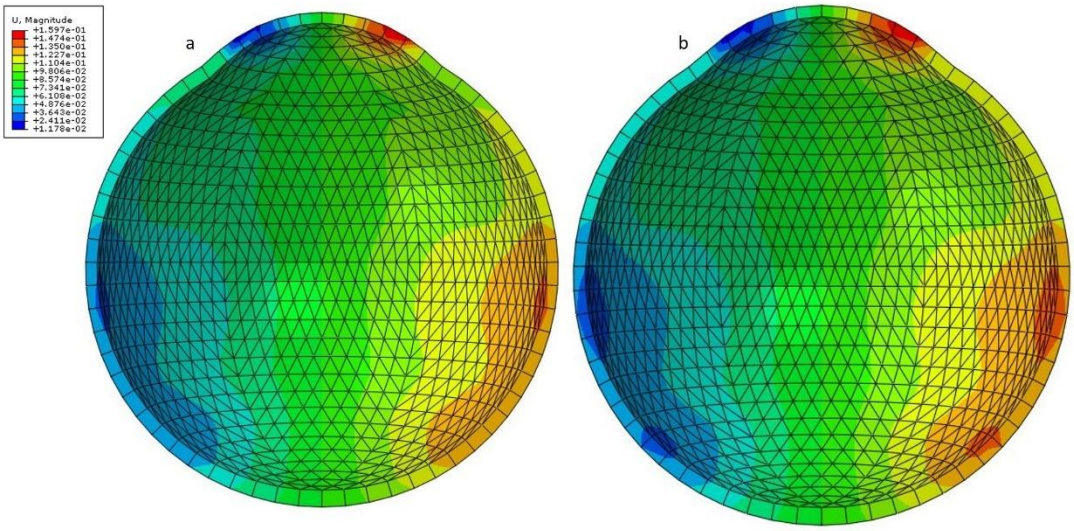

Figure 3.30: Finite element model of the ocular globe with displacement distribution plotted at 60 mmHg. (a) and (b) provide the displacement map of the models generated using the OcularBio mechanics group mesh generator and the new meshing algorithm, respectively.

ii Element type

As mentioned in Section 3.2.2, the meshing algorithm can generate hexahedral (type C3D6) and 8-node brick (type C3D8) elements. In order to choose the most suitable element type for all studies, a comparison between the two types of elements was carried out. The displacement of 2 random nodes in the vitreous were monitored, as can be seen in Figure 3.31

Figure 3.31a shows the displacement recorded at the monitoring point at a distance 8 mm from the centre of rotation. For the hexahedral elements, the point reached a maximum displacement of 2 mm. On the other hand, in the model using 8-noded elements, the point reached its maximum displacement of 1.9 mm with less than five milliseconds delay.

Figure 3.31b illustrates the displacement recorded for another point at 6 mm from the centre of rotation in the two models with hexahedral and 8-noded elements. The displacement was almost the same for the two models. The key difference recorded between the two models was the computational time, the model with the hexahedral elements has fewer nodes, therefore less computational time. Based on this result, the elements with the hexahedral shape was used in the study to represent the vitreous.

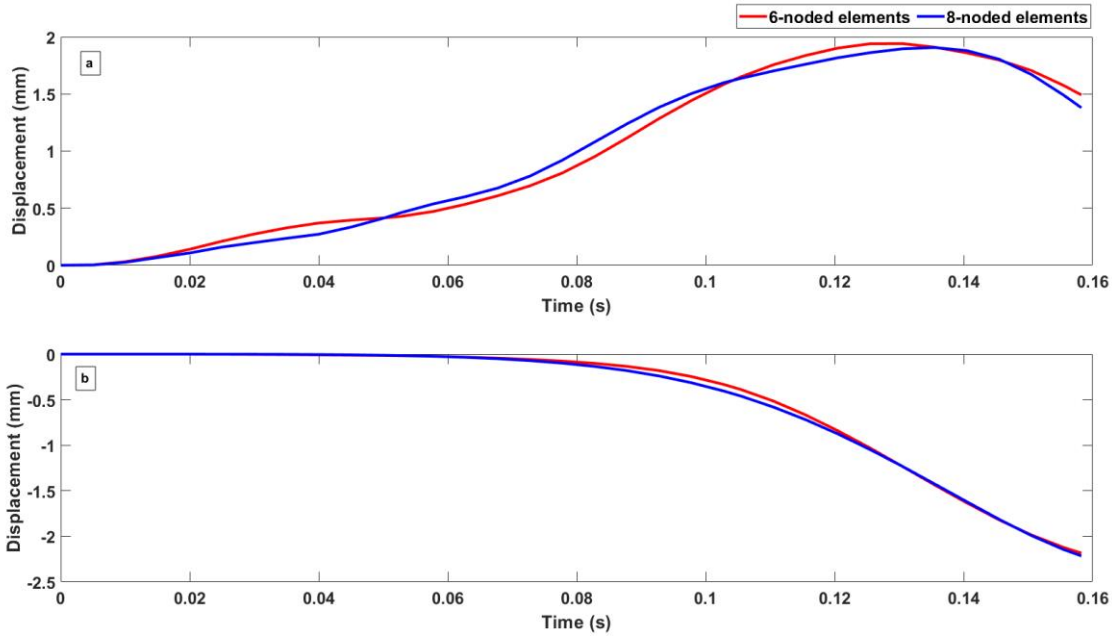

Figure 3.31: Vitreous displacement of points at (a) 8 mm and (b) 5 mm away from the centre in models with hexahedral and 8-noded elements

iii Human eye

Before the parametric studies were carried out, a mesh density study was conducted to ensure accuracy of the numerical solution as previously explained in Section 3.2.4. The mesh density study was carried out twice. First, for all the eye components except the liquified vitreous, and then, when the optimum mesh was chosen and the liquified vitreous was added, another mesh density study was conducted to determine the best mesh for the liquified vitreous.

The two first models with a very coarse mesh crashed as the elements were too large; therefore, these two models were taken out of the analysis. As it can be seen in Figure 3.32, the mesh convergence study for the ocular globe showed a 5.1% change in the vitreous deformation when the number of elements increased from 11188 to 24912. On the other hand, a much smaller difference in deformation, 1.2%, took place when the number of elements increased from 24912 to 129708. Therefore, the model containing 24912 elements was used in the study to represent the ocular globe.

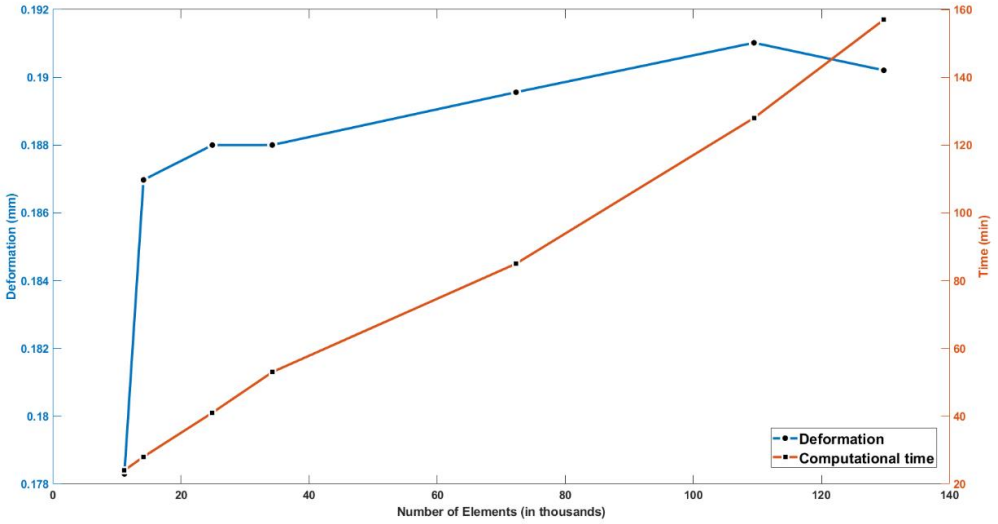

Figure 3.32: Vitreous displacement outputs and CPU computation time of the numerical models

For the liquified vitreous, Figure 3.33 shows that significant reductions in mesh density from 16200 elements to 4800 elements led to 70% reductions in analysis cost, causing only 1.9% in the liquified vitreous deformation. However, further reduction in the number of elements (from 4800 to 1200 elements) led to a change in the deformation by 34%. Therefore, a mesh density with 4800 liquified vitreous elements was selected for this study.

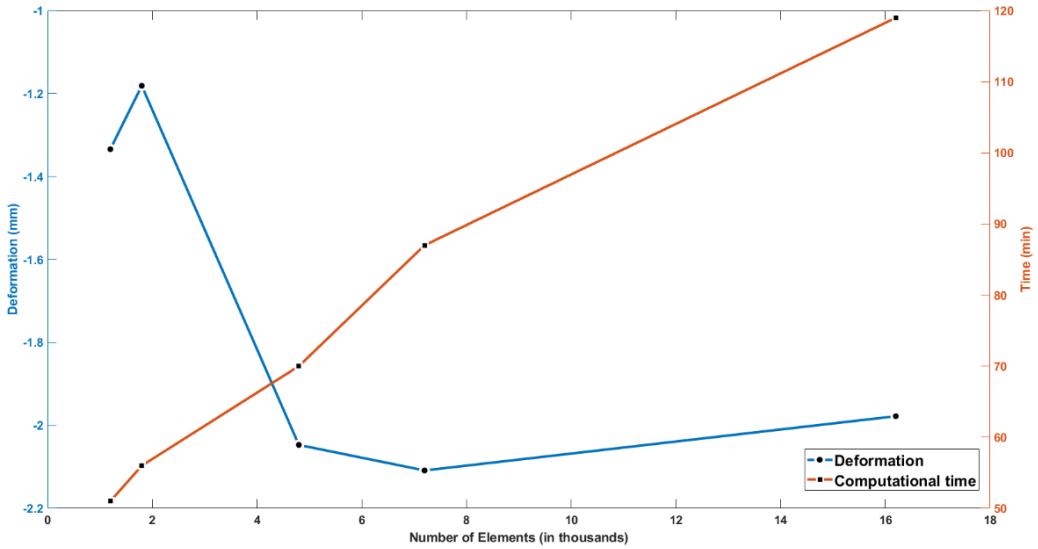

Figure 3.33: Liquified vitreous displacement outputs and CPU computation time of the numerical models

3.5.2 Tractional stress

As mentioned in Section 3.4, to calculate the stress causing the retina to detach, a stress rotation matrix was used to find the stress perpendicular to the sclera while the eye rotates. To validate this method, comparison between this stress and the CSTRESS output provided by ABAQUS was carried out. Figure 3.34 shows the stress on a point at 10.6 mm from the centre of the vitreous connecting the retina to the choroid. It can be seen that the peak stress calculated using stress rotation reached 4.2 Pa, while the stress extracted from ABAQUS reached 3.2 Pa. The RMS error between the stress calculated and the CSTRESS is 0.38 Pa.

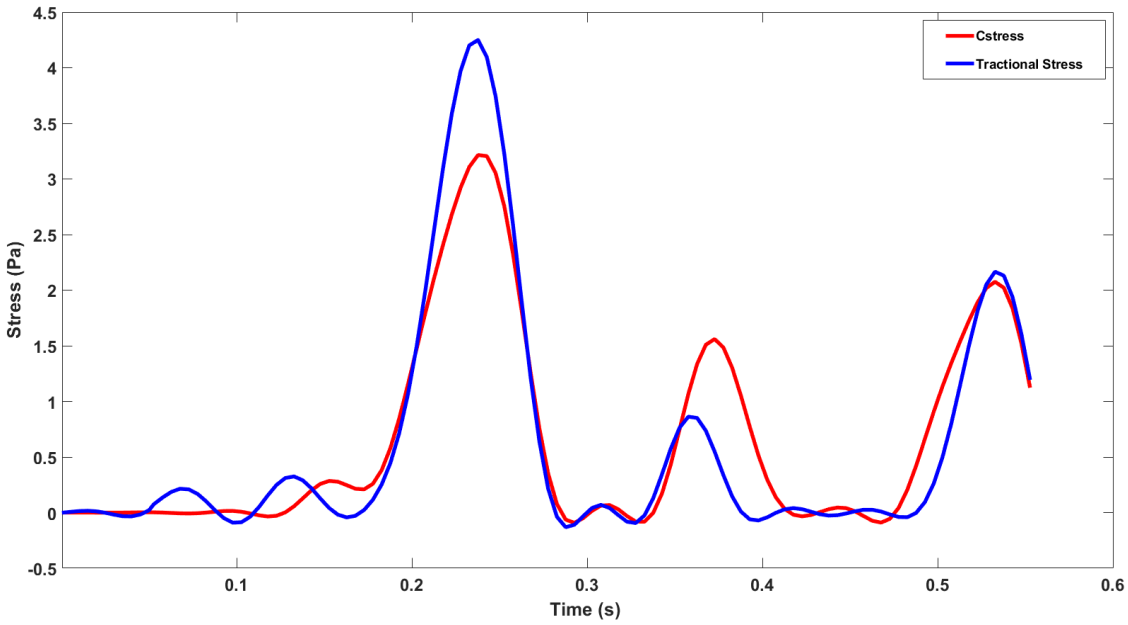

Figure 3.34: Stress perpendicular to the sclera using the CSTRESS option provided by ABAQUS and using stress rotation

3.5.3 IOP effect

The effect of (IOP) was neglected after conducting a comparison between cases with and without IOP and finding that the effect of ignoring IOP on traction forces was less than 1.2%. Figure 3.35 shows the stress on a retinal node with and without IOP.

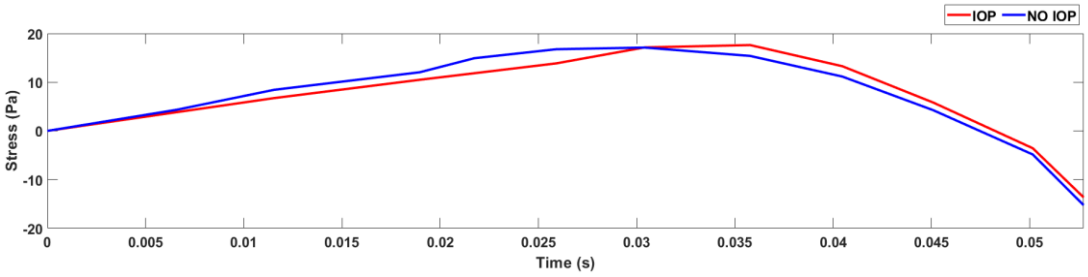

Figure 3.35: Stress on a retinal node with and without IOP

3.5.4 Parametric studies

i Effect of vitreous volume on retinal traction

This study aimed to investigate the effect of the vitreous volume on the retina. Eight models of the ocular globe were created, as mentioned in Section 3.3.1, and the traction stress at a point of interest was measured for each model. The point of interest was determined after analysing all the nodes of the retina to find where the maximum stress occurs. For the eight models, the same point of interest was used; this was the node where vitreous detachment starts, as illustrated in Figure 3.36. The same dynamic load was applied to all models to investigate the effect of saccadic and head movements on the retina.

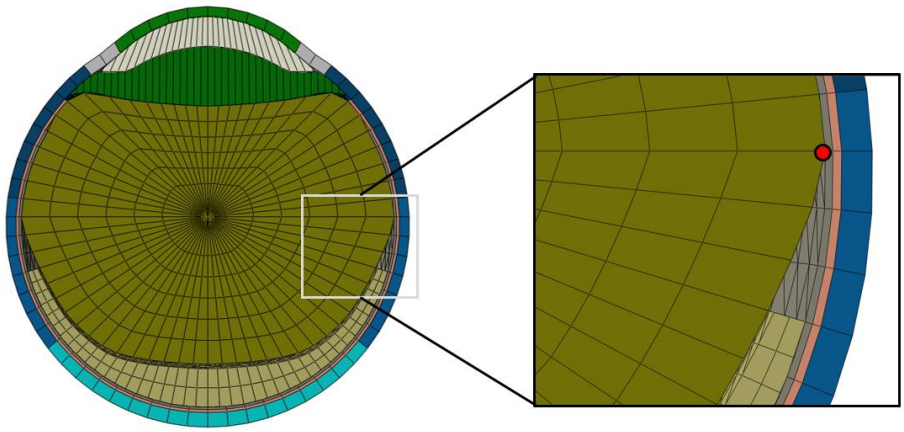

Figure 3.36: Eye model showing the point where stress was measured

Saccadic movements

Figure 3.37 shows traction on the points of interest over time, for the saccadic eye movement when the fluid cavity option was used to simulate the liquified vitreous. The tractions are compared to the applied whole eye rotations. The results show that maximum stress for all models occurred between 200 and 300 milliseconds. It is clear that, during the first step, while the eye was rotating, there was no sign of tension in any model. Tension only occurred during the second step, when the eye remained in the same position. It can be noticed that the 72.5% vitreous model achieved its maximum traction first, followed by the 75% vitreous model. Maximum traction was then consecutively achieved by all models. The maximum stress for all the models lays between 3.4 and 4.4 Pa. All model traction levels returned to 0 Pa at 400 ms before consecutively increasing again at 470 ms for models 72.5-82.5% vitreous. In contrast, the 85-90% vitreous models did not rise during this time span.

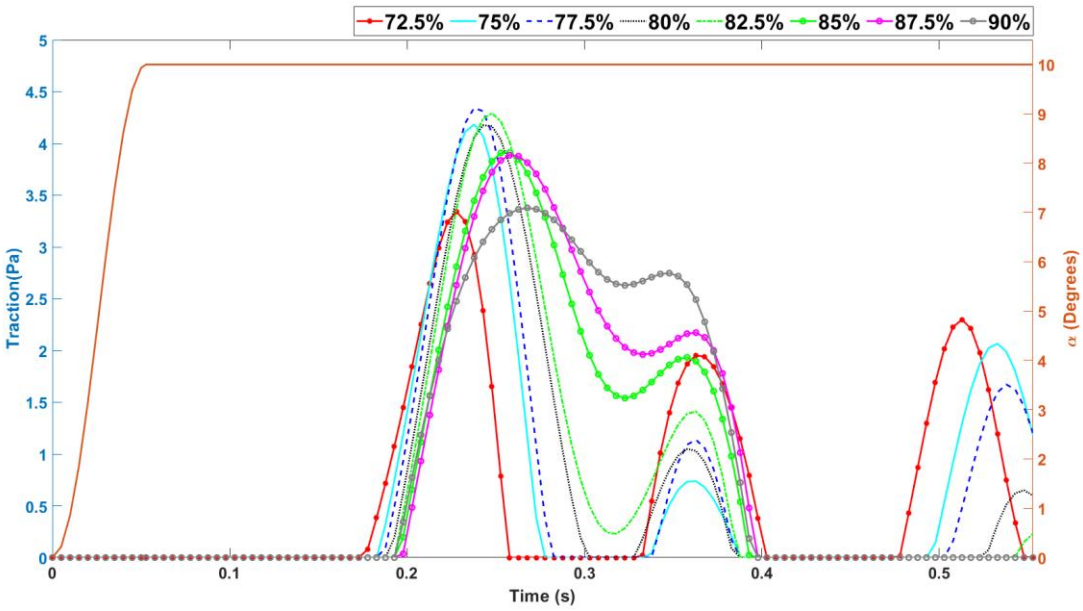

Figure 3.37: Traction on the point of interest over time for saccadic eye movements, using fluid cavity to simulate liquified vitreous

Meanwhile, Figure 3.38 compares the characteristics of the frequency domain of the models with different vitreous volumes. The power spectral density (PSD) diagram is used to normalise the amplitudes by the frequency resolution to give the amplitudes a similar appearance. PSD helps ensure that random data can be overlaid and compared independently of the frequency resolution used to measure the data [238, 239].

It can be observed that in the frequency range of 0-20 Hz, the normalised PSD amplitude of the model with 90% vitreous was the greatest. The amplitudes of 87.5% and 85% vitreous were very close to the maximum amplitude. The amplitude for the models with between 72.5-82.5% vitreous were small. It is clear that the dominant frequency for all the models is 5 Hz, and the amplitude increases when the volume of the vitreous increases.

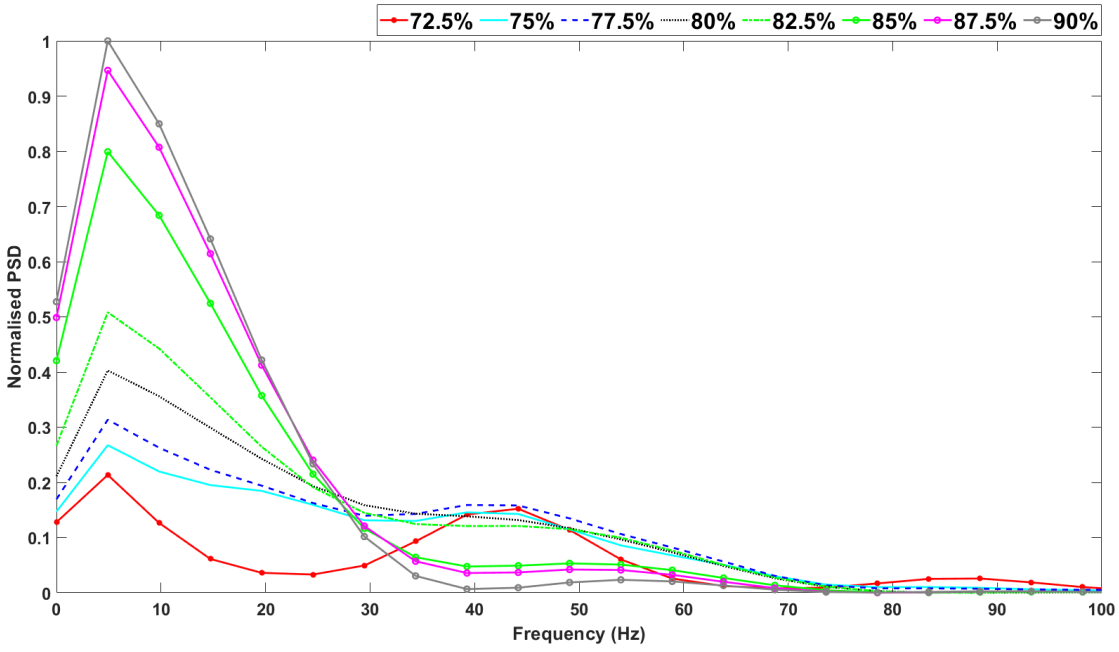

Figure 3.38: Power spectrum diagram at the points of interest for saccadic eye movements, using the fluid cavity to simulate liquified vitreous

Figure 3.39 illustrates traction on the point of interest over time for saccadic eye movement when continuum elements were used to model the liquified vitreous. The graph shows that the eye rotated 10^{o} clockwise for 52 ms then stayed still for 500 ms. In contrast to the fluid cavity models, all models' maximum traction occurred at different time steps. For instance, 72.5% and 75% vitreous models achieved the maximum stress between 450 and 550 milliseconds; however, the other models reached their maximum traction between 200 and 300 milliseconds. It is clear that the maximum traction for all the models lay between 3 and 4.2 Pa. Tension occurred immediately after the first step (at 52 milliseconds) with no signs of tension during the first step. Moreover, the tension started to occur in the model with 90% vitreous first, followed consecutively by all other models. This led to a phase difference between all models.

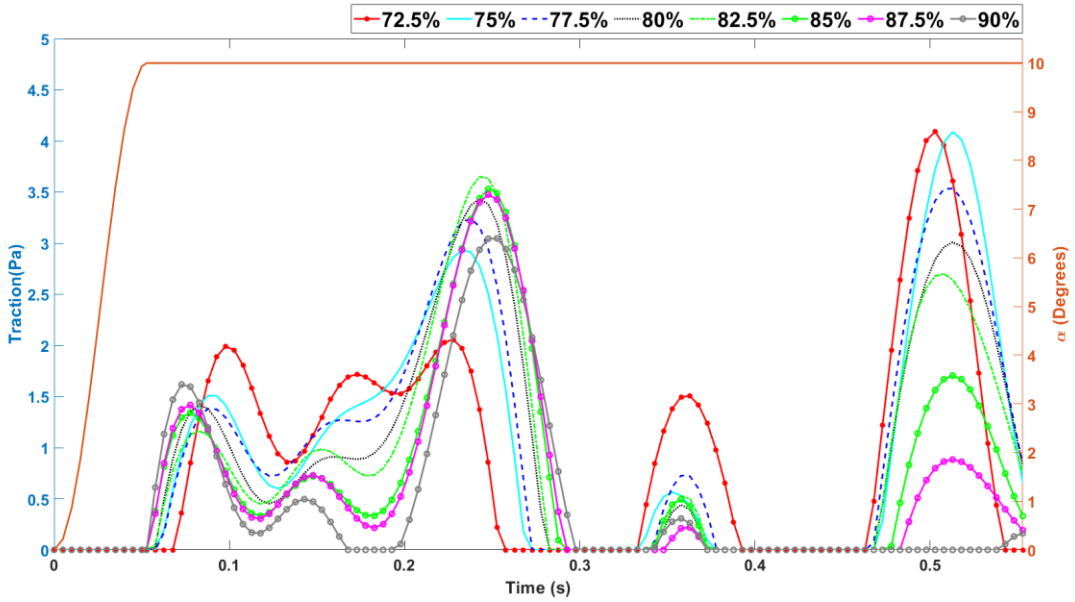

Figure 3.39: Traction on the point of interest over time, for the saccadic eye movements using continuum elements to simulate liquified vitreous

Power density analysis of the point of interest for all models is shown in Figure 3.40. It can be observed that the dominant frequencies are 4.9 and 44 Hz. The peak amplitude for all models occurred during the first dominant frequency. Even though a clear trend could not be observed in the amplitude, all the models' amplitudes were close, especially in the second dominant frequency. The 80% and 82.5% vitreous models achieved the maximum amplitude, while 72.5% and 90% achieved the lowest.

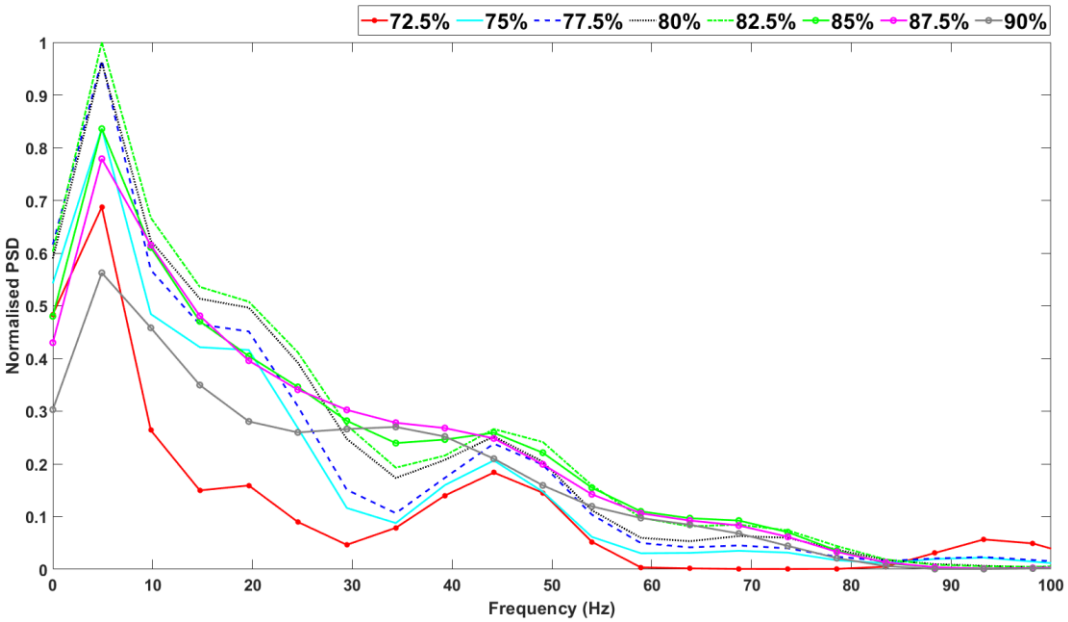

Figure 3.40: Power spectrum diagram at the points of interest, for the saccadic eye movements using continuum elements to simulate liquified vitreous

Head movements

The point of interest's traction for all models when head movement was applied is shown in Figure 3.41. These models were simulated using the FLUID CAVITY option in ABAQUS to represent the liquified vitreous. Figure 3.41 also indicates eye displacement during the simulation. The eye models exhibited a displacement of 2 mm to the right then stayed still for the rest of the simulation. The traction-time graph shows that the peak traction occurred during the first step between 0 and 50 milliseconds. Tension occurred in all models at exactly the same time, then fell back to zero at the end of the displacement step. The maximum traction for all models was between 23 and 29 Pa. It can also be seen that the traction of the 90%, 87.5% and 85% vitreous increased significantly at the start of the second step, achieving amplitudes of 15, 16, and 14 Pa, respectively. In contrast, the amplitude of the other models increased in the middle of the second step.

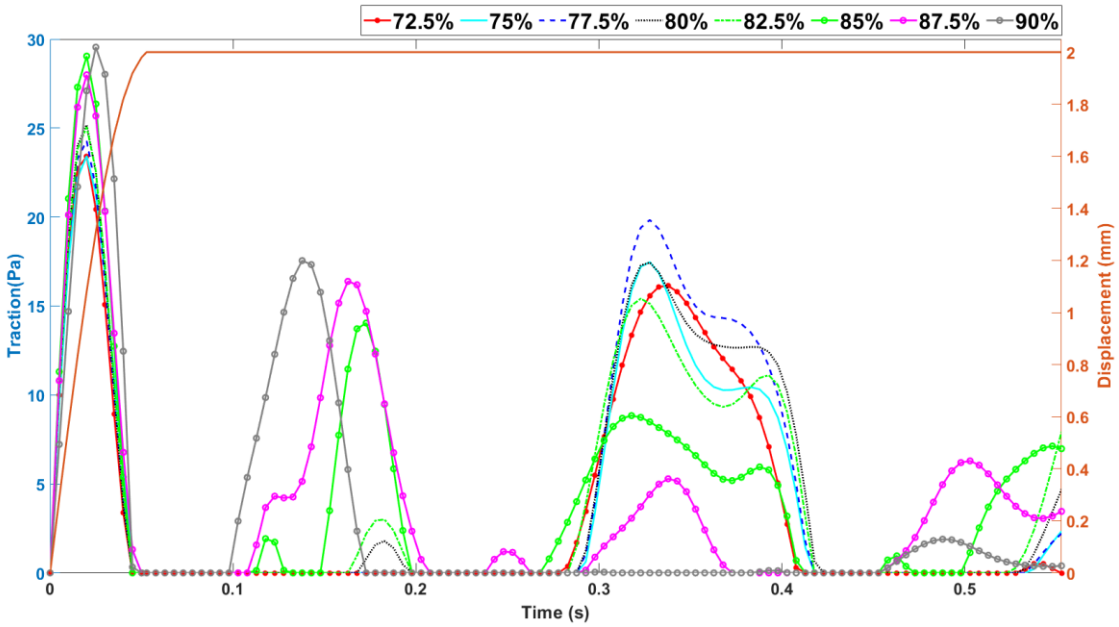

Figure 3.41: Traction on the point of interest over time for head movements, using the fluid cavity to simulate liquified vitreous

Meanwhile, Figure 3.42 shows the PSD of the points of interest for all models. It can be observed that, in the frequency range of 0-15 Hz, the normalised PSD amplitude of the 90% vitreous was the greatest, while the 72.5% and 75% vitreous models did not have a peak amplitude. In the second dominant frequency at 20 Hz, the 72.5%, 75%, 77.5%, 80%, and 82.5% models achieved amplitudes of 0.44, 0.43, 0.61, 0.51, and 0.37 respectively.

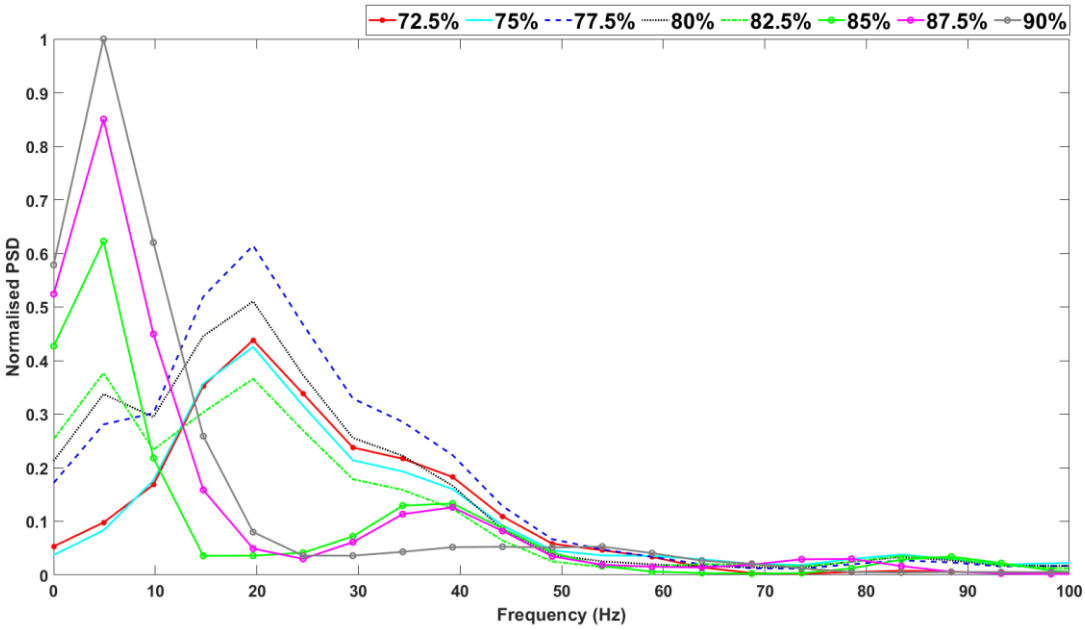

Figure 3.42: Power spectrum diagram at the points of interest for head movements, using the fluid cavity to simulate liquified vitreous

Figure 3.43 shows traction on the points of interest over time for head eye movements when continuum elements are used to simulate the liquified vitreous. Due to element distortion, all models crashed at the beginning of the second step, and only traction during the eye movement in the first step can be observed from the figure below. The traction-time graph shows that peak traction was between 15 and 19 Pa, which is less than the traction achieved by the models simulated using fluid cavity.

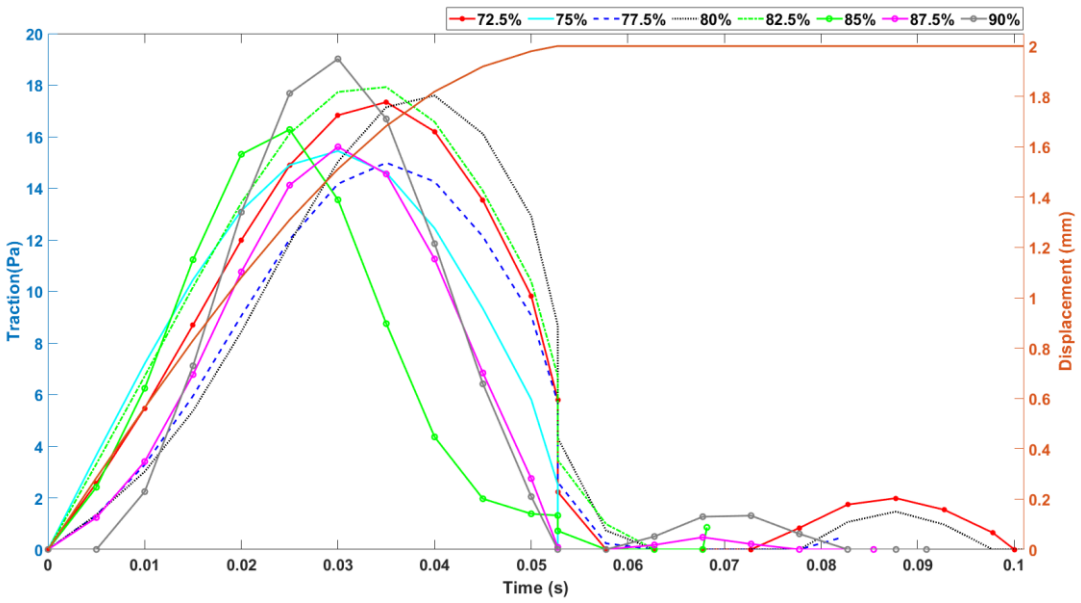

Figure 3.43: Traction on the point of interest over time for head movements, using continuum elements to simulate liquified vitreous

The frequency-domain graph showed that the maximum amplitude occurred in the 82.5% vitreous model, followed by the 75%, 77.5%, and 90% models. The results are only for the first step, as all the models failed to complete due to elements distortion.

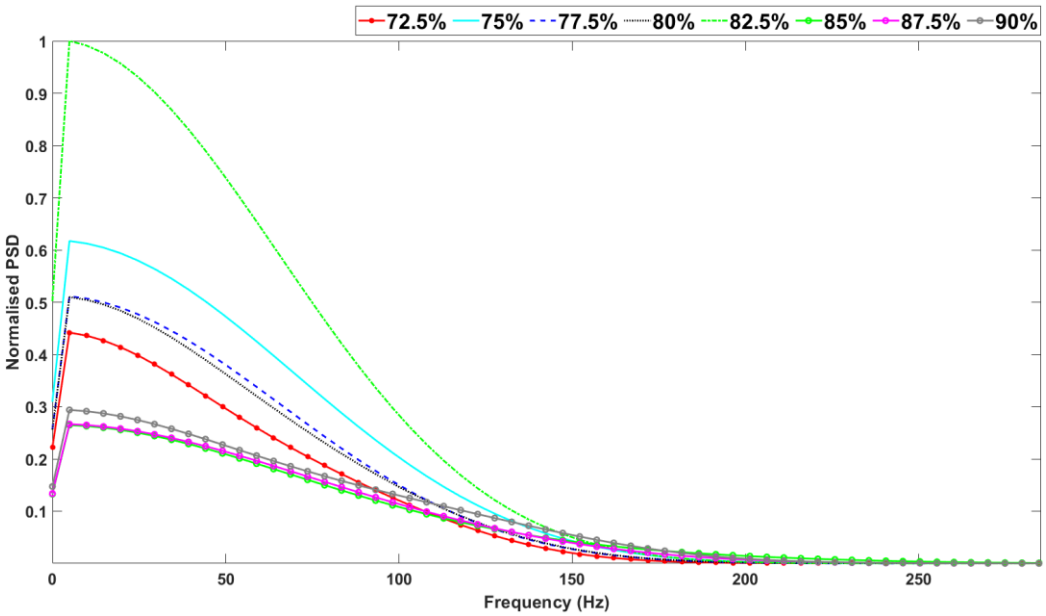

Figure 3.44: Power spectrum diagram at the points of interest for head movements, using continuum elements to simulate liquified vitreous

ii The effect of vitreous detachment size on the retina

This study aimed to investigate the effect of the vitreous size of detachment on the retina. Six models were created, as mentioned in Section 3.3.2, and the traction at a point of interest was measured. The point of interest varied from one model to another and the location of the point was based on the location where the vitreous starts to detach. Two models have their vitreous detachment starts above the equator, one model exactly at the equator (0°), and three models at 5°, 10° and 15° below the equator. The same dynamic load was applied to all the models to investigate the effect of saccades and head movements on the retina.

Saccadic movements

Figure 3.45 shows the traction on the points of interest over time, for the saccades eye movement when the fluid cavity option was used to simulate the liquified vitreous. The graph also shows the eye's rotational displacement over time. The maximum traction for all models lay between 2.5 and 4.7 Pa. The maximum traction for all cases was achieved during the second timepoint when the eye remained still. For instance, when the detachment location was 5° and 10° below the equator, traction peaked between 170 and 300 milliseconds. On the other hand, at 0° and 15° below the equator, peak traction occurred between 300 and 400 milliseconds. There were no signs of tension during the first step; tension started to take place at the start of the second step for all the models.

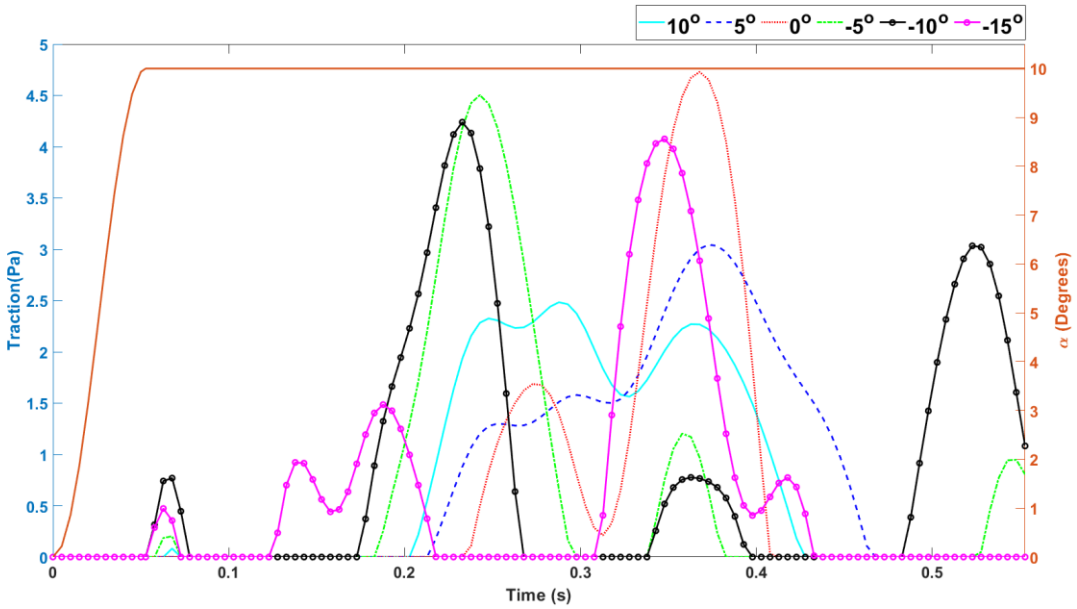

Figure 3.45: Traction on the point of interest over time for saccadic eye movements, using fluid cavity to simulate liquified vitreous

The power density diagram for all the points of interests is shown in Figure 3.46. It can be observed that the dominant frequency for all the cases was 5 Hz. The normalised PSD amplitude of the case was the greatest where the vitreous detachment initiated at 10° above the equator. The amplitudes of the models with vitreous detachment start at 10° and 15° below the equator were the lowest. It can also be observed that, in the frequency range of 20-80 Hz, all cases had another peak amplitude at a different frequency. However, this amplitude was a lot smaller than the one achieved during the first dominant frequency, especially for the models with vitreous detachment start at 10° and 5° above the equator.

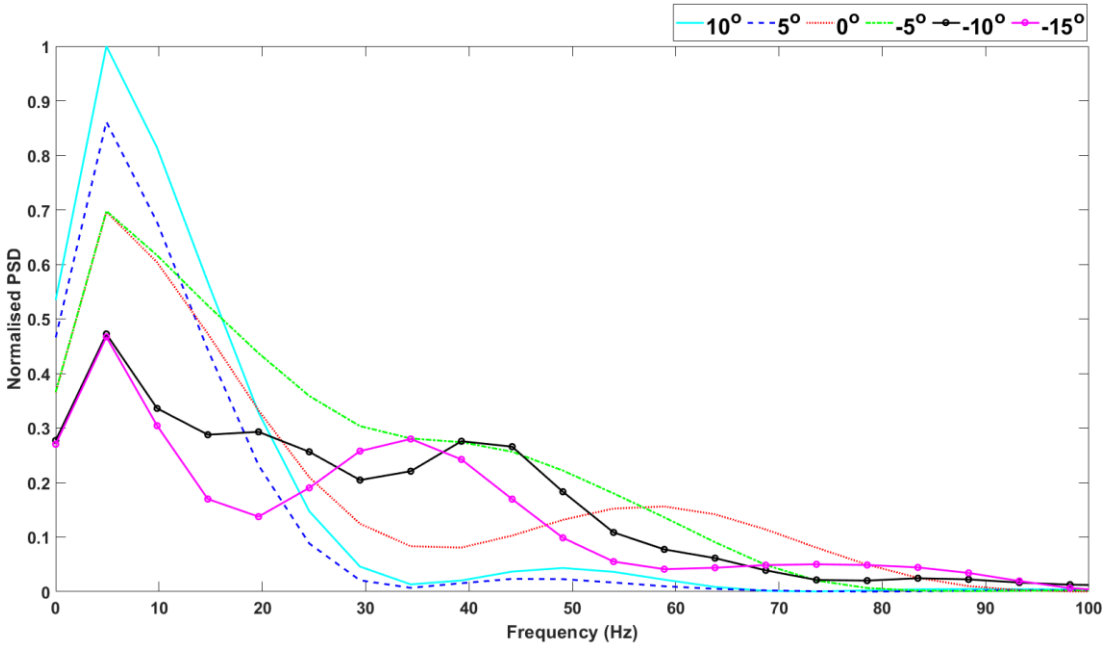

Figure 3.46: Power spectrum diagram at the points of interest for saccadic eye movements, using fluid cavity to simulate liquified vitreous

The point of interest's traction for all models when saccadic movement was applied is shown in Figure 3.47. These models were simulated using continuum elements to represent the liquified vitreous. It is clear that during the first step when the eye rotated clockwise, there was no traction applied on the points of interest for all cases. The maximum traction for all models was between 2.5 and 4.3 Pa. The traction-time graph shows that the peak traction occurred at different periods for all models. It can also be seen that the traction of the models where the vitreous detachment starts at 15°, 10° and 5° below the equator, increased significantly at the start of the second step achieving amplitudes of 2.7, 2.0, and 1.8 Pa, respectively. In contrast, the amplitude of the model with the vitreous detachment starting at the equator began to increase at around the middle of the second step.

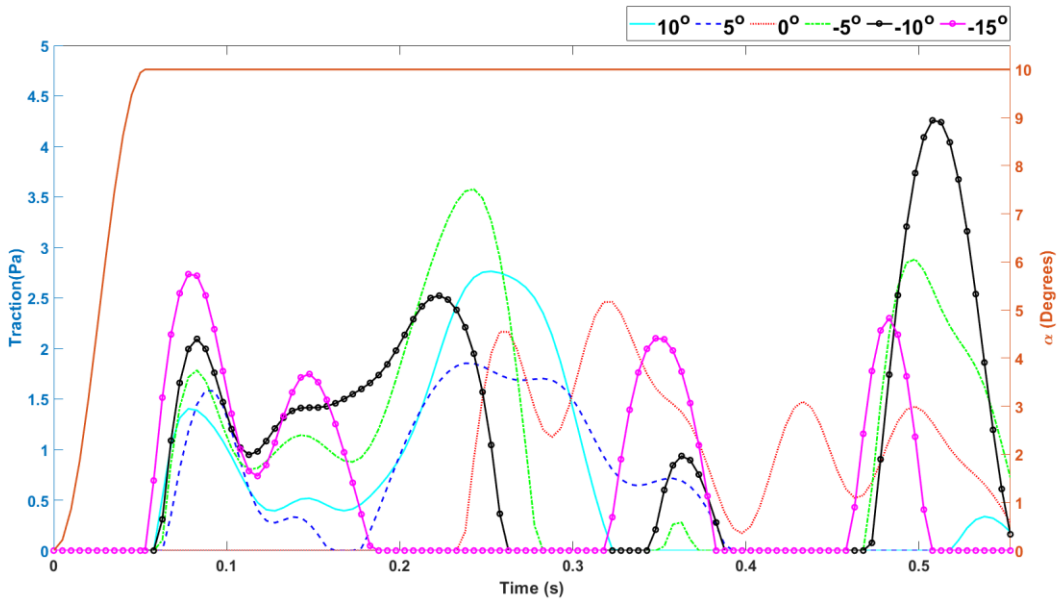

Figure 3.47: Traction on the point of interest over time, for the saccadic eye movements, using continuum elements to simulate liquified vitreous

The power density analysis of the points of interest is shown in Figure 3.48. It can be observed that the dominant frequency is 5 Hz for all the cases of the vitreous detachment. The peak amplitude for all the cases occurred during the first dominant frequency. The maximum PSD was reached by the case where the vitreous detachment starts at 5° below the equator. Then followed by the 10° and 0° above the equator models. Although a clear trend could not be detected from the diagram, all the cases' amplitudes were very close; except for the model with detachment at 15° below the equator.

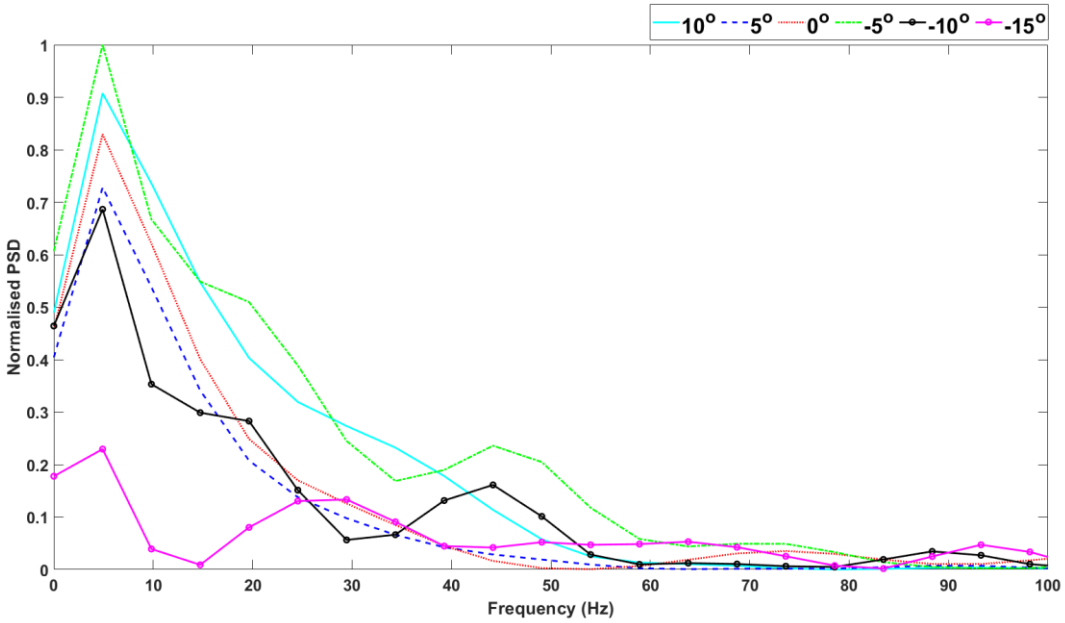

Figure 3.48: Power spectrum diagram at the points of interest for saccadic eye movements, using continuum elements to simulate liquified vitreous

Head movements

Figure 3.49 shows the traction on the points of interest over time, for the head eye movement when the FLUID CAVITY option was used in ABAQUS to simulate the liquified vitreous. The graph also shows the eye's displacement over time (in red). The maximum traction for all models lay between 15 and 39 Pa. The maximum traction for models with detachment below the equator was achieved in the first step during the eye transition; however, the two models with detachment starting above the equator achieved their maximum traction during the second step. For instance, when the detachment location was 5° and 10° above the equator, traction peaked between 160 and 250 milliseconds. On the other hand, for the models below the equator, peak traction occurred between 0 and 80 mm.

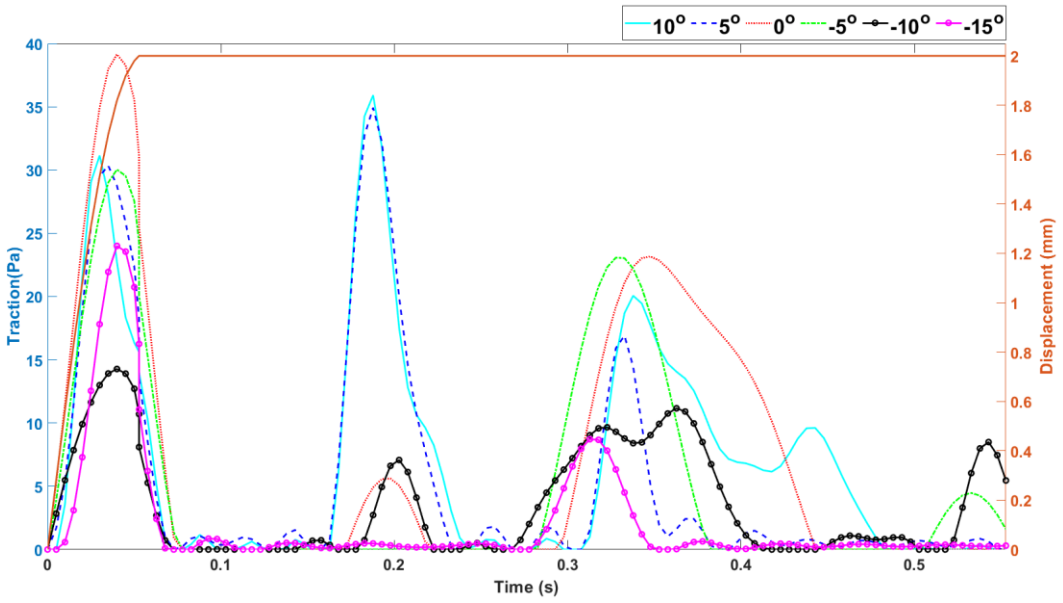

Figure 3.49: Traction on the point of interest over time for head movements, using fluid cavity to simulate liquified vitreous

The power density analysis of the points of interest is shown in Figure 3.50. It can be observed that the dominant frequency is 5 Hz for all the cases of the vitreous detachment. The peak amplitude for all the cases occurred during the first dominant frequency. The maximum PSD was reached by the case where the vitreous detachment starts at 10° above the equator. This was then followed by the 0° and 5° above the equator models. Although a clear trend could not be detected from the diagram, all cases' amplitudes were very close; except for the detachment at 10° and 15° below the equator.

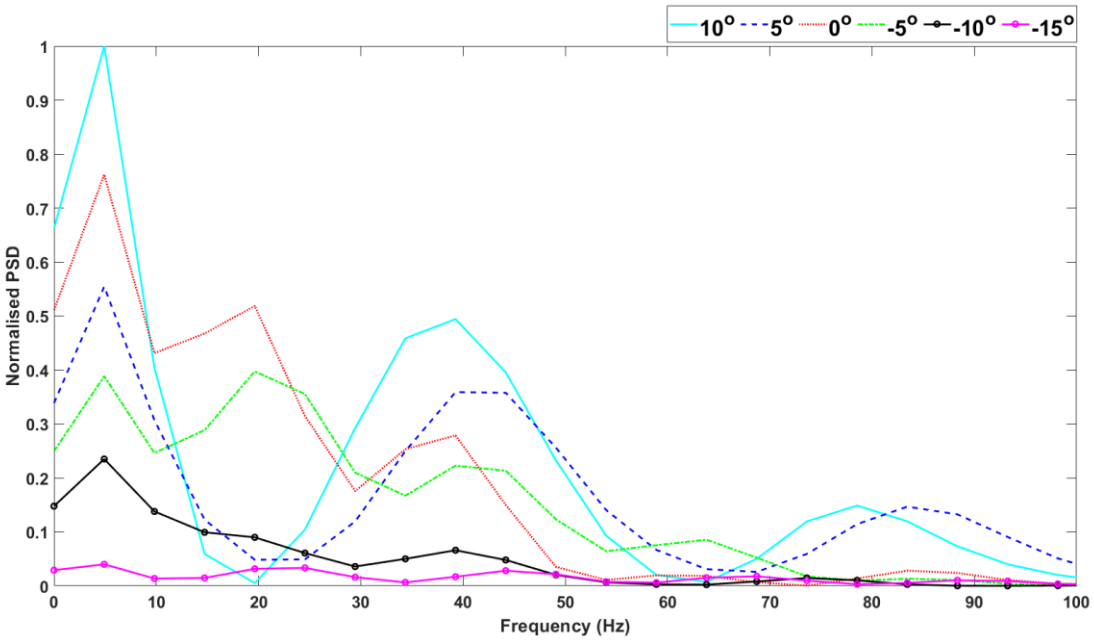

Figure 3.50: Power spectrum diagram at the points of interest for head movements, using fluid cavity to simulate liquified vitreous

Figure 3.51 shows the traction on the points of interest over time, for the head eye movement when the continuum elements were used to simulate the liquified vitreous. Due to elements distortion, all the models crashed at the beginning of the second step. Only the traction during the head movement in the first step can be observed from the figure below. The traction-time graph shows that the peak traction was between 7 and 38 Pa, almost the same as the traction achieved by the models simulated using fluid cavity.

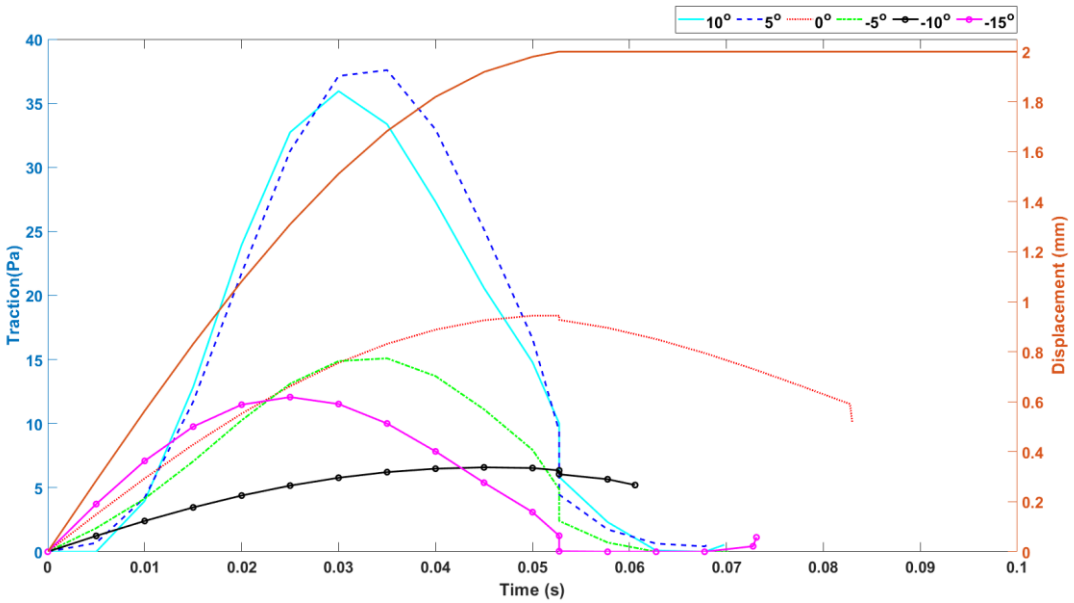

Figure 3.51: Traction at the point of interest over time for head movements, using continuum elements to simulate liquified vitreous

The frequency-domain graph (see Figure 3.52) showed that the maximum amplitude occurred in models with vitreous detachment initiating at 5° and 10° above the equator, followed by the 0° model. The models with detachment starting below the equator achieved very low amplitude. The results are only for the first step, as all the models failed to complete due to elements distortion.

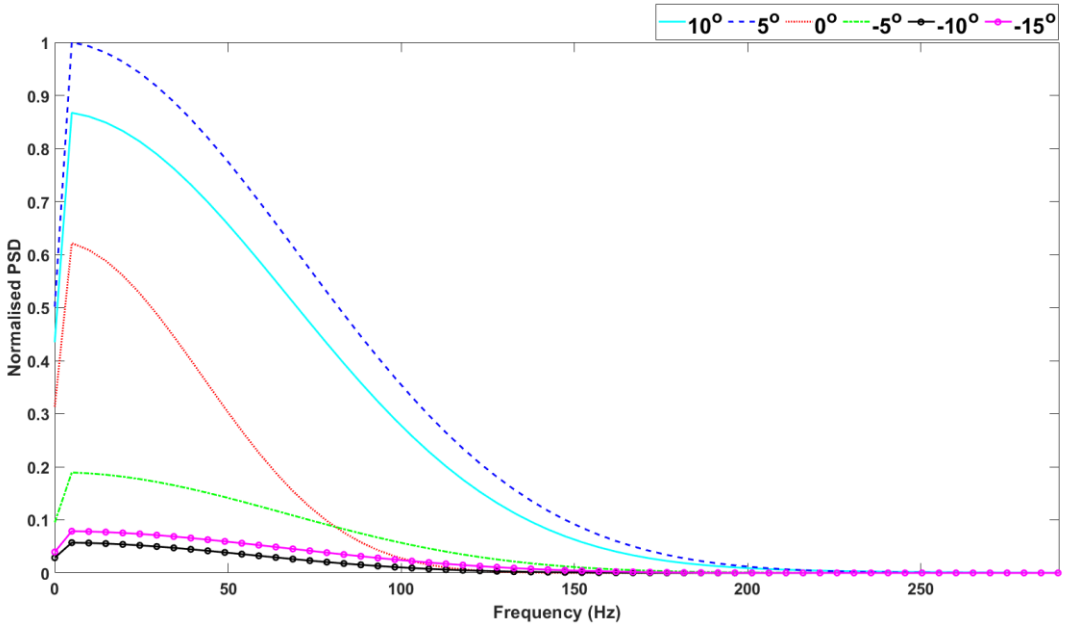

Figure 3.52: Power spectrum diagram at the points of interest for head movements, using continuum elements to simulate liquified vitreous

iii The effect of vitreous volume on the progression of retinal detachment

Saccades movements

Figure 3.53 shows the percentage of retinal detachment during the saccadic eye movements. The bar charts show the three angular rotations' results for the models simulated using fluid cavity and continuum elements to represent liquified vitreous. Figure 3.53a shows the percentage of elements removed during the 5^{o} rotation when the FLUID CAVITY option was used. The range of detachment for all the models is between 2-4%. The model with 72.5% vitreous achieved the least detachment, while the 80% vitreous model achieved the most/largest detachment. When continuum elements were used, the percentage of the retinal elements detached was between 2.8-4.2% (see Figure 3.53d).

In addition, during the 10^{o} rotation, the percentage of elements removed was similar for all models, ranging from 6.2% to 6.4% with no significant difference between models (see Figure 3.53b). The models with continuum elements to represent liquified vitreous can be seen in Figure 3.53e. Likewise, no significant difference between the eight models. They all range between 8% and 7%.

For the 15^{o} saccades, the percentage of elements removed increased gradually from 8% for the 72.5% vitreous model to 12% for the 90% vitreous, when the FLUID CAVITY option was used to simulate the liquified vitreous (see Figure 3.53c). Figure 3.53f shows the percentage of the elements removed when continuum elements were used to represent liquified vitreous. It can be observed that the minimum detachment occurred in the model with 72.5% vitreous, while maximum detachment occurred in the model with 90% vitreous. The rest of the models achieved very similar detachment, ranging between 13% and 15.7%.

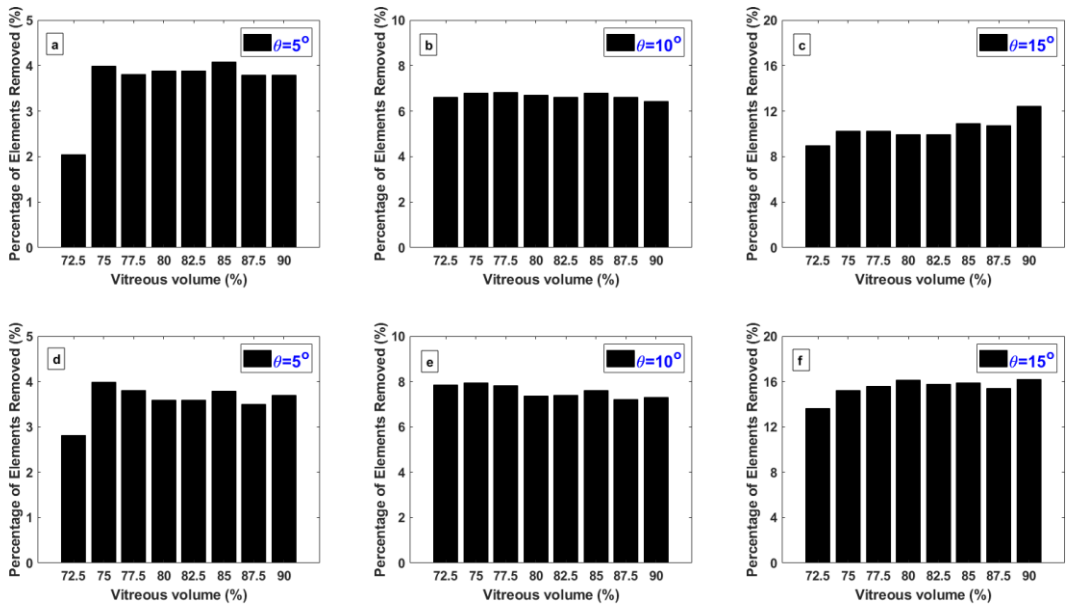

Figure 3.53: Percentage of detached retina during saccadic movement in tests involving (a,d) 5° rotation, (b,e) 10° rotation, and (c,f) 15° rotation when (a-c) FLUID CAVITY and (d-f) continuum elements were used to model liquified vitreous

Figure 3.54 shows the retinal detachment locations for the eight models with different vitreous volume when a 10° rotation was applied. Three different colours were used to indicate the timepoint at which the detachment occurred. The pink colour shows the elements detached during the first rotation (clockwise); the blue and green show the elements separated during the second and the third rotations, respectively. It is clear that the detachment initiated in the same location for all models and then started to propagate around the same axis. It can also be observed that the first rotation has the greatest detachment size in all models compared to the other two cycles.

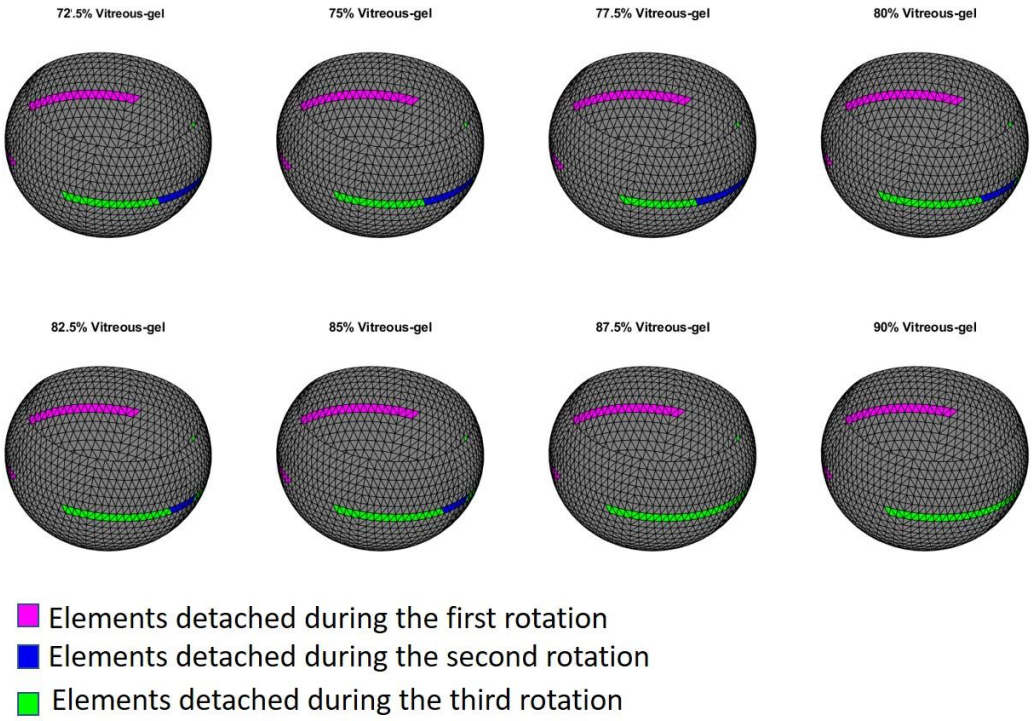

Figure 3.54: 3D rendering of the retina showing location of retinal detachment at each rotation

Head movements

Figure 3.55 shows the percentage of retinal elements detached during head movement when the eye model transitioned 2 millimetres along the positive x-axis, then back to the initial position and another 2 millimetres along the negative x-axis. Figure 3.55a shows the detachment when the FLUID CAVITY option simulates the liquified vitreous, while Figure 3.55b shows the same when continuum elements were used to model the liquified vitreous.

The range of detachment for all the models is between 43 and 49%. The models with 72.5% and 75% vitreous achieved the least detachment; the 85% vitreous model achieved the biggest detachment. However, no great differences between all models. On the other hand, when continuum elements were used, the range of the retinal elements detached was between 28-30%, with no significant difference between the eight models. It is important to note that due to elements distortion, these models crashed in the second cycle.

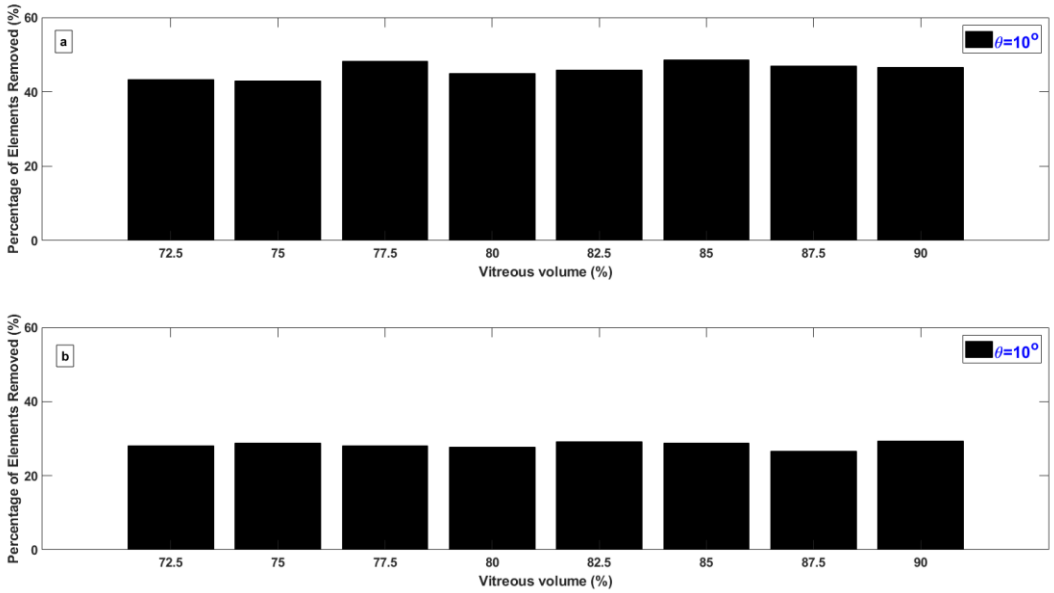

Figure 3.55: Percentage of detached retina during head movement for models with vitreous volume ranges between 72.5%-90% incorporating FLUID CAVITY option in ABAQUS (a) and continuum elements (b) to model liquified vitreous

Figure 3.56 shows the retinal detachment locations for the eight models with different vitreous volume when a 2 millimetres transition was applied. Three different colours were used to show the transition at which the detachment occurred. It is clear that for all the models, the detachment initiated in the same location on the positive x-axis. Then, when the eye moved back to its initial position, the detachment propagated along the axis. Meanwhile, when the eye model moved towards the negative x-axis, the detachment occurred in the eye's negative x-axis.

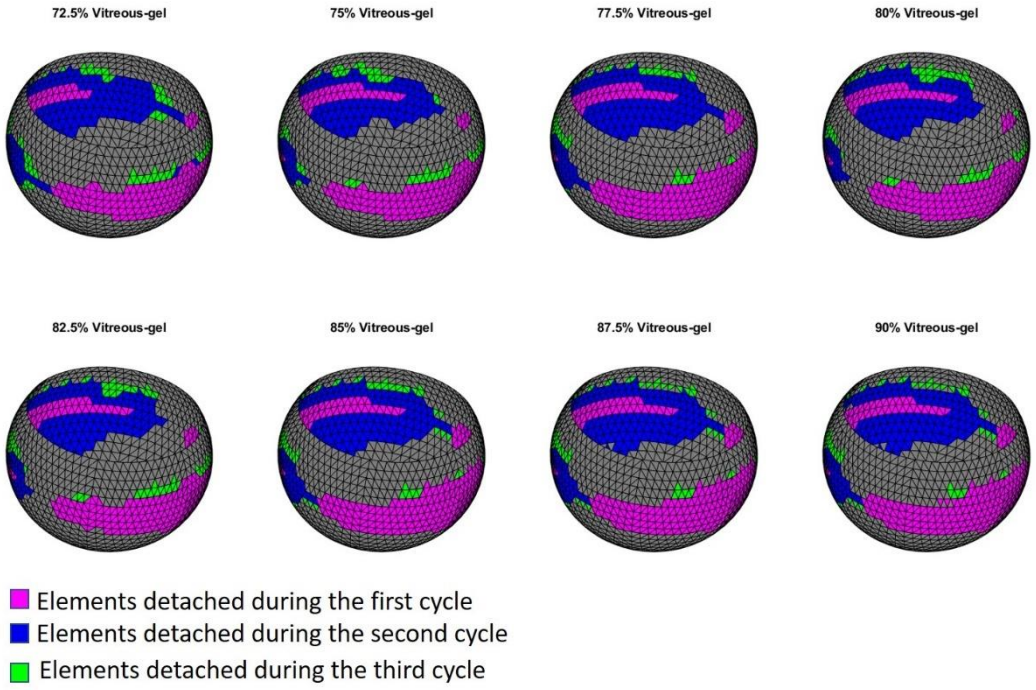

Figure 3.56: 3D rendering of the retina showing the location of retinal detachment at each step

iv Effect of vitreous attachment point on progression of retinal detachment

Saccades movements

Figure 3.57 shows the percentage of the elements detached during the saccadic eye movements for the three angular rotations for the models simulated using fluid cavity and continuum elements to represent liquified vitreous. Figure 3.57a shows the percentage of elements removed during the 5^{o} rotation when the FLUID CAVITY option was used. It is clear that during the 5^{o} rotation, the detachment only occurred in the model where the vitreous detachment starts at 10^{o} above the equator. When continuum elements were used, the model where the vitreous detachment starts at 10^{o} above the equator had the most detachment. The detachment then decreased gradually in the other models until it reached 0% in the model with vitreous detachment at 15^{o} below the equator.

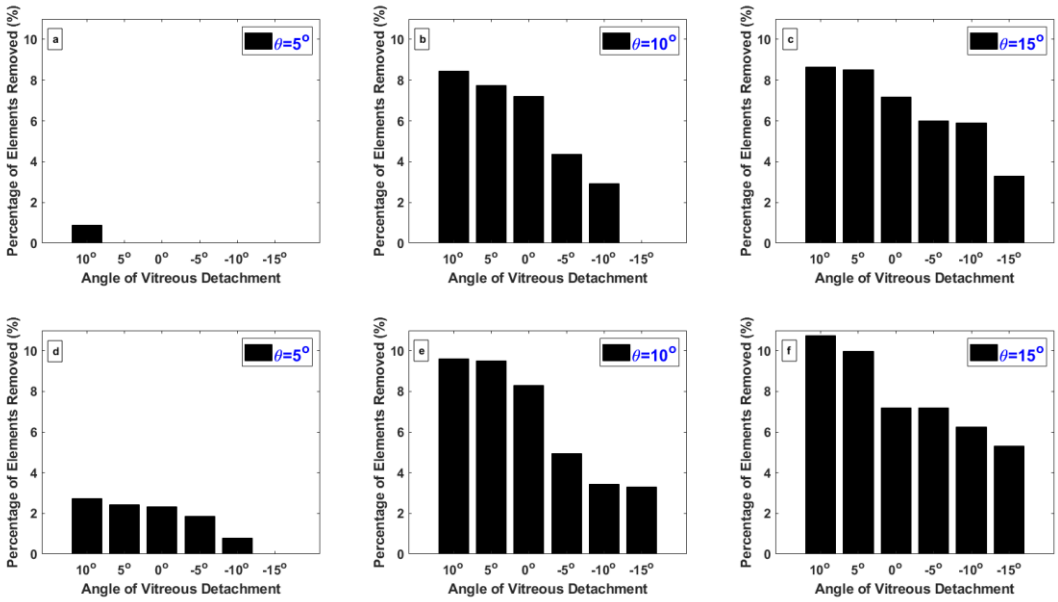

Figure 3.57: The percentage of the detached retina during saccades eye movement in tests involving (a,d) 5° rotation, (b,e) 10° rotation, and (c,f) 15° rotation

Meanwhile, during the 10° rotation, the highest detachment occurred in model with vitreous detachment starts at 10° above the equator, then decreased gradually until it reached zero in model with the last vitreous detachment. Models with detachment starts at 5° above the equator and at the equator had a very similar percentage of elements removed. Likewise, when continuum elements were used, the maximum detachment occurred in the model with biggest vitreous detachment; and the minimum was in model with the smallest detachment.

When the FLUID CAVITY option was used for the 15° saccades, the percentage of the elements detached was the highest compared to the other rotational angles. The same trend was achieved; the rate decreased gradually from 8.5% to 3.5%. Models with detachment 5° and 10° below the equator achieved almost the same percentage of elements removed. Figure 3.57f shows the percentage of the elements detached when continuum elements were used to simulate the liquified vitreous. There is a gradual decrease in the elements detached. The percentage of retinal detachment ranges from 10.5% to 5.5%.

Figure 3.58 shows the retinal detachment locations when the FLUID CAVITY option was used to model the liquified vitreous when the 10^{o} rotation was applied. Three different colours are used to show the rotations at which the detachment occurred. It is clear that, for all models, the detachment initiated in the same location on the positive x-axis. Then, when the eye moved back to its initial position, the detachment propagated along the x-axis. It can also be observed that the size of the retinal detachment decreased gradually with the decrease in the vitreous detachment. Model with the least vitreous detachment did not exhibit any retinal detachment during the three rotations.

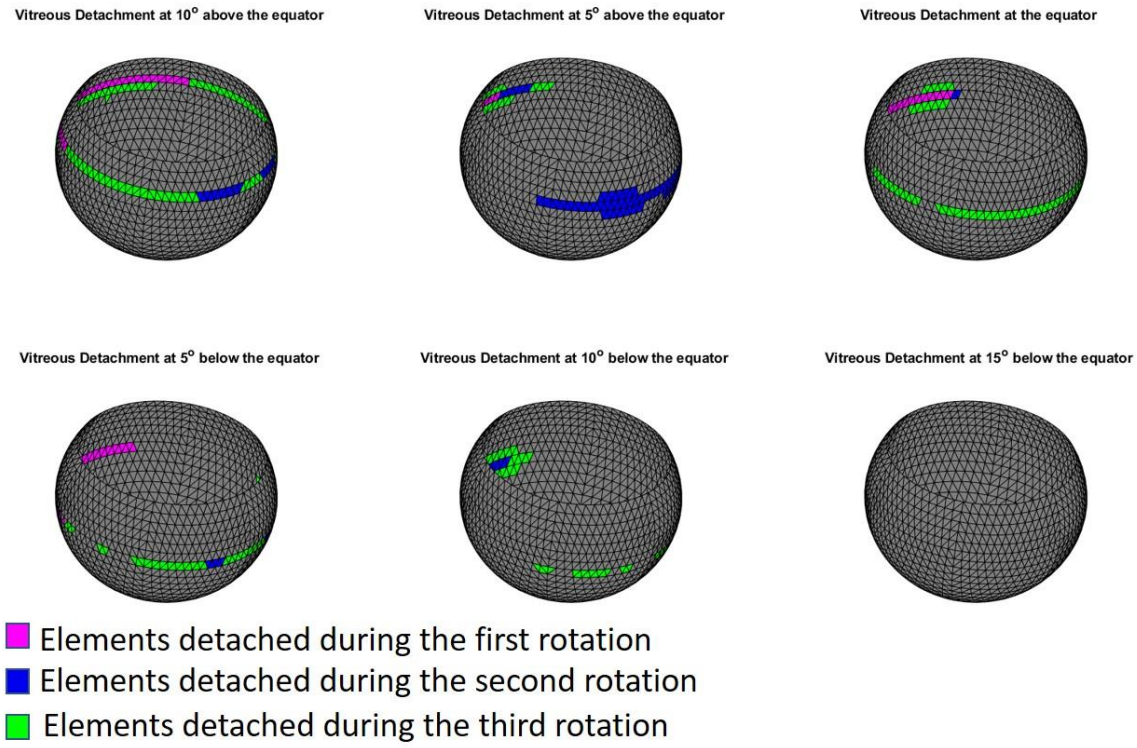

Figure 3.58: 3D rendering of the retina showing the location of retinal detachment at each rotation

Head movements

Figure 3.59 shows the percentage of retinal detachment when the vitreous attachment point was changed. It is clear that the number of detached elements was very close. The eye model with a vitreous detachment at the equator achieved the highest detachment, and the model with a vitreous detachment starting at 15° below the equator achieved the lowest.

On the other hand, for the models using continuum elements to represent the liquified vitreous, a clear trend can be seen. The number of elements removed increased with the decrease of vitreous detachment angle. However, it is essential to note that the models with continuum elements crashed before the third rotation due to elements distortion.

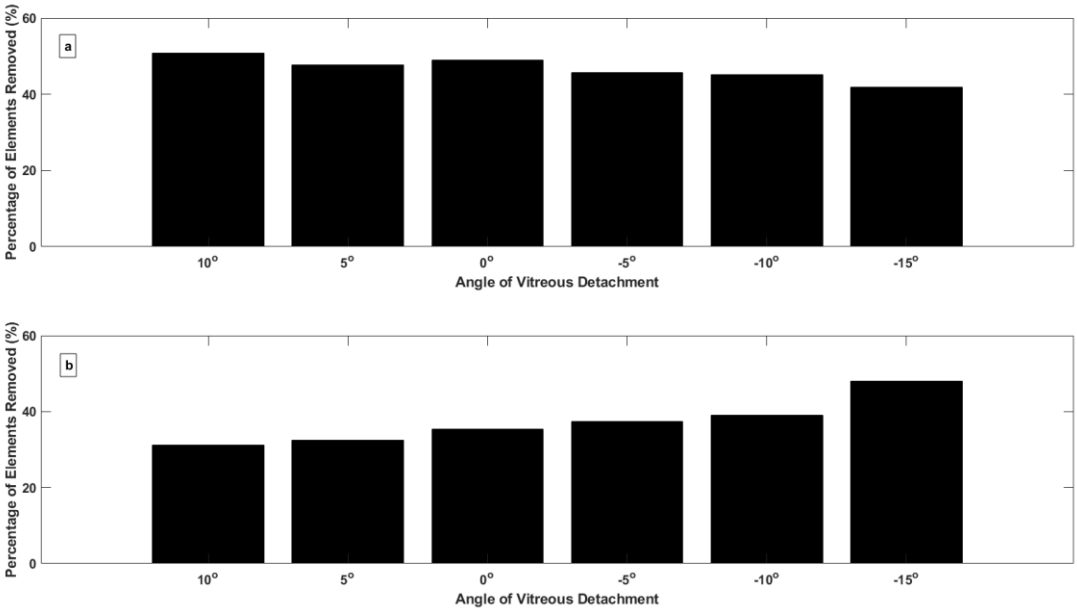

Figure 3.59: The detached retina percentage during the head movement for models with vitreous volume detachment ranges from 10° above the equator to 15° below the equator simulated using FLUID CAVITY (a) and continuum elements (b) to model liquified vitreous

Figure 3.60 shows the locations where the detachment initiated in the retina during the 2 mm transition when the FLUID CAVITY option simulates the liquified vitreous. It is clear that the detachment started on the right side of the retina, in the same direction of motion. Then, it propagated achieving the highest detachment during the second step (blue). As most of the retinal elements detached in the first and second step, only a few elements detached during the final transition.

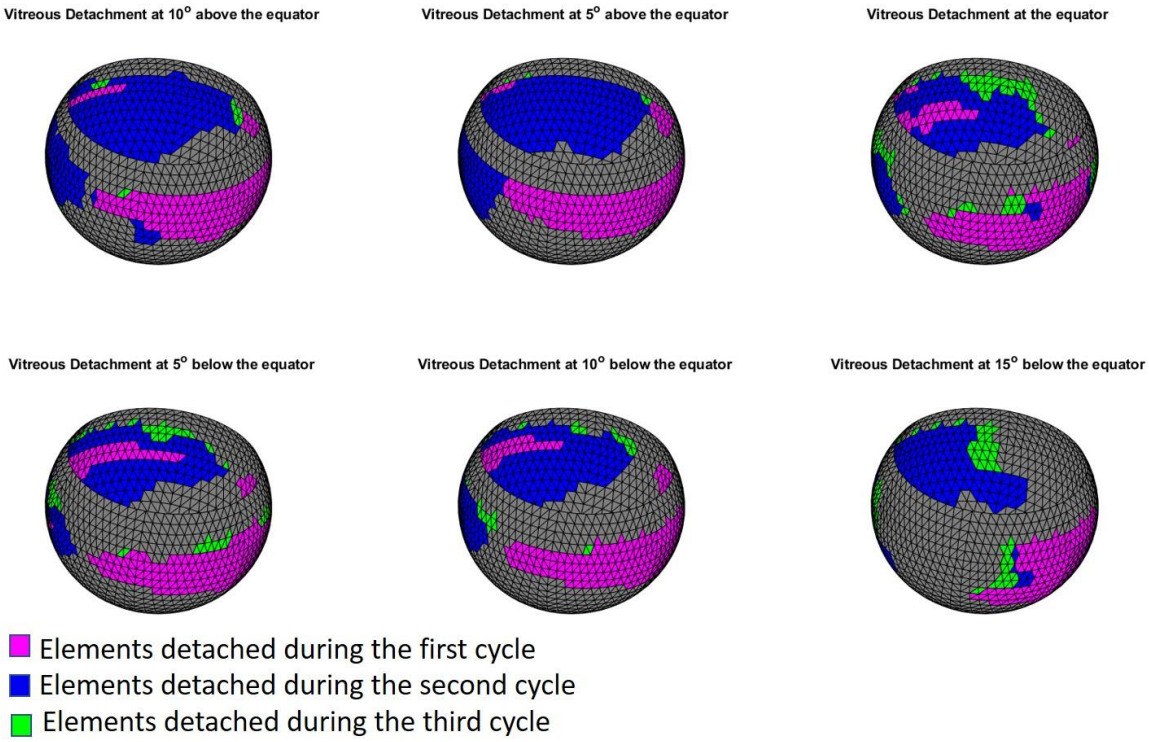

Figure 3.60: 3D rendering of the retina showing the location of retinal detachment at each step

3.5.5 Ultrasound scans

The eye model used in the present study was visually compared to ultrasound scans of human eyes. A numerical model was created to look as close as possible to the ultrasound scans. The boundary conditions applied on the eye model were chosen based on the ultrasound scans provided. The eye rotated clockwise twice before resting for a short period. Then the eye rotated anti-clockwise twice and rested again for a short time. The ultrasound images were obtained from the study by Vroon et al. [153] (Accutome B-scan Plus, Malvern, USA, and Quantel Medical cinescan B-scan, Cournon d'Auvergne, France).

Table 3-3 shows the ultrasound imaging of a patient with vitreous detachment. In addition, it shows the numerical model in similar states as the ultrasound images. A shows the start of eye rotation; B to E show the situation after each rotation. Finally, F shows the final state of the eye.

The main difference observed when comparing the numerical model to the images is during the initial state; the effect of the gravity on the ultrasound images led to different shape of the vitreous. However, starting from the second rotation, the model slowly achieved very similar behaviour.

Table 3-3: Comparison between ultrasound images and the numerical model

	Ultrasound	Model
(A) Initial State	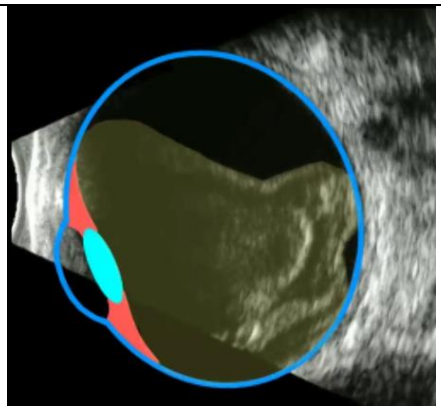	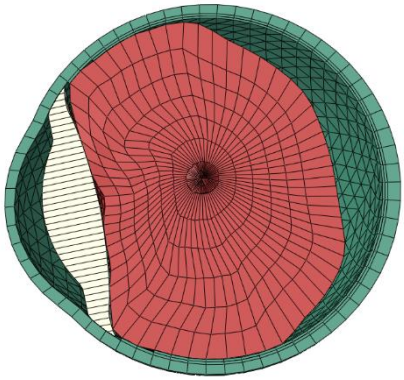
(B) After first rotation (clockwise)	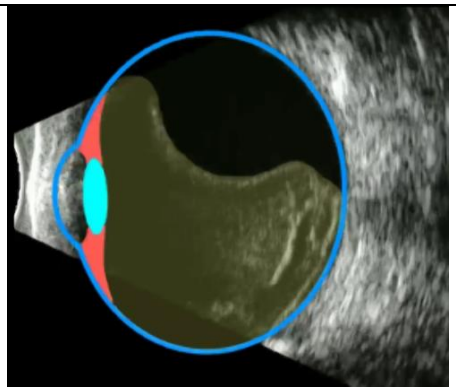	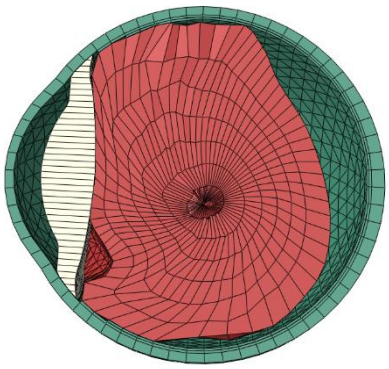

(C) After third rotation (clockwise)	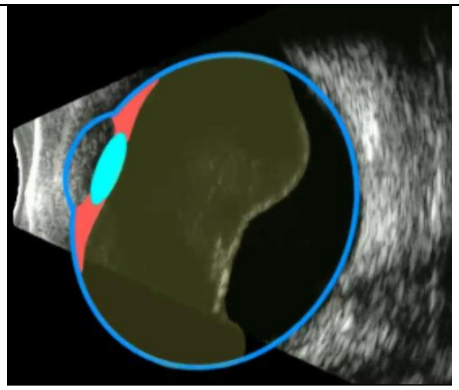	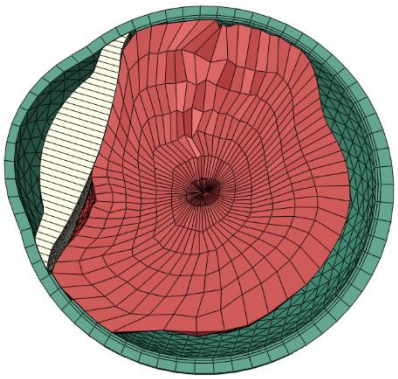
(D) After fourth rotation (anti-clockwise)	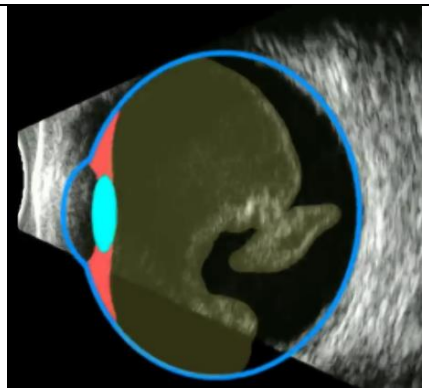	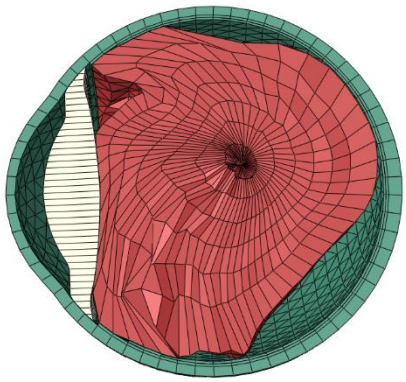
(E) After fifth rotation (anti-clockwise)	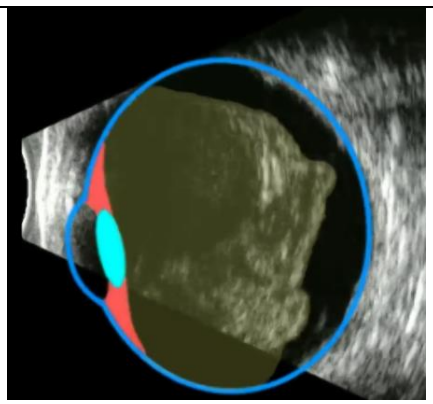	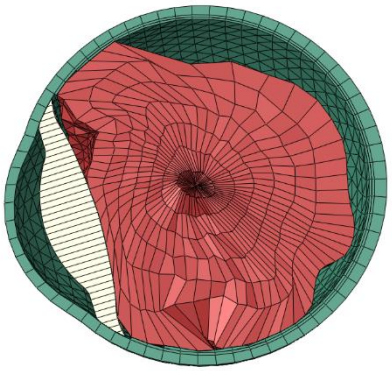

(F) Final state after resting	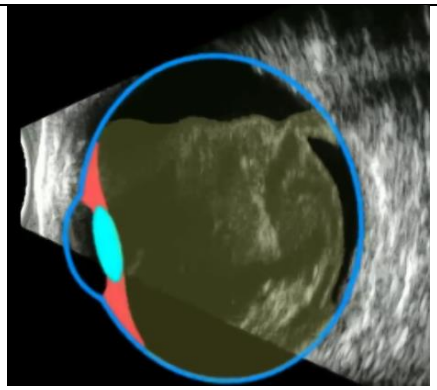	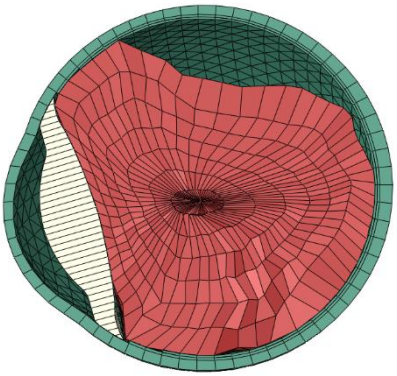

Figure 3.61: Comparison between ultrasound images and the numerical model

3.6 Discussion

The rheology and structure of the vitreous change as a result of ageing, including condensation and shortening of the collagen fibres. This process leads to shrinkage of the vitreous body [4]. The separation of the vitreous usually starts from the posterior pole and advances towards the periphery, which can result in PVD, in which the vitreous body becomes divided into two sections: the vitreous gel and the liquified vitreous [40]. Once the detachment has developed, eye rotations or head movements create traction forces on the retina, which can cause a retinal break or tear [5]. The present study aimed to further understand the effect of saccadic and head eye movements on retinal detachment progression. The study relied on idealised numerical 3D models of the ocular globe comprising components such as the aqueous, lens, choroid, retina and vitreous (gel and liquid), and simulating the conditions leading to retinal detachment. Researchers have investigated the human eye over the last decades using finite element modelling (FEM). The majority of these researches used finite element methods to study the damage caused in the eye due to impacts [2, 5, 32, 57]. A gap remains in our understanding of the interaction between the liquid and gel phases of the vitreous and its effect on the retinal detachment process. The finite element model presented in this study is the first 3D model that includes the interaction between the liquid and gel phases of the vitreous.

Results provide a feasible idea of the vitreous dynamics. Vitreous oscillations are observed to take place at least one time after saccadic and head movements. This agrees with the in vivo observations of Walton et al. [240] who reported the existence of at least one vitreous oscillation after saccades, before the eye comes to rest. Also, Repetto et al. [1] confirms that using a 2D model of the ocular globe to study the traction exerted by the detached vitreous on the retina.

The peak traction stress on the retina caused by the saccadic eye movement range from 4 to 7 Pa. This is two order of magnitude lower than the retina's adhesion force estimated experimentally by Liu et al. [2], which was 340 Pa. In addition, the peak traction is also seven times lower than the values achieved numerically by Vroon et al. [153]. This could be due to the vitreous material properties adopted Vroon's study being simplified and assumed to be elastic. The other reason that might have led to the difference in results between the current model and the model produced by Vroon is that Vroon et al. assumed the retina and the choroid as one component. Thus, when modelling retinal detachment, both retina and choroid were separated from the sclera, rather than from the choroid. Since the defined saccadic eye movement used in the current model (10^{o}) was greater than 95% of all saccades [196], it is doubtful that the traction caused by the most saccades will be significant enough to exceed the retinal adhesion.

In all the numerical simulations for both head and saccadic movements, it was observed that the traction stress is concentrated close to the vitreous attachment point. This agrees with the observations of Repetto et al. [1], who reported for their 2D model that the concentration of the maximum traction on the retina varies with the vitreous attachment point. This also agrees with Bayat et al. [199], who reported that the maximum stress produced was located on the equatorial plane at the cavity wall near the interface layer. Bayat et al. developed a 3D spherical model of only the vitreous to investigate how the oscillatory motions influence flow dynamics of partial vitreous liquefaction.

The peak traction on the retina caused by the head movement is within the range of 15 to 39 Pa. These values are ten times less than the retinal adhesion force achieved by Liu et al. [2], while the traction is very close to the value achieved by Vroon et al. Meanwhile, the head movement defined is small compared to those created by other everyday activities, only head movements can likely generate traction stress in equal magnitude to the adhesion of the retina. These preliminary results suggest that head movements are the primary factor in the progression of retinal detachment. This is in agreement with the observations of Angunawela et al. [197] who used a spherical model of the vitreous to evaluate the shear stress on the retina due to sudden eye movements and reported that sudden head movements could cause traction up to 16 Pa.

Three different eye rotations (5^o, 10^o, 15^o) were applied to study the dependence of the maximum traction on the amplitude of the saccadic rotation. It was observed that the retinal traction depends on the amplitude of the saccadic and head rotation. It appears that the traction increases with the amplitude of the rotation. This is in agreement with the observations of Repetto et al. [1].

The effect of changing the vitreous volume on the progression of retinal detachment showed that during saccadic eye movement caused by the eye rotation, the percentage of the retinal elements detached was very small and it did not vary a lot between models. This is because of the low traction achieved during saccades as it didn't exceed the value set to break the contact between the retina and the choroid. This also proves that the vitreous volume doesn't have a massive effect on the retinal traction as long as the vitreous detachment size is the same. This is in agreement with the observations of Repetto et al. [1], who reported that the maximum traction on the retina remained almost unchanged for all volumes of the vitreous.

Meanwhile, when the vitreous volume remained constant, and only the vitreous detachment size changed, an inverse relation was observed. Big vitreous detachment size led to higher traction, thus more significant retinal detachment. Models with small vitreous detachment size, such as 15^o below the equator, achieved almost no

separation in the retina for all the defined saccadic eye movements. These preliminary results suggest that the vitreous detachment size vehemently affects the progression of retinal detachment. These results agree with the results achieved by Repetto et al. [1], who suggest that the maximum traction experiences a slight increase at the vitreous attachment point when the size of the detachment increases. Moreover, these results agree with the findings of Di Michele et al. [198] who developed a spherical model of only the vitreous to study the retinal tractions during PVD. Di Michele et al. suggest that different shapes of PVD can be qualitatively associated with the intensity of the vitreoretinal tractions.

On the other hand, during head movement, the effect of changing the vitreous volume on the progression of the retinal detachment showed a slight increase in retinal detachment for most of the models. Even with high traction achieved due to the head movement, the difference between the eight models was not great. On the other hand, when the volume remained the same and the vitreous detachment changed, greater detachment occurred compared to changing the vitreous volume; however, the difference between all models was not significant.

Modelling the liquified vitreous using two methods, FLUID CAVITY and continuum elements, provided a preliminary investigation of the fluid-structure interaction between the vitreous and liquified vitreous. It was clear that, at low speed, the range of traction forces for the head and saccades movements was very close when the two methods were used. However, for larger rates, the FLUID CAVITY liquified vitreous showed more stability in the results. In contrast, many of the continuum elements liquified vitreous crashed due to elements distortion.

The ultrasound images provided a rough comparison with the numerical model, even though they displayed a simplified 2D representation of the vitreous detachment. The behaviour of the vitreous in the numerical model was very similar to the ultrasound scans. The vitreous in the model oscillated for almost the same time as the real vitreous. Comparing the ocular globe FE model to ultrasound scans has been conducted before by Vroon et al. [153]. However, in Vroon's model, the vitreous

model oscillates for an extended period, while the real vitreous does not. Vroon et al. suggested that the lack of damping in their model is due to the material properties' simplifications, especially for the vitreous.

This study aimed to focus on the tractional load caused by head and saccadic eye movements. Thus, gravity was not considered in the analysis. This was done to evaluate the tractions generated by eye movements purely. Future work should intend to consider the gravitational load to improve the simulation. The comparison between the ultrasound scans and the finite element model was beneficial; however, it would have been better for the comparison to be quantitative.

A novel meshing algorithm was developed especially for this study to allow an easy way to control the mesh density of all eye components and mesh any complicated geometry to simulate retinal detachment. This algorithm could mesh any spherical components of the human eye; future work will be needed to extend the algorithm to be able to mesh non-spherical components of the eye such as the fatty tissues and the orbit.

In conclusion, the study produces beneficial results on the role of eye movements in the initiation and progression of retinal detachment. The most recent and accurate material parameters have been utilised in these simulations. The preliminary results show that head movements are the main reason in the development of retinal detachment. This outcome could clarify the outcomes of an earlier study on the posturing advice's effectiveness [241]. This suggests that this modelling technique is beneficial in understanding the progression retinal detachment.

4. Experimental Evaluation of Viscoelasticity of Porcine Vitreous

4.1 Introduction

The eye's vitreous humour is a gel-like substance that fills the cavity behind the lens, it constitutes 80% of the eye's volume [242]. The vitreous consists of three parts; the vitreous base, the vitreous core and the peripheral part. All three parts share the same composition with 99% water, 0.9% salts, and 0.1% collagen fibrils [85, 89]. By the time the eye reaches its adult size, approximately 20% of the total vitreous volume would have turned into liquified vitreous [81]. Due to ageing, the vitreous has been reported to experience shrinking and liquefaction [125, 243], the cause of which is still not fully understood [112].

The vitreous has several functions, including mediating the growth of the eye [81], supporting ocular tissues [82, 83], and maintaining a clear path of light rays to the retina [81]. Deficiencies in the vitreous molecular structure and viscoelastic properties have been reported to increase the risk of developing glaucoma, RRD, retinal tear, retinal oedema, vitreous haemorrhage, and choroidal detachment [81, 112, 113]. Moreover, adhesion of the vitreous to the surrounding ocular structures may make the removal of the vitreous challenging during vitrectomy where the vitreous is to be replaced with silicone oil [89, 114].

There have been several attempts to describe the composition, structural and material properties of the vitreous. Studies investigated the vitreous shear relaxation modulus to estimate its viscoelastic behaviour. The studies used techniques that involved subjecting the vitreous to compression [92], explored relaxation of the scattering pattern [93], and used nuclear magnetic resonance [244], cavitation rheology [4] and cleated tools [115] to monitor behaviour. Using FEM to determine the material parameters has already been successfully applied, in various forms, to

ocular tests [60, 200, 202, 203]. For instance, Rossi et al. [5, 57] performed inverse analysis on experimental data obtained from test data of eye impact experiments carried out by Delori et al. [118]. While these efforts shed much light on the vitreous behaviour, the fact that some methods subjected the tissue to non-physiologic conditions led to a wide variation in the shear relaxation modulus reported in the literature. Saccadic eye movement has been modelled in several studies [153, 245, 246]; David et al. [46] investigated the vitreous behaviour due to eye movement by only comparing between a numerical and analytical model of the vitreous. However, no parameters were determined.

This study aims to measure the vitreous properties while maintaining and testing the tissue and testing in close to natural physiologic conditions. Vitreous specimens were tested while remaining in the posterior chamber and subjected to the dynamic conditions experienced in saccadic eye movements. Numerical inverse analysis based on the nonlinear FEM was then used to estimate the vitreous viscoelastic material properties based on its experimental behaviour.

Due to the scarcity of human tissues, the experiments were conducted using porcine eye. However, earlier studies have shown that porcine vitreous had similar behaviour to that of human tissue [177, 247]. This experimental set-up was designed and planned in collaboration with the Ocular Biomechanics Laboratory of Beihang University. The experiments took place in the Ocular Biomechanics Laboratory of Beihang and all the results analysis was carried out at university of Liverpool.

4.2 Methodology

4.2.1 Specimen preparation

Eighteen fresh porcine eyes were obtained from a local abattoir and used within 48h post-mortem. The eyes were obtained directly after the animals were slaughtered and washed, and all excess connective tissue was removed to ensure freshness. The

eyes were then transported to the Ocular Biomechanics Laboratory of Beihang University and tested on arrival.

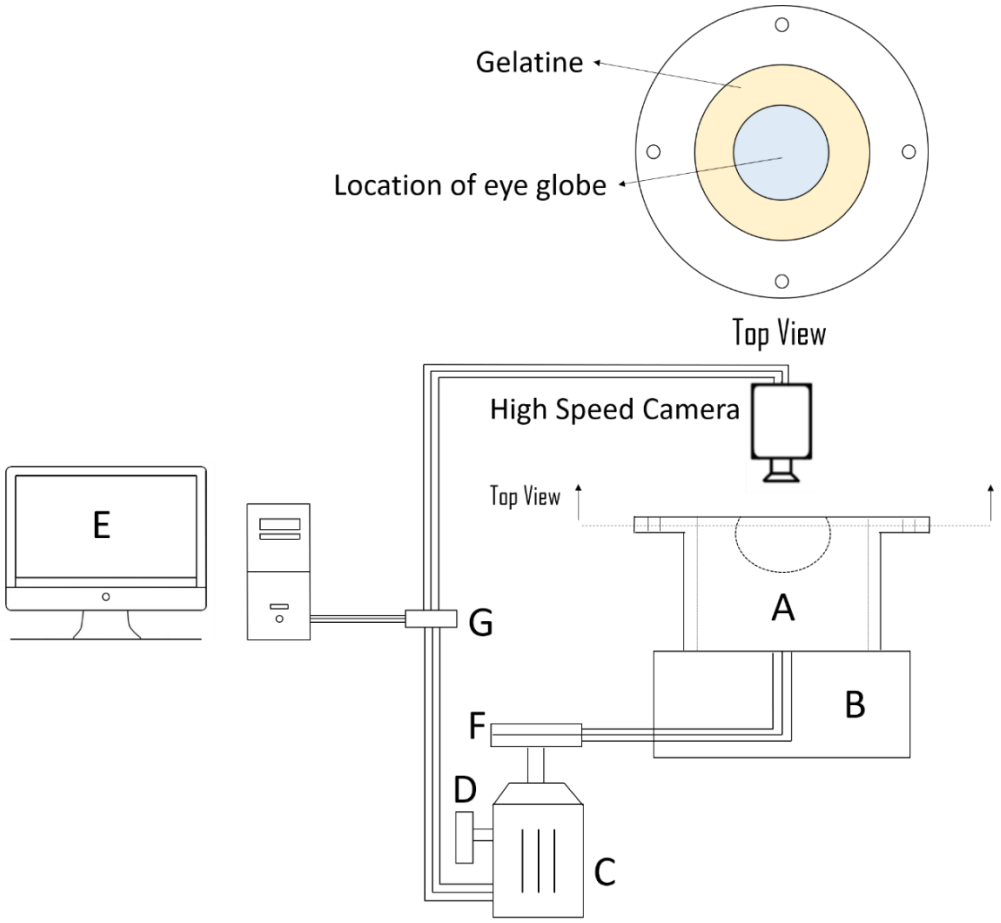

Figure 4.1: Schematic view of the test rig highlighting key components; A is the container, B is the metal platform, C is a motor, D is the decelerator, E is the computer, F is a reduction gear, and G is the data acquisition unit

A computer-controlled test rig was designed to support, load, and monitor eye globes' behaviour subjected to dynamic rotations representing saccadic eye movements, Figure 4.1. A container to enclose the eye specimen, Figure 4.2 and Figure 4.3, was designed and manufactured specifically for this experiment.

An eye specimen was placed in the container, glued to the base using water-based glue (Loctite, Henkel Corporation, Ohio, US), and surrounded by a gelatine material produced from Biowest Agarose (Gene Company Ltd, Chai Wan. Hong Kong). The gelatine was selected as its material properties are close to those of the orbital fat

that supports the eye in the ocular socket [29, 30]. This particular gelatine was chosen from trials for its clarity and low spring stiffness and because it had been reported not to alter collagen-based tissue chemically [248]. A comparison between two finite element models with no gelatine support and a model with gelatine support was conducted to determine the gelatine effect. After curing the gelatine, the specimen was placed in a freezer at -37°C for at least a day before being taken out to conduct the test. The eye specimen was cast into the gelatine support produced from Type-A gelatine flakes derived from porcine skin [249].

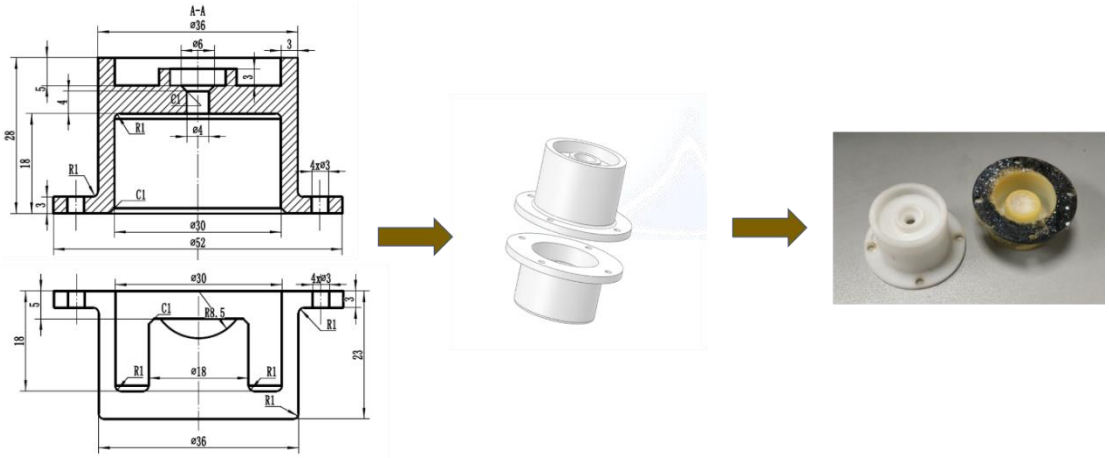

Figure 4.2: The process carried out to design and manufacture the eye specimen container

4.2.2 Experimental procedures

The eye globe was then taken out of the freezer and cut in half using a sharp blade moved on the container's surface. The container was then connected firmly to the centre of a circular metal platform, as shown in Figure 4.1, that experienced rotation produced by an electric motor (C), which was able to apply the required loading accelerations. The platform was also connected to a decelerator (D) to reduce the speed as needed. High-resolution images of the specimen were taken during the test every 2 ms. The power reaching the motor and the decelerator was controlled by a personal computer (E), which also recorded measurements by the rotation sensor attached to the metal plate and the images taken by the camera.

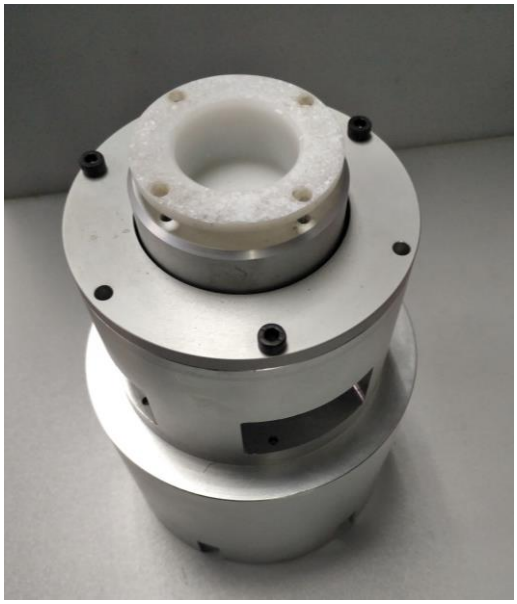

Figure 4.3: Experimental setup showing the container attached to the base controlling its rotation

After the tests, the camera images were analysed using digital image correlation software (ProAnalyst, Xcitex, Woburn, Massachusetts, USA) to trace the movement of several points of interest selected at different radii from the centre of the posterior chamber, Figure 4.4. Furthermore, the camera's initial image was used, along with eye dimension measurements taken before the test, in the construction of the finite element model of the test set up (utilised later in the inverse analysis exercise). Error in the measurement system was quantified by tracing multiple known locations within the container through Digital Image Correlation (DIC), and the RMS error between known locations and their associated measurement was calculated. The DIC technique has already been applied in earlier studies [250, 251], and showed successful results. During the quantification tests, all measurements were taken relative to a fixed point, the container's centre.

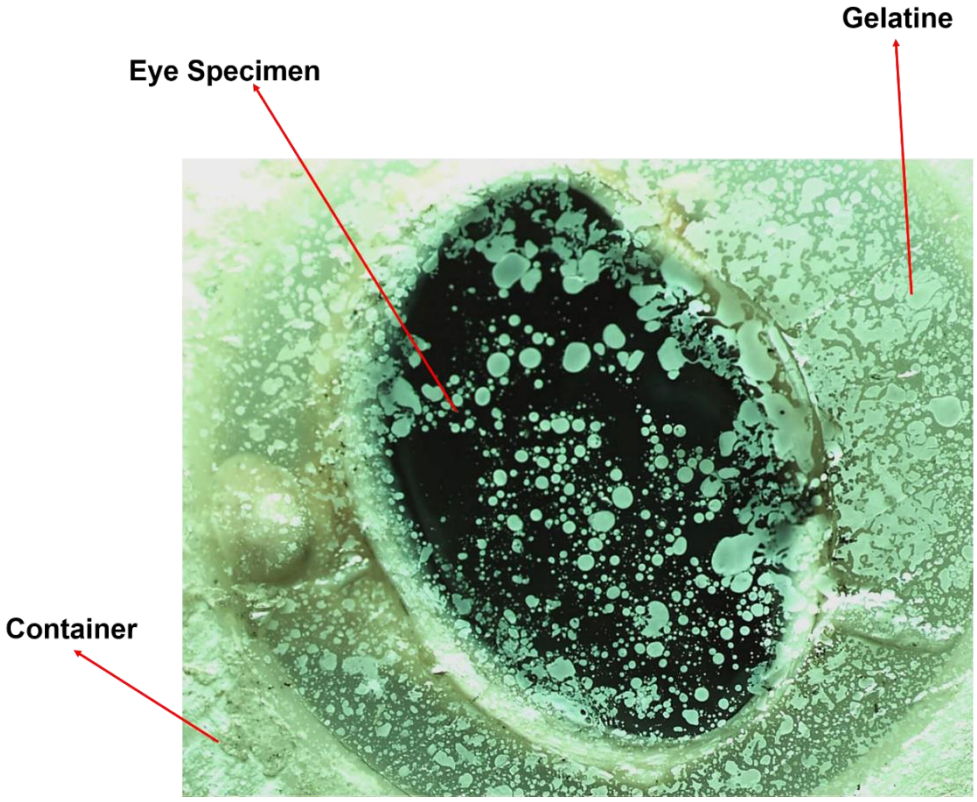

Figure 4.4 Picture taken of test rig showing eye specimen and gelatine

As saccadic eye movements rarely exceed 15° in amplitude [195], the specimens were subjected to three sets of tests with max rotations of 5˚, 10˚, and 15˚, respectively. The angular velocity adopted in the tests was also selected to emulate the normal conditions where the saccadic movement duration of the eye is only a function of the angle of eye rotation. An earlier study [194] showed that the angle of rotation ($\propto_o$ in degrees) and duration of rotation (T in seconds) were related according to the equation:

$$T = 0.021 \ \propto_o^{2/5} \tag{4.1}$$

Therefore, the angular displacement ($\propto$) and angular velocity (ω) of the saccades adopted in the tests were determined using the relationships [196]:

$$\propto (t) \ = \frac{\propto_o}{2}\left((1 - \cos\left(\frac{\pi}{T}t\right)\right) \tag{4.2}$$

$$\omega = \frac{\propto_o \ \pi}{2T}\sin(\frac{\pi}{T}t) \tag{4.3}$$

where t is the time at which $\propto$ and ω are calculated.

4.2.3 Numerical modelling

A numerical model was developed for use in the inverse analysis exercise intended to estimate the vitreous material behaviour. The model was built by the commercial finite element analysis (FEA) software ABAQUS (Release 6.14-2, Dassult Systemes, Johnston, Rhode Island, USA). The model included the semi eye globe tested along with the metal container and the gelatine material. The model representing the semi eye included the cornea, limbus, sclera, retina, and vitreous – it was created using a custom-built MATLAB code (The MathWorks, Inc., Natick, Massachusetts, USA).

i Porcine eye geometry

The model adopted the overall dimensions obtained for the porcine eye as captured by the initial camera image. The measurements were taken before the test of the corneal size and corneal and scleral thickness.

The initial images of the eye specimen were imported to MATLAB to determine its geometry. Using a custom-built code, the eye globe coordinates, in pixels, were identified, as shown in Figure 4.5. Using the same code, three lines were drawn from the container's inner edge to the opposite edge, as shown in Figure 4.6, and the length of each one was determined in pixels. The average length was then calculated to get the approximate inner diameter of the container in pixels.

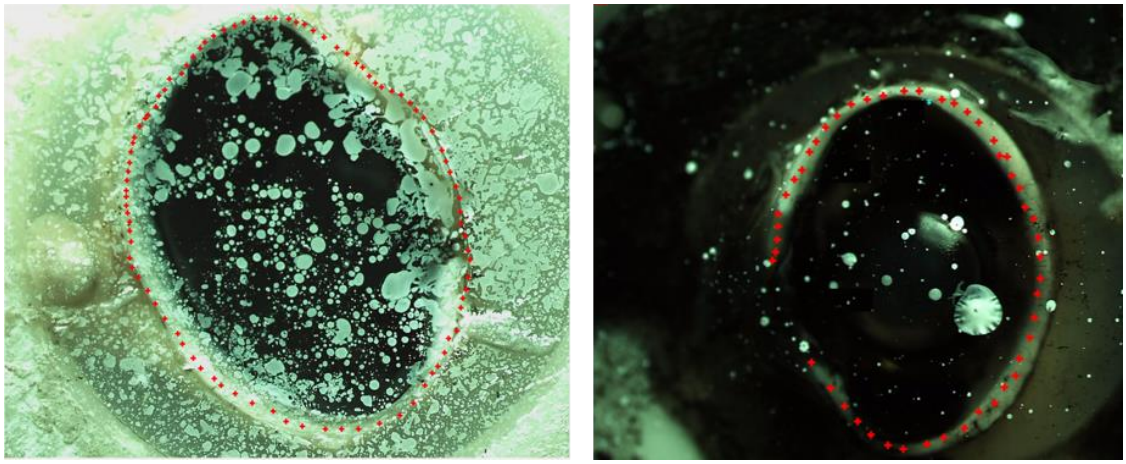

Figure 4.5: Pictures of the eye specimen showing the process taken to identify the porcine eye's geometry

The inner diameter of the container was calculated to be 30 mm; see Figure 4.2. By knowing the diameter in pixels and millimetres, a conversion factor was calculated by dividing the diameter in millimetres by the diameter in pixels. This factor was then multiplied by all the coordinates in pixels to convert them to millimetres. This process was repeated on two different pictures to ensure accuracy.

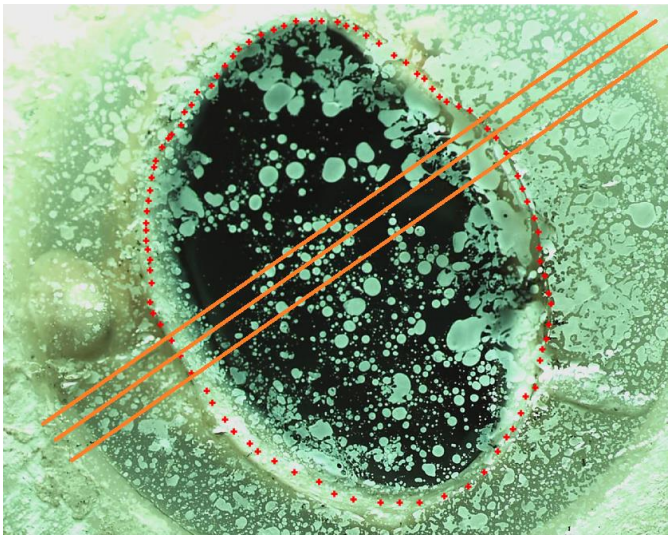

Figure 4.6: Image of the porcine eye specimen in the container, showing the lines drawn to determine the conversion factor from pixels to mm

These coordinates were then taken to a custom-made MATLAB code along with the thickness of the cornea and sclera. The outer geometry of the porcine eye was generated. The inner surface was then smoothed using another custom code to

achieve a flattened edge. The new cartesian coordinates of the cornea and sclera's outer and inner boundary were converted to spherical coordinates. All the nodes forming the eye's surface were duplicated around the z-axis with reasonable angular spacing between them to create a 180^{o} shape of the eye.

In order to create the retina, using the dimensions determined beforehand, the inner nodes of the sclera were duplicated and multiplied by its thickness function to create the inner layer of the retina.

As the lens and the aqueous were removed during the dissection process, the vitreous was created to fill the porcine globe's whole inner cavity. This was done by duplicating all the cornea's inner nodes, retina, and the anterior scleral region.

ii FE model creation

Using the same algorithm mentioned in section 3.2.2, the eye and the retina's outer layer were meshed. The cornea and sclera mesh was based on Nooshin and Tomatsuri configuration of diamatic domes [39, 235], using 6-noded continuum C3D6 elements. The sclera elements surrounded a layer of C3D6 elements representing the retina. Inside the retina elements, the vitreous filled the inner cavity, represented by C3D6 elements organised in multiple layers. The only exception was the innermost layer of vitreous elements that was formed of tetrahedral elements (type C3D4).

The container geometry was modelled in ABAQUS using the dimensions used in the manufacturing process. The container model was meshed with the ABAQUS-CAE automatic meshing tool using quadratic tetrahedron elements (type C3D10). In order to create the gelatine, the gelatine geometry was split into two sections, section A and section B. Section A represents the area between the eye and the container, and section B represents the area underneath the eye, filling the bottom of the container. For section A, the nodes of the outer layer of the eye model and the inner layer of the container model were exported to MATLAB. The inside of the container acted as the outer boundary of the gelatine and the outer nodes of the eye acted as the inner boundary. The container and the eye nodes were interpolated to have the same

number of nodes in order to form the outer and inner surface needed later for the mesh. Once the two surfaces were identified, the nodes were duplicated to form new layers in-between and meshed using the same algorithm used for the eye model. The gelatine elements were linear continuum elements (type C3D8), as shown in Figure 4.7. For section B, a geometry was created on ABAQUS using the container's inner and outer diameters and the height of the container base, where the eye sits. This was then meshed using ABAQUS automatic meshing tool using linear continuum elements (type C3D8). The two sections were then merged to act as one using the ABAQUS merging tool, as shown in Figure 4.7.

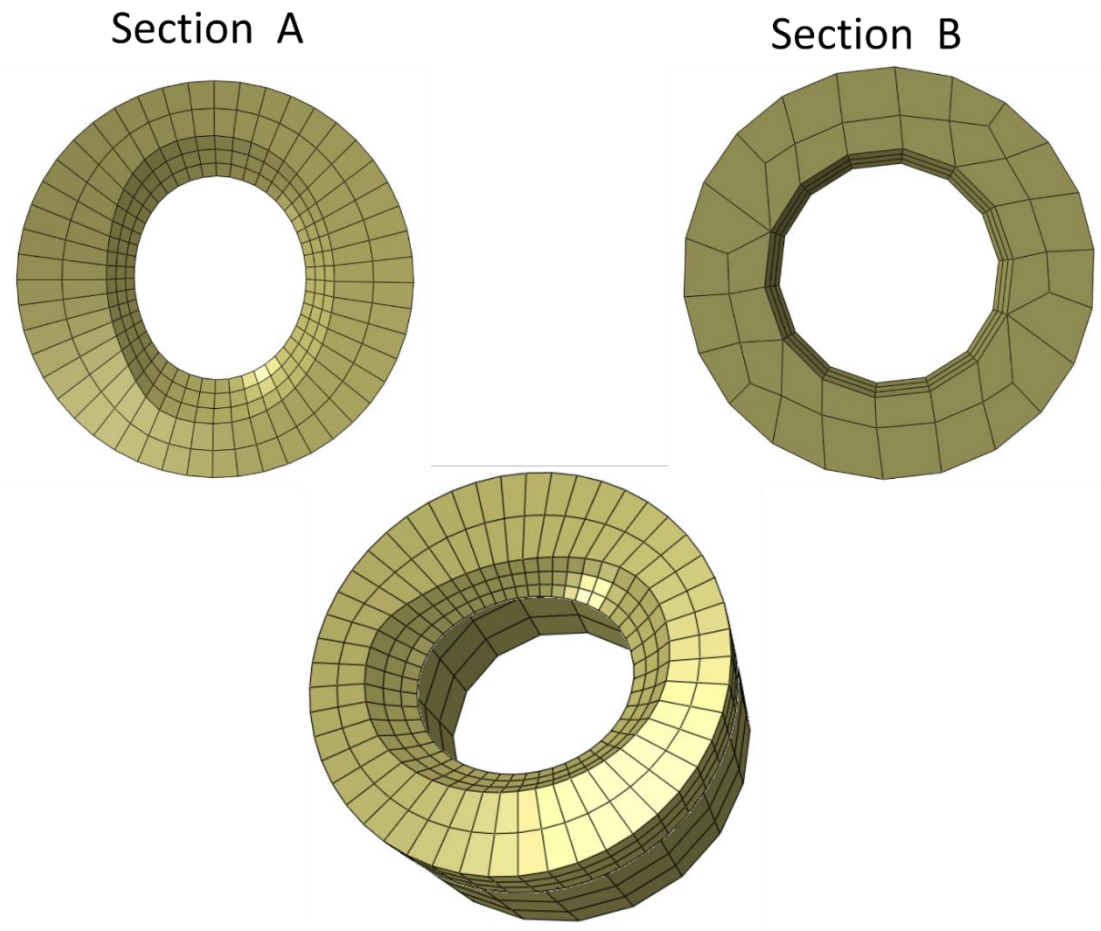

Figure 4.7: 3D rendering of the gelatine showing the mesh of the top section (A) and the bottom section (B) before and after merging

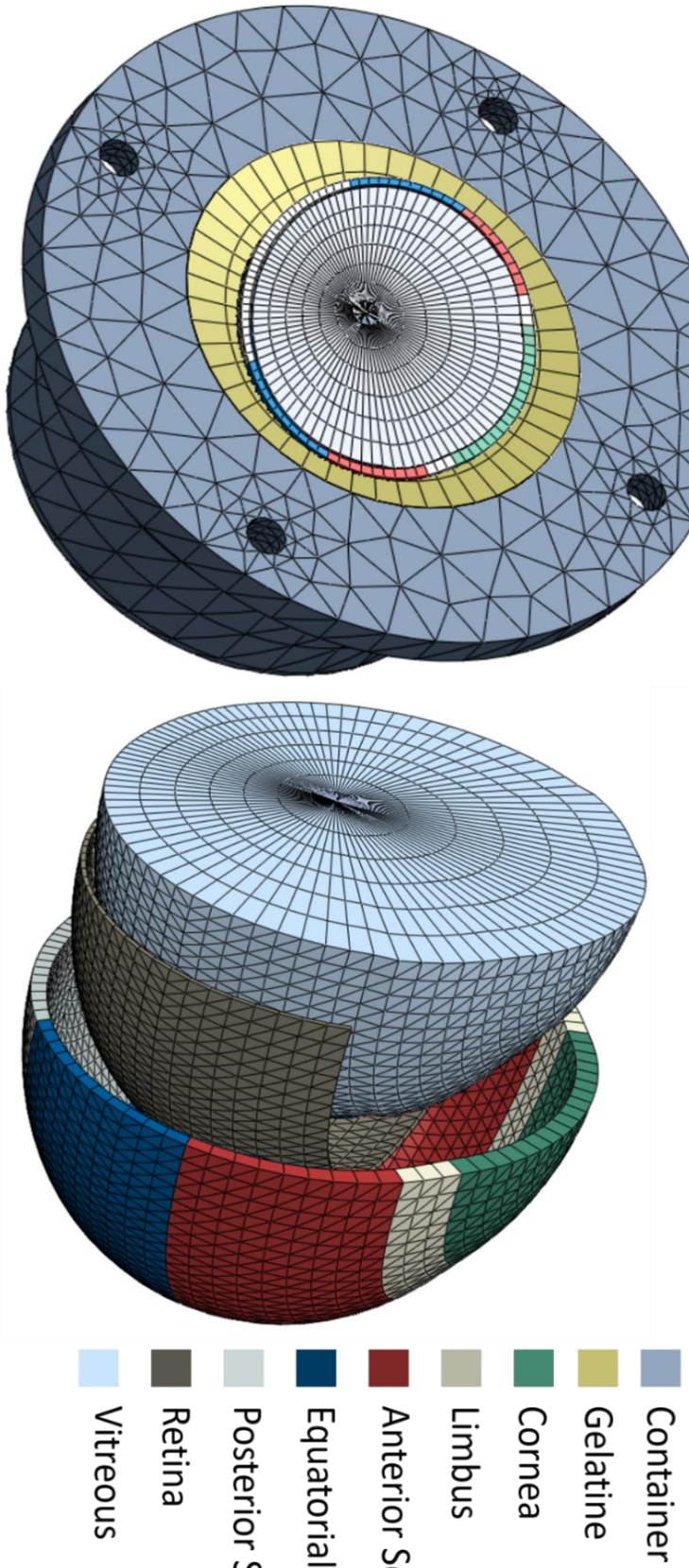

Figure 4.8: A 3D rendering of the numerical model showing the mesh layout of all parts

iii Porcine materials properties

The cornea, limbus, retina and sclera were assumed to follow the stress-strain behaviour reported in the literature for porcine eyes [60, 155]. Following earlier research, the eye model components were assumed to comply with Ogden's hyperelastic strain energy function [252], with the material parameters listed in Table 4-1 [154].

$$W = \frac{2\mu}{\alpha^2}\left(\overline{\lambda_1}^{\alpha} + \overline{\lambda_2}^{\alpha} + \overline{\lambda_3}^{\alpha} - 3\right) + \frac{1}{D}(J-1)^2 \qquad 4.4$$

In equation 4.4, W is the strain energy per unit volume; μ and α are the shear modulus and the strain hardening exponent, respectively, $\overline{\lambda_k}$ the deviatoric principal stretches = $J^{-1/3} \times \lambda_k$ (k=1, 2, 3), λ_1, λ_2, λ_3 the principal stretches, $J = \lambda_1 \lambda_2 \lambda_3$. D is a compressibility parameter $= \frac{3(1-2\nu)}{\mu(1+\nu)}$ calculated assuming the tissue was nearly incompressible [166],[167] with a Poisson's ratio, ν, of 0.48 [163, 168]. The numerical model's material characteristics were validated in earlier studies [39, 40, 58, 60, 153].

The container was modelled as a rigid body to consider the much higher stiffness of its material (steel) than the tissue components. The gelatine model was given the mechanical properties obtained from the manufacturers and shown in Table 4-1. A comparison was conducted between two finite element models with no gelatine support and a model with gelatine support to investigate the effect of the gelatine.

In consideration of the viscoelastic behaviour of the vitreous reported in the literature [46, 91-93, 175], the viscoelastic Prony constitutive model was adopted in the analysis [252]:

$$G(t) = G_0\,(t=0) = G_\infty + \sum_{i=1}^{N} G_i\, e^{-t/\tau_i} \qquad 4.5$$

where G is the shear relaxation modulus, G_0 and G_∞ are the short and long-term moduli, τ is the relaxation time and N is the function order. Values of these

parameters that best represent the vitreous behaviour, as observed in the experimental tests, were estimated from the inverse analysis exercise described below.

Table 4-1: Material properties of the different regions of the numerical model

	Constitutive model	**Constitutive model parameters**
Cornea [60]	Ogden	$\propto = 220.1$
	$n = 1$	$\mu = 0.0181$
Limbal region [60]	Ogden	$\propto = 127.2.1$
	$n = 1$	$\mu = 0.545$
Anterior sclera [60]	Ogden	$\propto = 162.3$
	$n = 1$	$\mu = 0.565$
Equatorial region [60]	Ogden	$\propto = 181.3$
	$n = 1$	$\mu = 0.642$
Posterior sclera [60]	Ogden	$\propto = 134.2$
	$n = 1$	$\mu = 0.621$
Retina[155]	Ogden	$\propto_1 = 0.00227$
	$n = 2$	$\mu_1 = 0.0811$
		$\propto_2 = 0.00421$
		$\mu_2 = 0.0.0652$
Gelatine	Ogden	$\propto_1 = 0.00239$
	$n = 1$	$\mu_1 = 0.005$

μ: shear modulus (MPa); α: strain hardening exponent;

iv Mesh convergence study

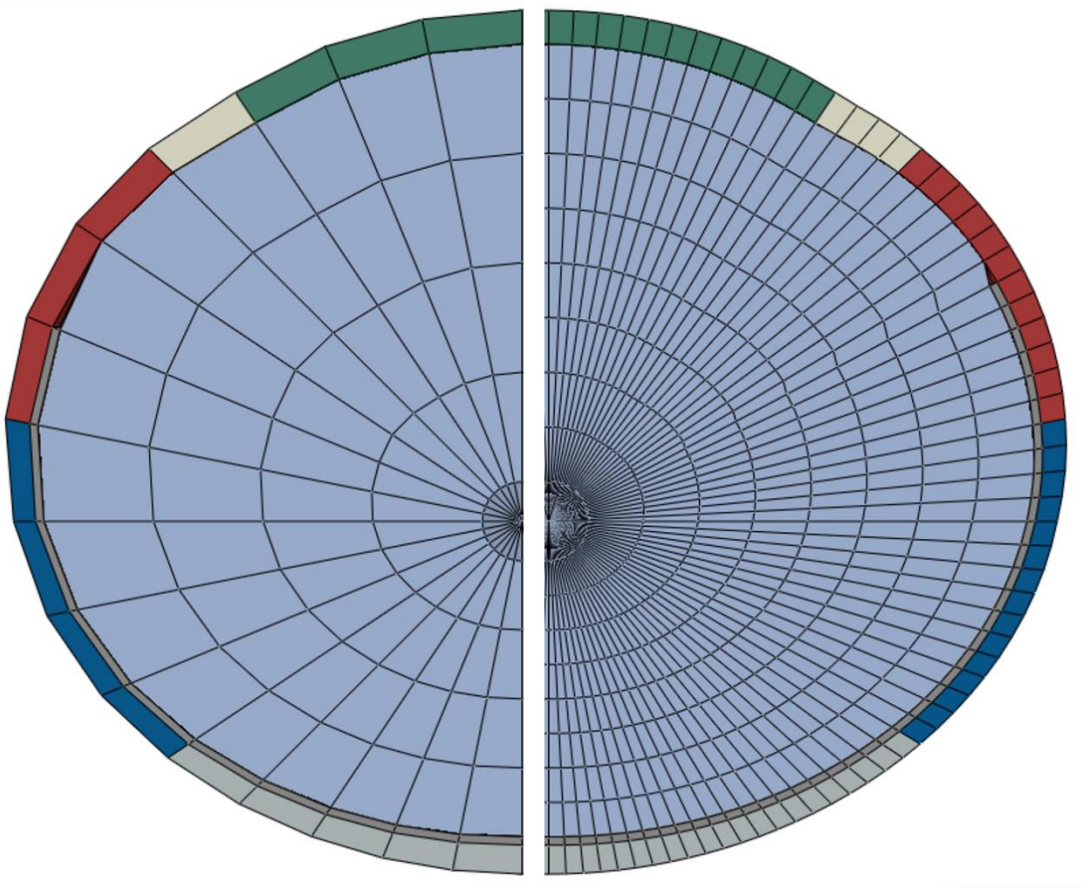

Figure 4.9: Geometry and material sections of the porcine eye showing the difference between coarse (left) and fine (right) mesh

The mesh density adopted in the model resulted from a mesh density study to balance accuracy of deformation prediction with computing time. The mesh was modified several times by firstly creating a mesh using the fewest/reasonable number of elements, and then a new mesh was recreated with denser element distribution, Figure 4.9. A model of the eye, rotating 15 degrees to the right and then staying still for 0.25 sec, was simulated and the displacements of several nodes and elements in the vitreous were identified in each mesh.

The flowchart in Figure 4.10 shows the nine models simulated in order to carry out the mesh convergence study. It shows the number of elements in the outer eye layer, vitreous, and retina.

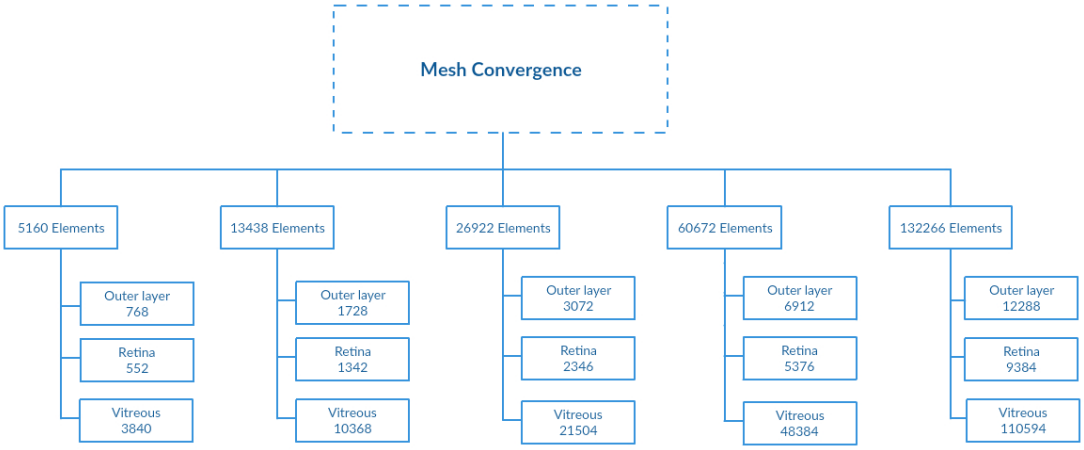

Figure 4.10: A flowchart showing the number of elements used for each model in the mesh convergence study

4.2.4 Particle swarm optimisation

This section presents the implementation of PSO with the finite element analysis solver. This technique was implemented in this study in order to identify the material parameters of the vitreous-gel. Interaction between ABAQUS and PSO was presented with the error calculation mechanism explained in the following section.

i Interaction with FE Solver

Interaction between ABAQUS and PSO was achieved using a custom-built MATLAB code. Optimisation of the vitreous parameters was carried out to determine the vitreous properties that would lead to the best possible match between the numerical predictions of the displacement of monitoring points and the corresponding experimental measurements. The technique used a group of particles whose positions represented the values of the parameters. A new ABAQUS job was created and performed to generate the output deformation curve through simulation. In order to assess fitness, which is how good the goal deformation curves match numerical curves for one particle, the error was calculated between numerical and target curves. In the next iteration, the algorithm updates the positions of these particles based on equation 2.37 after taking into consideration the best

neighbouring particle to minimise the error as much as possible. Then the algorithm evaluates these new particles and repeated the process in order to reach the threshold error.

The threshold error varies with different applications and computational cost, and it acts as a stopping criterion for the algorithm. After every iteration, the alteration between the experimental and the numerical results was calculated in order to direct the algorithm in adjusting the particle positions.

ii Error Calculation

RMS error between the numerical and experimental results was calculated using PSO. The following objective function was used to assess the results [206, 211, 253]:

$$RMS = \frac{1}{P}\sum_{j=1}^{P}\sqrt{\frac{1}{S}\sum_{i=1}^{S}(\theta_{i,j\ Exp} - \theta_{i,j\ Num})^2} \qquad 4.1$$

where P is the number of specimens, S is the total number of displacement levels at which the RMS is calculated, and θ_{Exp} and θ_{Num} , respectively represent experimental and numerical angular displacements at the monitoring points.

4.3 Results

4.3.1 Mesh convergence

i Porcine eye

Before the inverse analysis, the mesh density adopted in the model resulted from a mesh density study to balance deformation prediction accuracy with the computing time, per the methods described in Section 4.2.3. The mesh convergence study showed a 9.5% change in vitreous deformation when the number of elements increased from 3840 to 24192. A much smaller difference in deformation, of 0.36%, took place when the number of elements increased from 24192 to 110592. Based on these results (see Figure 4.11), the model employing 24192 elements was used in the study to represent the vitreous.

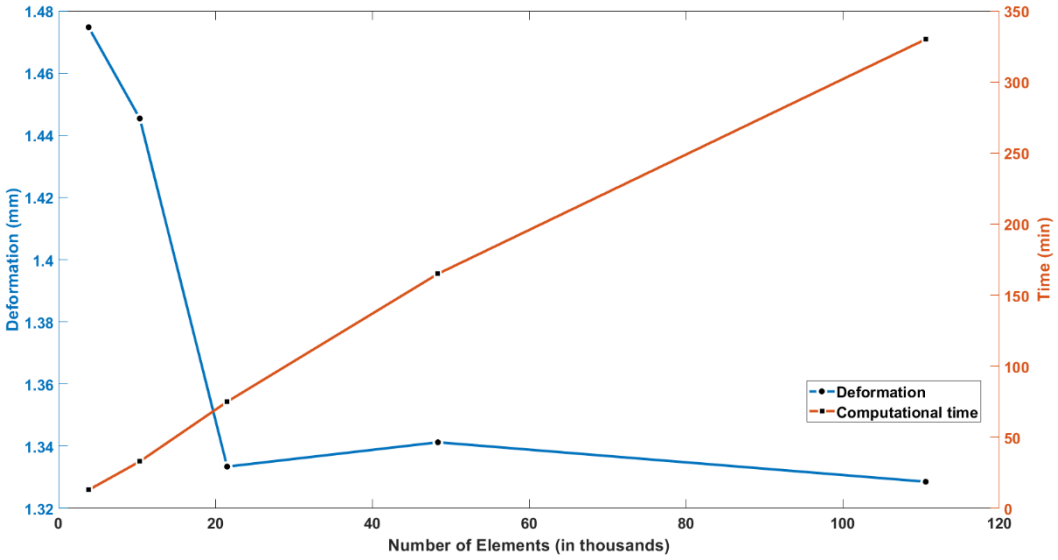

Figure 4.11: Porcine vitreous displacement outputs and CPU computation time of the numerical models

4.3.2 Gelatine effect

A comparison was conducted between two finite element models with and without gelatine support. The difference in angular displacement ranges between 0.04% and

0.28%. Figure 4.12 shows the angular displacement of two different points in the vitreous, with and without gelatine support.

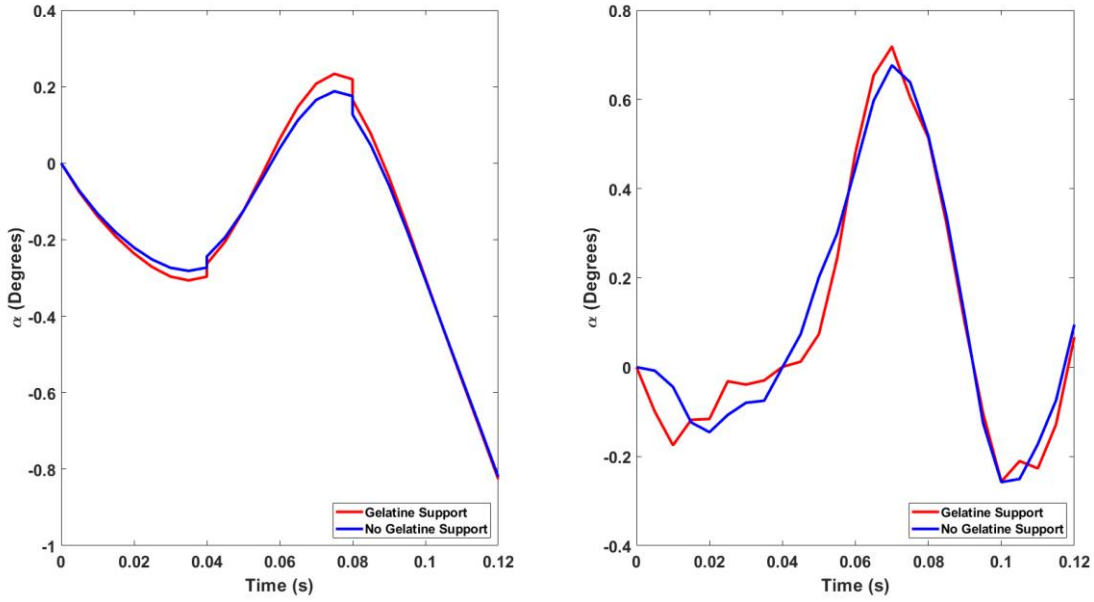

Figure 4.12: Angular displacement of two points at different radii with and without gelatine

4.3.3 Experimental results

Figure 4.13 shows the rotations recorded at three monitoring points at distances 5.4, 5.9, and 6.1 mm from the centre of rotation in three typical specimens tested under 5° maximum displacement. The rotations are compared to the applied whole eye rotations. In the first and second tests (5.4 and 5.9 mm from the centre of rotation), the monitoring point reached its maximum displacement in the first rotation cycle and reached a steady-state behaviour from the fifth cycle. On the other hand, in the other test (6.1 mm from the centre of rotation), the point reached its maximum displacement in the seventh cycle and reached a steady-state behaviour from the eighth cycle.

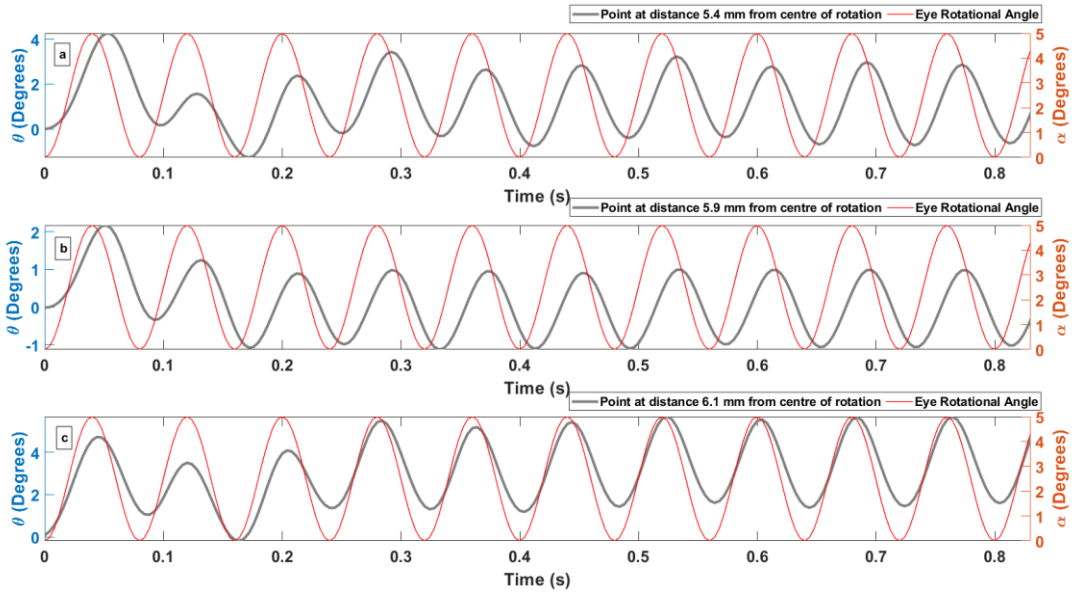

Figure 4.13: Experimental angular displacement at points with distances of (a) 5.4 mm (b) 5.9 mm and (c) 6.1 mm from the centre of rotation in typical tests involving 5° rotation

During the settling period, the response is called the transient response, followed by a steady-state response consisting of a sinewave [254]. Figure 4.14 illustrates the transient and steady-state responses for one point at a distance of 5.4 mm from the centre of rotation in tests with 5° maximum displacement. The transient state displacements were clearly unstable. However, the behaviour changed suddenly in the fifth loading cycle, indicating the start of the steady-state.

The experimental results show that, in tests with eye rotation up to 5°, the displacement monitored in the vitreous did not exceed 4.7° in the transient-state and 4.2° in the steady-state in all tests. The mean ratios between the steady-state displacement and transient-state displacement for all tests with 5° rotation were 3.3±0.7.

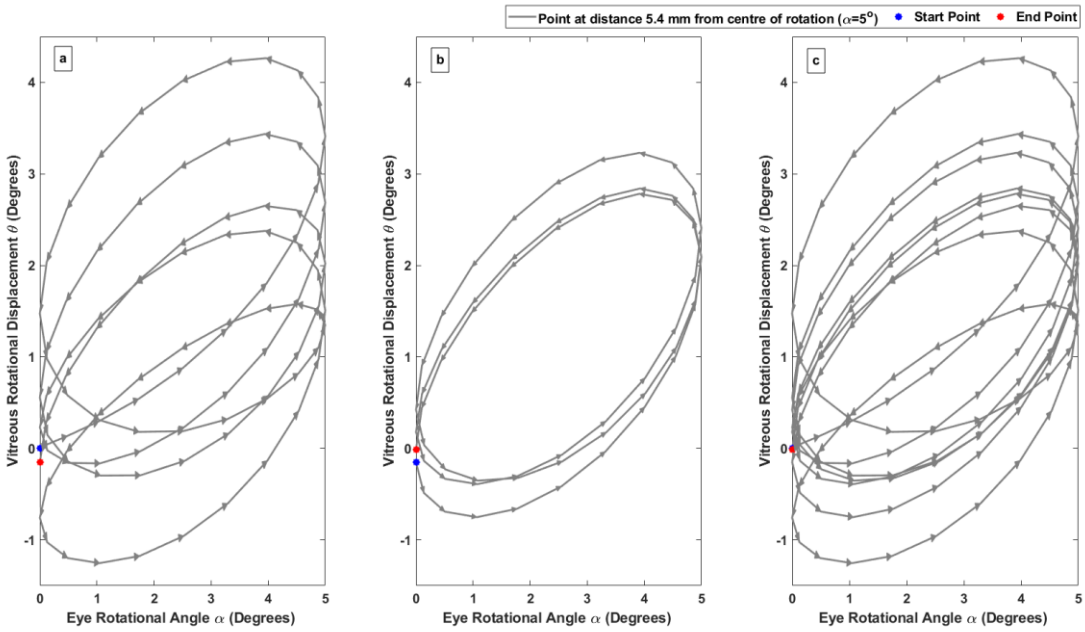

Figure 4.14: Dynamic behaviour at a point at a distance of 5.4 mm from the centre of rotation in a typical test under 5° maximum rotation. Part (a) depicts the transient-state behaviour, (b) depicts the steady-state behaviour, and (c) depicts the transient and steady states combined

Figure 4.15 shows the angular rotations for three monitoring points at distances 3.1, 3.8, and 8.9 mm from the centre of rotation in three different specimens tested under 10° maximum displacement. For the first point at 3.1 mm from the centre of rotation, it can be seen that it reached its maximum displacement in the third saccade and straight after that it reached a steady-state behaviour. For the second test, the point, not far from the first point, reached its maximum displacement in the seventh cycle and reached a steady-state behaviour from the ninth cycle. In contrast, a steady-state behaviour was evident in the third test from the first saccade with little difference noted in the second and later cycles.

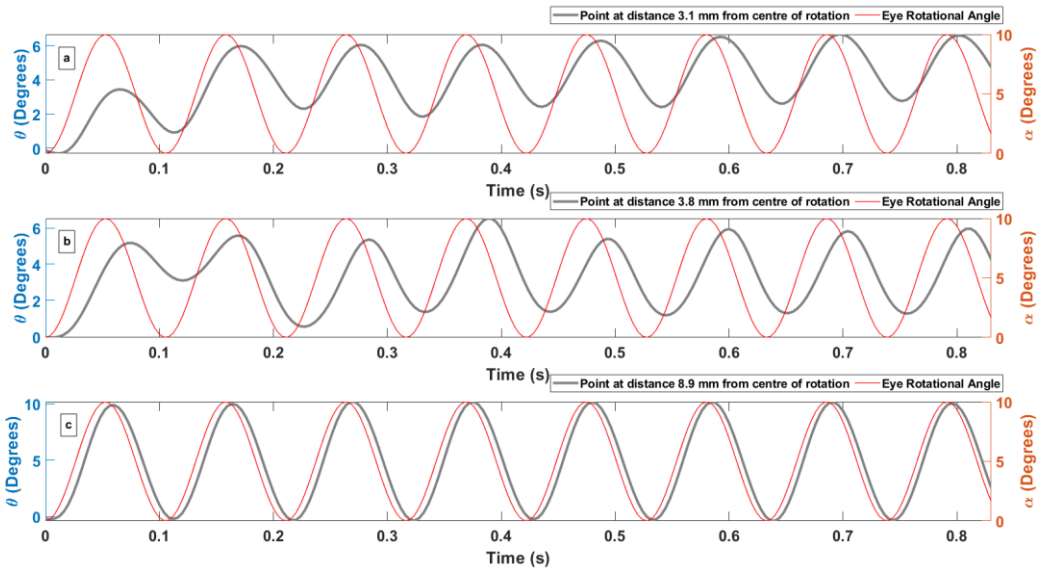

Figure 4.15: Experimental angular displacement at points with distances of (a) 3.1 mm (b) 3.8 mm and (c) 8.9 mm from the centre of rotation in typical tests involving 10° rotation

Figure 4.16 demonstrates the transient and steady-state responses for the point at 3.8 mm from the centre of rotation with a maximum displacement of 10°. It can be noticed that during the transient state, the behaviour was volatile compared to the steady-state. The experimental results show that the displacement monitored in the vitreous did not exceed 6.5° in the transient state and 4.2° in the steady-state. On the other hand, some points such as the point at 8.9 mm from the centre had no transient-state, while the maximum displacement in the steady-state was 10°.

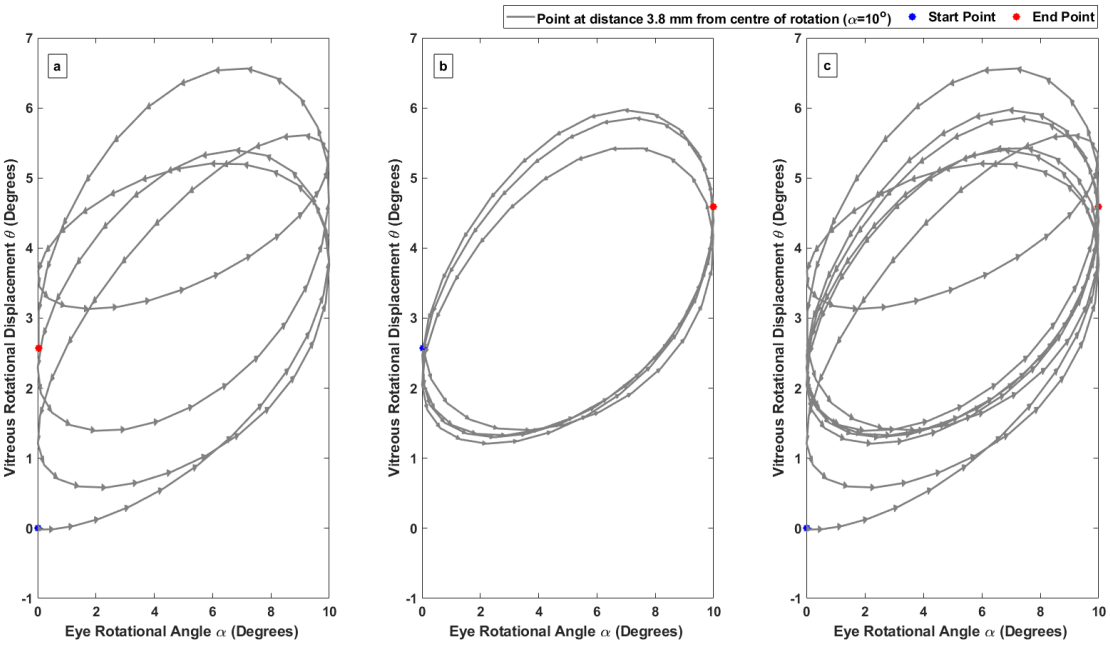

Figure 4.16: Dynamic behaviour at a point at a distance of 3.8 mm from the centre of rotation in a typical test under 10° maximum rotations. Part (a) depicts the transient-state behaviour, (b) depicts the steady-state behaviour, and (c) depicts the transient and steady states combined

Figure 4.17 shows the rotations recorded at three monitoring points at distances 5.9, 6.4, and 7.1 mm from the centre of rotation in three typical specimens tested under 15° maximum displacement. The rotations are compared to the applied whole eye rotations (red graph in Figure 4.17). In the first test, the monitoring point reached its maximum displacement in the seventh rotation cycle and reached a steady-state behaviour from the eighth cycle. On the other hand, in the second test, the point reached its maximum displacement in the first cycle and reached a steady-state behaviour from the second cycle. Finally, at 7.1 mm from the centre of rotation, the maximum rotation was reached at the first cycle; the steady-state behaviour was achieved after the eighth cycle.

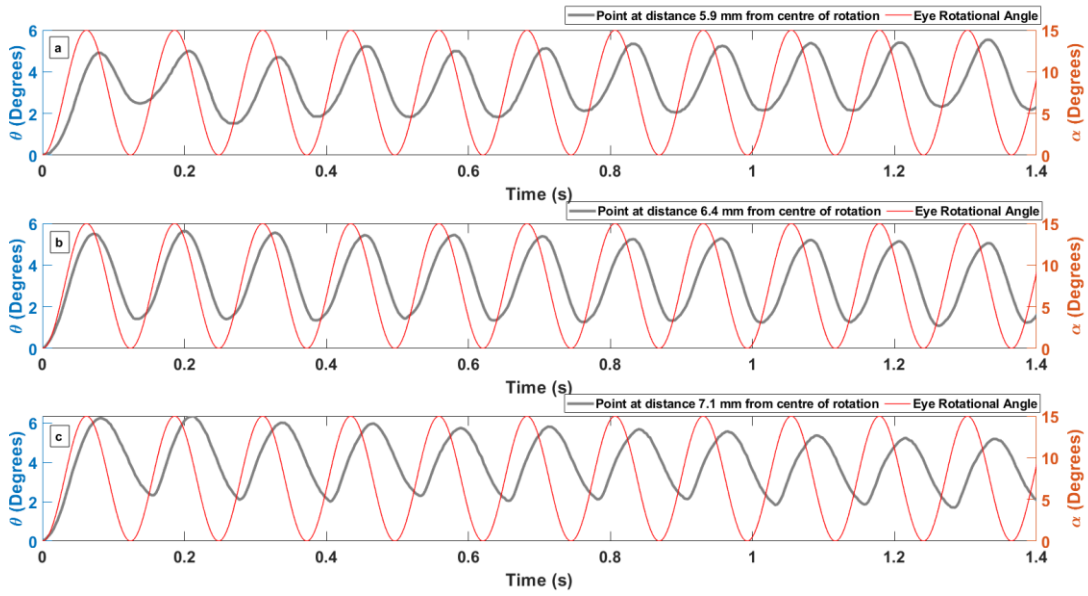

Figure 4.17: Experimental angular displacement at points with distances of (a) 5.9 mm (b) 6.4 mm and (c) 7.1 mm from the centre of rotation in typical tests involving 15° rotation

Figure 4.18 shows the transient state for the point at 6.4 mm from the centre of rotation with a maximum displacement of 15°. It can be noticed that the transient state only lasted for two cycles, followed by the steady-state behaviour, Figure 4.18b. The steady-state behaviour was more stable compared to the transient state. The experimental results show that the displacement monitored in the vitreous did not exceed 5.9° in the transient state and in the steady-state.

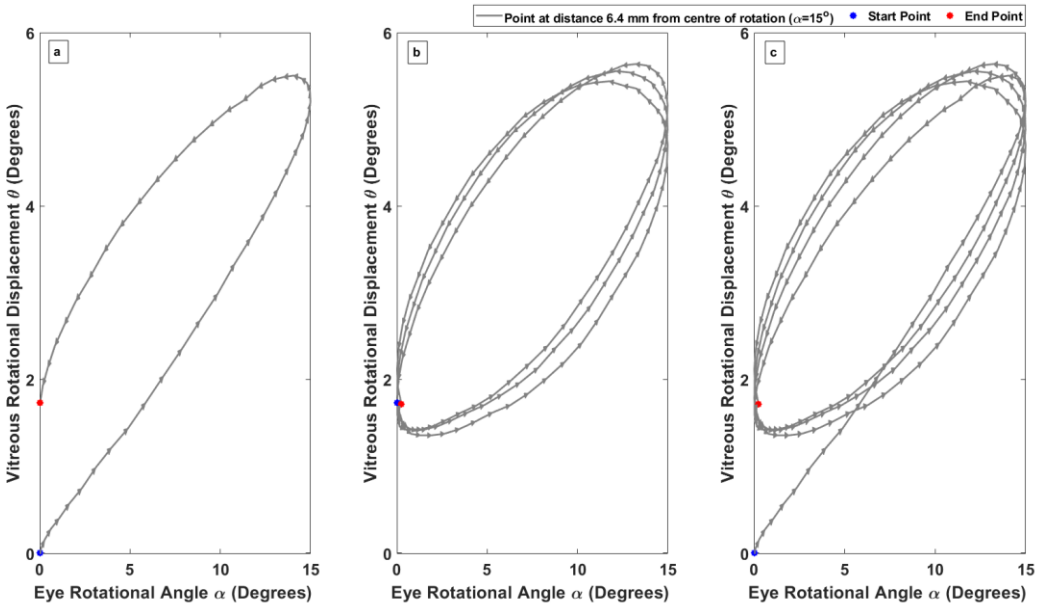

Figure 4.18: Dynamic behaviour at a point at a distance of 6.4 mm from the centre of rotation in a typical test under 15° maximum rotations. Part (a) depicts the transient-state behaviour, (b) depicts the steady-state behaviour, and (c) depicts the transient and steady states

4.3.4 Material parameter estimations

Inverse analysis was performed to derive a constitutive model for the vitreous in each eye tested that provided the best possible match (lowest RMS) with the results obtained experimentally. After using the inverse analysis to estimate values of the material parameters G_∞, G_o and τ, the exercise was repeated two more times for a randomly selected specimen to test the uniqueness of the material parameter estimations. The analysis was repeated twice while changing the initial values of the three parameters; once with double the initial values and once with half the initial values. The results showed that values of the three parameters changed within 2.8, 1.9 and 2.9% with changes in the initial values.

A typical subset of the results is presented in Figure 4.19, Figure 4.20, and Figure 4.21 for the specimens with maximum rotations of 5°, 10°, and 15°, respectively. For all specimens, the corresponding material parameters are:

$$G_o = 2.10 \pm 0.15\ Pa, \qquad G_\infty = 0.5 \pm 0.04\ Pa, \qquad \beta = 1.2 \pm 0.09\ s^{-1}$$

Figure 4.19 illustrates the experimental data versus the three points' numerical angular displacements at 5.4, 5.9, and 6.1 mm from the centre of rotation with maximum eye rotation of 5°. Comparing the mean curves for the three different specimens, the variation in displacement was small and has been accurately presented the most at the two points (5.4 and the 5.9 mm) closest to the centre of rotation. However, the variation in displacement was more considerable, and hence less accurately represented, at the 6.1 mm point, which led to the overall error in matching the displacement obtained experimentally.

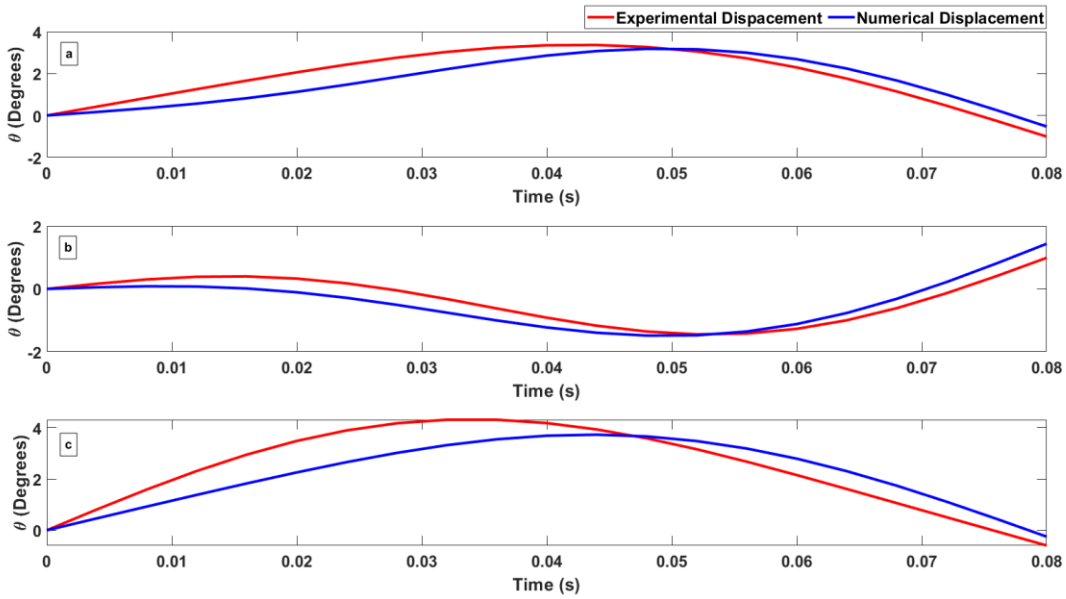

Figure 4.19: Experimental and numerical displacements at points at (a) 5.4, (b) 5.9, and (c) 6.1 mm in tests with maximum eye rotation of 5°

On the other hand, for the tests with maximum eye rotation of 10°, a typical subset of results is presented in Figure 4.20 for three specimens. Comparing the displacements for the three points, the point at 3.8 mm from the centre of rotation led to the largest variation in the displacement and highest RMS error. However, the two remaining points (3.1 and 8.9 mm) achieved better RMS error, due to the small variation in the displacement between the numerical and the experimental results.

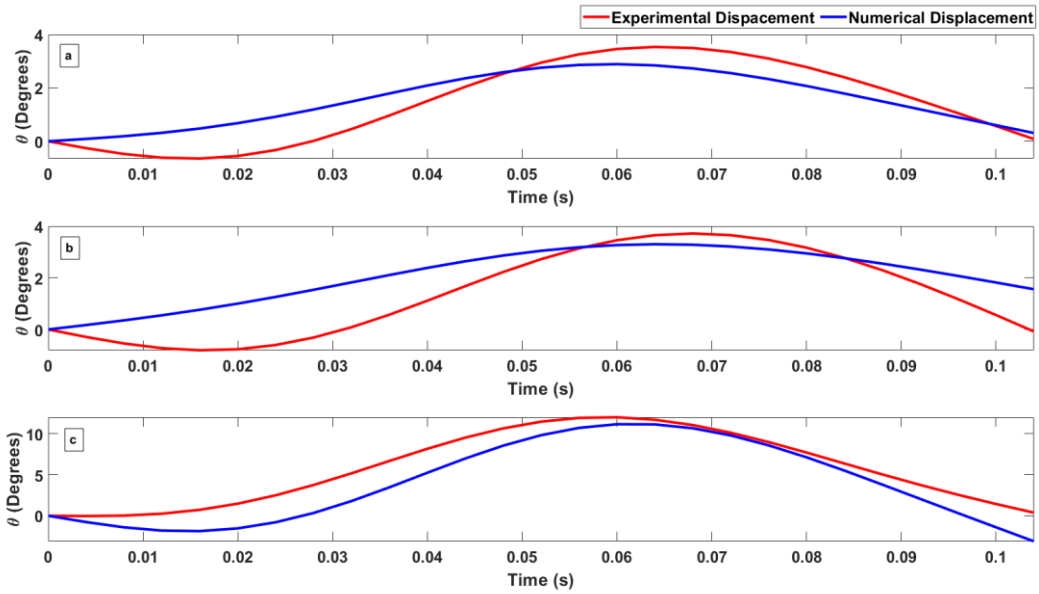

Figure 4.20: Experimental and numerical displacements at points at (a) 3.1, (b) 3.8, and (c) 8.9 mm in tests with maximum eye rotation of 10°

In the maximum eye rotation of 15° (Figure 4.21), the numerical displacement for the two points at 5.9 and 7.1 mm from the centre of rotation achieved larger error than the 6.4 mm point. Comparing the variation in displacement between the numerical and the experimental results, the second eye specimen achieved smaller error and more accurate representation. The instability in the other two points was due to the high rotational speed, which led to the distortion of some elements.

Inverse analysis was used to derive a constitutive model for the vitreous in each eye tested that provided the best possible match (lowest RMS) with the experimentally obtained displacement results. For all specimens, the corresponding material parameters are listed in Table 4-2.

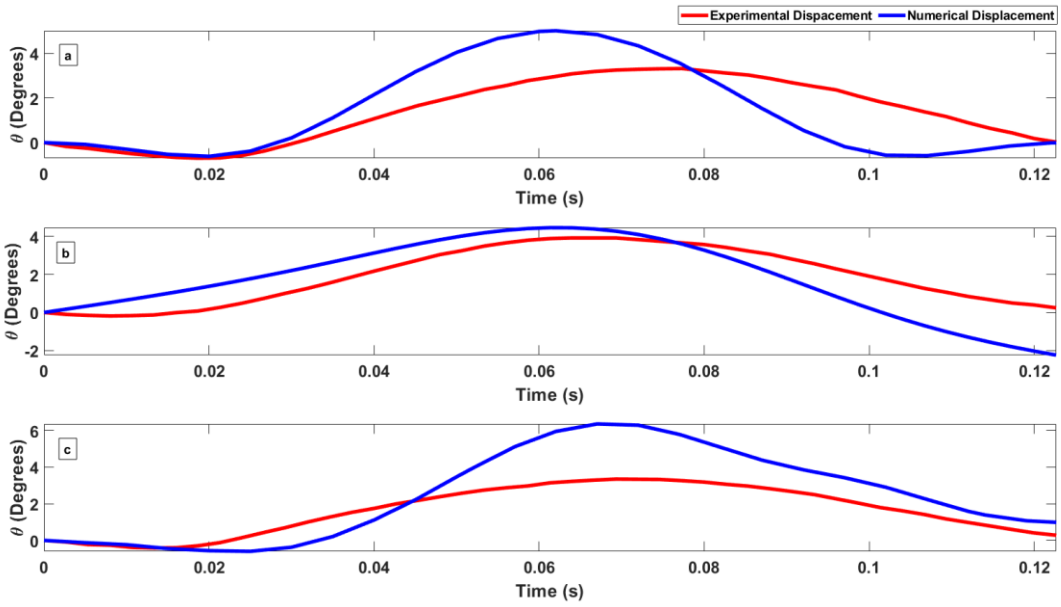

Figure 4.21: Experimental and numerical displacements at points at (a) 5.9, (b) 6.4, and (c) 7.1 mm in tests with maximum eye rotation of 15°

Table 4-2 Vitreous parameters as found numerically in the current study and in the literature

	Material Parameters	**Vitreous remained in eye**
Current study	$G_o = 2.10 \pm 0.15\ Pa,\quad G_\infty = 0.5 \pm 0.04\ Pa,\quad \beta = 1.2 \pm 0.09\ s^{-1}$	Yes
Rossi et al., 2011 [5]	$G_o = 10\ Pa,\quad G_\infty = 2\ Pa,\quad \beta = 0.01\ s^{-1}$	Yes
Liu et a.l, 2013 [2]	$G_o = 10\ Pa,\quad G_\infty = 0.3\ Pa,\quad \beta = 14.26\ s^{-1}$	No
Zimberlin et al., 2010 [4]	$E = 660\ Pa$	Yes
Zimberlin et al., 2010 [4]	$E = 120\ Pa$	No

E is the Elastic modulus; G_o Initial shear modulus; G_∞ long-term shear modulus; β viscoelastic decay constant

These values are compared with the results of earlier studies in Figure 4.22. While the values of G_∞ and β were intermediate between those reported by Rossi et al. and Liu et al, the value of G_o was below these of the two earlier studies [2, 5]. On the other hand, another earlier study by Zimberlin et al. [4] ignored the viscoelasticity of the vitreous and reported elastic modulus values. A further assessment of the material properties listed in Table 4-2 is presented in Figure 4.22 where a comparison is held between the numerically-predicted displacements at points at a distance of 5.4, 3.8, and 6.4 mm from the centre of rotation, for the 5°, 10°, and 15° eye rotations, respectively.

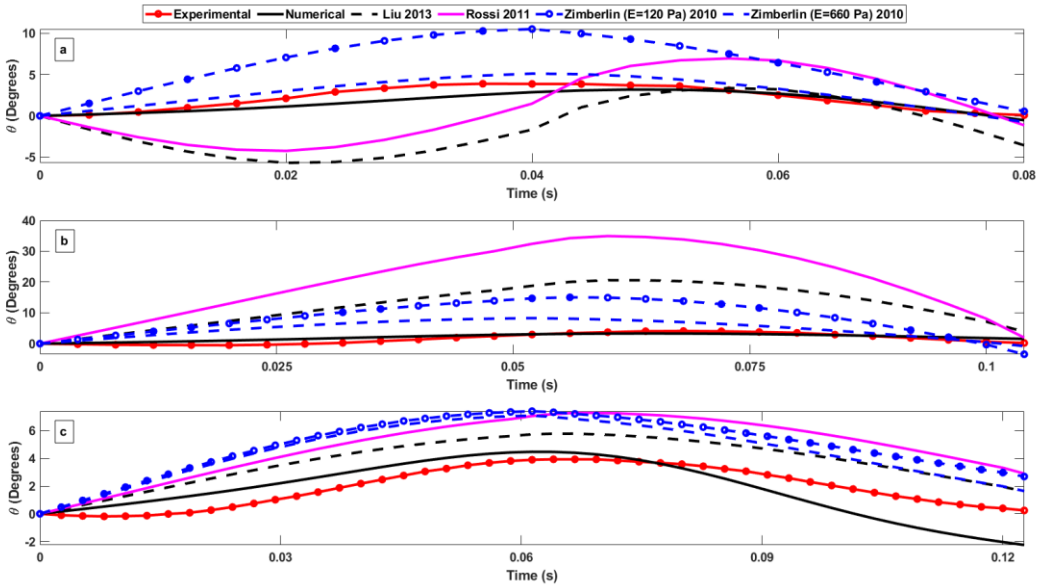

Figure 4.22 Experimental measurements and numerical predictions of displacements of points at (a) 5.4, (b) 3.8, and (c) 6.4 mm distance from the centre of rotation in tests with maximum eye rotation of (a) 5°, (b) 10°, and (c) 15°. Also presented are the numerical predictions of displacements based on the material properties reported in earlier studies

4.4 Discussion

The vitreous body has immense importance regarding the embryogenesis of the eye, the maintenance of its homeostasis, and its manifold interactions with neighbouring structures [169]. Deterioration in the vitreous properties can cause various diseases such as the vitreoretinal interface disease, retinal detachment and posterior vitreous detachment [255]. In this study, the vitreous properties were measured experimentally while keeping and testing the vitreous in close to its natural physiological conditions. Eye specimens were subjected to dynamic conditions simulating saccadic movements, and a numerical inverse analysis was used to estimate the biomechanical properties of the vitreous.

A significant advantage of the experimental method is that it allowed evaluation of the vitreous properties while keeping the tissue in its natural location, in the posterior chamber, thus avoiding the disturbance that could be caused by extraction. The specimens were also subjected to dynamic rotations simulating the vitreous main loading during eye movement.

Earlier experimental studies have tended to remove the vitreous from the posterior chamber before testing it mechanically – a process that may lead to changes in the mechanical properties. To test this assumption, Zimberlin et al. measured the vitreous mechanical properties in its native state and upon removal from the eye [4]. The resulting estimations of the vitreous elasticity modulus were very different: 660 Pa and 120 Pa in the former and latter cases.

In the same study, Zimberlin et al. adopted a cavitation rheology technique, in which a syringe needle was inserted into the posterior chamber to induce elastic instability via slow pressurisation [4]. The pressure at which the instability occurred was then related to the mechanical properties of the vitreous. However, the study assumed linear elastic vitreous behaviour and ignored the tissue's viscoelastic characteristics and, a result, its outcome could not be directly compared to the present study. Nevertheless, an indirect comparison could be held while using Zimberlin’s elastic

modulus in our numerical modelling of the test conditions, which resulted in slightly softer behaviour than that measured experimentally.

In another study by Liu et al. [2], the vitreous mechanical properties were obtained from an inverse analysis performed on experimental data. The experimental data were obtained from a rheology test, carried out by Lee et al. [176], using a magnetic microrheometer to study small volumes of vitreous samples after extraction from the eye. The viscoelastic model suggested by Liu led to larger predicted displacement – or smaller stiffness – than the experimental results of the present study, especially in the 5° and 10° rotational tests. While the long-term modulus, G_∞, reported by Liu was close to the value predicted in the present study, the initial shear modulus, G_o, and the decay constant, β, were larger than the values estimated herein due to the vitreous extraction carried out in Liu's study. Moreover, the variation in results is may be due to Lee et al. conducting the experiments up to 36 hours following extraction after death.

On the other hand, Rossi et al. [5] determined the vitreous material parameters using multi-objective optimisation performed on the test data of eye impact experiments carried out by Delori et al. [118]. The numerical simulation of Rossi et al. replicated the dynamic pressure subjected by a BB pellet on the eye. The parameters led to larger displacements than those measured in the current study. The initial shear modulus, the long-term modulus, and the decay constant reported by Rossi were more than four times larger than the values obtained in this study. The reason behind this large difference could be that the eye was simulated by Rossi et al. to freely move backwards, neglecting the effect of the ballistic gel used by Delori et al. Also, it is may be due to Delori conducting the test only 4 hours after the animal's death without the need to freeze the eye.

The use of porcine eyes is a limitation of the present study; however, earlier studies have shown that porcine vitreous had similar behaviour to that of human tissue [177, 247], also earlier studies have shown that porcine corneal and scleral tissue had similar behaviour to that of human tissue [256]. The difficulty in getting human eyes

in sufficient numbers had made it necessary to rely instead on porcine models. Future work will be needed to verify the applicability of the findings of this research to human tissue.

Furthermore, although the specimens were tested within 48 hours post-mortem, they may have experienced changes in their mechanical properties from their original state, which could have affected the vitreous deformation. A further limitation was the need to freeze the tissue before testing, which was necessary for specimen preparation. Bray [257] studied the effect of freezing on post-mortem vitreous and concluded that except for the potassium and magnesium, all other solutes were unaffected by freezing. Earlier studies indicated that the potassium level normally increases after death [258]. A recent study has also found that corneal and scleral tissue experienced negligible changes in mechanical behaviour upon freezing and thawing [259]. Still, there was no evidence that the same effect applied to the vitreous.

Moreover, the vitreous parameters were estimated by tracing the displacement of points at different radii from the posterior chamber's centre. Lee et al. [176] indicated a significant difference in the vitreous regions' rheological properties (anterior, central, posterior). However, Zimberlin et al. [4], Liu et al. [2] and Rossi et al. [5] neglected the effect of vitreous heterogeneity when modelling the vitreous. Therefore, future work will be needed to specify whether the three regions differ from each other.

In conclusion, the study has investigated the viscoelasticity of the vitreous humour experimentally to determine its initial and long-term shear moduli. The emphasis has been on testing and loading the vitreous in close to the natural physiologic conditions, and hence removing some of the possible sources of errors introduced in earlier research. The study produced estimations of the initial shear modulus and long-term shear modulus that were respectively smaller and larger than reported values.

5. Discussion and conclusion

5.1 Overview of study

This study aimed to investigate the effect of the vitreous shape and volume on retinal detachment initiation. A finite element model of the ocular globe was built from scratch to include all eye components. The model consists of the outer layer, aqueous, lens, retina, choroid, vitreous and the liquified vitreous. The geometry of the outer layer adopted in the study was built to be an idealised model. A meshing algorithm was developed to easily modify and mesh any irregular geometry of the eye globe. Bespoke software was created from scratch for the task of producing characteristic models. The software was written using MATLAB. A GUI was built to allow the program's use without the necessity to understand or run the underlining code. The Retina Detachment Generator (RDG) software allows the user to control the shapes of the lens, vitreous-gel, liquified-vitreous, and retina. The user could load an idealised model of the ocular globe or a patient-specific model. The bespoke software allows the user to choose the element type and mesh density before generating the model.

Four parametric studies were carried out to investigate the effect of the vitreous volume and detachment size on retinal detachment. The first parametric study investigated the traction produced due to the vitreous volume change while keeping the vitreous detachment size constant. On the other hand, the second parametric study, explored the traction applied by the vitreous on the retina, while keeping the vitreous volume consistent and changing the vitreous detachment size. The third and fourth parametric studies were a replicate of the first and second studies, respectively; however, they focused on the location where the RD occurs as well as retinal detachment progression. The traction produced by the vitreous and retinal detachment progression were investigated due to saccades and head movements. As most saccades don’t exceed 15^{o}, the models were subjected to a saccadic

movement of 10^o to study the vitreous tractional. An equivalent rectilinear movement of 2 mm transition was used to simulate head movement. Three different rotation angles (5^o,10^o,15^o) were applied to the models in parametric studies three and four.

The liquified vitreous was modelled using the FLUID CAVITY option provided by ABAQUS and using the continuum elements modelled to be softer than the vitreous gel. A comparison between the two methods was carried out.

The results showed that the traction produced due to the vitreous motion doesn't massively change with the change in vitreous volume. The head movement produced higher traction on the retina compared to saccades eye movement. The traction due to head movement was up to 39 Pa, which is almost 5 times the traction due to saccades eye movement. Despite difficulties in modelling the liquified vitreous using continuum elements, the models simulated by FLUID CAVITY and those with continuum elements showed similar values but different behaviour.

The model used the most recent and most accurate material parameters. Its initial results show that the primary factor in the progression of retinal detachment is the head movement. This suggests that this modelling method is useful in understanding the retinal detachment progression.

Another study was carried out to estimate the porcine vitreous material properties while testing it in close to its natural physiologic conditions.

Eighteen porcine eyes were tested within 48h post-mortem. A custom-built computer-controlled test rig was designed to support, load, and monitor eye globe behaviour while being subjected to dynamic rotation cycles mimicking saccadic eye movement. Specimens were glued to the base of a container, surrounded by gelatine, frozen, and cut in half to expose the vitreous. After thawing, the container was subjected to concentric dynamic rotations of up to 5°, 10°, or 15°, while taking 50-megapixel (MP) photos of the specimen every 2 ms. The images were analysed by a digital image correlation algorithm to trace the movement of marked points on the

vitreous surface with different radii from the centre of the posterior chamber. The initial camera image was used in building a finite element model of the test set up, which was used in an inverse analysis exercise to estimate the material properties of the vitreous.

Angular displacements of the monitored points were up to 3.3°, 4.1°, and 3.9° in response to eye rotations of 5°, 10°, and 15°, respectively. With the experimental relationships between eye rotation and angular displacements used as target behaviour, the inverse analysis exercise estimated the initial shear modulus, the long-term shear modulus and the viscoelastic decay constant of the porcine vitreous as 2.10±0.15 Pa, 0.50±0.04 Pa and 1.20 ±0.09 s^{-1}, respectively.

Consideration of the viscoelasticity of the vitreous was essential to represent its experimental behaviour. Testing the vitreous in close to its normal physiologic conditions produced estimations of the initial shear modulus and long-term shear modulus that were respectively smaller and larger than reported values [2, 4, 5].

5.2 Overall discussion

In the most basic anatomical terms, the ocular globe is divided into three sections: the posterior and interior chambers, and the vitreous chamber. The vitreous chamber is located at the back of the ocular globe and is the largest of all three chambers, taking up to 80% of the eye volume. The vitreous gel fills the space between the retina and the lens; it consists of 99% water, and the rest is a mixture of collagen, salts, proteins, and sugars. The vitreous plays a vital role in protecting the eye [82, 83]. It helps in holding its spherical shape, and the vitreous pressure helps to keep the retina in its place.

Due to ageing, the rheology and structure of the vitreous changes include condensation and shortening of the collagen fibres. This process leads to shrinkage of the vitreous body. This can result in PVD, in which the vitreous body is divided into two sections: vitreous gel and liquified vitreous. Eye rotation creates traction forces

on the retina, which could cause a retinal break or tear. When the liquified vitreous enters the area between the retina and the choroid, the retina starts to detach through the tear. This is called retinal detachment.

Several attempts have been made to describe the composition, structure, and material properties of the vitreous [4, 89, 92, 93, 115, 176, 244]. While these efforts shed much light on vitreous behaviour, some methods subjected the tissue to non-physiologic conditions and, thus, led to a wide variation in the parameters reported in the literature. Moreover, contradictions between the studies mentioned above propose that there are still gaps in the knowledge.

Saccadic eye movement has been modelled in several studies [153, 245, 246]. A saccade is a quick, simultaneous movement of the eyes between two phases of fixation. Only David et al. [46] studied the vitreous behaviour due to eye movement. They compared between a numerical and analytical model of the vitreous, however, no parameters were determined.

In this study, the vitreous properties were measured experimentally while keeping and testing the vitreous in close to its natural physiological conditions. This study used porcine eyes to build the methodology to determine the viscoelasticity of the vitreous. Eye specimens were subjected to dynamic conditions simulating saccade movements, and a numerical inverse analysis was carried out to estimate the biomechanical parameters of the vitreous.

The current technique overcomes the deficiencies in the data resulting from the limitation of extracting the vitreous from its original location. The inverse analysis results were compared to values reported in the literature [2, 4, 5]. When the vitreous was modelled to have elastic behaviour as assumed by Zimberlin et al. [4], it led to softer response compared to the present study. In another study by Liu et al. [2], the vitreous properties were determined after conducting an inverse analysis on experimental data obtained from a rheology test carried out by Lee et al. [176]. The results of Liu et al. led to larger predicted displacement compared to the experimental results of this study. The variation in the results may be due to the

vitreous extraction carried out by Lee et al., or/and conducting their experiment up to 36 hours after death.

Meanwhile, when the current study was compared to a model using the vitreous parameters obtained by Rossi et al. [5], they led to larger displacements than those measured in the current study. Rossi et al. determined their vitreous parameters using a multi-objective optimisation on an eye impact experiment conducted by Delori et al. [118]. Two reasons may be contributing to the variation in the results between Rossi's parameters and this study's experimental results. The first one may be due to Rossi ignoring the effect of the ballistic gel used by Delori to hold the eye. The second reason may be due to that Delori et al. didn't need to freeze the eye, and their tests were conducted within 4 hours after death.

The inverse analysis results are expected to form part of a wider data set if, and when, human ocular globes become accessible for testing. The limitation of human eyes accessibility limited this area of study. Future work will be needed to verify the applicability of the findings on human tissues and to study the changes that occur in the vitreous due to ageing. Several studies reported a significant difference in the properties of the vitreous regions [116, 176]. For simplicity, the present study neglected the effect of vitreous heterogeneity by taking an average value to describe the vitreous parameters. Also, the fact that the tests were carried out after 48 hours post-mortem could have affected the vitreous gel's mechanical properties, which led to different deformation. Finally, for specimen preparation, the porcine eyes were placed in the freezer prior to the experiment, which could have led to changes in the vitreous mechanical behaviour. However, Bray [257] studied the effect of freezing on post-mortem vitreous and concluded that except for the potassium and magnesium, all other solutes were unaffected by freezing. Earlier studies also indicated that the potassium level normally increases after death [258].

In addition to the experimental evaluation of vitreous behaviour, this present study aimed to further understand the effect of saccadic and head eye movements on retinal detachment progression. This was addressed by developing an idealized

numerical model of the ocular globe. These 3D models included components such as the aqueous, lens, choroid, retina, and vitreous (gel and liquid). The effect of the vitreous detachment size and the volume of the vitreous due to the eye movement was investigated.

Results provide a feasible idea of the vitreous dynamics. Vitreous oscillations are observed to take place at least one time after saccadic and head movements. This agrees with the in vivo observations of Walton et al. [240] who reported the existence of at least one vitreous oscillation after saccades, before the eye comes to rest. Also, Repetto et al. [1] confirms that using a 2D model of the ocular globe to study the traction exerted by the detached vitreous on the retina. Moreover, in all the numerical simulations for both head and saccadic movements, it was observed that the traction stress is concentrated close to the vitreous attachment point. This agrees with the observations of Repetto et al., who reported for their 2D model that the concentration of the maximum traction on the retina varies with the vitreous attachment point. Three different eye rotations (5^o, 10^o, 15^o) were applied to study the dependence of the maximum traction on the amplitude of the saccadic rotation. It was also observed that the retinal traction depends on the amplitude of the saccadic and head rotation. It appears that the traction increases with the amplitude of the rotation. This is in agreement with the observations of Repetto et al. [1].

In a study carried out by Vroon et al. [153], they group measured the peak traction produced on the retina by the vitreous to be within the range of 30-35 Pa due to head and saccadic movements. These values are ten times lower than the values measured experimentally, which was 340 Pa [2]. However, the simplifications adopted in Vroon et al.'s model led to a lack of damping in the vitreous when comparing to the ultrasound scans. In this present study, the retina's peak traction loads due to saccadic eye movements range between 4-7 Pa, which is a factor of hundred times lower than the adhesion force of the retina. Since the eye movements rarely exceed 15^o [195], and the 10^o rotation used in this study is larger than 95% of

all saccades [196], it is unlikely that the traction caused by most of the saccadic eye movements will overcome retinal adhesion.

The head movement defined in the present study is set at 2 mm, covered over the same time span as the saccadic movements. This movement is smaller than those created by jogging, yet more extensive than those experienced by walking [189]. It is similar to the movement caused by sitting down [192]. In this present study, the retina's peak traction loads due to head movements range between 23-29 Pa, which is a factor of ten times lower than the adhesion force of the retina. Moreover, these values are seven times larger than those created by saccadic eye movements.

The dependency of the model on specific parameters such as the vitreous volume was investigated by allowing the retina to separate from the choroid. Eight models with a vitreous volume ranging from 72.5% to 90% were created to determine the size of the retinal detachment produced by each. An average retinal adhesion traction of 3 Pa was defined in all models to allow the retina to detach from the choroid. In this study, the percentage of retinal detachment ranges between 2-4% for the 5^{o} rotation, 6.5-8% for the 10^{o} rotation and 8.5-16% for the 15^{o} rotation, when both continuum elements and FLUID CAVITY option were used to simulate the liquified vitreous. On the other hand, when head movement was applied, the detachment ranges between 43-48%. This study explains the consequences of the traction load produced due to the head and saccadic movement mentioned earlier. Moreover, especially during saccadic movement, the difference in results between the eight models was small, suggesting that the vitreous volume is not the main factor leading to retinal detachment. This is in agreement with the observations of Repetto et al. [1], who reported that the maximum traction on the retina remained almost unchanged for all volumes of the vitreous.

On the other hand, the model's dependency on the size of vitreous detachment was investigated. Six models with constant volume and different vitreous detachment size were created. The detachment size of the vitreous ranges from straight below the vitreous base to 15^{o} below the equator of the eye. The same retinal adhesion

load of 3 Pa was defined. For saccadic eye movements, the retina's detachment ranges between 0 and 2.2% for the 5^{o} rotation, 0 and 9.9% for the 10^{o} rotation, and 4 and 11% for the 15^{o} rotation, when both continuum elements and FLUID CAVITY option were used to simulate the liquified vitreous. On the other hand, when the head movement was applied, the detachment ranges between 41 and 51%. This study suggests a directly proportional relationship between the detachment of the vitreous and the detachment of the retina. These results suggest that the vitreous detachment size vehemently affects the progression of retinal detachment. These results agree with the results achieved by Repetto et al. [1], who suggest that the maximum traction experiences a slight increase at the vitreous attachment point when the size of the detachment increases.

Comparing the numerical model to ultrasound scans was very beneficial. This provided an excellent qualitative comparison between the real vitreous and the modelled vitreous. The results showed that, after the vitreous gained momentum, especially in the fourth and fifth rotation, the two vitreous bodies (real and model) behaved correspondingly. The lack of damping achieved by Vroon et al. [153] when comparing their model to ultrasound scans was overcome in this study due to the use of the correct material properties of the vitreous and the eye components as the lens.

Modelling the liquified vitreous using two methods, FLUID CAVITY and continuum elements, provided a preliminary investigation of the fluid-structure interaction between the vitreous and liquified vitreous. It was clear that, at low speed, the range of traction forces for the head and saccades movements was very close when the two methods were used. However, for larger rates, the FLUID CAVITY liquified vitreous showed more stability in the results. In contrast, many of the continuum elements liquified vitreous crashed due to element distortion.

This study's results are likely to form a better understanding of retinal detachment if, and when, clear ultrasound scans become accessible for validation. The limitation of clear ultrasound scans availability restricted this area of study. Moreover, the

effect of gravity was not considered in the analysis; it would be beneficial to investigate the impact of the gravitational load on the calculated traction. For the purpose of simplicity, boundary conditions were used to simulate the head and saccadic eye movements. Future work will be needed to consider the effect of the extraocular muscles and the orbit in causing the movement of the eyeball. The results of this study are expected to form part of a wider data set if, and when, the rheology and structure of the vitreous due to ageing become available. The limitation of changes of the vitreous parameters with ageing limited this area of study.

5.3 Conclusions

The project aimed to improve the understanding of effect of head and saccades movements on the progression of retinal detachment and to quantify effect of the interaction between the vitreous and its neighbouring structures. Based on the findings of this research, the following conclusions could be drawn:

- The study presented an algorithm to create and mesh a complete FEM of the ocular globe to investigate retinal detachment pathology. The models and tools developed in this study are suitable for modification. The ability to easily model such features will be beneficial when modelling real-life retinal detachment scenarios and investigating eye behaviour;
- The study produced useful results on the role of head and saccadic eye movements in the development of retinal detachment; it indicated that head movements are more likely to lead to retinal detachment progression;
- The study investigated the effect of the vitreous volume and detachment size on the progression of retinal detachment; it shows that vitreous detachment size is directly proportional to the progression of retinal detachment;
- Numerical simulations for different amplitudes of the saccadic motion were carried while fixing all other parameters; results showed that the traction on the retina increases with the rotation amplitude;

- The study has also investigated the viscoelasticity of the vitreous humour experimentally in order to determine its shear moduli. The study's goal has been in testing and loading the vitreous in close to its natural physiologic conditions, hence removing some of the possible sources of errors introduced in previous research. The research produced estimations of the initial and long-term shear moduli that were respectively smaller and larger than reported values

6. Appendices

6.1 Input File

```
*Heading
** Job name: Model_85 Model name: Model_85
** Generated by: Abaqus/CAE 6.14-2
*Preprint, echo=NO, model=NO, history=NO, contact=NO
**
** ==================================================================================
** PARTS
** ==================================================================================
**
*Part, name=EYE
*Node
*NODE,NSET=EyeNodes,INPUT=Node_File.inp
*ELEMENT, ELSET=EyeElements, TYPE=C3D6, INPUT=Element_File.inp
*ELEMENT, ELSET=ChoroidElements, TYPE=C3D6, INPUT=Coroid_Element_File.inp
*ELEMENT, ELSET=RetinaElements, TYPE=C3D6, INPUT=Retina_Element_File.inp
 **********************************************************************
 *Elset, elset=C1
 1537, 1538, 1539, 1540, 1541, 1542, 1543, 1544, 1545, 1546, 1547, 1548, 1549, 1550, 1551, 1552
 1553, 1554, 1555, 1556, 1557, 1558, 1559, 1560, 1561, 1562, 1563, 1564, 1565, 1566, 1567, 1568
 1569, 1570, 1571, 1572, 1573, 1574, 1575, 1576, 1577, 1578, 1579, 1580, 1581, 1582, 1583, 1584
 1585, 1586, 1587, 1588, 1589, 1590, 1591, 1592, 1593, 1594, 1595, 1596, 1597, 1598, 1599, 1600
 1601, 1602, 1603, 1604, 1605, 1606, 1607, 1608, 1609, 1610, 1611, 1612, 1613, 1614, 1615, 1616
 1617, 1618, 1619, 1620, 1621, 1622, 1623, 1624, 1625, 1626, 2353, 2354, 2355, 2356, 2357, 2358
 2359, 2360, 2361, 2362, 2363, 2364, 2365, 2366, 2367, 2368, 2369, 2370, 2371, 2372, 2373, 2374
 2375, 2376, 2377, 2378, 2379, 2380, 2381, 2382, 2383, 2384, 2385, 2386, 2387, 2388, 2389, 2390
 2391, 2392, 2393, 2394, 2395, 2396, 2397, 2398, 2399, 2400, 2401, 2402, 2403, 2404, 2405, 2406
 2407, 2408, 2409, 2410, 2411, 2412
*Elset, elset=LIMBUS
 1627, 1628, 1629, 1630, 1631, 1632, 1633, 1634, 1635, 1636, 1637, 1638, 1639, 1640, 1641, 1642
 1643, 1644, 1645, 1646, 1647, 1648, 1649, 1650, 1651, 1652, 1653, 1654, 1655, 1656, 1657, 1658
 1659, 1660, 1661, 1662, 1663, 1664, 1665, 1666, 1667, 1668, 1669, 1670, 1671, 1672, 1673, 1674
 1675, 1676, 1677, 1678, 1679, 1680, 1681, 1682, 1683, 1684, 1685, 1686, 1687, 1688, 1689, 1690
 1691, 1692, 1693, 1694, 1695, 1696, 1697, 1698, 1699, 1700, 1701, 1702, 1703, 1704, 2413, 2414
 2415, 2416, 2417, 2418, 2419, 2420, 2421, 2422, 2423, 2424, 2425, 2426, 2427, 2428, 2429, 2430
 2431, 2432, 2433, 2434, 2435, 2436, 2437, 2438, 2439, 2440, 2441, 2442, 2443, 2444, 2445, 2446
 2447, 2448, 2449, 2450, 2451, 2452, 2453, 2454, 2455, 2456, 2457, 2458, 2459, 2460, 2461, 2462
 2463, 2464, 2465, 2466, 2467, 2468, 2469, 2470, 2471, 2472, 2473, 2474, 2475, 2476, 2477, 2478
 **********************************************************************
*INCLUDE, INPUT=MPC_Choroid.inp
*Nset, nset=RETINA_V
*INCLUDE, INPUT=MPC_retina.inp
*Nset, nset=S1
*INCLUDE, INPUT=S1.inp
*Nset, nset=S2
*INCLUDE, INPUT=S2.inp
*Nset, nset=S3
*INCLUDE, INPUT=S3.inp
**********************************************************************
** Section: Section-1-S3
*Solid Section, elset=S3, material=MS3
,
** Section: Section-2-S2
*Solid Section, elset=S2, material=MS2
,
** Section: Section-3-C1
*Solid Section, elset=C1, material=MC1
,
```

```
** Section: Section-4-LIMBUS
*Solid Section, elset=LIMBUS, material=MLIMBUS
,
** Section: Section-5-S1
*Solid Section, elset=S1, material=MS1
,
** Section: Section-9-RETINA
*Solid Section, elset=RetinaElements, material=RETINA
,
** Section: Section-9-Choroid
*Solid Section, elset=GlueElements, material=Choroid
,
*End Part
**
*Part, name=liquified_vitreous
**============================================================================
**
*NODE,NSET=LiquidNodes,INPUT=liquified_vitreous_Node_File_85.inp
**
*ELEMENT, ELSET=LiquidElements, TYPE=C3D6, INPUT=liquified_vitreous_Element_File_85.inp
**
*SOLIDSECTION, ELSET=LiquidElements, MATERIAL=WATER
**
*End Part
**********************************************************************
*Part, name=LENS
**============================================================================
**
*NODE,NSET=LensNodes,INPUT=lens_Node_File.inp
**
*ELEMENT, ELSET=LensElements, TYPE=C3D6, INPUT=lens_Element_File.inp
**
*SOLIDSECTION, ELSET=LensElements, MATERIAL=lens
**
*End Part
**********************************************************************
*Part, name=Aqueous
**============================================================================
**
*NODE,NSET=AqueoussNodes,INPUT=Aqueous_Node_File.inp
**
*ELEMENT, ELSET=AqueousElements, TYPE=C3D6, INPUT=Aqueous_Element_File.inp
**
*SOLIDSECTION, ELSET=AqueousElements, MATERIAL=Aqueous
**
*End Part
**********************************************************************
*Part, name=Vitreous
**============================================================================
**
*NODE,NSET=VitNodes,INPUT=vitreous_Node_File_85.inp
*ELEMENT, ELSET=VitElements, TYPE=C3D6, INPUT=vitreous_Element_File_85.inp
*Element, type=C3D4
*ELEMENT, ELSET=VitElementsCentre, TYPE=C3D4, INPUT=vitreous_Element_center_85.inp
*Nset, nset=VITREOUS_R
*INCLUDE, INPUT=MPC_Vit_retina.inp
*Nset, nset=VITREOUS_E
```

```
*INCLUDE, INPUT=MPC_Vit_Choroid.inp
**
*SOLIDSECTION, ELSET=VitreousElements, MATERIAL=V1
**
*End Part
**********************************************************************
** ==================================================================
** ASSEMBLY
** ==================================================================
*Assembly, name=Assembly
**
*Instance, name=EYE-1, part=EYE
*End Instance
**
*Instance, name=VITREOUS-1, part=VITREOUS
*End Instance
**
*Instance, name=LENS-1, part=LENS
*End Instance
**
*Instance, name=liquified_vitreous-1, part=liquified_vitreous
*End Instance
**
*Instance, name=Aqueous-1, part=Aqueous
*End Instance
**********************************************************************
** ==================================================================
** Amplitude
** ==================================================================
*INCLUDE, INPUT=Amp.inp
** ==================================================================
** MATERIALS
** ==================================================================
*Amplitude, name=AMP-3
*INCLUDE, INPUT=materials.inp
** ==================================================================
** INTERACTION PROPERTIES
** ==================================================================
**
*Surface Interaction, name=COH
*Friction
0.,
*Surface Behavior, pressure-overclosure=HARD
**********************************************************************
** ==================================================================
** BOUNDARY CONDITIONS
** ==================================================================
** STEP: Step-1
**
*Step, name=Step-1, nlgeom=YES
*Dynamic, Explicit
, 0.0527496
*Bulk Viscosity
0.3, 5.
** Mass Scaling: Semi-Automatic
**               Whole Model
*Variable Mass Scaling, dt=1e-06, type=below min, frequency=1
```

```
**
**
** BOUNDARY CONDITIONS
**
** Name: Disp-BC-1 Type: Displacement/Rotation
*Boundary, op=NEW
** Name: Disp-BC-2 Type: Displacement/Rotation
*Boundary, op=NEW
** Name: Disp-BC-3 Type: Displacement/Rotation
*Boundary, op=NEW
** Name: Disp-BC-4 Type: Displacement/Rotation
*Boundary, op=NEW, amplitude=AMP-3
RP-3, 5, 5, 0.174533
** Name: Disp-BC-5 Type: Displacement/Rotation
*Boundary, op=NEW, amplitude=AMP-3
RP-3, 1, 1
** Name: Disp-BC-6 Type: Displacement/Rotation
*Boundary, op=NEW
EYE-1.YZERONODES, 2, 2
**
** OUTPUT REQUESTS
**
*Restart, write, number interval=1, time marks=NO
**
** FIELD OUTPUT: F-Output-1
**
*Output, field, time interval=0.005
*Node Output
A, RF, U, V
**
** FIELD OUTPUT: F-Output-2
**
*Element Output, directions=YES
EVF, LE, PE, PEEQ, PEEQVAVG, PEVAVG, S, SVAVG
**
** FIELD OUTPUT: F-Output-3
**
*Output, field, variable=PRESELECT, time interval=0.005
**
** HISTORY OUTPUT: H-Output-1
**
*Output, history, variable=PRESELECT
*End Step
***
```

7. References

1. Repetto, R., Tatone, A., Testa, A., and Colangeli, E., *Traction on the retina induced by saccadic eye movements in the presence of posterior vitreous detachment.* Biomech Model Mechanobiol, 2011. **10**(2): p. 191-202.

2. Liu, X., Wang, L., Wang, C., Sun, G., Liu, S., and Fan, Y., *Mechanism of traumatic retinal detachment in blunt impact: a finite element study.* J Biomech, 2013. **46**(7): p. 1321-1327.

3. Salicone, A., Smiddy, W. E., Venkatraman, A., and Feuer, W., *Visual recovery after scleral buckling procedure for retinal detachment.* Ophthalmology, 2006. **113**(10): p. 1734-1742.

4. Zimberlin, J. A., Mcmanus, J. J., and Crosby, A. J., *Cavitation rheology of the vitreous: mechanical properties of biological tissue.* Soft Matter, 2010. **6**(15).

5. Rossi, T., Boccassini, B., Esposito, L., Iossa, M., Ruggiero, A., Tamburrelli, C., and Bonora, N., *The pathogenesis of retinal damage in blunt eye trauma: finite element modeling.* Invest Ophthalmol Vis Sci, 2011. **52**(7): p. 3994-4002.

6. Sabra, A. I., *Theories of Light from Descartes to Newton.* Philosophy, 1968. **43**(165): p. 291-293.

7. Hentschel, K., *A History of Optics from Greek Antiquity to the Nineteenth Century.* Annals of Science, 2014. **71**.

8. Lindberg, D. C. and Lindberg, D. C., *Theories of Vision from Al-kindi to Kepler*. 1981: University of Chicago Press.

9. Zubairy, M. S., *A Very Brief History of Light*, in *Optics in Our Time*, M.D. Al-Amri, M. El-Gomati, and M.S. Zubairy, Editors. 2016, Springer International Publishing: Cham. p. 3-24.

10. Smith, A. M., *Ptolemy and the Foundations of Ancient Mathematical Optics: A Source Based Guided Study*. 1999: American Philosophical Society.

11. Levin, F. S., *Surfing the Quantum World*. 2017: Oxford University Press.

12. Huff, T. E., *The Rise of Early Modern Science: Islam, China, and the West*. 3 ed. 2017, Cambridge: Cambridge University Press.

13. Rashed, R., *A Pioneer in Anaclastics: Ibn Sahl on Burning Mirrors and Lenses.* Isis, 1990. **81**(3): p. 464-491.

14. Al-Khalili, J., *In retrospect: Book of Optics.* Nature, 2015. **518**(7538): p. 164-165.

15. Rosen, E., *Kepler. By Max Caspar. Translated and edited by C. Doris Reliman. (New York: Abelard-Schuman. 1959. Pp. 401. $7.50.).* The American Historical Review, 1960. **66**(1): p. 150-151.

16. Li, X., *Incidence and epidemiological characteristics of rhegmatogenous retinal detachment in Beijing, China.* Ophthalmology, 2003. **110**(12): p. 2413-2417.

17. Wilkinson, C. P., *Interventions for asymptomatic retinal breaks and lattice degeneration for preventing retinal detachment.* Cochrane Database Syst Rev, 2012. **3**(3): p. Cd003170.

18. Van De Put, M. a. J., Hooymans, J. M. M., and Los, L. I., *The incidence of rhegmatogenous retinal detachment in The Netherlands.* Ophthalmology, 2013. **120**(3): p. 616-622.

19. Haimann, M. H., Burton, T. C., and Brown, C. K., *Epidemiology of retinal detachment.* Arch Ophthalmol, 1982. **100**(2): p. 289-292.

20. Basinger, B. C., Rowley, A. P., Chen, K., Humayun, M. S., and Weiland, J. D., *Finite element modeling of retinal prosthesis mechanics.* J Neural Eng, 2009. **6**(5): p. 055006.

21. He, M., Zeng, J., Liu, Y., Xu, J., Pokharel, G. P., and Ellwein, L. B., *Refractive error and visual impairment in urban children in southern china.* Invest Ophthalmol Vis Sci, 2004. **45**(3): p. 793-799.

22. Lin, L. L., Shih, Y. F., Hsiao, C. K., and Chen, C. J., *Prevalence of myopia in Taiwanese schoolchildren: 1983 to 2000.* Ann Acad Med Singap, 2004. **33**(1): p. 27-33.

23. Rose, K. A., Morgan, I. G., Smith, W., Burlutsky, G., Mitchell, P., and Saw, S. M., *Myopia, lifestyle, and schooling in students of Chinese ethnicity in Singapore and Sydney.* Arch Ophthalmol, 2008. **126**(4): p. 527-530.

24. Thylefors, B. and Négrel, A. D., *The global impact of glaucoma.* Bulletin of the World Health Organization, 1994. **72**(3): p. 323-326.

25. Humphrey, J., *Continuum biomechanics of soft biological tissues.* Proceedings of The Royal Society A: Mathematical, Physical and Engineering Sciences, 2003. **459**: p. 3-46.

26. Elsheikh, A., Alhasso, D., Gunvant, P., and Garway-Heath, D., *Multiparameter correction equation for Goldmann applanation tonometry.* Optom Vis Sci, 2011. **88**(1): p. E102-112.

27. Elsheikh, A., Wang, D., Kotecha, A., Brown, M., and Garway-Heath, D., *Evaluation of Goldmann applanation tonometry using a nonlinear finite element ocular model.* Ann Biomed Eng, 2006. **34**(10): p. 1628-1640.

28. Norman, R. E., Flanagan, J. G., Sigal, I. A., Rausch, S. M., Tertinegg, I., and Ethier, C. R., *Finite element modeling of the human sclera: influence on optic nerve head biomechanics and connections with glaucoma.* Exp Eye Res, 2011. **93**(1): p. 4-12.

29. Sinha Roy, A. and Dupps, W. J., Jr., *Effects of altered corneal stiffness on native and postoperative LASIK corneal biomechanical behavior: A whole-eye finite element analysis.* J Refract Surg, 2009. **25**(10): p. 875-887.

30. Kapnisis, K., Doormaal, M. V., and Ross Ethier, C., *Modeling aqueous humor collection from the human eye.* J Biomech, 2009. **42**(15): p. 2454-2457.

31. Uchio, E., Ohno, S., Kudoh, J., Aoki, K., and Kisielewicz, L. T., *Simulation model of an eyeball based on finite element analysis on a supercomputer.* The British journal of ophthalmology, 1999. **83**(10): p. 1106-1111.

32. Karimi, A., Razaghi, R., Navidbakhsh, M., Sera, T., and Kudo, S., *Computing the stresses and deformations of the human eye components due to a high explosive detonation using fluid–structure interaction model.* Injury, 2016. **47**(5): p. 1042-1050.

33. Stitzel, J. D., Duma, S. M., Cormier, J. M., and Herring, I. P., *A nonlinear finite element model of the eye with experimental validation for the prediction of globe rupture.* Stapp Car Crash J, 2002. **46**: p. 81-102.

34. Hans, S. A., Bawab, S. Y., and Woodhouse, M. L., *A finite element infant eye model to investigate retinal forces in shaken baby syndrome.* Graefes Arch Clin Exp Ophthalmol, 2009. **247**(4): p. 561-571.

35. Karimi, A., Razaghi, R., Navidbakhsh, M., Sera, T., and Kudo, S., *Quantifying the injury of the human eye components due to tennis ball impact using a computational fluid–structure interaction model.* Sports Engineering, 2015. **19**(2): p. 105-115.

36. Uchio, E., *Simulation model of an eyeball based on finite element analysis on a supercomputer.* Journal of Opthalmology, 1999. **83**: p. 1106-1111.

37. Scott, J. A., *A finite element model of heat transport in the human eye.* Phys Med Biol, 1988. **33**(2): p. 227-241.

38. Ooi, E.-H., Ang, W.-T., and Ng, E.-Y.-K., *A boundary element model of the human eye undergoing laser thermokeratoplasty.* Computers in Biology and Medicine, 2008. **38**(6): p. 727-737.

39. Elsheikh, A. and Wang, D., *Numerical modelling of corneal biomechanical behaviour.* Comput Methods Biomech Biomed Engin, 2007. **10**(2): p. 85-95.

40. Elsheikh, A., Geraghty, B., Alhasso, D., Knappett, J., Campanelli, M., and Rama, P., *Regional variation in the biomechanical properties of the human sclera.* Experimental Eye Research, 2010. **90**(5): p. 624-633.

41. Elsheikh, A., Alhasso, D., and Rama, P., *Biomechanical properties of human and porcine corneas.* Exp Eye Res, 2008. **86**(5): p. 783-790.

42. Lanchares, E., Calvo, B., Cristóbal, J. A., and Doblaré, M., *Finite element simulation of arcuates for astigmatism correction.* Journal of Biomechanics, 2008. **41**(4): p. 797-805.

43. Wang, Z., Pokki, J., Ergeneman, O., Nelson, B., and Hirai, S., *Viscoelastic interaction between intraocular microrobots and vitreous humor: A finite element approach*. Vol. 2013. 2013. 4937-4940.

44. Schutte, S., Van Den Bedem, S. P., Van Keulen, F., Van Der Helm, F. C., and Simonsz, H. J., *A finite-element analysis model of orbital biomechanics.* Vision Res, 2006. **46**(11): p. 1724-1731.

45. Modarreszadeh, A. and Abouali, O., *Numerical simulation for unsteady motions of the human vitreous humor as a viscoelastic substance in linear and non-linear regimes.* Journal of Non-Newtonian Fluid Mechanics, 2014. **204**: p. 22-31.

46. David, T., Smyed, S., Dabbsd, T., and Teifi, J., *A model for the fluid motion of vitreous humour of the human eye during saccadic movement.* Physics in Medicine & Biology, 1998. **43**(6): p. 1385–1399.

47. Repetto, R., Stocchino, A., and Cafferata, C., *Experimental investigation of vitreous humour motion within a human eye model.* Phys Med Biol, 2005. **50**(19): p. 4729-4743.

48. Kirchhof, B., Oh, K. T., Hartnett, M. E., and Landers, M. B., *Chapter 95 - Pathogenetic Mechanisms of Retinal Detachment*, in *Retina (Fifth Edition)*, S.J. Ryan, S.R. Sadda, D.R. Hinton, A.P. Schachat, S.R. Sadda, C.P. Wilkinson, P. Wiedemann, and A.P. Schachat, Editors. 2013, W.B. Saunders: London. p. 1616-1621.

49. Goldman, D. R., *31.2 - Rhegmatogenous Retinal Detachment*, in *Atlas of Retinal OCT: Optical Coherence Tomography*, D.R. Goldman, N.K. Waheed, and J.S. Duker, Editors. 2018, Elsevier. p. 174-179.

50. Brinton, D. A., Wilkinson, C. P., Hilton, G. F., and American Academy Of, O., *Retinal detachment : principles and practice.* 2009.

51. Ismail, Z., Fitt, A. D., and Please, C. P., *A fluid mechanical explanation of the spontaneous reattachment of a previously detached Descemet membrane.* Math Med Biol, 2013. **30**(4): p. 339-355.

52. Gariano, R. F. and Kim, C. H., *Evaluation and management of suspected retinal detachment.* Am Fam Physician, 2004. **69**(7): p. 1691-1698.

53. Fatt, I. and Shantinath, K., *Flow conductivity of retina and its role in retinal adhesion.* Exp Eye Res, 1971. **12**(2): p. 218-226.

54. Quintyn, J. C. and Brasseur, G., *Subretinal fluid in primary rhegmatogenous retinal detachment: physiopathology and composition.* Surv Ophthalmol, 2004. **49**(1): p. 96-108.

55. Gonzalez, G. and Fitt, A., *The mathematical modelling of human eyes - a PHD study.* 2003. **39**.

56. Sigal, I. A., Flanagan, J. G., Tertinegg, I., and Ethier, C. R., *Finite element modeling of optic nerve head biomechanics.* Invest Ophthalmol Vis Sci, 2004. **45**(12): p. 4378-4387.

57. Esposito, L., Clemente, C., Bonora, N., and Rossi, T., *Modelling human eye under blast loading.* Comput Methods Biomech Biomed Engin, 2015. **18**(2): p. 107-115.

58. Elsheikh, A., Ross, S., Alhasso, D., and Rama, P., *Numerical study of the effect of corneal layered structure on ocular biomechanics.* Curr Eye Res, 2009. **34**(1): p. 26-35.

59. Kling, S. and Hafezi, F., *Corneal biomechanics – a review.* Ophthalmic and Physiological Optics, 2017. **37**(3): p. 240-252.

60. Whitford, C., Joda, A., Jones, S., Bao, F., Rama, P., and Elsheikh, A., *Ex vivo testing of intact eye globes under inflation conditions to determine regional variation of mechanical stiffness.* Eye Vis (Lond), 2016. **3**: p. 21.

61. Sebastian, E., *The Complexity and Origins of the Human Eye: A Brief Study on the Anatomy, Physiology, and Origin of the Eye* 2010, Liberty University

62. Unal, N. and Elcioglu, O., *Anatomy of the eye from the view of Ibn Al-Haitham (965-1039). The founder of modern optics.* Saudi Med J, 2009. **30**(3): p. 323-328.

63. Goezinne, F. *Retinal detachment surgery : pre and postoperative prognostic factors*. 2013.

64. Dubbelman, M., Weeber, H. A., Van Der Heijde, R. G., and Völker-Dieben, H. J., *Radius and asphericity of the posterior corneal surface determined by corrected Scheimpflug photography.* Acta Ophthalmol Scand, 2002. **80**(4): p. 379-383.

65. Jonuscheit, S., Doughty, M. J., and Button, N. F., *On the use of Orbscan II to assess the peripheral corneal thickness in humans: a comparison with ultrasound pachometry measures.* Ophthalmic Physiol Opt, 2007. **27**(2): p. 179-189.

66. Aghaian, E., Choe, J. E., Lin, S., and Stamper, R. L., *Central corneal thickness of Caucasians, Chinese, Hispanics, Filipinos, African Americans, and Japanese in a glaucoma clinic.* Ophthalmology, 2004. **111**(12): p. 2211-2219.

67. Chen, M. J., Liu, Y. T., Tsai, C. C., Chen, Y. C., Chou, C. K., and Lee, S. M., *Relationship between central corneal thickness, refractive error, corneal curvature, anterior chamber depth and axial length.* J Chin Med Assoc, 2009. **72**(3): p. 133-137.

68. Doughty, M. J. and Jonuscheit, S., *An assessment of regional differences in corneal thickness in normal human eyes, using the Orbscan II or ultrasound pachymetry.* Optometry, 2007. **78**(4): p. 181-190.

69. Galgauskas, S., Norvydaitė, D., Krasauskaitė, D., Stech, S., and Ašoklis, R. S., *Age-related changes in corneal thickness and endothelial characteristics.* Clin Interv Aging, 2013. **8**: p. 1445-1450.

70. Summers Rada, J. A., Shelton, S., and Norton, T. T., *The sclera and myopia.* Experimental Eye Research, 2006. **82**(2): p. 185-200.

71. Mcbrien, N. A., Jobling, A. I., and Gentle, A., *Biomechanics of the sclera in myopia: extracellular and cellular factors.* Optom Vis Sci, 2009. **86**(1): p. E23-30.

72. Wolff, E., Bron, A. J., Tripathi, R. C., and Tripathi, B. J., *Wolff's anatomy of the eye and orbit*. 1997, London; Weinheim; Tokyo: Chapman & Hall medical.

73. Norman, R. E., Flanagan, J. G., Rausch, S. M., Sigal, I. A., Tertinegg, I., Eilaghi, A., Portnoy, S., Sled, J. G., and Ethier, C. R., *Dimensions of the human sclera: Thickness measurement and regional changes with axial length.* Exp Eye Res, 2010. **90**(2): p. 277-284.

74. Olsen, T. W., Aaberg, S. Y., Geroski, D. H., and Edelhauser, H. F., *Human sclera: Thickness and surface area.* American Journal of Ophthalmology, 1998. **125**(2): p. 237-241.

75. Michael, R. and Bron, A. J., *The ageing lens and cataract: a model of normal and pathological ageing.* Philosophical transactions of the Royal Society of London. Series B, Biological sciences, 2011. **366**(1568): p. 1278-1292.

76. Davson, H., *PART 4 - THE LENS*, in *The Physiology of the Eye (Third Edition)*, H. Davson, Editor. 1972, Academic Press. p. 86-111.

77. Shiomi, T., Ishio, H., Hori, H., Takada, H., Omori, M., Hasegawa, S., Matsunuma, S., Hasegawa, A., Kanda, T., and Miyao, M., *Simultaneous Measurement of Lens Accommodation and Convergence to Real Objects*. Vol. 6773. 2011. 363-370.

78. Patel, I. and West, S. K., *Presbyopia: prevalence, impact, and interventions.* Community eye health, 2007. **20**(63): p. 40-41.

79. Avtar, R. and Srivastava, R., *Modelling the flow of aqueous humor in anterior chamber of the eye.* Applied Mathematics and Computation, 2006. **181**(2): p. 1336-1348.

80. Moses, R. A. and Hart, W. M., *Adler's Physiology of the Eye*. 1987: Mosby (Periodicals).

81. Sebag, J., *Ageing of the vitreous.* Eye (Lond), 1987. **1 (Pt 2)**: p. 254-262.

82. Jacobson, B., Dorfman, T., and Basu, P. K., *Inhibition of Vascular Endothelial Cell Growth and Trypsin Activity by Vitreous* Eye (Lond), 1985. **41**: p. 581 - 595.

83. Foulds, W. S., *Is Your Vitreous Really Necessary? The role of the vitreous in the eye with particular reference to retinal attachment, detachment and the mode of action of vitreous substitutes.* Eye (Lond), 1987. **1**: p. 641-664.

84. J., S., *The Vitreous - Structure, Function, and Pathobiology*, ed. Verlag. 1989, New York: Springer.

85. Bishop, P., *Structural macromolecules and supramolecular organisation of the vitreous gel.* Progress in Retinal and Eye Research, 2000. **19**(3): p. 323-344.

86. Veckeneer, M., Van Overdam, K., Bouwens, D., Feron, E., Mertens, D., Peperkamp, E., Ringens, P., Mulder, P., and Van Meurs, J., *Randomized clinical trial of cryotherapy versus laser photocoagulation for retinopexy in conventional retinal detachment surgery.* Am J Ophthalmol, 2001. **132**(3): p. 343-347.

87. Lincoff, H., Stopa, M., Kreissig, I., Madjarov, B., Sarup, V., Saxena, S., and Brodie, S., *Cutting the encircling band.* Retina, 2006. **26**(6): p. 650-654.

88. Rauscher, F. M., Gedde, S. J., Schiffman, J. C., Feuer, W. J., Barton, K., and Lee, R. K., *Motility disturbances in the tube versus trabeculectomy study during the first year of follow-up.* Am J Ophthalmol, 2009. **147**(3): p. 458-466.

89. Sharif-Kashani, P., Hubschman, J. P., Sassoon, D., and Kavehpour, H. P., *Rheology of the vitreous gel: effects of macromolecule organization on the viscoelastic properties.* J Biomech, 2011. **44**(3): p. 419-423.

90. Devenyi, R. G. and De Carvalho Nakamura, H., *Combined scleral buckle and pars plana vitrectomy as a primary procedure for pseudophakic retinal detachments.* Ophthalmic Surg Lasers, 1999. **30**(8): p. 615-618.

91. Yoon, S., Aglyamov, S., Karpiouk, A., and Emelianov, S., *Spatial Variations of Viscoelastic Properties of Porcine Vitreous Humors.* Correspondence, 2013. **60**(11): p. 2453-2460.

92. Bettelheim, F. A. and Wang, T. J. Y., *Dynamic Viscoelastic Properties of Bovine Vitreous.* Exl: Eye Res, 1976. **23**: p. 435-441.

93. Zimmerman, R. L., *In vivo measurements of the viscoelasticity of the human vitreous humor.* BIOPHYS. J., 1980. **29**: p. 539-544.

94. Swann, D. A. and Constable, I. J., *Vitreous structure. I. Distribution of hyaluronate and protein.* Invest Ophthalmol, 1972. **11**(3): p. 159-163.

95. Balazs, E. A., Laurent, T. C., Laurent, U. B. G., Deroche, M. H., and Bunney, D. M., *Studies on the structure of the vitreous body: VIII. Comparative biochemistry.* Archives of Biochemistry and Biophysics, 1959. **81**(2): p. 464-479.

96. Bishop, P. N., Takanosu, M., Le Goff, M., and Mayne, R., *The role of the posterior ciliary body in the biosynthesis of vitreous humour.* Eye (Lond), 2002. **16**(4): p. 454-460.

97. Kuhn, F. and Aylward, B., *Rhegmatogenous retinal detachment: a reappraisal of its pathophysiology and treatment.* Ophthalmic Res, 2014. **51**(1): p. 15-31.

98. Sebag, J., *Anomalous posterior vitreous detachment: a unifying concept in vitreo-retinal disease.* Graefes Arch Clin Exp Ophthalmol, 2004. **242**(8): p. 690-698.

99. Vroon, J., *Finite Element modeling of retinal detachment*, in *School of Engineering*. 2017, Delft University of Technology: Delft University of Technology.

100. Denlinger, J. L., Eisner, G., and Balazs, E. A., *Age-related changes in the vitreus and lens of rhesus monkeys (Macaca mulatta).* Exp Eye Res, 1980. **31**(1): p. 67-79.

101. Los, L. I., *The rabbit as an animal model for post-natal vitreous matrix differentiation and degeneration.* Eye (Lond), 2008. **22**(10): p. 1223-1232.

102. Sebag, J., *Age-related changes in human vitreous structure.* Graefe's Archive for Clinical and Experimental Ophthalmology, 1987. **225**(2): p. 89-93.

103. Byer, N. E., *Natural history of posterior vitreous detachment with early management as the premier line of defense against retinal detachment.* Ophthalmology, 1994. **101**(9): p. 1503-1513; discussion 1513-1504.

104. Los, L. I., Van Der Worp, R. J., Van Luyn, M. J., and Hooymans, J. M., *Age-related liquefaction of the human vitreous body: LM and TEM evaluation of the role of proteoglycans and collagen.* Invest Ophthalmol Vis Sci, 2003. **44**(7): p. 2828-2833.

105. Sebag, J., *Anatomy and pathology of the vitreo-retinal interface.* Eye (Lond), 1992. **6 (Pt 6)**: p. 541-552.

106. Mojana, F., Cheng, L., Bartsch, D. U., Silva, G. A., Kozak, I., Nigam, N., and Freeman, W. R., *The role of abnormal vitreomacular adhesion in age-related macular degeneration: spectral optical coherence tomography and surgical results.* Am J Ophthalmol, 2008. **146**(2): p. 218-227.

107. Wilmarth, P. A., Tanner, S., Dasari, S., Nagalla, S. R., Riviere, M. A., Bafna, V., Pevzner, P. A., and David, L. L., *Age-related changes in human crystallins determined from comparative analysis of post-translational modifications in young and aged lens: does deamidation contribute to crystallin insolubility?* J Proteome Res, 2006. **5**(10): p. 2554-2566.

108. Machemer, R., *The development of pars plana vitrectomy: a personal account.* Graefes Arch Clin Exp Ophthalmol, 1995. **233**(8): p. 453-468.

109. Recchia, F. M., Ruby, A. J., and Carvalho Recchia, C. A., *Pars plana vitrectomy with removal of the internal limiting membrane in the treatment of persistent diabetic macular edema.* Am J Ophthalmol, 2005. **139**(3): p. 447-454.

110. Kathawate, J. and Acharya, S., *Computational modeling of intravitreal drug delivery in the vitreous chamber with different vitreous substitutes.* International Journal of Heat and Mass Transfer, 2008. **51**(23): p. 5598-5609.

111. Maurice, D., *Review: practical issues in intravitreal drug delivery.* J Ocul Pharmacol Ther, 2001. **17**(4): p. 393-401.

112. Pokki, J., Ergeneman, O., Sevim, S., Enzmann, V., Torun, H., and Nelson, B. J., *Measuring localized viscoelasticity of the vitreous body using intraocular microprobes.* Biomed Microdevices, 2015. **17**(5): p. 85.

113. Stein, J., Zacks, D., Grossman, D., Grabe, H., Johnson, M., and Sloan, F., *Adverse Events After Pars Plana Vitrectomy Among Medicare Beneficiaries.* Arch Ophthalmol, 2009. **127**(12): p. 1656–1663.

114. Ryan, E. H., Jr and Mittra, R. A., *Scleral Buckling vs Vitrectomy: The Continued Role for Scleral Buckling in the Vitrectomy Era.* Archives of Ophthalmology, 2010. **128**(9): p. 1202-1205.

115. Nickerson, C. S., Park, J., Kornfield, J. A., and Karageozian, H., *Rheological properties of the vitreous and the role of hyaluronic acid.* J Biomech, 2008. **41**(9): p. 1840-1846.

116. Lee, B., Litt, M., and Buchsbaum, G., *Rheology of the vitreous body: Part 2. Viscoelasticity of bovine and porcine vitreous.* Biorheology, 1994. **31**(4): p. 327-338.

117. Aguayo, J., Glaser, B., Mildvan, A., Cheng, H. M., Gonzalez, R. G., and Brady, T., *Study of vitreous liquifaction by NMR spectroscopy and imaging.* Invest Ophthalmol Vis Sci, 1985. **26**(5): p. 692-697.

118. Delori, F., Pomerantzeff, O., and Cox, M. S., *Deformation of the globe under high-speed impact: it relation to contusion injuries.* Invest Ophthalmol, 1969. **8**(3): p. 290-301.

119. Koplin, R., Ritterband, D., Schorr, E., Seedor, J., and Wu, E., *The Scrub's Bible, How to Assist at Cataract and Corneal Surgery with a Primer on the Anatomy of the Human Eye and Self Assessment.* 2020.

120. Chen, K., Rowley, A. P., Weiland, J. D., and Humayun, M. S., *Elastic properties of human posterior eye.* J Biomed Mater Res A, 2014. **102**(6): p. 2001-2007.

121. Williamson, T., *Vitreoretinal surgery, second edition*. 2013. 1-429.

122. Bruce, K. and Bruce, S., *Berne & Levy Physiology*. 2017: Elsevier 2018.

123. Colucciello, M., *Rhegmatogenous Retinal Detachment.* The Physician and Sportsmedicine, 2009. **37**(2): p. 59-65.

124. Schepens, C. L. and Marden, D., *Data on the natural history of retinal detachment. Further characterization of certain unilateral nontraumatic cases.* Am J Ophthalmol, 1966. **61**(2): p. 213-226.

125. Sodhi, A., Leung, L. S., Do, D. V., Gower, E. W., Schein, O. D., and Handa, J. T., *Recent trends in the management of rhegmatogenous retinal detachment.* Surv Ophthalmol, 2008. **53**(1): p. 50-67.

126. Wilkinson, C. P. and Bhavsar, A. R., *1 - Scleral buckling surgery*, in *Retina and Vitreous Surgery*, A.R. Bhavsar, Editor. 2009, W.B. Saunders: Edinburgh. p. 1-14.

127. Johnson, L. V., Hageman, G. S., and Blanks, J. C., *Interphotoreceptor matrix domains ensheath vertebrate cone photoreceptor cells.* Invest Ophthalmol Vis Sci, 1986. **27**(2): p. 129-135.

128. Marmor, M. F., Yao, X. Y., and Hageman, G. S., *Retinal adhesiveness in surgically enucleated human eyes.* Retina, 1994. **14**(2): p. 181-186.

129. Yao, X. Y., Hageman, G. S., and Marmor, M. F., *Retinal adhesiveness is weakened by enzymatic modification of the interphotoreceptor matrix in vivo.* Invest Ophthalmol Vis Sci, 1990. **31**(10): p. 2051-2058.

130. Kim, R. Y., Yao, X. Y., and Marmor, M. F., *Oxygen dependency of retinal adhesion.* Invest Ophthalmol Vis Sci, 1993. **34**(6): p. 2074-2078.

131. Marmor, M. F. and Negi, A., *Pharmacologic modification of subretinal fluid absorption in the rabbit eye.* Arch Ophthalmol, 1986. **104**(11): p. 1674-1677.

132. Kita, M., Negi, A., Kawano, S., Honda, Y., and Maegawa, S., *Measurement of retinal adhesive force in the in vivo rabbit eye.* Invest Ophthalmol Vis Sci, 1990. **31**(4): p. 624-628.

133. Kita, M. and Marmor, M. F., *Retinal adhesive force in living rabbit, cat, and monkey eyes. Normative data and enhancement by mannitol and acetazolamide.* Invest Ophthalmol Vis Sci, 1992. **33**(6): p. 1879-1882.

134. Marmor, M. F., Abdul-Rahim, A. S., and Cohen, D. S., *The effect of metabolic inhibitors on retinal adhesion and subretinal fluid resorption.* Investigative Ophthalmology & Visual Science, 1980. **19**(8): p. 893-903.

135. Deguillebon, H., De La Tribonniere, M., and Pomerantzeff, O., *Adhesion between retina and pigment epithelium. Measurement by peeling.* Arch Ophthalmol, 1971. **86**(6): p. 679-684.

136. Regillo, C. D., Sergott, R. C., and Brown, G. C., *Successful scleral buckling procedures decrease central retinal artery blood flow velocity.* Ophthalmology, 1993. **100**(7): p. 1044-1049.

137. Singh, D. V., Sharma, Y. R., and Pal, N., *Scleral Buckling versus Primary Vitrectomy.* Ophthalmology, 2006. **113**(7): p. 1246-1247.

138. Tewari, H. K., Kedar, S., Kumar, A., Garg, S. P., and Verma, L. K., *Comparison of scleral buckling with combined scleral buckling and pars plana vitrectomy in the management of rhegmatogenous retinal detachment with unseen retinal breaks.* Clin Exp Ophthalmol, 2003. **31**(5): p. 403-407.

139. Hedaya, J., Nigam, N., and Freeman, W. R., *Scleral Buckling versus Vitrectomy.* Ophthalmology, 2008. **115**(9): p. 1634-1635; author reply 1635.

140. Heimann, H., Bartz-Schmidt, K. U., Bornfeld, N., Weiss, C., Hilgers, R. D., and Foerster, M. H., *Scleral buckling versus primary vitrectomy in rhegmatogenous retinal detachment: a prospective randomized multicenter clinical study.* Ophthalmology, 2007. **114**(12): p. 2142-2154.

141. Mcauliffe, P. F. and Heinemann, M. H., *The use of pneumatic retinopexy to delay surgical repair of a retinal detachment associated with the ganciclovir intraocular device.* Ophthalmic Surg Lasers, 1998. **29**(3): p. 244-246.

142. Böhm, P. and Záhorcová, M., *[Pneumatic retinopexy--method of choice in treatment of retinal detachment].* Cesk Slov Oftalmol, 2003. **59**(3): p. 154-159.

143. Pavlović, S., Latinović, S., and Tomić, Z., *[Treatment of retinal detachment using pneumatic retinopexy].* Med Pregl, 1992. **45**(11-12): p. 395-397.

144. Ando, F., Hirose, H., Nagasaka, T., Takahashi, K., and Sekiryu, T., *Treatment of retinal detachment with giant tear by pneumatic retinopexy.* Eur J Ophthalmol, 1993. **3**(4): p. 201-206.

145. Sharma, T., Badrinath, S. S., Mukesh, B. N., Gopal, L., Shanmugam, M. P., Bhende, P., Bhende, M., Shetty, N. S., and Agrawal, R., *A multivariate analysis of anatomic success of recurrent retinal detachment treated with pneumatic retinopexy.* Ophthalmology, 1997. **104**(12): p. 2014-2017.

146. Van Meurs, J. C., Feron, E., Van Ruyven, R., Mulder, P., and Veckeneer, M., *Postoperative laser coagulation as retinopexy in patients with rhegmatogenous retinal detachment treated with scleral buckling surgery: a prospective clinical study.* Retina, 2002. **22**(6): p. 733-739.

147. Friberg, T. R. and Eller, A. W., *Laser pneumatic retinopexy for repair of recurrent retinal detachment after failed scleral buckle--ten years experience.* Ophthalmic Surg Lasers, 2001. **32**(1): p. 13-18.

148. Clemens, S., *[Scleral buckling surgery and pneumatic retinopexy].* Ophthalmologe, 2008. **105**(5): p. 499.

149. Peyman, G. A. and Schulman, J., *Proliferative vitreoretinopathy and chemotherapeutic agents.* Surv Ophthalmol, 1985. **29**(6): p. 434-442.

150. Machemer, R., Buettner, H., and Parel, J. M., *Vitrectomy, a pars plana approach. Instrumentation.* Mod Probl Ophthalmol, 1972. **10**: p. 172-177.

151. Vander, J. F., Eagle, R. C., Jr., Brown, G. C., Arbizo, V., Shakin, E. P., and Reber, R., *Retinal tolerance of an implantable light source for use during vitrectomy surgery.* Ophthalmic Surg, 1991. **22**(12): p. 735-739.

152. Chen, K. and Weiland, J. D., *Anisotropic and inhomogeneous mechanical characteristics of the retina.* J Biomech, 2010. **43**(7): p. 1417-1421.

153. Vroon, J., De Jong, J. H., Aboulatta, A., Eliasy, A., Van Der Helm, F. C. T., Van Meurs, J. C., Wong, D., and Elsheikh, A., *Numerical study of the effect of head and eye movement on progression of retinal detachment.* Biomech Model Mechanobiol, 2018. **17**(4): p. 975-983.

154. Ogden, R. W., *Large deformation isotropic elasticity: on the correlation of theory and experiment for compressible rubberlike solids.* Royal Society, 1972. **328**(1575).

155. Qian, X., Zhang, K., and Liu, Z., *A method to determine the mechanical properties of the retina based on an experiment in vivo.* Biomed Mater Eng, 2015. **26 Suppl 1**: p. S287-297.

156. Kolb, H., Fernandez, E., and Nelson, R., *Webvision: The Organization of the Retina and Visual System*, in *Webvision: The Organization of the Retina and Visual System*, H. Kolb, E. Fernandez, and R. Nelson, Editors. 1995, University of Utah Health Sciences Center: Salt Lake City (UT).

157. Anderson, K., El-Sheikh, A., and Newson, T., *Application of structural analysis to the mechanical behaviour of the cornea.* J R Soc Interface, 2004. **1**(1): p. 3-15.

158. Gefen, A., Shalom, R., Elad, D., and Mandel, Y., *Biomechanical analysis of the keratoconic cornea.* J Mech Behav Biomed Mater, 2009. **2**(3): p. 224-236.

159. Salimi, S., Park, S. S., and Freiheit, T., *Dynamic response of intraocular pressure and biomechanical effects of the eye considering fluid-structure interaction.* J Biomech Eng, 2011. **133**(9): p. 091009.

160. Nejad, T. M., Foster, C., and Gongal, D., *Finite element modelling of cornea mechanics: a review.* Arq Bras Oftalmol, 2014. **77**(1): p. 60-65.

161. Whitford, C., Studer, H., Boote, C., Meek, K. M., and Elsheikh, A., *Biomechanical model of the human cornea: considering shear stiffness and regional variation of collagen anisotropy and density.* J Mech Behav Biomed Mater, 2015. **42**: p. 76-87.

162. Chagnon, G., Ohayon, J., Martiel, J.-L., and Favier, D., *Chapter 1 - Hyperelasticity Modeling for Incompressible Passive Biological Tissues*, in *Biomechanics of Living Organs*, Y. Payan and J. Ohayon, Editors. 2017, Academic Press: Oxford. p. 3-30.

163. Yu, J. G., Bao, F. J., Feng, Y. F., Whitford, C., Ye, T., Huang, Y. B., Wang, Q. M., and Elsheikh, A., *Assessment of corneal biomechanical behavior under posterior and anterior pressure.* J Refract Surg, 2013. **29**(1): p. 64-70.

164. Moran, R., Smith, J. H., and Garcia, J. J., *Fitted hyperelastic parameters for Human brain tissue from reported tension, compression, and shear tests.* J Biomech, 2014. **47**(15): p. 3762-3766.

165. Groves, R. B., Coulman, S. A., Birchall, J. C., and Evans, S. L., *Quantifying the mechanical properties of human skin to optimise future microneedle device design.* Comput Methods Biomech Biomed Engin, 2012. **15**(1): p. 73-82.

166. Grupcheva, C. N., Malik, T. Y., Craig, J. P., and Mcghee, C. N., *In vivo confocal microscopy of corneal epithelial ingrowth through a laser in situ*

keratomileusis flap buttonhole. J Cataract Refract Surg, 2001. **27**(8): p. 1318-1322.

167. Dhaliwal, D. K., Romanowski, E. G., Yates, K. A., Hu, D., Mah, F. S., Fish, D. N., and Gordon, Y. J., *Valacyclovir inhibition of recovery of ocular herpes simplex virus type 1 after experimental reactivation by laser in situ keratomileusis.* J Cataract Refract Surg, 2001. **27**(8): p. 1288-1293.

168. Bao, F., Deng, M., Zheng, X., Li, L., Zhao, Y., Cao, S., Yu, A. Y., Wang, Q., Huang, J., and Elsheikh, A., *Effects of diabetes mellitus on biomechanical properties of the rabbit cornea.* Exp Eye Res, 2017. **161**: p. 82-88.

169. Schulz, A., Wahl, S., Rickmann, A., Ludwig, J., Stanzel, B. V., Von Briesen, H., and Szurman, P., *Age-Related Loss of Human Vitreal Viscoelasticity.* Transl Vis Sci Technol, 2019. **8**(3): p. 56.

170. Shafaie, S., Hutter, V., Brown, M. B., Cook, M. T., and Chau, D. Y. S., *Diffusion through the ex vivo vitreal body - Bovine, porcine, and ovine models are poor surrogates for the human vitreous.* Int J Pharm, 2018. **550**(1-2): p. 207-215.

171. Filas, B. A., Zhang, Q., Okamoto, R. J., Shui, Y. B., and Beebe, D. C., *Enzymatic degradation identifies components responsible for the structural properties of the vitreous body.* Invest Ophthalmol Vis Sci, 2014. **55**(1): p. 55-63.

172. Colter, J., Williams, A., Moran, P., and Coats, B., *Age-related changes in dynamic moduli of ovine vitreous.* J Mech Behav Biomed Mater, 2015. **41**: p. 315-324.

173. Tokita, M., Fujiya, Y., and Hikichi, K., *Dynamic viscoelasticity of bovine vitreous body.* Biorheology, 1984. **21**(6): p. 751-756.

174. Huang, D., Chen, Y. S., Xu, Q., Hanes, J., and Rupenthal, I. D., *Effects of enzymatic degradation on dynamic mechanical properties of the vitreous and intravitreal nanoparticle mobility.* Eur J Pharm Sci, 2018. **118**: p. 124-133.

175. Silva, A. F., Alves, M. A., and Oliveira, M. S. N., *Rheological behaviour of vitreous humour.* Rheologica Acta, 2017. **56**(4): p. 377-386.

176. Lee, B., Litt, M., and Buchsbaum, G., *Rheology of the vitreous body. Part I: Viscoelasticity of human vitreous.* Biorheology, 1992. **29**(5-6): p. 521-533.

177. Tram, N. K. and Swindle-Reilly, K. E., *Rheological Properties and Age-Related Changes of the Human Vitreous Humor.* Front Bioeng Biotechnol, 2018. **6**: p. 199.

178. Zhang, W. and Xu, Y., *2 - Constitutive Models of Polycarbonate*, in *Mechanical Properties of Polycarbonate*, W. Zhang and Y. Xu, Editors. 2019, Elsevier. p. 29-77.

179. Hu, Z., Zhang, J., Zhang, Z., Chen, J., and You, Y., *A consolidation model for estimating the settlement of warm permafrost.* Computers and Geotechnics, 2016. **76**: p. 43-50.

180. Schweizer, T., *Rheology. Concepts, Methods, and Applications.* Applied Rheology, 2006. **16**: p. 240-241.

181. Guedes, R. M., *Creep and Fatigue in Polymer Matrix Composites*, in *Creep and Fatigue in Polymer Matrix Composites (Second Edition)*, R.M. Guedes, Editor. 2019, Woodhead Publishing. p. xiii-xiv.

182. Epaarachchi, J. A., *17 - The effect of viscoelasticity on fatigue behaviour of polymer matrix composites*, in *Creep and Fatigue in Polymer Matrix Composites*, R.M. Guedes, Editor. 2011, Woodhead Publishing. p. 492-513.

183. Kumar, B., *Appendix: Laplace Transformations*, in *Science of Compression Bandages*, B. Kumar, A. Das, and R. Alagirusamy, Editors. 2014, Woodhead Publishing India. p. 157.

184. Chae, S.-H., Zhao, J.-H., Edwards, D. R., and Ho, P. S., *Characterization of the Viscoelasticity of Molding Compounds in the Time Domain.* Journal of Electronic Materials, 2010. **39**(4): p. 419-425.

185. Chae, S.-H., Zhao, J.-H., Edwards, D., and Ho, P., *Characterization of the Viscoelasticity of Molding Compounds in the Time Domain.* Journal of Electronic Materials, 2010. **39**: p. 419-425.

186. Abaqus, *ABAQUS 6.14-2 Documentation.* 2016.

187. Graczykowski, C., *Adaptive Inflatable Structures for protecting wind turbines against ship collisions*, in *Institute of Fundamental Technological Research*. 2006, Institute of Fundamental Technological Research: Poland.

188. Bussone, G., Diener, H.-C., Pfeil, J., and Schwalen, S., *Topiramate 100 mg/day in migraine prevention: a pooled analysis of double-blind randomised controlled trials.* International Journal of Clinical Practice, 2005. **59**(8): p. 961-968.

189. Kavanagh, J. J., Barrett, R. S., and Morrison, S., *Upper body accelerations during walking in healthy young and elderly men.* Gait Posture, 2004. **20**(3): p. 291-298.

190. Woodman, P. D. and Griffin, M. J., *Six axes of head acceleration during ambulation.* Proceedings of Internoise, 1996. **96**: p. 1719-1724.

191. Allen, M. E., Weir-Jones, I., Motiuk, D. R., Flewin, K. R., Goring, R. D., Kobetitch, R., and Broadhurst, A., *Acceleration perturbations of daily living. A comparison to 'whiplash'.* Spine (Phila Pa 1976), 1994. **19**(11): p. 1285-1290.

192. Arndt, S. R., Cargill, R. S., and Hammoud, P. E. S., *Head Accelerations Experienced during Everyday Activities and While Riding Roller Coasters.* Proceedings of the Human Factors and Ergonomics Society Annual Meeting, 2004. **48**(16): p. 1973-1977.

193. Lamansky, S., *Bestimmung der Winkelgeschwindigkeit der Blickbewegung, respective Augenbewegung.* Archiv für die gesamte Physiologie des Menschen und der Tiere, 1869. **2**(1): p. 418-422.

194. Yarbus, A. Y., *Eye movements and vision*. 1967, New York: Plenum Press.

195. Lancaster, W., *Fifty Years' Experience in Ocular Motility.* Am J Ophthal, 1941. **24**: p. 741-748.

196. Bahill, A. T., Adler, D., and Stark, L., *Most naturally occurring human saccades have magnitudes of 15 degrees or less.* Investigative Ophthalmology & Visual Science, 1975. **14**(6): p. 468-469.

197. Angunawela, R. I., Azarbadegan, A., Aylward, G. W., and Eames, I., *Intraocular fluid dynamics and retinal shear stress after vitrectomy and gas tamponade.* Invest Ophthalmol Vis Sci, 2011. **52**(10): p. 7046-7051.

198. Di Michele, F., Tatone, A., Romano, M. R., and Repetto, R., *A mechanical model of posterior vitreous detachment and generation of vitreoretinal tractions.* Biomech Model Mechanobiol, 2020. **19**(6): p. 2627-2641.

199. Bayat, J., Emdad, H., and Abouali, O., *Numerical simulation of the fluid dynamics in a 3D spherical model of partially liquefied vitreous due to eye*

movements under planar interface conditions. Applied and Computational Mechanics, 2019. **50**: p. 387-394.

200. Abyaneh, M. H., Wildman, R. D., Ashcroft, I. A., and Ruiz, P. D., *A hybrid approach to determining cornea mechanical properties in vivo using a combination of nano-indentation and inverse finite element analysis.* Journal of the Mechanical Behavior of Biomedical Materials, 2013. **27**: p. 239-248.

201. Girard, M. J., Suh, J. K., Bottlang, M., Burgoyne, C. F., and Downs, J. C., *Scleral biomechanics in the aging monkey eye.* Invest Ophthalmol Vis Sci, 2009. **50**(11): p. 5226-5237.

202. Nguyen, T. D. and Boyce, B. L., *An inverse finite element method for determining the anisotropic properties of the cornea.* Biomech Model Mechanobiol, 2011. **10**(3): p. 323-337.

203. Zhang, K., Qian, X., Mei, X., and Liu, Z., *An inverse method to determine the mechanical properties of the iris in vivo.* BioMedical Engineering OnLine, 2014. **13**(1): p. 66.

204. Perez, B. C., Morris, H. J., Hart, R. T., and Liu, J., *Finite element modeling of the viscoelastic responses of the eye during microvolumetric changes.* J Biomed Sci Eng, 2013. **6**(12a): p. 29-37.

205. Eberhart, R. and Kennedy, J. *A new optimizer using particle swarm theory*. in *MHS'95. Proceedings of the Sixth International Symposium on Micro Machine and Human Science*. 1995.

206. Liu, X., Liu, H., and Duan, H., *Particle swarm optimization based on dynamic niche technology with applications to conceptual design.* Advances in Engineering Software, 2007. **38**(10): p. 668-676.

207. Janson, S., Merkle, D., and Middendorf, M., *Molecular docking with multi-objective Particle Swarm Optimization.* Applied Soft Computing, 2008. **8**(1): p. 666-675.

208. Lian, Z., Gu, X., and Jiao, B., *A novel particle swarm optimization algorithm for permutation flow-shop scheduling to minimize makespan.* Chaos, Solitons & Fractals, 2008. **35**(5): p. 851-861.

209. Thakker, R. A., Patil, M. B., and Anil, K. G., *Parameter extraction for PSP MOSFET model using hierarchical particle swarm optimization.* Engineering Applications of Artificial Intelligence, 2009. **22**(2): p. 317-328.

210. Mthembu, L., Marwala, T., Friswell, M. I., and Adhikari, S. *Finite element model selection using Particle Swarm Optimization*. in *Dynamics of Civil Structures, Volume 4*. 2011. New York, NY: Springer New York.

211. Chen, J., Tang, Y., Ge, R., An, Q., and Guo, X., *Reliability design optimization of composite structures based on PSO together with FEA.* Chinese Journal of Aeronautics, 2013. **26**(2): p. 343-349.

212. Tang, Y., Chen, J., and Peng, W., *Probabilistic Optimization of Laminated Composites Considering Both Ply Failure and Delamination Based on PSO and FEM.* Tsinghua Science & Technology, 2009. **14**: p. 89-93.

213. Elias De Oliveira, M., Hasler, C.-C., Zheng, G., Studer, D., Schneider, J., and Büchler, P., *A multi-criteria decision support for optimal instrumentation in scoliosis spine surgery.* Structural and Multidisciplinary Optimization, 2012. **45**(6): p. 917-929.

214. Mathworks, *Global optimization toolbox: User's guide (r2017a).* 2017.

215. Wang, H., Wu, Z., Rahnamayan, S., Li, C., Zeng, S., and Jiang, D., *Particle swarm optimisation with simple and efficient neighbourhood search strategies.* International Journal of Innovative Computing and Applications, 2011. **3**: p. 97-104.

216. Schmitt, M. and Wanka, R., *Particle Swarm Optimization Almost Surely Finds Local Optima*. 2013.

217. Sun, W. and Chang, X., *An Improved Harmony Search Algorithm for Power Distribution Network Planning.* Journal of Electrical and Computer Engineering, 2015. **2015**: p. 753712.

218. Rocha, M. and Neves, J., *Preventing Premature Convergence to Local Optima in Genetic Algorithms via Random Offspring Generation*. 1999. 127-136.

219. Khatibi Bardsiri, V., Jawawi, D. N. A., Hashim, S. Z. M., and Khatibi, E., *A PSO-based model to increase the accuracy of software development effort estimation.* Software Quality Journal, 2013. **21**(3): p. 501-526.

220. Salehizadeh, S. M. A., Yadmellat, P., and Menhaj, M. B. *Local Optima Avoidable Particle Swarm Optimization*. in *2009 IEEE Swarm Intelligence Symposium*. 2009.

221. Parsopoulos, K. and Vrahatis, M., *Particle swarm optimizer in noisy and continuously changing environments*. 2001. p. 289-294.

222. Hassan, R., Cohanim, B., and De Weck, O., *A Comparison of Particle Swarm Optimization and the Genetic Algorithm*. Vol. 2. 2005.

223. Schutte, J. F., Koh, B. I., Reinbolt, J. A., Haftka, R. T., George, A. D., and Fregly, B. J., *Evaluation of a particle swarm algorithm for biomechanical optimization.* J Biomech Eng, 2005. **127**(3): p. 465-474.

224. Magalhães, R., Elsheikh, A., Büchler, P., Whitford, C., and Wang, J., *Application of particle swarm optimization in inverse finite element modeling to determine the cornea´s mechanical behavior.* Acta Scientiarum - Technology, 2017. **39**: p. 325-331.

225. Sebag, J., *The vitreous: structure, function and pathobiology.* Springer, 1989.

226. Aboulatta, A., Abass, A., Makarem, A., Eliasy, A., Zhou, D., Chen, D., Liu, X., and Elsheikh, A., *Experimental evaluation of the viscoelasticity of porcine vitreous.* Journal of The Royal Society Interface, 2021. **18**(175): p. 20200849.

227. Sodhi, A., *DIAGNOSTIC AND SURGICAL TECHNIQUES.* SURVEY OF OPHTHALMOLOGY, 2008. **53**(1): p. 50-67.

228. Lincoff, K. a. U., *Minor surgery for the repair of retinal detachment emanating from retinoschisis.* Ophthalmologica, 2009. **3**(87): p. 281–284.

229. *Density of ocular components of the bovine eye.* Optometry and vision science : official publication of the American Academy of Optometry, 2009. **10**(86): p. 1187–1195.

230. Repetto, R., *A model for the fluid motion of vitreous humour of the human eye during saccadic movement.* Phys. Med. Biol., 1998. **43**: p. 1385-1399.

231. Modarreszadeh, A., *Nu- merical simulation for unsteady motions of the human vitreous humor as a viscoelastic substance in linear and non-linear regimes.* Journal of Non-Newtonian Fluid Mechanics, 2014. **204**: p. 22-31.

232. Zhou, D., Abass, A., Eliasy, A., Studer, H. P., Movchan, A., Movchan, N., and Elsheikh, A., *Microstructure-based numerical simulation of the mechanical behaviour of ocular tissue.* Journal of The Royal Society Interface, 2019. **16**(154): p. 20180685.

233. Piñero, D. P., Plaza Puche, A. B., and Alió, J. L., *Corneal diameter measurements by corneal topography and angle-to-angle measurements by optical coherence tomography: Evaluation of equivalence.* Journal of Cataract & Refractive Surgery, 2008. **34**(1).

234. Hashemi, H., Khabazkhoob, M., Emamian, M. H., Shariati, M., Yekta, A., and Fotouhi, A., *White-to-white corneal diameter distribution in an adult population.* Journal of Current Ophthalmology, 2015. **27**(1): p. 21-24.

235. Nooshin, H., *Space structures and configuration processing.* Progress in Structural Engineering and Materials, 1998. **1**(3): p. 329-336.

236. Chen, K., Rowley, A. P., Weiland, J. D., and Humayun, M. S., *Elastic properties of human posterior eye.* Journal of Biomedical Materials Research Part A, 2014. **102**(6): p. 2001-2007.

237. Power, E. D., Stitzel, J. D., Duma, S. M., Herring, I. P., and West, R. L., *Investigation of Ocular Injuries from High Velocity Objects in an Automobile Collision.* SAE Transactions, 2002. **111**: p. 211-218.

238. Parsons, S., Boonman, A. M., and Obrist, M. K., *Advantages and Disadvantages of Techniques for Transforming and Analyzing Chiropteran Echolocation Calls.* Journal of Mammalogy, 2000. **81**(4): p. 927-938.

239. Bonte, M. H. A., De Boer, A., and Liebregts, R., *Determining the von Mises stress power spectral density for frequency domain fatigue analysis including out-of-phase stress components.* Journal of Sound and Vibration, 2007. **302**(1): p. 379-386.

240. Walton, K. A., Meyer, C. H., Harkrider, C. J., Cox, T. A., and Toth, C. A., *Age-Related Changes in Vitreous Mobility as Measured by Video B Scan Ultrasound.* Experimental Eye Research, 2002. **74**(2): p. 173-180.

241. De Jong, J. H., Vigueras-Guillén, J. P., Simon, T. C., Timman, R., Peto, T., Vermeer, K. A., and Van Meurs, J. C., *Preoperative Posturing of Patients with Macula-On Retinal Detachment Reduces Progression Toward the Fovea.* Ophthalmology, 2017. **124**(10): p. 1510-1522.

242. Purves D, A. G., Fitzpatrick D, Et Al., *Anatomy of the Eye*. Neuroscience. Vol. 2nd edition. 2001, Sunderland Sinauer Associates.

243. Romano, M. R., Comune, C., Ferrara, M., Cennamo, G., De Cilla, S., Toto, L., and Cennamo, G., *Retinal Changes Induced by Epiretinal Tangential Forces.* J Ophthalmol, 2015. **2015**: p. 372564.

244. James, A., Bert Glaser, A. M., Cheng, H.-M., Gonzalez, R. G., and Brady, T., *Study of Vitreous Liquifaction by NMR Spectroscopy and Imaging.* Invest Ophthalmol Vis Sci, 1985. **26**: p. 692-697.

245. Fisher, L. K., Wang, X., Tun, T. A., Chung, H.-W., Milea, D., and Girard, M. J. A., *Gaze-evoked deformations of the optic nerve head in thyroid eye disease.* bioRxiv, 2020: p. 2020.2003.2019.999706.

246. Karami, A. and Eghtesad, M., *Simulation of Active Eye Motion Using Finite Element Modelling.* Latin American Journal of Solids and Structures, 2018. **15**.

247. Shrader, S. M. and Greentree, W. F., *Gottingen Minipigs in Ocular Research.* Toxicol Pathol, 2018. **46**(4): p. 403-407.

248. Bayless, K. J., Kwak, H.-I., and Su, S.-C., *Investigating endothelial invasion and sprouting behavior in three-dimensional collagen matrices.* Nature Protocols, 2009. **4**(12): p. 1888-1898.

249. Imani, R., Hojjati Emami, S., Parisa, R., Moshtagh, E., Baheiraei, N., Ali, Sharifi, M., Rahnama Moshtagh, P., and Sharifi, A. M., *Preparation and*

Characterization of Agarose-Gelatin Blend Hydrogels as a Cell Encapsulation Matrix: An In-Vitro Study. Journal of Macromolecular Science Part B Physics, 2012. **51**: p. 1606-1616.

250. Myers, K. M., Coudrillier, B., Boyce, B. L., and Nguyen, T. D., *The inflation response of the posterior bovine sclera.* Acta Biomaterialia, 2010. **6**(11): p. 4327-4335.

251. Boyce, B. L., Grazier, J. M., Jones, R. E., and Nguyen, T. D., *Full-field deformation of bovine cornea under constrained inflation conditions.* Biomaterials, 2008. **29**(28): p. 3896-3904.

252. Haojie, M., *Basic Finite Element Method as Applied to Injury Biomechanics*. 2018: Academic Press.

253. Elias De Oliveira, M., Hasler, C.-C., Zheng, G., Studer, D., Schneider, J., and Büchler, P., *A multi-criteria decision support for optimal instrumentation in scoliosis spine surgery.* Structural and Multidisciplinary Optimization, 2011. **45**(6): p. 917-929.

254. Bechlioulis, C. P. and Rovithakis, G. A., *Adaptive control with guaranteed transient and steady state tracking error bounds for strict feedback systems.* Automatica, 2009. **45**(2): p. 532-538.

255. Foos, R. Y. and Wheeler, N. C., *Vitreoretinal juncture. Synchysis senilis and posterior vitreous detachment.* Ophthalmology, 1982. **89**(12): p. 1502-1512.

256. Olsen, T. W., Sanderson, S., Feng, X., and Hubbard, W. C., *Porcine Sclera: Thickness and Surface Area.* Investigative Ophthalmology & Visual Science, 2002. **43**(8): p. 2529-2532.

257. Bray, M., *The effect of chilling, freezing, and rewarming on the postmortem chemistry of vitreous humor.* J Forensic Sci, 1984. **29**(2): p. 404-411.

258. Schoning, P. and Strafuss, A., *Postmortem Biochemical Changes in Canine Vitreous Humor.* Journal of Forensic Sciences, 1980. **25**(1): p. 53-59.

259. Abass, A., Eliasy, A., Geraghty, B., Elabd, M., Hassan, A., and Elsheikh, A., *Effect of freezing and thawing on the biomechanical characteristics of porcine ocular tissues.* J Biomech, 2019. **87**: p. 93-99.